Time domain non-Gaussian optimization of wind excited tall buildings under vulnerability constraints

Dissertation

submitted to and approved by the

Department of Architecture, Civil Engineering and Environmental Sciences
University of Braunschweig – Institute of Technology

and the

Faculty of Engineering
University of Florence

in candidacy for the degree of a
Doktor-Ingenieur (Dr.-Ing.) /
Dottore di Ricerca in Mitigation of risk due to natural hazards on structures and infrastructures[*)]

by
Seymour Milton John Spence
16.01.1978 from London (GB)

Submitted on	22 September 2009
Oral examination on	06 November 2009
Professorial advisors	Prof. Dieter Dinkler
	Prof. Massimiliano Gioffré

2009

*) Either the German or the Italian form of the title may be used.

Time Domain Non-Gaussian Optimization of Wind Excited Tall Buildings under Vulnerability Constraints

Seymour MJ Spence
University of Florence

The design of modern skyscrapers is dominated by numerous proposals for buildings of irregular geometric profile. However this newly found architectural freedom has complicated the structural analysis and successive optimization of tall buildings. Traditionally, both the analyses and optimization of these structures, is carried out considering a certain number of idealized equivalent static wind loads. These are calculated by firstly defining appropriate dynamic amplification factors derived from random vibration analyses carried out in the frequency domain, and secondly by combining aerodynamic information derived from wind tunnel tests using the high frequency force balance with non directional extreme wind models. This procedure has a number of shortcomings including the fact that the inherently directional nature of extreme wind climates is neglected, the impossibility of including higher modes in the dynamic description of the structural system as the high frequency force balance allows the estimation of only the first three generalized forces, the impossibility of considering any non-gaussian response features due to working in the more efficient but less versatile frequency domain, and lastly the danger of producing optimum structural systems the safety of which depend on the idealized static loads. This procedure can be justified to a certain extent for traditional prismatic tall buildings exhibiting uncoupled linear mode shapes as for these buildings the entity of the errors due to these simplifications are generally considered known and negligible. The adaptation of these techniques for the design of more general systems is the objective of numerous ongoing research projects. Another active research direction is that based on defining alternative and less restrictive procedures that can account for the previously cited difficulties. This thesis belongs to the second category.

The first objective of this work is to revisit the previously cited limitations and to assess their importance on the response of both regular and irregular buildings. Especially in light of the incredible increase in computational power which has opened the doors to the adoption of more sophisticated analyses techniques. In particular experimental wind tunnel tests were carried out on two tall buildings, one with a regular geometric profile and another with irregular vertical geometry. The importance of considering higher mode contributions in the response estimation of

building systems with non-linear coupled fundamental mode shapes and irregular geometry are investigated and compared to systems with regular profiles and uncoupled quasi linear mode shapes. It is seen that higher modes, and in particular their background components, play an important role in the accurate estimation of second order response characteristics. The particular sensitivity of coupled irregular systems is demonstrated. The presences of strong non-gaussian response features is seen for both systems which is in stark contrast to what can be found in literature for the response of tall buildings. The far greater sensitivity to wind direction of the geometrically irregular building is also observed.

The second objective of this research is the definition of a framework that rigorously combines the directional characteristics of both the extreme wind climate and building aerodynamics in a component-wise reliability model that ensures consistent estimates of responses with specified mean recurrence intervals. This objective is aimed at providing an alternative procedure to the common erroneous assumption that the mean recurrence interval or inverse of the annual probability of failure of a critical load effect may be estimated as the mean recurrence interval of the mean wind speed causing the response level. In particular a reliability model is proposed that introduces limit state functions with specified vulnerability levels. This allows for the identification of limit states, in terms of the maximum mean wind speeds for each wind direction (level cut sets), that allow for the rigorous estimation of the response levels with specified mean recurrence intervals through the resolution of time-invariant reliability integrals.

The third and final objective of the present research is the formulation of a component-wise reliability-based design optimization technique which allows for the automatic design of steel tall buildings subject to probabilistic constraints on both the member level capacity ratios as well as on the global inter-story drift ratios. To this end an efficient reliability-based design optimization scheme is proposed based on decoupling the traditionally nested optimization loop from the reliability analysis. The decoupling is achieved by assuming the level cut sets containing the mean wind speeds generating a response with specified exceedance probability independent of changes in the design variable vector. This hypothesis results in a series of conservative designs during convergence. The decoupled optimization problem is solved by defining a series of approximate explicit sub-problems in terms of the second order response statistics of the constrained functions.

To my family and in particular my mother... and to my future wife

ACKNOWLEDGEMENTS

A huge and heartfelt thanks to my friend and tutor Prof. Massimiliano Gioffrè for his never ending support, encouragement and invaluable advice over the past years. A special thanks to Prof. Vittorio Gusella for his always insightful comments and suggestions over the course of my studies. I would also like to thank Prof. Claudio Borri and Prof. Udo Peil for having the audacity to imagine and then realize the International Doctoral Course. A particular thanks to Dr. Emil Simiu and Prof. Mircea Grigoriu for the precious advice and encouragement they gave me during my stays at their Institutions. I would also like to thank Prof. Dieter Dinkler for his useful comments and suggestions in reviewing this work. A special thanks to my family, and in particular to my mother, for their unwavering support throughout this long and winding road. Finally I would like to thank Enrica Bernardini for her tremendous help and patience in correcting the final version of this manuscript.

Table of Contents

List of Tables

List of Figures

Preface

Recent trends in the design of tall buildings have seen an ever increasing number of proposals for super tall constructions with irregular geometric forms. However, the methods with which they are analyzed were developed primarily in the sixties and seventies and are based on a number of assumptions that hold true for tall buildings of a regular geometric form and uncoupled fundamental mode shapes. In particular, the inherently dynamic nature of the system is analyzed in the frequency domain. The reason for this was mainly dictated by the impossibility of efficiently solving large systems of ordinary differential equations. The global wind forces are derived from the base bending and torsional moments measured in specific wind tunnel tests using the High Frequency Force Balance (HFFB). This, at the time of its development, represented the only viable method for ascertaining wind loads on tall buildings. Instrumentation allowing the simultaneous measurement of hundreds of pressure taps did not yet exist. The dynamic characteristics are then combined with the loading information to produce a number of idealized Equivalent Static Wind Loads (ESWLs) used in the design and optimization of the structural system. This framework is classed as the traditional approach.

Inherent to this approach are a number of shortcomings. Firstly, by using the HFFB only the generalized forces of the fundamental modes can be estimated. Therefore, any resonant and background contributions of modes other than the first three cannot be considered. Secondly, because the dynamic analysis is carried out in the frequency domain, no information is known about the probabilistic nature of the extreme response. Thirdly, the definition of appropriate ESWLs is greatly complicated in the case of buildings with complex geometric forms and non linear coupled mode shapes. This leads to ever more conservative loads which ultimately defeat every purpose of optimizing the structural system.

The adequacy of considering only the fundamental mode shapes in the response analysis has it roots in a number of studies carried out on prismatic tall buildings with uncoupled modes shapes considering exclusively the alongwind and acrosswind response. From these studies it emerged that the relative importance of higher modes seemed negligible. However, no consideration was given to the effects that a more complex geometric profile may have on the results.

The loss of information concerning the probabilistic nature of the response is

bypassed by simply taking the response of tall buildings to be gaussian. This is motivated by citing the central limit theorem. While this may be true for certain geometric forms, it should not be so easily applied to the response of tall buildings which will depend, for certain wind directions, on highly non-gaussian wind pressure fields which may posses a high level of correlation therefore putting into doubt the applicability of the central limit theorem.

Optimization techniques used in the traditional design of tall buildings are reliant on the idealized ESWLs. A structure optimized under inadequate ESWLs can be dangerously susceptible to failure due to particular loading conditions not accounted for by the ESWLs. On the other hand, due to the nature of an idealized ESWL as an envelope incorporating various worse case loading scenarios, the load is unlikely to give an accurate description of the particular loading condition affecting an active constraint, therefore hindering the results achieved by the optimization algorithm.

The problems outlined above are the main motivations for this study. The research entails two main stages. Firstly experimental wind tunnel tests are carried out on two 1/500 scale tall buildings using 126 simultaneously measured pressure taps considering a full range of wind directions. The two buildings are characterized by their geometric profiles. One has a regular prismatic form while the other has a complex irregular geometry. In particular the irregular building is the Bank of China building. From the pressure measurements the wind loads for each building are estimated. By defining a coupled dynamic system for the Back of China building, calibrated to the effective modal characteristics as reported in literature, and an uncoupled dynamic system of similar characteristics for the regular building, a thorough investigation of the two responses is carried out. In particular the effects of mode truncation are explored considering a full range of wind directions for both the dynamic systems highlighting important differences. Then a systematic study is carried out into the effects of complex geometric profiles and coupled dynamic systems on the hypothesis of gaussianity of the response of tall buildings. Again this is carried out for a full range of wind directions highlighting an incredible sensitivity of the results to this parameter and to the buildings profile. The difference in importance of the background dynamic response between the two systems is then investigated.

Secondly the structural optimization of tall frameworks is reexamined with the goal of defining an efficient Reliability-Based Design Optimization (RBDO) procedure that avoids the need to define ESWLs. Not only that, but a formulation is searched that allows the optimization of the structure to rigorously estimated reliability levels while considering multiple load cases and component-wise probabilistic constraints on both local and global responses. In particular, each local and global response component with a specified acceptable annual probability of failure, or inverse of the Mean Recurrence Interval (MRI), is to be carried out while rigorously combining the aerodynamic and climatological information through a component-wise reliability model that is capable of accurately handling highly non-linear limit state functions.

Chapter 1

Tall Buildings and the Wind Hazard

The purpose of this chapter is to introduce the reader to the basic definition of the wind hazard and how this affects the design of tall buildings. Two areas will be examined. Firstly the diffrent extreme wind events that ultimatly define the wind hazard for a given region will be introduced. Secondly the wind directionality problem will be extensivly reviewed with emphasis on the shortcomings of current approches when applied to the design of tall buildings.

1.1 The wind Hazard

The windstorms that characterize the wind hazard in a given site are produced by the transformation of thermal energy through thermodynamic and mechanical phenomena into mechanical energy giving rise to air motion and so wind. Various forms of windstorms may be produced by this transformation.

Extra-tropical storms are generated by the collision, at and above midlatitudes, of cold polar air transported by easterly winds and hot tropical air carried by westerly winds. The collision of these two weather fronts characterized by very different air temperatures generates large scale windstorms known as extra-tropical storms [1.16]. These storms occur over a very large area, in the order of thousands of kilometers, and have a weak vortex structure giving rise to what are known as straight winds.

Hurricanes are defined as tropical cyclones exhibiting sustained winds of 120 km/h or more. Tropical cyclones, known as typhoons in the Far East and simply as cyclones in Australia and the Indian Ocean, are generated by the latent heat released as a result of the condensation of water vapor over warm tropical oceans. The structures of tropical cyclones are defined by translating vortexes with diameters that can reach hundreds of kilometers, figure 1.1. They are relatively small

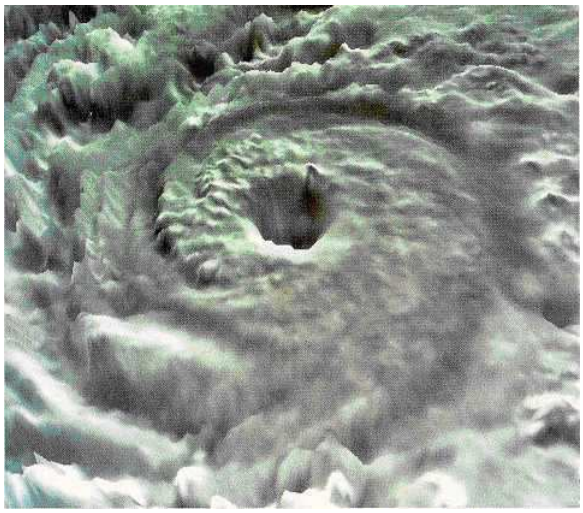

Figure 1.1: Typical vortex structure of a hurricane.

compared to extra-tropical storms but can generate some of the most destructive winds on earth. At the center of the vortex, known as the eye of the storm, there is a region of relatively calm winds. Surrounding the eye is the region of most intense winds and rainfall called the eye wall. The winds in this region are vertical. Outside the eye wall are weaker horizontal winds. Where the two regions intersect the wind flow presents a strong updraft which is not accounted for in current engineering practice. Because of the meteorologically speaking small size and relative low frequency of these events, adequate sampling can be hard to obtain.

Furthermore, there are many types of local storms that affect a variety of regions. Some common events include Foehn winds which develop downwind of mountain ridges, jet-effect winds that occur in topographical features such as gorges, and Tornadoes which are vortex like storms that can generate winds in excess of 400 km/h and are among some of the most severe extreme wind events on earth. One of the most common local storm events is the thunderstorm. The essential conditions for the development of thunderstorms is the existence of warm moist air in the lower atmosphere coupled with colder dense air at higher altitudes. This causes the warm moist air to rise leading to the formation of heavy rain drops due to condensation. The falling rain drops drag down the surrounding air generating what is known as a downdraft with wind speeds that can exceed 110 km/h.

1.2 The Atmospheric Boundary Layer

In the design of structures against wind it is the wind flow within the vicinity of the building which is of interest. Therefore the study of the lowest few hundred meters of the atmosphere is of fundamental interest. This region of the atmosphere is termed the atmospheric boundary layer. This region can be defined as the region of the Earth's atmosphere where the effects of the surface (friction, heating and cooling) are felt directly on a time scale of less than a day, and in which significant fluxes of momentum, heat or matter are carried by turbulent motions on a scale of the order of the depth of the boundary layer or less [1.14]. A couple of features of the boundary layer that are of particular interest to the design of wind sensitive structures are the variations with height of the mean wind profile and the atmospheric turbulence. The following paragraphs will briefly describe the models used to define these features.

1.2.1 Wind profiles

The nearer the air flow is to the surface of the earth the slower it will move. This is due to shear stress brought about by the roughness of the surface of the earth. As the distance from the surface increases so does the wind speed creating a profile. The exact shape of this profile depends on the particular surface roughness. At a certain height above the ground the influence of the surface roughness is negligible. This height is referred to as the gradient height and also depends on the surface roughness. In a state of equilibrium (i.e. the mean vertical velocity profile remains constant with streamwise distance) typical of strong wind conditions, the gradient height typically varies from 270 m over open terrain to about 500 m over urban areas [1.11, 1.10]. It should also be observed that for equilibrium conditions to be present in the atmospheric boundary layer the free wind must travel a significant distance over a constant surface roughness. When equilibrium is reached, the momentum required to overcome the surface shear stress exactly balances the supplied momentum [1.7].

Various mathematical models exist for describing the variation with height of the mean wind vector within the atmospheric boundary layer. One such model for horizontally homogeneous terrain is the power law given by the expression:

$$\bar{V}(z) = \bar{V}(z_{ref}) \left(\frac{z}{z_{ref}} \right)^{\alpha} \tag{1.1}$$

where $\bar{V}(z)$ is the mean wind speed at height z; $\bar{V}(z_{ref})$ is the wind speed at a reference height z_{ref} which is generally 10 m above the ground. The exponent α is a characteristic of the underlying roughness of the surface which increases in value for increased roughness and of the averaging time used to describe mean wind vector; it has typical values of 0.17 in open country terrain and 0.24 for an average urban environment.

The power law model provides adequate correlation with experimental data for the upper region of the atmospheric boundary layer [1.7, 1.8]. However for the lower

regions, which are of greatest interest to the design of buildings, the power law is in general insufficient.

A mathematical model capable of adequately describing the lower regions of the atmospheric boundary layer is the logarithmic law. Indeed this model has long superseded the power law in metrological practice and is also used in the Eurocode [1.1] and in the commentary to the ASCE 7-05 Standard [1.2]. This model is described by the following expression:

$$\bar{V}(z) = \frac{1}{k} u_* In \frac{z}{z_0} \tag{1.2}$$

where $k \simeq 0.4$ is the von Kármán constant, u_* is the surface friction velocity (if τ_s is the surface shear stress, $\tau_s = \rho_a u_*^2$, where ρ_a is the density of air) and z_0 is an empirical measure of the surface roughness called the roughness length. Appropriate values for z_0 can be found in both the Eurocode [1.1] and the ASCE 7-05 commentary [1.2]. One of the more recent classifications for various roughness types can be found in [1.34].

The mean wind speed vector not only increases with height but also rotates somewhat with respect to its direction near the surface. This horizontal rotation is known as the veering angle and is clockwise in the northern hemisphere and anticlockwise in the southern hemisphere. For buildings of heights between 300 to 500 m the veering angle can reach values of 7° to 10° with respect to the mean wind speed vector at 10 m elevation [1.29]. This angle, function of height, is generally neglected in most engineering applications as it is in general of the order of the resolution of the measured wind direction. However as the need and desire to use more refined resolutions increases this will no longer be the case and the veering angle will have to be considered.

Finally, it should be observed that due to the turbulent nature of the wind flow within the atmospheric boundary layer the mean wind vector depends on the averaging time. Indeed the shorter this is the higher the resulting average will be. Due to the variety of averaging times adopted in international codes and standards there exists various approximate expressions that allow the comparison of wind speeds averaged over different times [1.29, 1.31].

1.2.2 Atmospheric turbulence

Atmospheric turbulence is what characterizes the air flow within the boundary layer. It is turbulence that gives the wind speed its distinctive fluctuating nature. It is generated by the formation of large systems of eddies, local vortices, that decay into smaller ones. The eddies are generated by surface roughness (mechanical turbulence) and convective movements (metrological turbulence). For intense wind speeds, like those in storms, the metrological component can be neglected. This situation is defined as a neutrally stable condition [1.26]. The surface roughness

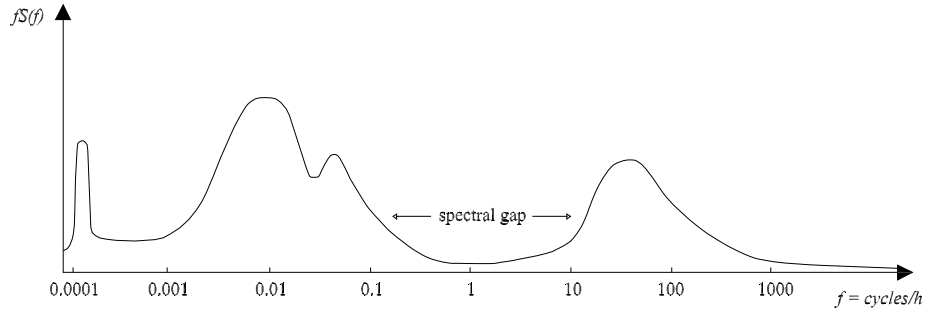

Figure 1.2: Van der Hoven spectrum.

plays an important role in determining the turbulence of a certain air flow. The greater the roughness the greater the turbulence will be.

In 1957 Van der Hoven [1.32] calculated the spectrum of the longitudinal fluctuating wind speed as shown in figure 1.2. From the analysis of the spectrum it is clear that the energy content of the fluctuating wind speed can be divided into two distant regions, one of low frequency content and another of high frequency content (atmospheric turbulence). These two regions are divided by what is known as the spectral gap that ranges between periods of 10 minutes to 1 hour. It is this feature of the boundary layer wind flow that allows the stochastic wind field to be modeled by a mean component, function of time, and by a probabilistically stationary fluctuating component function of both time and space.

The region of high frequency content of the wind field is of particular interest to the design of tall buildings as it is this contribution that can cause significant dynamic effects due to resonance [1.31]. Many approximate expressions exist that attempt to describe the high frequency region of the longitudinal fluctuating wind [1.20, 1.28, 1.9]. One of the more widely used is that proposed by Von Kármán which is given by the following expression:

$$\frac{fS_{V_x}(f)}{\sigma^2_{V_x}} = \frac{4f_r}{(1+70.8f_r^2)^{\frac{5}{6}}} \tag{1.3}$$

where f is the frequency, S_{V_x} is the power spectral density function of the longitudinal wind speed, σ_{V_x} is the standard deviation and f_r is the reduced frequency defined as a function of the integral length scale through the equation:

$$f_r = \frac{fL_{V_x}}{\bar{V}_x} \tag{1.4}$$

where $\bar{V}_x$ is the mean wind speed and L_{V_x} is known as the integral length scale.

The integral length scale is in its own right an important descriptor of the turbulence of an air flow. It is of the average size of the gusts carried in the

mean flow. There are nine scales of turbulence corresponding to the three spatial dimensions. The scales of turbulence represent the length, width, and height of the gusts in each of the three spatial dimensions. Of interest for the design of buildings are the integral scales in the direction of the mean flow (longitudinal direction), L_{V_x}, L_{V_y} and L_{V_z} which are the gust sizes in the along wind direction, in the across wind direction, and in the vertical direction, respectively. The longitudinal integral scale, L_{V_x} is evaluated by:

$$L_{V_x} = \bar{V}_x(z) \int_0^\infty C_x(\delta)\ d\delta \tag{1.5}$$

where $\bar{V}_x(z)$ is the mean longitudinal wind speed at height z; $C_x(\delta)$ is the auto-correlation function for fluctuations in the longitudinal direction. Information on appropriate turbulence lengths is quite uncertain. Measurements seem to suggest that L_{V_x} increases with height above ground as the terrain roughness increases [1.31].

Another important descriptor of turbulence is the turbulence intensity, I, given at a height above ground z, as:

$$I_z = \frac{\sigma_{V_x}(z)}{\bar{V}_x(z)} \tag{1.6}$$

where σ_{V_x} is the standard deviation of the wind speed at height z: the smoother the terrain the less the turbulence intensity will be.

1.2.3 Dependency between wind flow and storm type

The models presented in this section were developed for strong straight winds like those classically found in synoptic wind events. Models for other types of extreme wind events, such as hurricanes and thunderstorms, may vary from these models. In the case of hurricanes it appears that, for sufficiently large distances from the eye of the storm, winds seem to take on a relatively straight nature [1.30] with a profile similar to that encountered for synoptic events for heights up to 500 m [1.31]. Above 500 m wind speeds appear to decrease [1.27]. It has been observed that hurricanes also present some transient non-stationary features [1.22, 1.36, 1.33]. The quantification of the non-stationary nature of hurricane winds on tall buildings, and buildings in general, is still an open problem. In 2000 Kawai [1.22] addressed the influence of time varying typhoon mean wind speed on the structural response of tall buildings using a quasi-stationary model which was considered applicable only when the structural natural period is sufficiently small compared to the time scale of variation of the mean wind speed.

In current practice thunderstorms are also modeled as straight winds with the condition that the 3 s peak gust at 10 m above ground is the same for both flows. Due to the local nature of thunderstorms this is considered conservative [1.29]. It should be observed however that thunderstorms present significantly different

properties to strong straight synoptic winds in terms of their unique mean wind speed profiles, rapid time varying mean wind speed, and spatially strongly correlated wind fluctuations [1.13, 1.25]. Characterization and modelling of these transient winds and their effects on structures through field observations, numerical, and physical simulations have been receiving increasing attention in recent years [1.21, 1.4, 1.6, 1.17, 1.18, 1.15, 1.19, 1.35, 1.5, 1.24]. However no model or unified approach for dealing with these effects has yet emerged. Indeed the study of thunderstorms and appropriate models for describing them is still a very open problem.

The scope of this thesis is not the in depth modelling of hurricanes and thunderstorms. The models adopted will be based on the current practice therefore considering them as stationary events that can be described from the models developed for strong straight winds. While this hypothesis is strong in the case of thunderstorms, it is not considered restrictive for hurricanes, especially for a sufficient distance from the eye of the storm a condition which is nearly always satisfied.

1.3 The wind directionality problem

Under the assumption that aeroelastic effects are negligible, any response $R(\bar{V}, \alpha)$ of a linearly elastic structure excited by a wind speed $\bar{V}$ blowing from direction α may be expressed in the following form:

$$R(\bar{V}, \alpha) = a(\alpha)\bar{V}^{b(\alpha)} \tag{1.7}$$

where $a(\alpha)$ and $b(\alpha)$ are directional constants. Equation (1.7) explicitly accounts for the directional properties of the wind climate through $\bar{V}$ and the directional aerodynamics of the structure through $a(\alpha)$ and $b(\alpha)$. Both $a(\alpha)$ and $b(\alpha)$ depend in fact on the particular aerodynamic characteristics of the structure for a given direction. In the case of dynamically sensitive structures, they may be estimated through dynamic analysis of the structure subject to loads gathered through appropriate wind tunnel tests. For rigid structures $b(\alpha) = 2$ while for dynamically sensitive such as a tall building, $b(\alpha)$ will generally assume values between 2 and 3.

If the response of interest is the external pressure, than $a(\alpha)$ is proportional to the peak pressure coefficient $\mathcal{C}_{pk}(\alpha)$ with proportionality factor $\rho_a/2$, where ρ_a is the density of air. In particular $b(\alpha)$ will be equal to 2 even for dynamically sensitive structures giving:

$$\mathcal{P}(\bar{V}, \alpha) = \frac{\rho_a}{2}\mathcal{C}_{pk}(\alpha)\bar{V}^2 \tag{1.8}$$

Because the external pressure is independent of the dynamic characteristics of a structure if aeroelastic effects are neglected, in order to define equivalent static wind loads based on the external pressure distribution a dynamic argumentation factor is necessary that accounts for the dynamic nature of the structure. This factor is however itself a function of the incident wind direction.

1.3.1 Non directional models: the codes

The approach of standards and codes for estimating the global response of any structure, dynamic or not, is the definition of a number of appropriate equivalent static wind loads based on equation (1.8) and, so, on the external pressure field. This is achieved through the definition of a suitable extreme wind climate, $\bar{V}$, and a number of coefficients that take into consideration factors such as site topography, site exposure and the eventually dynamic sensitivity of the building under consideration.

The extreme wind climate $\bar{V}$ will not in general depend on direction. Practically, this means that all the directional wind speeds are amassed into a single directionless population on which a probabilistic model is inferred. From this model, directionless design wind speeds can be determined. The dependency of the response on the directional characteristics of both structural aerodynamics and extreme wind climate is then accounted for through a directionality factor. For instance the approach specified in the analytical procedure of the ASCE 7 standard [1.2] consists in defining a wind directionality factor, K_d, that multiplies the response obtained from simultaneously considering the aerodynamically most severe direction excited by the maximum extreme wind speed. In terms of (1.8) the situation is represented as:

$$\mathcal{P}(\bar{V}, \alpha) = K_d \frac{\rho_a}{2} \max[\mathcal{C}_{pk}(\alpha)] \max[\bar{V}^2(\alpha)] \tag{1.9}$$

This procedure is conceptually equivalent to rotating the building about its vertical axis so that the aerodynamically most unfavorable direction coincides with the direction of the largest wind speed during a year or a storm, and then multiplying the wind effect so obtained by K_d. Therefore K_d has the onerous task of estimating the probability of this scenario. The Eurocode [1.1] also defines a directional factor, $\mathcal{C}_{dr}$. However it leaves the determination of appropriate values to the various national annexes while recommending a value of 1 which is equivalent to not considering directional effects at all.

One of the difficulties in trying to define a coefficient to account for the directional aerodynamic and wind climate characteristic is the large number of parameters on which it depends. Indeed not only does it depend on the wind climate, building aerodynamics and particular building orientation, but it can also be shown to depend on the Mean Recurrence Interval (MRI) of the desired wind effect [1.3]. It is therefore unreasonable to think that a blanket value can guarantee satisfactory results.

It should also be observed that directional effects are greatly amplified in the case of dynamically sensitive structures such as tall buildings. Indeed the response of this type of structure will be far more sensitive to small changes in wind direction due to the insurgence of resonance. This means that any semi-empirical directionality factor runs the risk of severely underestimating or overestimating the actual wind effect. It must be understood however that wind codes and standards have the tremendously difficult task of reducing to a bare minimum the fundamentally com-

plex wind structure interaction phenomena. Therefore it could be argued that, for rigid structures at least, the simplifications used in defining the wind directionality factor is in line with other assumptions like those used to reduce the vast quantity of aerodynamic data to a few numbers contained in tables and plots. Indeed dynamically sensitive structures are in reality only covered to a certain extent by codes and standards with limitations placed on both height and expected resonant amplification. Therefore codes, by their own admittance, should not be the only source of information on the wind effects on tall buildings that are expected to have significant resonant amplification.

The remainder of this section will be dedicated to examining several detailed approaches used in conjunction with wind tunnel tests with the aim of accounting for the directional dependency that a particular response has on the aerodynamic and extreme wind climate.

1.3.2 Directional models

Sector by sector approach

Due to its simplicity the sector by sector approach is probably one of the most widely adopted techniques used to account for the wind directionality problem. The approach is based on separate estimates of the effects induced by wind blowing from each of the sectors of the compass, that is, by each of the sectorial wind speeds.

To illustrate the technique imagine defining $i = 1, 2, ..., q$ sectors for which the extreme wind speeds, $\bar{V}_i$, are known for various MRIs. Now consider the sectorial responses of a particular wind effect $R_i(\bar{V}_i(N)) = a_i \bar{V}_i^{b_i}(N)$ obtained considering the sectorial wind speeds $\bar{V}_i(N)$ all with the same MRI of N years. The sectorial design criterion consists in taking the largest of the sectorial responses $R_m = \max_i[R_i(\bar{V}_i(N))]$ with the belief that this represents the largest response with an MRI of N years. However it can be demonstrated that this is not the case. Indeed the response obtained this way will have an MRI that must be less than N years [1.29]. This important result will be demonstrated in the following.

Denoting with $\hat{i}$ the sector in which R_m occurs, from the definition of the sectorial design criterion the response $R_m = R_{\hat{i}} = R_i(\bar{V}_{\hat{i}}(N))$ has a probability of non occurrence during a year of $P_R(R \leq R_m) = 1/(1 - 1/N)$ which corresponds to a MRI of N years. The wind speeds blowing from sectors other than $\hat{i}$ that will induce the same response R_m by definition must have an MRI greater than N. However there will in general exist a wind speed blowing from a sector other than $\hat{i}$ that will induce the response R_m. This will be true for all sectors. Therefore denoting with $\hat{\bar{V}}(N_i)$, $(i = 1, 2, ..., q)$ the sectorial wind speeds that induce the response R_m, the probability that $R \leq R_m$ regardless of wind direction is equal to the probability that $\bar{V}_1 \leq \hat{\bar{V}}_1(N_1)$ and $\bar{V}_2 \leq \hat{\bar{V}}_2(N_2)$ and,..., and $\bar{V}_q \leq \hat{\bar{V}}_q(N_q)$, therefore:

$$P_R(R \leq R_m) = \text{Prob}[\bar{V}_1 \leq \hat{\bar{V}}_1(N_1), \bar{V}_2 \leq \hat{\bar{V}}_2(N_2), ..., \bar{V}_q \leq \hat{\bar{V}}_q(N_q)] \tag{1.10}$$

By assuming that the speeds $\bar{V}_1, \bar{V}_2, ..., \bar{V}_q$ are mutually independent it follows from (1.10) that:

$$\begin{aligned} P_R(R \leq R_m) = \text{Prob}[\bar{V}_1 \leq \hat{\bar{V}}_1(N_1)]\text{Prob}[\bar{V}_2 \leq \hat{\bar{V}}_2(N_2)]... \\ \text{Prob}[\bar{V}_q \leq \hat{\bar{V}}_q(N_q)] < \frac{1}{1-\frac{1}{N}} \end{aligned} \tag{1.11}$$

which means that the MRI of the response R_m is in reality less than N years. Obviously the sectorial wind speeds are not independent, however for the sector by sector approach to properly predict the MRI of the response the wind speeds would have to be perfectly correlated. A condition that is obviously impossible. Therefore the sector by sector approach is unconservative.

Approach based on the mean outcrossing rate

An alternative method for estimating the N year response $R_N(V, \alpha)$ (where $\bar{V}$ is indicated simply by V in the rest of this section for the sake of clarity) that attempts to account for the directional aerodynamic and extreme wind climate is the approach based on the estimation of the mean outcrossing rate of an appropriate 2-dimensional limit state boundary. Indeed by rearranging (1.7) it is possible to estimate the wind speed $V_R(\alpha)$ necessary to induce in the structure a response level R for a wind direction α. The equation is shown below:

$$V_R(\alpha) = \left[\frac{R}{a(\alpha)}\right]^{\frac{1}{b(\alpha)}} \tag{1.12}$$

By varying the direction of the wind speed in the interval $[0, 2\pi]$ it is possible to construct a 2-dimensional limit state boundary in the $V - \alpha$ space representing the wind velocity necessary to induce the response R. A typical boundary for various response levels is shown in figure 1.3. In the life time of a structure, the wind speed will vary both in direction and speed describing a continuous curve in the $V - \alpha$ space. It is the estimation of the average number of times that this curve up-crosses the various boundaries that is of interest.

By considering the reference system defined by the normal n, and tangent s, to the response boundary, (figure 1.3), it can be shown that the two dimensional out-crossing rate is given by:

$$N(R) = \int_{\delta R} \int_0^{\infty} p_1(v_n, v_s) \dot{v}_n g_{\dot{V}_n | V_n, V_s}(\dot{v}_n | v_n, v_s) d\dot{v}_n dv_s \tag{1.13}$$

where v_n and v_s are the normal and tangential components of the wind velocity vector V with respect to the response boundary δR; p_1 is the joint probability density function of the of v_n and v_s; $\dot{v}_n$ is derivative process of V normal the boundary response while g is the probability density function of $\dot{v}_n$ conditional on $V = V_R$.

From a practical point of view it is far more convenient to write (1.13) in polar coordinates using the following transformation:

$$p_1(v_n, v_s) = \frac{1}{V} p(V, \alpha) \tag{1.14}$$

$$dv_s = \sqrt{1 + \left(\frac{1}{V_R}\frac{dV_R}{d\alpha}\right)^2} V_R d\alpha \tag{1.15}$$

$$\dot{v}_n = (\dot{V}_R + \frac{dV_R}{d\alpha}\dot{\alpha})\sqrt{1 + \left(\frac{1}{V_R}\frac{dV_R}{d\alpha}\right)^2} \tag{1.16}$$

This allows (1.13) to be written in the following way:

$$N(R) = \int_0^{2\pi}\int_0^{\infty} p(V, \alpha)\dot{v}_n f_{\dot{V}_n|V_R,\alpha}(\dot{v}_n|V_R, \alpha)\sqrt{1 + \left(\frac{1}{V_R}\frac{dV_R}{d\alpha}\right)^2} d\alpha d\dot{v}_n \tag{1.17}$$

where p is the joint probability density function between V_R and α. While the estimation of p is quite straightforward through the use of a generalized Weibull distribution, the unbiased and reliable estimation of the averages $E[\dot{V}_n(\dot{V}, \dot{\alpha}, V_R, \alpha)g(\dot{V}|V_R, \alpha)]$ represents the biggest obstacle to the implementation of this method.

A widely adopted technique for estimating $N(R)$, first proposed in [1.12], consists in considering firstly the random process defined by the wind velocity independent

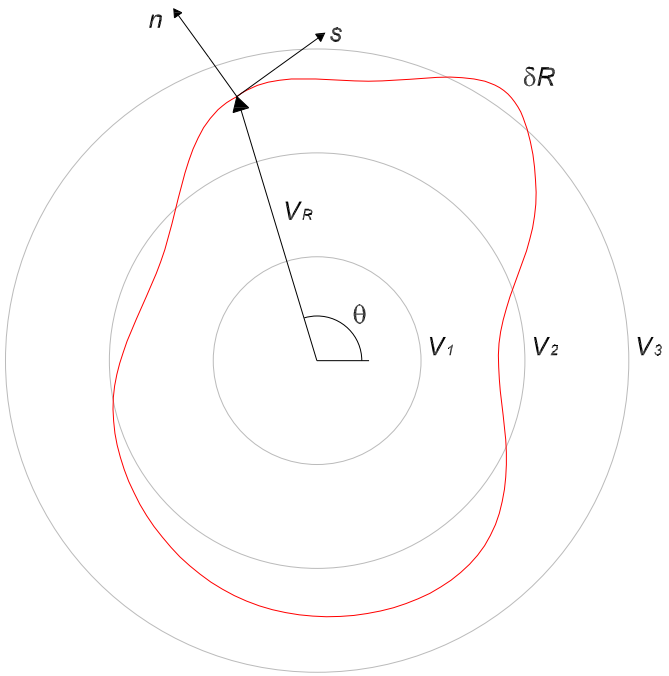

Figure 1.3: Typical response boundary.

from the derivative process $\dot{V}_n$ and secondly the derivative processes $\dot{V}$ and $\dot{V}_n$ interchangeable. These hypotheses are equivalent to considering the dependency on wind direction of the average $E[\dot{v}_n g_{\dot{V}_n|V_n,V_s}(\dot{v}_n|v_n,v_s)]$ to be negligible, a proposal deemed unacceptable by some authors [1.29] given the anisotropy of the wind vector process. These assumptions allow (1.17) to take on the following form:

$$N(R) = \int_0^\infty \dot{V} f_{\dot{V}}(\dot{V}) dV \int_0^{2\pi} p(V_R, \alpha) \sqrt{1 + \left(\frac{1}{V_R}\frac{dV_R}{d\alpha}\right)^2} d\alpha \tag{1.18}$$

This allows the average $E[\dot{V} f_{\dot{V}}(\dot{V})]$ to be estimated directly from a non directional model of the wind climate. In particular if the derivative process is considered to be not only independent from the process V, but also normally distributed, than the average $E[\dot{V} f_{\dot{V}}(\dot{V})]$ may be estimated through the expression:

$$\int_0^\infty \dot{V} f_{\dot{V}}(\dot{V}) dV = \sqrt{2\pi}\nu\sigma_V \tag{1.19}$$

in which σ_V is the standard deviation of the s wind climate model while ν is the cycling rate of this climate model given by:

$$\nu = \frac{1}{2\pi}\frac{\sigma_{\dot{V}}}{\sigma_V} \tag{1.20}$$

where $\sigma_{\dot{V}}$ is the standard deviation of the derivative process. This allows equation (1.13) to be written as:

$$N(R) = \sqrt{2\pi}\nu\sigma_V \int_0^{2\pi} p(V_R, \alpha) \sqrt{1 + \left(\frac{1}{V_R}\frac{dV_R}{d\alpha}\right)^2} d\alpha \tag{1.21}$$

with ν expressed in terms of occurrences per annum, $N(V_R)$ gives the yearly crossing rate. Consequently the return period for the response level V_R is:

$$T(R) = \frac{1}{N(R)} \tag{1.22}$$

While formally elegant, it has been observed that methods based on the estimation of the mean out-crossing rates, and particular equation (1.21), tend to underestimate the response with specified MRIs, a concern observed in [1.29]. As mentioned the difficulty in this approach is mainly in estimating the averages $E[\dot{v}_n g_{V_n|\dot{V}_n,V_s}(\dot{v}_n|v_n,v_s)]$. In the formulation presented herein, the assumption that $E[\dot{v}_n g_{V_n|\dot{V}_n,V_s}(\dot{v}_n|v_n,v_s)]$ does not depend on the wind direction is seen as particularly severe especially for wind climates characterized by the presence of hurricanes which have a significant directional swing during their passage. It should also be observed that by assuming $\dot{V}$ normally distributed alongside the independence of $\dot{V}$ from V_R, will in general lead to underestimation of the mean crossing-rate in the case of non gaussian processes such as V. Another formulation to estimate the mean out-crossing rate can be found in [1.23]. This method uses another set of equally strong assumptions in order to estimate $N(R)$. In particular it is necessary to estimate not only $\dot{V}$ but also $\dot{\alpha}$ which presents a number of practical difficulties.

1.3.3 An open problem

The wind directionality problem outlined above represents an open problem that is often overlooked. This is probably because for standard buildings wind is not usually the governing effect or at least is in line with other effects. Therefore simple non-directional approach is indeed adequate. This is not the case however for wind sensitive structures such as tall buildings where the proper combination of aerodynamic and climatological information is paramount for guaranteeing an adequate level of safety and ensuring an economical design solution.

Bibliography

[1.1] *Actions on structures General action Part 1-4: Wind action, prEN 1991-1-4:*. 2004.

[1.2] *Minimum design loads for buildings and other structures*. ASCE 7-05, American Society of Civil Engineers, Reston, VA, 2005.

[1.3] R. Antonio, C. C. P., and E. Simiu. Database assisted design and wind directionality effects. In *Bluff body aerodynamics and applications, 4th international colloquium*, pages 213–216, Bocham, 2000.

[1.4] M. T. Chay, F. Albermani, and R. Wilson. Numerical and analytical simulation of downburst wind loads. *Eng. Struct.*, 28:240254, 2006.

[1.5] M. T. Chay and C. W. Letchford. Pressure distributions on a cube in a simulated thunderstorm downburst. part a: Stationary downburst observations. *J. Wind. Eng. Ind. Aerodyn.*, 90:711732, 2002.

[1.6] E. C. C. Choi. Field measurement and experimental study of wind speed profile during thunderstorms. *J. Wind. Eng. Ind. Aerodyn.*, 92:275290, 2004.

[1.7] N. J. Cook. *The designers guide to wind loading of building structures Part 1: Background, Damage Survey, Wind Data and Structural Classification*. Butterworths, London, 1986.

[1.8] N. J. Cook. *The designers guide to wind loading of building structures Part 2: Static structures*. Butterworths, London, 1990.

[1.9] A. G. Davenport. The spectrum of horizontal gustiness near the ground in high winds. *Quart. J. Roy. Meteorol. Soc.*, 87:194–211, 1961.

[1.10] A. G. Davenport. The dependence of wind loads on meteorological parameters. *Proc. International Seminar on Wind Effects on Buildings and Structures*, 1967.

[1.11] A. G. Davenport. The relationship of wind structure to wind loading. *Symposium on Wind Effects on Buildings and Strutures*, 1974.

[1.12] A. G. Davenport. The prediction of risk under wind loading. In *2nd International Conference on Structural Safety and Reliability*, pages 511–538, Munich, Germany, 1977.

[1.13] T. T. Fujita. Downbursts: Meteorological features and wind field characteristics. *J. Wind. Eng. Ind. Aerodyn.*, 36:7586, 1990.

[1.14] J. R. Garrat. *The atmospheric boundary layer*. Cambridge University Press, Cambridge, 1992.

[1.15] K. D. Gast and J. L. Schroeder. Supercell rear-flank downdraft as sampled in the 2002 thunderstorm outflow experiment. In *Int. Conf. on Wind Engineering (11ICWE)*, page 22332240, Lubbock, Tex., 2003.

[1.16] L. Gomes and B. J. Vickery. *On the Prediction of Extreme Wind Speeds from Parent Distribution*. University of Sydney, Sydney, 1974.

[1.17] F. L. Haan, P. P. Sarkar, and N. Spencer-Berger. An active method for nonstationary wind gust generation. In *11th Int. Conf. on Wind Engineering (11ICWE)*, page 22412248, Lubbock, Tex., 2003.

[1.18] H. Hangan, Z. Roberts, D. Xu, and J.-D. Kim. Downburst simulation: Experimental and numerical challenges. In *11th Int. Conf. on Wind Engineering (11ICWE)*, page 22412248, Lubbock, Tex., 2003.

[1.19] J. D. Holmes and S. E. Oliver. An empirical model of a downburst. *Eng. Struct.*, 22:11671172, 2000.

[1.20] J. C. Kaimal. Spectral characteristics of surface-layer turbulence. *J. Royal Meteorol. Soc.*, 98:563–589, 1972.

[1.21] A. Kareem, K. Butler, and D. Kwon. Modeling and simulation of transient wind load effects. In *4th USJapan Workshop on Wind Engineering (UJNR)*, page 159168, Tsukuba, Japan, 2006.

[1.22] H. Kawai. Response of structure during a typhoon wind. In CD-ROM, editor, *8th ASCE Specialty Conf. on Probabilistic Mechanics and Structural Reliability (PCM-2000)*, pages 1–6, 2000.

[1.23] M. F. Lepage and P. Irwin. A technique for combining historical wind data with wind tunnel tests to predict extreme wind loads. In *USNCWE*, pages 71–78, 1985.

[1.24] C. W. Letchford and M. T. Chay. Pressure distributions on a cube in a simulated thunderstorm downburst. part b: Moving downburst observations. *J. Wind. Eng. Ind. Aerodyn.*, 90:733753, 2002.

[1.25] C. W. Letchford, C. Mans, and M. T. Chay. Thunderstorms-their importance in wind engineering (a case for the next generation wind tunnel). *J. Wind. Eng. Ind. Aerodyn.*, 89:3143, 2001.

[1.26] H. A. Panofsky and J. A. Dutton. *Atmospheric Turbulence: Models and Methods for Engineering Applications*. John Wiley Sons, New York, 1984.

[1.27] M. D. Powell, T. A. Reinhold, and P. J. Vickery. Reduced drag coefficient for high wind speeds in tropical cyclones. *Nature*, 422:279283, 2003.

[1.28] E. Simiu. Wind spectra and dynamic alongwind response. *J. Struct. Div.*, 100:1897–1910, 1972.

[1.29] E. Simiu and T. Miyata. *Design of Buildings and Bridges for Wind*. John Wiley Sons, Hoboken, New Jersey, 2006.

[1.30] E. Simiu, V. C. Patel, and J. F. Nash. Mean wind profiles in hurricanes. *J. Eng. Mech. Div., ASCE*, 102:265273, 1976.

[1.31] E. Simiu and R. H. Scanlan. *Wind effects on structures: Fundamentals and applications to design 3rd Ed.* Wiley-Interscience, New York, 1996.

[1.32] I. Van der Hoven. Power spectrum of horizontal wind speed in the frequency range from 0.0007 to 900 cycles per hour. *Journal of Meteorology*, 14:160–164, 1957.

[1.33] L. Wang and A. Kareem. Modeling and simulation of transient winds in downbursts/hurricanes. In CD-ROM, editor, *10th Americas Conf. on Wind Eng. (10ACWE)*, pages 1–12, 2005.

[1.34] J. Wieringa. Representative roughness parameters for homogeneous terrain. *Boundary-Layer Meteorology*, 63(4):323–363, 1993.

[1.35] G. S. Wood, K. C. S. Kwok, N. A. Motteram, and D. F. Fletcher. Physical and numerical modeling of thunderstorm downbursts. *J. Wind. Eng. Ind. Aerodyn.*, 89:535552, 2001.

[1.36] Y. L. Xu and J. Chen. Characterizing nonstationary wind speed using empirical decomposition. *J. Struct. Eng.*, 130(6):912920, 2004.

Chapter 2

Traditional methods for the Wind Analysis of Tall Buildings

The response analysis of tall buildings subject to extreme wind events has been the focus of numerous studies and experimental research. Over the years various methods have emerged to form a well established and universally accepted approach. These methods are however based on a number of hypotheses, some more reasonable then others. This chapter will attempt to describe what has now become the traditional approach to the design and analysis of tall buildings against extreme wind events. In particular, effort will be made to highlight those hypotheses that are deemed obsolete in light of recent advances in both knowledge and technology.

2.1 Structural dynamics of tall buildings

The wind induced response of structures can be divided into three parts [2.25, 2.26]: (1) the mean response, given by the mean component of the wind load, (2) the background or quasi-static response caused by the fluctuating component of the wind load whose frequencies differ significantly from the natural frequencies of vibration of the structure, and (3) the resonant response due to the fluctuating wind force components with frequencies equal or close to the structural natural frequencies. The resonant part of the response is associated with dynamic amplification effects.

The relative importance of the fluctuating components of the response strongly depends on the dynamic characteristics of the structure. In particular, the natural frequencies associated with the first modes of the building will determine whether the fluctuating dynamic response is mainly driven by the background response or by the resonant response. Due to their size and slenderness, tall buildings will in general have several natural frequencies of vibration of less then 1 Hz; this makes them susceptible to significant resonance when excited by extreme wind events. Therefore, in the design and analysis of tall buildings dynamic, and in particular

resonant effects, must be estimated. Over the years certain methods have become the norm. These methods will be the focus of the following paragraphs. It should be appreciated that the following methods assume aeroelastic effects to be negligible.

2.1.1 Formulation of the equations of motion

The global behavior of tall buildings can be modeled by an equivalent dynamic system considering each floor as a rigid diaphragm with three degrees of freedom (i.e. x- and y-displacement, relative to the ground, of the center of mass, and θ-rotation about a vertical axis through the center of mass). The concept of rigid floor diaphragms was introduced nearly 40 years ago as a means of increasing the efficiency of the solution process associated with structural dynamics [2.8]. The equations of motion are formulated at the storey mass centers as the resulting eigenvalue problem is computationally simpler [2.21]. Under these hypotheses the dynamic equilibrium of an N-story building with mass and stiffness eccentricities which can vary from floor to floor is given by:

$$\mathbf{M}\ddot{\mathbf{z}}(t) + \mathbf{C}\dot{\mathbf{z}}(t) + \mathbf{K}\mathbf{z}(t) = \mathbf{f}(t) \tag{2.1}$$

In which:

$$\mathbf{M} = \begin{bmatrix} \mathbf{M}_x & \mathbf{0} & \mathbf{0} \\ \mathbf{0} & \mathbf{M}_y & \mathbf{0} \\ \mathbf{0} & \mathbf{0} & \mathbf{J} \end{bmatrix} \tag{2.2}$$

$$\mathbf{K} = \begin{bmatrix} \mathbf{K}_{xx} & \mathbf{K}_{xy} & \mathbf{K}_{x\theta} \\ \mathbf{K}_{xy}^T & \mathbf{K}_{yy} & \mathbf{K}_{y\theta} \\ \mathbf{K}_{x\theta}^T & \mathbf{K}_{y\theta}^T & \mathbf{K}_{\theta\theta} \end{bmatrix} \tag{2.3}$$

$$\mathbf{C} = \begin{bmatrix} \mathbf{C}_{xx} & \mathbf{C}_{xy} & \mathbf{C}_{x\theta} \\ \mathbf{C}_{xy}^T & \mathbf{C}_{yy} & \mathbf{C}_{y\theta} \\ \mathbf{C}_{x\theta}^T & \mathbf{C}_{y\theta}^T & \mathbf{C}_{\theta\theta} \end{bmatrix} \tag{2.4}$$

$$\mathbf{z} = \{\mathbf{z}_x^T(t) \quad \mathbf{z}_y^T(t) \quad \mathbf{z}_\theta^T(t)\}^T \tag{2.5}$$

$$\mathbf{f} = \{\mathbf{f}_x^T(t) \quad \mathbf{f}_y^T(t) \quad \mathbf{f}_\theta^T(t)\}^T \tag{2.6}$$

where the displacement response sub-vectors are $\mathbf{z}_x(t) = \{z_{x1}(t), z_{x2}(t), ..., z_{xN}(t)\}^T$, $\mathbf{z}_y(t) = \{z_{y1}(t), z_{y2}(t), ..., z_{yN}(t)\}^T$ and $\mathbf{z}_\Theta(t) = \{z_{\theta 1}(t), z_{\theta 2}(t), ..., z_{\theta N}(t)\}^T$; the mass sub-matrices are $\mathbf{M}_x = \mathbf{M}_y = \text{diag}[m_i]$ for $i = 1, 2, ..., N$, in which m_i is the lumped mass of floor i, while the sub-matrix of moments of inertia of the floor diaphragms is $\mathbf{J} = \text{diag}[J_i]$ for $i = 1, 2, ..., N$, in which J_i represents the polar moment of inertia of floor i about a vertical axis through the center of mass. $\mathbf{K}_{xx}$, $\mathbf{K}_{yy}$, $\mathbf{K}_{\theta\theta}$, $\mathbf{K}_{xy}$, $\mathbf{K}_{x\theta}$, $\mathbf{K}_{y\theta}$ and $\mathbf{C}_{xx}$, $\mathbf{C}_{yy}$, $\mathbf{C}_{\theta\theta}$, $\mathbf{C}_{xy}$, $\mathbf{C}_{x\theta}$, $\mathbf{C}_{y\theta}$ are the sub-matrices of the stiffness and damping of the building respectively, while $\mathbf{f}$ is the vector of the zero mean fluctuating components $\mathbf{f} = \{\mathbf{f}_x^T \quad \mathbf{f}_y^T \quad \mathbf{f}_\theta^T\}^T$ of the wind load acting at

the center of mass of each floor given, for the directions x, y and θ, where the sub-vectors are $\mathbf{f}_x(t) = \{f_{x1}(t), f_{x2}(t), ..., f_{xN}(t)\}^T$, $\mathbf{f}_y(t) = \{f_{y1}(t), f_{y2}(t), ..., f_{yN}(t)\}^T$ and $\mathbf{f}_\theta(t) = \{f_{\theta 1}(t), f_{\theta 2}(t), ..., f_{\theta N}(t)\}^T$.

Having divided the wind load into a mean component and a fluctuating zero mean component, the total response of a linear system will obviously be given by the sum of the mean response and the dynamic response. While the dynamic response is obtained by (7.7), the mean response is simply given by:

$$\mathbf{K}\bar{\mathbf{z}} = \bar{\mathbf{f}} \tag{2.7}$$

where $\bar{\mathbf{z}}$ is the mean displacement response and $\bar{\mathbf{f}}$ is the mean force vector.

Equation (7.7) is a set of $3N$ coupled equations of motion governing the dynamic response of a particular building. By formulating the equations in the centers of mass of each floor the mass matrix will always assume the form shown in (2.2). As regards the stiffness matrix of (2.3), its terms will vary depending on the characteristics of the structure under consideration. In particular, for a building with centers of mass aligned on a single vertical axis and structural elements orientated in two perpendicular directions x and y, the stiffness sub-matrices are given by [2.20, 2.14]:

$$\mathbf{K}_{ii} = \begin{bmatrix} k_{i1}+k_{i2} & -k_{i2} & 0 & \cdots & 0 \\ -k_{i2} & k_{i2}+k_{i3} & -k_{i3} & \cdots & 0 \\ \vdots & \vdots & \vdots & & \vdots \\ 0 & 0 & 0 & \cdots & k_{iN} \end{bmatrix} \quad i = x, y, \theta \tag{2.8}$$

$$\mathbf{K}_{x\theta} = \begin{bmatrix} e_{y1}k_{x1}+e_{y2}k_{x2} & -e_{y2}k_{x2} & 0 & \cdots & 0 \\ -e_{y2}k_{x2} & e_{y2}k_{x2}+e_{y3}k_{x3} & -e_{y3}k_{x3} & \cdots & 0 \\ \vdots & \vdots & \vdots & & \vdots \\ 0 & 0 & 0 & \cdots & e_{yN}k_{xN} \end{bmatrix} \tag{2.9}$$

$$\mathbf{K}_{y\theta} = \begin{bmatrix} e_{x1}k_{y1}+e_{x2}k_{y2} & -e_{x2}k_{y2} & 0 & \cdots & 0 \\ -e_{x2}k_{y2} & e_{x2}k_{y2}+e_{x3}k_{y3} & -e_{x3}k_{y3} & \cdots & 0 \\ \vdots & \vdots & \vdots & & \vdots \\ 0 & 0 & 0 & \cdots & e_{xN}k_{yN} \end{bmatrix} \tag{2.10}$$

$$\mathbf{K_{xy}} = \mathbf{K_{yx}} = \mathbf{0} \tag{2.11}$$

in which k_{il} is the stiffness of the lth storey in ith direction ($i = x, y, \theta$), while e_{xl} and e_{yl} are the eccentricities between the centers of resistance and mass at the lth floor. Furthermore, if a building not only has the centers of mass aligned on a vertical axis, but also has coincident resistance and mass centers, $\mathbf{K_{x\theta}}$ and $\mathbf{K_{y\theta}}$ will also be null matrices and the building will experience uncoupled mode shapes. The advantage of this will become clear in the following part of this chapter.

2.1.2 Modal analysis

The coupled equations of motion of (7.7) can be solved through modal analysis [2.7, 2.9]. In this framework the modal frequencies ω_k and mode shapes $\boldsymbol{\phi}_k$ for $k = 1, 2, ..., 3N$, are the roots and non trivial solution of the following equations respectively [2.7, 2.9]:

$$\det(\omega^2 \mathbf{M} + \mathbf{K}) = 0 \tag{2.12}$$

$$(-\omega_k^2 \mathbf{M} + \mathbf{K})\boldsymbol{\phi}_k = 0 \tag{2.13}$$

Due to the orthogonality of the mode shapes [2.7, 2.9], if Rayleigh damping is considered the coupled system of (7.7) may be transformed into a set of $3N$ uncoupled single degree of freedom equations of motion:

$$\ddot{q}_k(t) + 2\zeta_k \omega_k \dot{q}_k(t) + \omega_k^2 q_k(t) = \frac{f_k(t)}{\boldsymbol{\phi}_k^T \mathbf{M} \boldsymbol{\phi}_k} \tag{2.14}$$

where ζ_k, and ω_k are the kth generalized damping ratio and circular frequency respectively, while $f_k(t)$ is the generalized force given by:

$$f_k(t) = \boldsymbol{\phi}_k^T \mathbf{f}(t) \tag{2.15}$$

The vector $\mathbf{q}(t)$ represents the generalized displacements and is linked to the vector $\mathbf{z}$ by:

$$\mathbf{q}(t) = \boldsymbol{\Phi}^{-1} \mathbf{z}(t) \tag{2.16}$$

where $\boldsymbol{\Phi} = \begin{bmatrix} \boldsymbol{\phi}_1 & \boldsymbol{\phi}_2 & \dots & \boldsymbol{\phi}_{3N} \end{bmatrix}$ is the modal matrix. Therefore from the knowledge of the global mass matrix, circular frequencies, damping ratios, mode shapes and time varying floor loads, the modal equations of motion can be solved. The advantage of this method compared to direct integration of (7.7) is twofold. Firstly, as mentioned, the coupled system in (7.7) is now an uncoupled system; secondly it is not generally necessary to solve all the uncoupled equations to adequately estimate the response. Indeed, due to the frequency content of the exciting function, namely the wind load, the first few modes will in general be sufficient for an accurate response estimation.

Following this framework the response displacements and accelerations in the global reference system can be expressed in terms of the contributions of $j = 1, 2, ..., n \leq 3N$ modes. The displacements for example are given by:

$$\mathbf{z}(t) \approx \begin{bmatrix} \boldsymbol{\phi}_1 & \boldsymbol{\phi}_2 & \dots & \boldsymbol{\phi}_n \end{bmatrix} \{q_1, q_2, \dots, q_n\}^T \tag{2.17}$$

Likewise the accelerations are given by:

$$\ddot{\mathbf{z}}(t) \approx \begin{bmatrix} \boldsymbol{\phi}_1 & \boldsymbol{\phi}_2 & \dots & \boldsymbol{\phi}_n \end{bmatrix} \{\ddot{q}_1, \ddot{q}_2, \dots, \ddot{q}_n\}^T \tag{2.18}$$

In a similar fashion, from the knowledge of the generalized displacements $\mathbf{q}$, any other response parameter of interest R (for example the bending moment in a specific member) may be calculated by:

$$R(t) = \{\Lambda_1, \Lambda_2, \ldots, \Lambda_n\}\{q_1, q_2, \ldots, q_n\}^T \tag{2.19}$$

where $\{\Lambda_1, \Lambda_2, ..., \Lambda_n\}^T = \mathbf{\Lambda}$ is the vector of modal participation coefficients for R, representing the static response of R under the modal inertial load with a unit generalized displacement:

$$\Lambda_j = \{\boldsymbol{\vartheta}_x^T \quad \boldsymbol{\vartheta}_y^T \quad \boldsymbol{\vartheta}_\theta^T\} \begin{Bmatrix} \hat{\mathbf{f}}_{jx} \\ \hat{\mathbf{f}}_{jy} \\ \hat{\mathbf{f}}_{j\theta} \end{Bmatrix} \tag{2.20}$$

where the ith component of the subvector $\hat{\mathbf{f}}_{js}$, given by

$$\hat{f}_{jsi} = \omega_j^2 m_{is} \phi_{jsi} \tag{2.21}$$

is the jth modal inertial load with a unit generalized displacement acting at the mass center; the ith component ϑ_{si} of the subvector $\boldsymbol{\vartheta}_s$ is the influence function representing the response R under a unit load acting at the mass center of the ith floor along the s direction; $m_{ix} = m_{iy} = m_i$ and $m_{i\theta} = J_i$.

As described previously the dynamic response can be divided into a background quasi-static response and a resonant response. In a similar fashion the modal contributions may be divided into background and resonant components. Indeed the response superposition method of (2.19) can be replaced by the static correction method [2.7]:

$$R(t) = \{\Lambda_1, \Lambda_2, \ldots, \Lambda_n\}\{q_{1r}, q_{2r}, \ldots, q_{nr}\}^T + \{\Lambda_1, \Lambda_2, \ldots, \Lambda_n\}\{q_{1b}, q_{2b}, \ldots, q_{nb}\}^T \tag{2.22}$$

where $q_{jb}(t) = f_j(t)/k_j$ is the jth background (quasi-static) generalized displacement with $k_j = \omega_j^2 \boldsymbol{\phi}_j^T \mathbf{M} \boldsymbol{\phi}_j$ which is the jth generalized stiffness and $q_{jr}(t) = q_j(t) - q_{jb}(t)$ is the jth resonant generalized displacement, i.e. the generalized displacement excluding the quasi-static component.

It should be noticed that the quantification of the background response $R_b(t)$ including all mode contributions is equivalent to the quasi-static analysis in terms of the influence function, i.e.

$$R_b(t) = \{\Lambda_1, \Lambda_2, \ldots, \Lambda_{3N}\} \begin{Bmatrix} q_{1b} \\ q_{2b} \\ \vdots \\ q_{3Nb} \end{Bmatrix} = \{\boldsymbol{\vartheta}_x^T \quad \boldsymbol{\vartheta}_y^T \quad \boldsymbol{\vartheta}_\theta^T\} \begin{Bmatrix} \mathbf{f}_x \\ \mathbf{f}_y \\ \mathbf{f}_\theta \end{Bmatrix} \tag{2.23}$$

A particular solution of equations (2.12) and (2.13) is obtained when the centers of mass and stiffness for each floor are coincident and lay on a vertical axis, and

each floor is characterized by coincident principal directions. Under this scenario, as mentioned, the off diagonal stiffness sub-matrices of (2.3) will be null. The consequence of this is that the fundamental mode shapes derived from the solution of (2.13) will be defined as uncoupled. What this means is that within the reference system with vertical axis passing through the centers of mass of each floor, and horizontal axes aligned with the principal floor directions, the first three mode shapes (fundamental modes) will be characterized by displacements occurring exclusively in one of the principal floor directions or by a rotation around the vertical axis. Otherwise the building will, in general, experience coupled modes, that is fundamental mode shapes characterized by simultaneous displacements in at least two directions.

It should also be appreciated that if the building has well separated fundamental frequencies (but this is an unlikely event in the case of typical tall buildings) the mode shapes will become uncoupled even if the mass and stiffness centers do not lie on a single vertical axis.

2.2 Frequency domain response analysis

2.2.1 General theory

It has become the norm to carry out the response analysis of tall buildings in the frequency domain using the theory of random vibrations [2.27, 2.22]. The reason for the preference of these methods over, for example, time domain techniques, is the computational advantage they enjoy, and by the fact that the analysis of tall buildings was developed primarily during the 1970s when fast and efficient Ordinary Differential Equation (ODE) solvers did not exist, therefore making frequency domain analysis the only applicable method.

Based on the theory of random vibration [2.27, 2.9] the spectral density matrix of the generalized displacement response vector $\mathbf{S}_q$ [2.2, 2.23] can be obtained from the spectral density matrix of the generalized forces $\mathbf{S}_Q$:

$$\mathbf{S}_q(\omega) = \mathbf{H}(\omega)\mathbf{S}_Q(\omega)\mathbf{H}^*(\omega) \tag{2.24}$$

where $S_{Q_{ij}}(\omega)$ is XPSD of the generalized forces Q_i and Q_j while $\mathbf{H} = \text{diag}[H_j]$ is the complex mechanical transfer function with H_j defined as [2.27, 2.9]:

$$H_j(\omega) = \frac{1}{m_j\omega_j^2[1-(\omega/\omega_j)^2 + 2i\zeta_j\omega/\omega_j]} \tag{2.25}$$

where m_j is the generalized mass and $\mathbf{H}^*(\omega)$ is the complex conjugate of $\mathbf{H}(\omega)$.

From the XPSD matrices of the generalized displacements it is possible to express the PSD, $S_R(\omega)$, of a specific response R through its modal participation coefficients, $\mathbf{\Lambda} = \{\Lambda_1, \Lambda_2, ..., \Lambda_n\}^T$, as:

$$S_R(\omega) = \mathbf{\Lambda}^T\mathbf{S}_q(\omega)\mathbf{\Lambda} \tag{2.26}$$

If the response parameter coincides with the displacement, velocity, or acceleration at the mass center of the ith floor in the s direction, Λ_j, is respectively given by ϕ_{jsi}, $\omega_j\phi_{jsi}$ and $\omega_j^2\phi_{jsi}$ for $s = x, y, \theta$.

Substituting equation (2.24) into (2.26), one obtains the PSD of the physical response from the XPSD of the generalized forces:

$$S_R(\omega) = \mathbf{\Lambda}^T\mathbf{H}(\omega)\mathbf{S}_Q(\omega)\mathbf{H}^*(\omega)\mathbf{\Lambda} \tag{2.27}$$

Equation (2.27) represents the full spectral approach with contributions to $S_R(\omega)$ from all the cross modal correlations. Indeed, as will be discussed, equation (2.27) is rarely rigorously resolved when estimating the response of tall buildings.

From the definition of the PSD function as the Fourier transform [2.32] of the autocorrelation function of the random process $R(t)$, the RMS of R, σ_R, can be calculated by the integration of the one sided PSD, $S_R(\omega)$, of the response process:

$$\sigma_R^2 = \int_0^\infty S_R(\omega)d\omega \tag{2.28}$$

An alternative and widely adopted way of expressing σ_R is through combination of the RMS modal responses σ_{jj} and cross modal responses σ_{jk}, which, using sum notation for clarity, is:

$$\sigma_R^2 = \sum_{j=1}^{3N}\Lambda_{R_j}^2\sigma_{q_{jj}}^2 + \sum_{j=1}^{3N}\sum_{j=1}^{3N}\Lambda_{R_j}\Lambda_{R_k}\sigma_{q_{jk}}^2 \tag{2.29}$$

in which $\sigma_{q_{jk}}^2$ is given by:

$$\sigma_{q_{jk}}^2 = \mathrm{Re}\Big[\int_0^\infty H_j(\omega)H_k^*(\omega)S_{Q_{jk}}(\omega)d\omega\Big] \tag{2.30}$$

Equation (2.29) represents the Complete Quadratic Combination (CQC) [2.33] of the various modal contributions; if only the first part of the right hand side is considered, it coincides with the Square Root of the Sum of Squares (SRSS) rule. Equation (2.29) may also be written in terms of the modal correlation coefficient given by:

$$r_{jk} = \frac{\sigma_{q_{jk}}^2}{\sigma_{q_{jj}}\sigma_{q_{kk}}} = \frac{\mathrm{Re}[\int_0^\infty H_j(\omega)H_k^*(\omega)S_{Q_{jk}}(\omega)d\omega]}{\int_0^\infty |H_j(\omega)|^2 S_{Q_{jj}}(\omega)d\omega \int_0^\infty |H_k(\omega)|^2 S_{Q_{kk}}(\omega)d\omega} \tag{2.31}$$

while (2.29) becomes:

$$\sigma_R^2 = \sum_{j=1}^{3N}\Lambda_{R_j}^2\sigma_{q_{jj}}^2 + \sum_{j=1}^{3N}\sum_{k=1}^{3N}\Lambda_{R_j}\Lambda_{R_k}r_{jk}\sigma_{q_{jj}}\sigma_{q_{kk}} \tag{2.32}$$

It is often convenient to express σ_R in terms of its background σ_{Rb} and resonant σ_{Rr} contributions. Indeed, due to the lack of correlation that exists between the resonant and background physical and modal responses, (2.32) may be written as:

$$\sigma_R^2 = \sigma_{Rb}^2 + \sigma_{Rr}^2 = \sum_{j=1}^{3N} \Lambda_{R_j}^2 (\sigma_{q_{jjb}}^2 + \sigma_{q_{jjr}}^2) + \sum_{j=1}^{3N} \sum_{k=1}^{3N} \Lambda_{R_j} \Lambda_{R_k} (r_{jkb} \sigma_{q_{jjb}} \sigma_{q_{kkb}} + r_{jkr} \sigma_{q_{jjr}} \sigma_{q_{kkr}}) \tag{2.33}$$

where $\sigma_{q_{jjb}}$ and $\sigma_{q_{jjr}}$ are the background and resonant modal responses while r_{jkb} and r_{jkr} are the background and resonant modal correlation coefficients given respectively by:

$$r_{jkb} = \frac{\sigma_{q_{jkb}}^2}{\sigma_{q_{jjb}} \sigma_{q_{kkb}}} = \frac{\mathrm{Re}[\int_0^{f'} H_j(\omega) H_k^*(\omega) S_{Q_{jk}}(\omega) d\omega]}{\int_0^{f'} |H_j(\omega)|^2 S_{Q_{jj}}(\omega) d\omega \int_0^{f'} |H_k(\omega)|^2 S_{Q_{kk}}(\omega) d\omega} \tag{2.34}$$

$$r_{jkr} = \frac{\sigma_{q_{jkr}}^2}{\sigma_{q_{jjr}} \sigma_{q_{kkr}}} = \frac{\mathrm{Re}[\int_{f'}^{\infty} H_j(\omega) H_k^*(\omega) S_{Q_{jk}}(\omega) d\omega]}{\int_{f'}^{\infty} |H_j(\omega)|^2 S_{Q_{jj}}(\omega) d\omega \int_{f'}^{\infty} |H_k(\omega)|^2 S_{Q_{kk}}(\omega) d\omega} \tag{2.35}$$

where f' is a frequency smaller than or equal to the natural frequency of the first vibrational mode.

While the mechanical coupling due to any 3D mode shape is accounted for through the modal participation coefficients, the double sum of the right hand side of (2.29) or (2.32) represents the contribution of the modal correlation (inter-modal coupling) due to statistical coupling. This may be accurately quantified through the solution of equations (2.31) or (2.34) and (2.35), and therefore from the knowledge of the XPSD of the generalized forces. An important class of buildings is that exhibiting negligible inter-modal coupling, i.e. with r_{jkb} and r_{jkr} nearly equal to zero. This occurs when a building has uncoupled mode shapes together with regular geometric form (such as rectangular prism). These conditions are often satisfied by traditional tall buildings. Indeed, under these circumstances, even if the building has relatively closely spaced frequencies the inter-modal correlation will be negligible due to the low correlation between the generalized forces. Obviously the task of estimating the RMS of a particular response is greatly facilitated in these cases as only the PSD of the generalized forces is necessary for the accurate determination of σ_R through what now becomes a SRSS combination. Indeed traditional methods for the analysis of tall buildings in general neglect the effect of inter-modal correlation. In recent years however, tall building design has moved away from simple geometric forms leading to a vast number of proposed buildings that have coupled 3D modes. This has produced a number of studies aiming at a better understanding of the role of modal correlation and at the formulation of effective methods for estimating equations (2.31) or (2.34) and (2.35) [2.28, 2.19, 2.6, 2.5, 2.4]. The next section will outline some of the proposed resolution methods.

2.2.2 Resolution methods

In order to implement the procedure outlined in the previous section it is necessary to estimate the modal correlation coefficients, r_{ijb} and r_{ijr}, and the RMS modal displacement responses, $\sigma_{q_{jjb}}$ and $\sigma_{q_{jjr}}$. A number of techniques have been proposed over the years. In particular the following procedure proposed in [2.5, 2.4] and based on techniques developed mainly for seismic response analysis [2.28, 2.19] has become the baseline.

In this method the background modal displacement RMS is estimated as:

$$\sigma^2_{q_{jjb}} = \int_0^{f'} |H_j(\omega)|^2 S_{Q_{jj}}(\omega) d\omega \approx \frac{1}{m_j^2 \omega_j^2} \int_0^{\infty} S_{Q_{jj}}(\omega) d\omega \tag{2.36}$$

while the resonant modal RMS is estimated based on the white noise assumption. Indeed, due to the relatively low damping of tall buildings the mechanical transfer function will behave like a narrow band filter. Therefore the resonant RMS of the jth generalized displacement may be approximated by assuming the generally broad band power spectral density function of the generalized forces, $S_{Q_{jj}}(\omega)$, to be white noise giving:

$$\sigma^2_{q_{jjr}} = \int_{f'}^{\infty} |H_j(\omega)|^2 S_{Q_{jj}}(\omega) d\omega \approx \frac{1}{8 m_j^2 \omega_j^3 \zeta_j} S_{Q_{jj}}(\omega_j) \tag{2.37}$$

It follows that the background modal correlation coefficients can be estimated as:

$$r_{jkb} \approx \frac{\int_0^{\infty} \mathrm{Re}[S_{Q_{jk}}(\omega)] d\omega}{\sqrt{\int_0^{\infty} S_{Q_{jj}}(\omega) d\omega} \sqrt{\int_0^{\infty} S_{Q_{kk}}(\omega) d\omega}} = \frac{\sigma^2_{Q_{jkb}}}{\sigma_{Q_{jjb}} \sigma_{Q_{kkb}}} = r_{Q_{kj}} \tag{2.38}$$

while the resonant modal correlation coefficients can be estimated from the closed form expression [2.13]:

$$r_{jkr} = \alpha_{jkr} \rho_{jkr} \tag{2.39}$$

where:

$$\alpha_{jkr} \approx \frac{\mathrm{Re}[S_{Q_{jk}}(\bar{\omega})]}{\sqrt{S_{Q_{jj}}(\bar{\omega})} \sqrt{S_{Q_{kk}}(\bar{\omega})}} \tag{2.40}$$

where $\bar{\omega}$ is a circular frequency equal to ω_j or ω_k, while ρ_{jkr} is given in [2.13]:

$$\rho_{jkr} = \frac{8\sqrt{\xi_j \xi_k}(\beta_{jk}\xi_j + \xi_k)\beta_{jk}^{2/3}}{(1-\beta_{jk}^2)^2 + 4\xi_j\xi_k\beta_{jk}(1+\beta_{jk}^2) + 4(\xi_j^2 + \xi_k^2)\beta_{jk}^2} \tag{2.41}$$

where $\beta_{jk} = \omega_j/\omega_k$ with $0 \leq \rho_{jkr} \leq 1$, $\rho_{jjr} = \rho_{kkr} = 1$ and $\rho_{jkr} = \rho_{kjr} \ll 1$ when ω_j and ω_k are well separated. It is important to understand the role α_{jkr} plays in determining the resonant modal correlation. Indeed this parameter represents the effect that the partially correlated generalized forces have on the resonant correlation

which not only depends on the modal frequencies and damping ratios. Also, in general, $|\alpha_{jkr}| \leq 1$, and only when the generalized forces are fully correlated $|\alpha_{jkr}| = 1$. This is an importance difference between structures subject to wind loading compared to seismic loading with a single ground motion input for which $|\alpha_{jkr}| = 1$, [2.4, 2.6, 2.5, 2.34].

The white noise assumption used in the estimation of r_{ijb}, r_{ijr}, $\sigma_{q_{jjb}}$ and $\sigma_{q_{jjr}}$ is not deemed acceptable by some authors [2.16, 2.17]. Instead it is proposed to estimate the modal correlation coefficient, r_{jk}, through the spectral moment method. By taking into account both the real and imaginary parts of the product between the modal admittance function and XPSD matrix of the generalized forces, the resonant inter-modal correlation coefficient may be expressed as:

$$r_{jk} = \frac{1}{\sqrt{\psi_{jj}\psi_{kk}}}[\psi_{0,jk} + \beta_{jk}^{(1)}\psi_{2,jk} + \beta_{jk}^{(2)}\psi_{4,jk} - \beta_{jk}^{(3)}\psi_{1,jk} - \beta_{jk}^{(4)}\psi_{3,jk}] \tag{2.42}$$

where ψ_{jj} denotes the spectral moment of the response of a single degree of freedom oscillator with natural frequency ω_j, while $\psi_{m,jk}$ represents the cross spectral moments of the responses associated with modes j and k as:

$$\psi_{jj} = \int_0^\infty |H_j(\omega)|^2 S_{Q_{jj}}(\omega) d\omega \tag{2.43}$$

$$\psi_{m,jk} = \begin{cases} \int_0^\infty \omega^m |H_j(\omega)|^2 |H_k(\omega)|^2 \mathrm{Re}[S_{Q_{jk}}(\omega)] d\omega, & m = 0, 2, 4 \\ \int_0^\infty \omega^m |H_j(\omega)|^2 |H_k(\omega)|^2 \mathrm{Im}[S_{Q_{jk}}(\omega)] d\omega, & m = 1, 3 \end{cases} \tag{2.44}$$

while the coefficients $\beta^{(1)}$, $\beta^{(2)}$, $\beta^{(3)}$ and $\beta^{(4)}$ are given in terms of the modal frequencies and damping ration as:

$$\beta_{jk}^{(1)} = \frac{4\xi_j\xi_k\omega_j\omega_k - \omega_j^2 - \omega_k^2}{\omega_j^2\omega_k^2} \tag{2.45}$$

$$\beta_{jk}^{(2)} = \frac{1}{\omega_j^2\omega_k^2} \tag{2.46}$$

$$\beta_{jk}^{(3)} = \frac{2(\xi_k\omega_j - \xi_j\omega_k)}{\omega_j\omega_k} \tag{2.47}$$

$$\beta_{jk}^{(4)} = \frac{2(\xi_j\omega_j - \xi_k\omega_k)}{\omega_j^2\omega_k^2} \tag{2.48}$$

2.3 The total response and the peak factor

In the design of buildings it is the maximum value of the response process $R(t)$ that is of interest. In particular, it is common practice to consider as the design value the maximum response with a specified probability of non-exceedance for an

observation period T. If the response process $R(t)$ is normalized so as to have zero mean and unit variance, the maximum response, with a specified probability of non-exceedance during an observation period T, defines what is known as the peak factor g of the process $R(t)$. Therefore the total maximum response, including the mean response may be written as:

$$R_{\mathrm{Tot}_{\max}} = \mu_R + g_R \sigma_R \tag{2.49}$$

Likewise the minimum response is given by:

$$R_{\mathrm{Tot}_{\min}} = \mu_R - g_R \sigma_R \tag{2.50}$$

where μ_R and σ_R are the mean and the standard deviation of R. If $R(t)$ is distributed symmetrically around its mean, g will take on the same value for both the maximum and minimum total responses allowing (2.49) and (2.50) to be simply written as:

$$R_{\mathrm{Tot}_{\max \text{ or } \min}} = \mu_R \pm g_R \sigma_R \tag{2.51}$$

Equations (2.49) and (2.50) may also be formulated in terms of the background and resonant responses as:

$$R_{\mathrm{Tot}_{\max}} = \mu_R + \sqrt{g_{R_b}^2 \sigma_{R_b}^2 + g_{R_r}^2 \sigma_{R_r}^2} \tag{2.52}$$

$$R_{\mathrm{Tot}_{\min}} = \mu_R - \sqrt{g_{R_b}^2 \sigma_{R_b}^2 + g_{R_r}^2 \sigma_{R_r}^2} \tag{2.53}$$

where g_{R_b} and g_{Rr} are the background and resonant peak factors respectively. Equations (2.52) and (2.53) can also be simplified if both $R_b(t)$ and $R_r(t)$ are symmetrically distributed around their means. The next sections will describe how the peak factor is estimated for stationary random processes.

2.3.1 Out-crossing rates of univariate random processes

The 1-dimensional level crossing problem addresses the number of times that a univariate random process $\{R(t), -\infty < t < \infty\}$ crosses the level r in the time interval $(t, t + \Delta t)$. Each crossing of level r with positive slope is defined as an up-crossing. In particular, if $R(t)$ is differentiable, then there must be a finite number of up-crossings in the interval $(t, t + \Delta t)$. An up-crossing will occur in $(t, t + \Delta t)$ if:

$$R(t) < r,\ \dot{R}(t) > 0,\ R(t) + \dot{R}(t)\Delta t > r \tag{2.54}$$

where $\dot{R}(t)$ is the derivative process. The probability of this occurring is given by:

$$\mathrm{Prob}\{(r - \dot{R}(t)\Delta t < R(t) < r) \cap (\dot{R} > 0)\} \tag{2.55}$$

which also corresponds to the average number of up-crossings in the interval $(t, t + \Delta t)$. As $\Delta t \longrightarrow 0$, the number of up-crossings that can occur are zero or one.

Therefore, denoting the up-crossing rate of the level r as $\nu^+(r,t)$, the mean up-crossing rate of $R(t)$ is given by:

$$\nu^+(r,t) = \lim_{\Delta t \to 0} \frac{1}{\Delta t} \text{Prob}\{(r - \dot{R}(t)\Delta t < R(t) < r) \cap (\dot{R} > 0)\} \tag{2.56}$$

which yields:

$$\nu^+(r,t) = \int_0^\infty \dot{r} p_{R\dot{R}}(r,\dot{r},t) d\dot{r} \tag{2.57}$$

where $p_{R\dot{R}}(r,\dot{r},t)d\dot{r}$ is the joint probability density function of $\{R(t), \dot{R}(t)\}$. Equation (2.57) is the well known Rice formula [2.24] a rigorous proof of which can be found in [2.10]. Equation (2.57) may also be written in the following form [2.27]:

$$\nu^+(r,t) = p_R(r,t) \int_0^\infty \dot{r} p_{R|\dot{R}}(\dot{r},t) d\dot{r} \tag{2.58}$$

where p_R is the probability density function of $R(t)$ while $p_{R|\dot{R}}$ is the conditional probability density function of $\dot{R}$ given R.

Equally the down-crossing rate, $\nu^-(r,t)$, is defined as the average number of times that $R(t)$ crossing with negative slope the level r. The following expressions, which are analogous to equations (2.57) and (2.58), can be written:

$$\nu^-(r,t) = -\int_0^\infty \dot{r} p_{R\dot{R}}(r,\dot{r},t) d\dot{r} \tag{2.59}$$

$$\nu^-(r,t) = -p_R(r,t) \int_0^\infty \dot{r} p_{R|\dot{R}}(\dot{r},t) d\dot{r} \tag{2.60}$$

If $R(t)$ is a stationary process the mean crossing rates become time invariant, i.e. $\nu^+(r,t) = \nu^+(r)$ and $\nu^-(r,t) = \nu^-(r)$.

In the case that $R(t)$ is a stationary gaussian random process, the conditional probability $p_{R|\dot{R}}$ is given by:

$$\int_0^\infty \dot{r} p_{R|\dot{R}}(\dot{r},t) d\dot{r} = \frac{\sigma_{\dot{R}}}{\sqrt{2\pi}} \tag{2.61}$$

where $\sigma_{\dot{R}}$ is the variance of $\dot{R}$ given by:

$$\sigma_{\dot{R}} = \sqrt{\int_0^\infty \omega^2 S_R(\omega) d\omega} \tag{2.62}$$

while the mean crossing rate will be given by:

$$\nu^+(r) = \frac{1}{2\pi} \frac{\dot{\sigma}_{\dot{R}}}{\sigma_R} \exp\left[-\frac{1}{2}\left(\frac{r-\mu_R}{\sigma_R}\right)^2\right] \tag{2.63}$$

Because the Gaussian distribution is symmetric with respect to the mean μ_R, the mean up-crossing rate coincides with the mean down-crossing rate.

2.3.2 Maxima distributions of stationary processes

With the aim of determining the maximum response with a specified probability of non-exceedance during an observation period T that is of interest in the design of buildings, consider the stationary response process $R(t)$, denote with R_T the maximum value assumed by R in the interval $(0, T)$. And let $N(t)$ denote the discrete, random number of up-crossings of the level r by the random process $R(t)$ in the time interval $T = (t_2 - t_1)$. If level r is large enough, the up-crossings may be considered rare and independent. The up-crossings may therefore be defined by a Poisson process with mean intensity $\nu^+(r)$. The probability of obtaining k up-crossings during the interval $T = (t_2 - t_1)$ will therefore be given by:

$$\text{Prob}[n(t_2) - n(t_1) = k] = \frac{[\nu^+(r)T]^k}{k!}\exp[\nu^+(r)T] \tag{2.64}$$

By its own definition, the distribution of R_T will be given by (2.64) when no up-crossing of level r occur during the interval T:

$$P_{R_T}(r) = \text{Prob}[n(t_2) - n(t_1) = 0] = \exp[\nu^+(r)T] \tag{2.65}$$

By substituting (2.63) into (2.65), the peak distribution of a stationary gaussian process is defined as:

$$P_{R_T}(r) = \exp\left\{\nu_0 T \exp\left[-\frac{1}{2}\left(\frac{r-\mu_R}{\sigma_R}\right)^2\right]\right\} \tag{2.66}$$

where $\nu_0 = \sigma_{\dot{R}}/2\pi\sigma_R$ is the mean up-crossing rate of the level $r = 0$. The corresponding density function will be given by:

$$p_{R_T}(r) = \frac{T}{\sigma_R}\left(\frac{r-\mu_R}{\sigma_R}\right)\nu^+(r)\exp[\nu^+(r)T] \tag{2.67}$$

the foundations of which can be found in the works of Rice [2.24].

Equations (2.66) and (2.67) are the basis on which Davenport developed his closed form equation for estimating the expected peak of a stationary Gaussian process [2.11, 2.12]. Indeed, by neglecting terms of order $(2\text{In}(\nu_0 T))^{-3/2}$ in the Taylor expansions necessary for solving the underlying integrals, the expected value of the normalized peak distribution of R_T may be estimated by the well known formula:

$$E[R_T] = \sqrt{2\text{In}(\nu_0 T)} + \frac{0.5772}{\sqrt{2\text{In}(\nu_0 T)}} \tag{2.68}$$

while the variance is given by:

$$\sigma^2_{R_T} = \frac{\pi^2}{6}\frac{1}{2\text{In}(\nu_0 T)} \tag{2.69}$$

For tall buildings ν_0 may be assumed equal to the first fundamental frequency of the structure. Equation (7.8) is widely used for estimating the peak factor, g, of a wind-excited structural response. As mentioned, equation (2.67) was developed based on the "Poisson approximation". It should be understood however that, while this approximation is generally valid for broad band processes, it may fall short for very narrow band processes and threshold levels of practical interest [2.22]. Cartwright and Longuet-Higgins [2.3] introduced a bandwidth parameter to account for its effect on the extreme value. This was further refined by Vanmarcke [2.30] who proposed an improved formula with a different bandwidth parameter.

2.4 The generalized wind forces

As described it is customary to perform the dynamic response analysis of tall buildings through modal analysis. Fundamental to this approach is the estimate of the generalized forces of equation (5.3). Indeed while the other modal parameters, such as the generalized mass and stiffness, are easily quantified through finite element analysis, the generalized forces depend on the time varying distribution of the external wind pressure. In order to quantify these forces it is therefore necessary to perform a number of wind tunnel tests. Two main approaches exist for this purpose. The first is based on the integration of the external wind pressure field characterized through Synchronous Multi-Pressure Sensing System (SMPSS) measurements. The second method is based on the High Frequency Force Balance (HFFB) which attempts to directly quantify the first three generalized forces through the measurement of the base bending moments [2.29]. The first method will be extensively described in the following chapter. The rest of this section will be dedicated to the HFFB approach, especially considering the historical role this method has in the characterization of the external wind load on tall buildings.

2.4.1 The High Frequency Force Balance (HFFB)

The HFFB measures the base bending moments in two primary directions, the torsional moment and shear forces at the base of a rigid model of the building. The measurements are referred to a reference system with origin (that is the HFFB center) which usually coincides with the geometric center of the model base. The measured moments will therefore coincide with those calculated by multiplying the sectional forces (obtained reducing the external wind field to line loads acting on a vertical axis passing through the HFFB center) with the distance from the origin. However, the equations of motion are customarily formulated in the centers of mass of each floor which in general do not lay on a vertical axis, or pass through the HFFB center. It can be shown that the generalized quantities of equation (2.14) do not change if a new set of reference centers is taken instead of the mass centers [2.36]; then, in order to relate the HFFB measurements to the generalized forces,

these can be calculated through the mode shapes referred to the HFFB reference system. The generalized forces in the HFFB reference system may be obtained from the mode shapes calculated at the centers of mass of each floor by the following transformation:

$$\begin{cases} \phi^b_{ijx} = \phi^m_{ijx} + e^m_{ijy}\phi^m_{ij\theta} \\ \phi^b_{ijy} = \phi^m_{ijy} - e^m_{ijx}\phi^m_{ij\theta} \\ \phi^b_{ij\theta} = \phi^m_{ij\theta} \end{cases} \tag{2.70}$$

where the subscripts m and b denote the quantities at the mass and HFFB centers respectively while e^m_{ijy} and e^m_{ijx} denote the distances between the mass and HFFB centers at the various floors. Using a different notation, the generalized forces of equation (5.3) can be expressed as:

$$f_j(t) = \sum_{i=1}^{N} \phi^b_{ijx} f^b_{ijx}(t) + \phi^b_{ijy} f^b_{ijy}(t) + \phi^b_{ij\theta} f^b_{ij\theta}(t) \tag{2.71}$$

or equivalently as:

$$f_j(t) = \sum_{i=1}^{N} \phi^b_{ijx} f^b_{ijx}(t) + \sum_{i=1}^{N} \phi^b_{ijy} f^b_{ijy}(t) + \sum_{i=1}^{N} \phi^b_{ij\theta} f^b_{ij\theta}(t) = f_{jx}(t) + f_{jy}(t) + f_{j\theta}(t) \tag{2.72}$$

where $f^b_{ijx}(t)$, $f^b_{ijy}(t)$ and $f^b_{ij\theta}(t)$ are the floor loads referred to the HFFB reference system. It is clear from equation (2.72) that if the translational components of the mode shapes vary linearly over the building height while the torsional component is uniform, i.e.

$$\begin{cases} \phi^b_{ijs} = \phi^b_{js0}\left(\dfrac{z_i}{H}\right) & (s = x, y) \\ \phi^b_{ij\theta} = \phi^b_{j\theta 0} \end{cases} \tag{2.73}$$

where ϕ^b_{js0} for $s = x, y$ and $\phi^b_{j\theta 0}$ are constants while H is the height of the building. Then the first three generalized forces may be written as:

$$f_j(t) = \left(\frac{\phi^b_{jx0}}{H}\right) M^b_x(t) + \left(\frac{\phi^b_{jy0}}{H}\right) M^b_y(t) + \phi^b_{j\theta 0} M^b_\theta(t) \tag{2.74}$$

where $M^b_x(t)$, $M^b_y(t)$ and $M^b_\theta(t)$ are the measured base moments. Equation (2.74) is further simplified in the case of uncoupled mode shapes and gives, for $j = 1, 2, 3$:

$$\begin{cases} f_1(t) = \left(\dfrac{\phi^b_{1x0}}{H}\right) M^b_x(t) \\ f_2(t) = \left(\dfrac{\phi^b_{2y0}}{H}\right) M^b_y(t) \\ f_3(t) = \phi^b_{3\theta 0} M^b_\theta(t) \end{cases} \tag{2.75}$$

This result is particularly useful for the frequency domain response analysis of buildings with uncoupled mode shapes. Indeed, for this particular class of buildings (to which the vast majority of traditional tall buildings belong), inter-modal correlation is typically negligible. Therefore, if the first three generalized forces are deemed sufficient and the response is classed as gaussian, then the dynamic response may be completely characterized by the PSD of the first three generalized forces and so by virtue of (2.75) the PSD of the base bending moments. In this case, it is not even necessary to evaluate the XPSD matrix of the base moments. This simplified procedure with the above mentioned assumptions may be defined as the classic approach to wind design of tall buildings. The incredible simplicity and directness of this technique, coupled with the fact that tall buildings until recently have predominantly had simple geometric forms, has assured its success as the predominant method to determine wind loads on tall buildings. However, the technique has two significant limitations. Firstly, it is assumed that modes other than the first three do not contribute to the response, and secondly, the translational mode shapes are rarely linear, while the torsional mode shape is practically never uniform. While it is not possible to overcome the first point, attempts to alleviate the second are commonly adopted through the selection of appropriate mode correction schemes.

2.4.2 Mode correction schemes

As pointed out, equations (2.74) and (2.75) are valid only in the case of linear sway and uniform twist mode shapes. This condition is rarely satisfied, especially for the twist mode. In order to continue using the results of equations (2.74) and (2.75), albeit in an approximate fashion, mode correction factors [2.31, 2.1, 2.35, 2.36, 2.37, 2.15, 2.18], $\eta(t)$, may be defined that allow (2.74) to be written as:

$$f_j(t) = \eta_{jx}(t)\left(\frac{\phi^b_{jx0}}{H}\right)M^b_x(t) + \eta_{jy}(t)\left(\frac{\phi^b_{jy0}}{H}\right)M^b_y(t) + \eta_{j\theta}(t)\phi^b_{j\theta 0}M^b_\theta(t) \tag{2.76}$$

where $\eta_{jx}(t)$, $\eta_{jy}(t)$ and $\eta_{j\theta}(t)$ are the generally time dependent mode correction factors for the x, y and θ directions of the jth mode shape.

The difficulty lays in defining appropriate values for the correction factors. Indeed, by definition the mode correction factors are given by:

$$\eta_{js}(t) = \frac{\sum_{i=1}^{N}\phi^b_{ijs}f^b_{is}(t)}{\sum_{i=1}^{N} z_i^{\beta_s} f^b_{is}(t)} \tag{2.77}$$

where $\beta_s = 1$ when $s = y$ or x while for s = θ $\beta_s = 0$. Therefore the correction factors depend on the distribution of the wind loads over the buildings height, but this is an information that is not available from HFFB tests. Therefore the mode shape corrections have to be estimated using empirical or analytical formulations based on presumed wind loading models where the dependency on time of (2.77) is rarely considered [2.15, 2.18].

Alternatively the mode shape corrections may be defined in the frequency domain as [2.6]:

$$\eta_{js}^2(f) = \frac{\sum_{i=1}^{N}\sum_{k=1}^{N}\phi_{ijs}^b\phi_{kjs}^b S_{F_{iks}}^b(f)}{\sum_{i=1}^{N}\sum_{k=1}^{N} z_i^{\beta_s} z_k^{\beta_s} S_{F_{iks}}^b(f)} \tag{2.78}$$

where $S_{F_{iks}}^b(f)$ is the XPSD of the floor loads in the HFFB reference system. From (2.78) it is possible to estimate the XPSD matrix of the generalized forces as:

$$\mathbf{S}_Q(f) = \boldsymbol{\eta}(f)\mathbf{S}_M(f)\boldsymbol{\eta}(f)^T \tag{2.79}$$

where $\mathbf{S}_M(f)$ is the XPSD of the base moments.

Bibliography

[2.1] D. W. Boggs and J. A. Peterka. Aerodynamic model tests of tall buildings. *Journal of Engineering Mechanics*, 115(3):618–635, 1985.

[2.2] E. O. Brigham. *The fast Fourier transform*. Prentice-Hall, Englewood Cliffs, New Jersey, 1974.

[2.3] D. E. Cartwright and M. S. Longuet-Higgins. Note on the distribution of the largest value of a random function with application to gust loading. *Proc. Roy. Soc. of London*, A(237):212–232, 1956.

[2.4] X. Chen and A. Kareem. Coupled building response analysis using HFFB: Some new insights. In *Proc., 5th Bluff Body Aerodynamics and Applications (BBAAV)*. Ottawa, 2004.

[2.5] X. Chen and A. Kareem. Coupled dynamic analysis and equivalent static wind loads on buildings with three-dimensional modes. *Journal of Structural Engineering*, 131(7):1071–1082, 2005.

[2.6] X. Chen and A. Kareem. Dynamic wind effects on buildings with 3D coupled modes: Application of high frequency force balance measurements. *Journal of Engineering Mechanics*, 131(11):1115–1125, 2005.

[2.7] A. K. Chopra. *Dynamics of structures: Theory and applications to earthquake engineering. 2nd Ed.* Prentice-Hall, New York, 2000.

[2.8] R. W. Clough, I. P. King, and E. L. Wilson. Structural analysis of multistory buildings. *J. Struct. Div.*, 89(8), 1963.

[2.9] R. W. Clough and J. Penzien. *Dynamics of structures. 3rd Ed.* Computers and Structures, Inc., Berkeley, 1995.

[2.10] H. Cramer and M. R. Leadbetter. *Stationary and related stochastic processes sample function properties and their applications*. John Whiley, New York, 1967.

[2.11] A. G. Davenport. The application of statistical concepts to the wind loading of structures. *Proceedings Institution of Civil Engineering*, 19:449–472, 1961.

[2.12] A. G. Davenport. Note on the distribution of the largest value of a random function with application to gust loading. *Proceedings Institution of Civil Engineering*, 28:187–196, 1964.

[2.13] A. Der Kiureghian. Structural response to stationary excitation. *J. Eng. Mech. Div.*, 106(6):1195–1213, 1980.

[2.14] H. Hejal and A. K. Chopra. *Earthquake response of torsionally-coupled buildings*. Report no. UBC/EERC-87/20, University of California, Berkeley, 1987.

[2.15] J. D. Holmes, A. Rofail, and L. Aurelius. High frequency base balance methodologies for tall buildings with torsional and coupled resonant modes. In *Proceedings of the 11th International Conference on wind engineering*, pages 2381–2388. Texas Tech Univ., Lubbock, Texas, 2003.

[2.16] M. F. Huang, C. M. Chan, K. C. S. Kwok, and P. A. Hitchcock. Dynamic analysis of wind induced lateral-torsional response of tall buildings with coupled modes. In *Proc., 12th Int. Conf. Wind Eng.*, pages 295–302. Cairns, Australia, 2003.

[2.17] M. F. Huang, C. M. Chan, K. C. S. Kwok, and P. A. Hitchcock. Cross correlations of modal responses of tall buildings in wind-induced lateral-torsional motion. *Journal of Engineering Mechanics*, 135(8):802–812, 2009.

[2.18] P. A. Irwin and J. Xie. Wind loading and serviceability of tall buildings in tropical cyclone regions. In *Proc., 3rd AsiaPacific Symp. on Wind Engineering*. Univ. of Hong Kong, Hong Kong, 1993.

[2.19] A. Kareem. Lateral-torsional motion of tall buildings. *Journal of Structural Engineering*, 111(11):2479–2496, 1985.

[2.20] A. Kareem. Dynamic response of high-rise buildings to stochastic. *Journal of Wind Engineering and Industrial Aerodynamics*, 41-44:1101–1112, 1992.

[2.21] H. N. Li, T. H. Yi, and G. X. Wang. Measurement and analysis of wind-induced response of tall building based on GPS technology. *Adv. Struct. Eng.*, 10(1):83–93, 2007.

[2.22] D. L. Lutes and S. Sarkani. *Random vibrations: analysis of structural and mechanical systems*. Elsevier Butterworth-Heinemann, Burlington, Massachusetts, 2004.

[2.23] A. Papoulis and S. Unnikrishna Pillai. *Probability, Random Variables and Stochastic Processes 4th Ed.* McGraw-Hill, New York, 2002.

[2.24] S. O. Rice. Mathematical analysis of random noise. *Bell System Technical Journal*, 23:282–332, 1944 and 24:46-156 1945.

[2.25] E. Simiu and T. Miyata. *Design of Buildings and Bridges for Wind*. John Wiley Sons, Hoboken, New Jersey, 2006.

[2.26] E. Simiu and R. H. Scanlan. *Wind effects on structures: Fundamentals and applications to design 3rd Ed.* Wiley-Interscience, New York, 1996.

[2.27] T. T. Soong and M. Grigoriu. *Random vibration of mechanical and structural systems*. PTR Prentice Hall, Englewood Cliffs, New York, 1993.

[2.28] A. Tallin and B. Ellingwood. Wind induced lateral-torsional motion of buildings. *Journal of Structural Engineering*, 111(10):2197–2213, 1985.

[2.29] T. Tschanz. Measurement of total aerodynamic loads using elastic models with high natural frequencies. In *International Workshop on Wind Tunnel Modeling Criteria and Techniques in Civil Engineering Applications*. Gaithersburg, Maryland, 1982.

[2.30] E. H. Vanmarcke. On the distribution of the first-passage time for normal stationary random processes. *J. Applied Mech.*, 14:217–243, 1975.

[2.31] P. J. Vickery, S. C. Steckley, N. Isyumov, and B. J. Vickery. The effect of mode shape on the wind induced response of tall buildings. In *Proceedings of the 5th United States National Conference on wind engineering*, pages 1B–41–1B–48. Lubbock, Texas, 1985.

[2.32] N. Wiener. Generalized harmonic analysis. *Acta Mathematica*, 55(118), 1930.

[2.33] E. L. Wilson, A. Der Kiureghian, and E. P. Bayo. A replacement for the srss method in seismic analysis. *Earthquake Engineering and Structural Dynamics*, 9:187–192, 1981.

[2.34] J. Xie, S. Kumar, and S. Gamble. Wind loading study for tall buildings with similar dynamic properties in orthogonal directions. In *Proc., 11th Int. Conf. Wind Eng.*, pages 2390–2396. Lubbock, Texas, 2003.

[2.35] Y. L. Xu and K. C. S. Kwok. Mode shape corrections for wind tunnel tests of tall buildings. *Engineering Structures*, 15:618–635, 1993.

[2.36] D. Y. N. Yip. *Wind-induced dynamic response of tall buildings with coupled 3D modes of vibration*. Ph.D. thesis. University of Auckland, Auckland, 1995.

[2.37] Y. Zhou, A. Kareem, and M. Gu. Mode shape corrections for wind load effects. *Journal of Engineering Mechanics*, 128(1):15–23, 2002.

Chapter 3

Structural Optimization Algorithms

The automatic design of structural systems subject to environmental loads has long been identified as an important method for obtaining the high performance levels often requested by designers. Many studies have been carried out over the past few decades with the aim of identifying appropriate methods for achieving this goal. This chapter will define a particular type of optimization problem of interest to this thesis and the most recent resolution methods will be presented.

3.1 Structural optimization

The term structural optimization refers to the task of searching for the best possible design of a structural system while ensuring all the safety performance requirements dictated by codes. The definition of what is the best design depends on the objectives that are desired by the designer. A common goal is the minimization of the material cost of the structural system. This type of optimization is defined as mono-objective as there is only one goal that is of interest. In the case of two or more goals the optimization is defined as multi-objective. Whether the problem be multi- or mono-objective, there are two main types of structural optimization: topological optimization, in which the objective is minimized allowing the layout of the structural system to change, and section sizing optimization in which the topology of the structural system is fixed. The system properties that are allowed to change during the minimization of the objective are known as design variables.

Over the years numerous approaches have been developed that search for the solution to the general problem outlined above. In particular resolution algorithms are often categorized by their robustness which refers to the capability of a particular approach to solve a wide range of problems. However, often a higher degree of robustness implies a higher degree of inefficiency. While for small scale problems

(with a handful of design variables and constraints) robustness is desirable, for large scale problems (often with several thousand design variables and constraints) the efficiency of a resolution method becomes fundamental. Therefore for many practical optimization problems, such as the member size optimization of tall buildings, the only possible route is the development of specific problem orientated resolution schemes. For an extensive review of the general aspects of structural optimization the following references can be consulted [3.2, 3.21, 3.43, 3.50, 3.54, 3.55, 3.56].

The optimization problems of interest to this thesis are large scale member sizing problems. The remainder of this chapter will focus on the formal definition of the problem and appropriate resolution methods. The final sections will then define the problem in a dynamic setting.

3.2 Member sizing optimization

3.2.1 Problem formulation

The class of problems referred herein as member sizing optimization problems may be stated mathematically as:

$$\text{minimize} \qquad W = \sum_{e=1}^{N_E} \gamma_e L_e x_e \tag{3.1}$$

subject to:

$$d_{kl}(\mathbf{x}) \leq d_k^U \qquad k = 1, 2, ..., N_D \qquad l = 1, 2, ..., N_L \tag{3.2}$$

$$b_{el}(\mathbf{x}) \leq b_e^U \qquad e = 1, 2, ..., N_E \qquad l = 1, 2, ..., N_L \tag{3.3}$$

$$x_e^L \leq x_e \leq x_e^U \qquad e = 1, 2, ..., N_E \tag{3.4}$$

where x_e, γ_e and L_e represent, respectively, the cross-sectional area, specific weight and length of the eth element, N_E is the total number of elements, d_{kl} represents the value of the kth global behavioral constrained function under the lth load condition and d_k^U is the corresponding upper limit, b_{el} is the absolute value of the constrained local level capacity function in the eth element under the lth load case, b_e^U the corresponding upper limit while x_e^U and x_e^L denotes the upper and lower limits of the design variable, x_e.

It can be seen that the objective function W is a linear function of the design variables x_e. Unfortunately this is not the case for the constraint functions d_{kl} and b_{el}. These are non-linear functions of the design variables. Indeed the nodal displacements and element internal forces are linear functions of the elements of the inverse of the stiffness matrix. However, the stiffness matrix has elements in the form of $E_i A_i / L_i$ and $E_i I_i / L_i^\alpha$ for frames, where I_i represents moment of inertia of the member sections and α is an appropriate exponent. This makes the displacements and forces non-linear functions of the cross-sectional properties of the members.

Therefore the optimization problem outlined in equations (3.1)÷(3.4) represents what is referred to as a Non-Linear Programming (NLP) problem. It can also be demonstrated that this class of problem will in general be non-convex [3.21].

A technique called design variable linking is often used in the optimal design of structures, not only for reducing the number of independent variables but also for satisfying certain design requirements (e.g. certain symmetry properties) and for simplifying the manufacturing procedure. For example, in the case of N_E element cross-sectional areas, these could be linked into N_V independent design variables $\{y_1, y_2, ..., y_{N_v}\}^T$. Although complicated functions can, theoretically, be employed for variable linking, the most common linking relation used in practice is that each independent variable controls several element cross-sections, which can be symbolically written as

$$x_e \mid_{e \in S_i} = y_i \tag{3.5}$$

where S_i is the set of elements controlled by the ith independent variable.

3.2.2 Resolution methods

The resolution of the NLP problem outlined in equations (3.1)÷(3.4) has been the focus of numerous studies over the past century. Various strategies have been implemented based on three major optimization approaches, namely the heuristic search techniques, methods based on Mathematical Programming (MP), and finally methods based on Optimality Criteria (OC).

The common denominator of heuristic search techniques is their dependency, in a lesser or greater sense, on a stochastic approach to find the desired solution. Search methods belonging to this class are Genetic Algorithms (GA) [3.24, 3.20], Simulated Annealing (SA) [3.1, 3.40], Evolution Strategies (ES) [3.46, 3.51] and Tabu Searchs (TS) [3.18, 3.19]. What makes these techniques so desirable compared to other methods is their extraordinary robustness. Indeed, no gradients of the constraints or objective function need to be evaluated. However, as mentioned earlier, with robustness comes inefficiency. For example the method proposed in [3.35, 3.34] to solve the member sizing optimization problem required hundreds of iterations with structural reanalysis in order to converge. This makes these methods extremely undesirable if the structural analysis is time-consuming, as for instance in the case of a time domain-based dynamic analysis.

Mathematical programming [3.23, 3.4] algorithms such as the successive quadratic programming method [3.53], the generalized reduced gradient method [3.39], the method of moving asymptotes [3.52], the method of feasible directions [3.54] have all been used for solving structural optimization problems such as (3.1)÷(3.4). Successive Quadratic Programming (SQP) methods are regarded as the standard general-purpose mathematical programming algorithms for solving NLP problems [3.17]. Such methods make use of local curvature information derived from linearization of the original functions, by using their derivatives with respect to the design vari-

ables at points obtained in the process of optimization. Thus, a Quadratic Programming (QP) model (or sub-problem) is constructed from the initial non-linear optimization problem. A local minimizer is found by solving a sequence of these QP sub-problems using a quadratic approximation of the objective function. The most time-consuming part of any optimization algorithm based on MP methods is the sensitivity analysis phase [3.42], which is a central characteristic of all MP optimization methods. The calculation of the sensitivity coefficients follows the application of a relatively small perturbation to each primary design variable. Several techniques have been developed which can be mainly distinguished by their numerical efficiency and their implementation aspects [3.7].

The Achilles' heel of all MP algorithms for solving large scale optimization problems is that their efficiency depends largely on the number of design variables [3.59] and not on the number of constraints. This is particularly restrictive for many real world applications as these will tend to have a far greater number of design variables compared to constraints.

Optimality criteria methods [3.47], in the context of computer-based structural optimization, were initiated in the late 1960s by Berke, Venkayya, Khot and others [3.5, 3.57, 3.6] and later in a unified form – in this case they are known as dual methods – by Fleury [3.15]. They are derived on the basis of the flexibility formulation of matrix analysis and the Kuhn-Tucker optimality condition. Since these methods deal with discretized structural systems, they are often termed Discretized Optimality Criteria (DOC) methods. Over the years the class of problems to which OC methods can be applied has grown [3.47, 3.48, 3.60, 3.58, 3.61, 3.59, 3.10, 3.8, 3.9, 3.11].

The particular characteristic of these methods that make them so competitive for large scale optimization problems is that their capability is mainly limited by the number of active behavioral constraints while their convergence rates, in terms of number of structural analysis performed, are similar to those of MP algorithms [3.59]. It is the limited number of redesign cycles, in the order of tens, that makes OC and MP methods far more attractive than heuristic search techniques for problems with computationally cumbersome structural analysis.

OC methods become particularly attractive for large scale problems with relatively few governing behavioral constraints such as the member size optimization of tall buildings [3.10, 3.8, 3.9, 3.11]. Indeed for these types of problems the capcity constraints of (3.3) may be dealt with through the Fully Stressed Design (FSD) criterion [3.45, 3.10, 3.21, 3.44] while the displacement constraints are treated by rigorous optimality criteria. This approach will not guarantee the optimum as the sensitivities of the capacity constraints are not evaluated. However, for problems governed by global behavioral constraints the solution will present a very good approximation [3.10, 3.8, 3.9, 3.11].

As mentioned earlier this thesis is concerned with large scale member size optimization of structures with relatively few governing behavioral constraints. For this reason the optimization algorithm adopted is based on the DOC-FSD procedure.

3.3 Optimization based on optimality criteria

The sub-set of the member size optimization problem outlined in equations (3.1)÷(3.4) that are of interest to the present study are those governed by the global behavioral constraints of (3.2). For these problems it is extremely convenient to account for the capacity constraints of (3.3) through a zero order approximation. This can be achieved by defining the lower limits on the design variables, x_e^L, by setting the corresponding capacity constraint to its limiting value, b_e^U. These new lower limits will be denoted x_e^{bL}. This procedure of defining the lower limits will, in presence of only capacity constraints, lead to a FSD design. In real engineering problems there will most probably be upper limits, x_e^U, to respect for the design variables as well. The problem will therefore take on the following form:

$$\text{minimize} \qquad W = \sum_{e=1}^{N_E} \gamma_e L_e x_e \tag{3.6}$$

subject to:

$$d_{kl}(\mathbf{x}) \leq d_k^U \qquad k = 1, 2, ..., N_D \qquad l = 1, 2, ..., N_L \tag{3.7}$$

$$\max(x_e^L, x_e^{bL}) \leq x_e \leq x_{eU} \qquad e = 1, 2, ..., N_E \tag{3.8}$$

3.3.1 The optimality conditions

For the sake of simplicity in the following a single loading condition will be considered, i.e. $N_L = 1$, therefore the subscript l will be dropped.

The necessary optimality conditions for the constrained NLP problem (3.6)÷(3.8) may be obtained by applying the Kuhn-Tucker conditions to equations (3.6)÷(3.8) [3.29] which can be expressed, in this particular case, as:

$$\gamma_e L_e + \sum_{k=1}^{N_D} \lambda_k \frac{\partial d_k}{\partial x_e} \begin{cases} = 0 & \text{if} \quad \max(x_e^L, x_e^{bL}) \leq x_e \leq x_e^U \\ \geq 0 & \text{if} \quad x_e = \max(x_e^L, x_e^{bL}) \\ \leq 0 & \text{if} \quad x_e = x_e^U \end{cases} \tag{3.9}$$

with $e = 1, 2, ..., N_E$ and where the Lagrange multipliers, λ_k, are bounded by:

$$\lambda_k \begin{cases} = 0 & \text{if} \quad d_k - d_k^U < 0 \\ > 0 & \text{if} \quad d_k - d_k^U = 0 \end{cases} \tag{3.10}$$

Equation (3.10) requires some additional explanation. Out of the N_D behavioral constraints, only some of these will be active ($d_k = d_k^U$) at the optimal design and thus enter the optimality condition. The inactive constraints ($d_k < d_k^U$) are eliminated by setting $\lambda_k = 0$ for the appropriate values of k.

By omitting the sizing constraints of equations (3.8), the design optimization problem of equations (3.6) and (3.7) can be seen as the unconstrained minimization of the following lagrangian function:

$$L(\mathbf{x}, \boldsymbol{\lambda}) = \sum_{e=1}^{N_E} \gamma_e L_e x_e + \sum_{k=1}^{N_D} \lambda_k d_k(\mathbf{x}) \tag{3.11}$$

subject to the conditions of equations (3.10) concerning the Lagrange multipliers with $\boldsymbol{\lambda}$ given by $\boldsymbol{\lambda} = \{\lambda_1, ..., \lambda_{N_D}\}$. Indeed, by differentiating the lagrangian function with respect to the design variables and setting the derivative to zero, the following stationary condition of the lagrangian function is found:

$$\gamma_e L_e + \sum_{k=1}^{N_D} \lambda_k \frac{\partial d_k}{\partial x_e} = 0 \tag{3.12}$$

This together with the conditions on the Lagrange multipliers coincide with the Kuhn-Tucker conditions for the constrained optimization defined by equations (3.6) and (3.7) while omitting the side constraints of equation (3.8).

The solution of the problem defined in equations (3.6)÷(3.8) is found in an appropriate design variable vector $\tilde{\mathbf{x}}$ and associated vector of Lagrange multipliers $\tilde{\boldsymbol{\lambda}}$ satisfying the conditions outlined in the section. The problem therefore becomes the definition of a suitable algorithm for the determination of these last. In the next section an iterative algorithm, first developed by Berke, Venkayya and Khot [3.5, 3.57, 3.6] and later refined by Haftka [3.21] and applied to the optimization statically loaded tall buildings by Chan [3.10, 3.8, 3.9, 3.11] will be presented.

3.3.2 Redesign procedure

For an active design variable, $\max(x_e^L, x_e^{bL}) \leq x_e \leq x_e^U$, the stationary conditions of equation (3.12) can be used to derive a linear recursive relation for the iterative determination of the optimum value of the design variable $\tilde{\mathbf{x}}$.

To find the recursive relation consider the following rearrangement of equation (3.12), written in the optimum design point:

$$1 = -\frac{\sum_{k=1}^{N_D} \tilde{\lambda}_k \dfrac{\partial d_k}{\partial \tilde{x}_e}}{\gamma_e L_e} \qquad e = 1, 2, ..., N_E \tag{3.13}$$

By multiplying both sides of (3.13) by $(\tilde{x}_e)^\eta$ and taking the ηth root, the following expression is simply obtained:

$$\tilde{x}_e = \tilde{x}_e \left(-\frac{\sum_{k=1}^{N_D} \tilde{\lambda}_k \dfrac{\partial d_k}{\partial \tilde{x}_e}}{\gamma_e L_e} \right)^{1/\eta} \tag{3.14}$$

Obviously, for a generic design variable vector not satisfying the optimality conditions, the equality between the left and right-hand side of equation (3.14) does not hold. Now, consider a first approximation of the design variable vector, $\mathbf{x}^{(1)}$, and a first approximation of the lagrangian multipliers vector, $\boldsymbol{\lambda}^{(1)}$. Substituting these values into the right-hand side of equation (3.14), it can be demonstrated [3.37] that the left-hand side will give a better approximation, $\mathbf{x}^{(2)}$, of optimum design variable vector $\tilde{\mathbf{x}}$.

$$x_e^{(2)} = x_e^{(1)} \left(-\frac{\sum_{k=1}^{N_D} \lambda_k^{(1)} \dfrac{\partial d_k}{\partial x_e^{(1)}}}{\gamma_e L_e} \right)^{1/\eta} \tag{3.15}$$

Based on this result, a recurrence relation for the design variable can be written, which, for the τth step takes the following form:

$$x_e^{(\tau+1)} = x_e^{(\tau)} \left(-\frac{\sum_{k=1}^{N_D} \lambda_k^{(\tau)} \dfrac{\partial d_k}{\partial x_e^{(\tau)}}}{\gamma_e L_e} \right)^{1/\eta} \tag{3.16}$$

where $\tau + 1$ and τ are the iteration numbers, and the parameter η determines the step size. Equation (3.16) is an exponential recursive relation.

From equation (3.16), a more convenient linear recursive relation can be derived. This can be achieved by, firstly, rearranging equation (3.16):

$$x_e^{(\tau+1)} = x_e^{(\tau)} \left[1 + \left(-\frac{\sum_{k=1}^{N_D} \lambda_k^{(\tau)} \dfrac{\partial d_k}{\partial x_e^{(\tau)}}}{\gamma_e L_e} - 1 \right) \right]^{1/\eta} \tag{3.17}$$

Since, near optimum, $\left(-\sum_{k=1}^{N_D} \lambda_k^{(\tau)} \frac{\partial d_k}{\partial x_e^{(\tau)}} / (\gamma_e L_e) \right)$ is nearly equal to unity,

$$\left(-\frac{\sum_{k=1}^{N_D} \lambda_k^{(\tau)} \dfrac{\partial d_k}{\partial x_e^{(\tau)}}}{\gamma_e L_e} \right) - 1 \ll 1$$

Hence, from the binomial theorem (considering only the linear term):

$$\left[1 + \left(-\frac{\sum_{k=1}^{N_D} \lambda_k^{(\tau)} \dfrac{\partial d_k}{\partial x_e^{(\tau)}}}{\gamma_e L_e} - 1 \right) \right]^{1/\eta} \approx 1 + \frac{1}{\eta} \left(-\frac{\sum_{k=1}^{N_D} \lambda_k^{(\tau)} \dfrac{\partial d_k}{\partial x_e^{(\tau)}}}{\gamma_e L_e} - 1 \right) \tag{3.18}$$

Then, substituting this last result into equation (3.18), the following linear recursive relation is found [3.37, 3.10, 3.8, 3.9, 3.11]:

$$x_e^{(\tau+1)} = x_e^{(\tau)} \left[1 + \frac{1}{\eta} \left(- \frac{\sum_{k=1}^{N_D} \lambda_k^{(\tau)} \dfrac{\partial d_k}{\partial x_e^{(\tau)}}}{\gamma_e L_e} - 1 \right) \right] \qquad e = 1, 2, ..., N_E \tag{3.19}$$

To apply equation (3.19) to the τth design variable vector $\mathbf{x}^{(\tau)}$ for finding $\mathbf{x}^{(\tau+1)}$, the τth vector of lagrangian multipliers $\boldsymbol{\lambda}^{(\tau)}$ must be determined. To this end consider the change in the kth behavioral constraint, $(d_k^{(\tau+1)} - d_k^{(\tau)})$, due to the changes $(x_e^{(\tau+1)} - x_e^{(\tau)})$ in the eth design variable, i.e.

$$(d_k^{(\tau+1)} - d_k^{(\tau)}) = \sum_{e=1}^{N_E} \left(\frac{\partial d_k}{\partial x_e^{(\tau)}} \right) (x_e^{(\tau+1)} - x_e^{(\tau)}) \tag{3.20}$$

By rearranging (3.19) for the design variables:

$$x_e^{(\tau+1)} - x_e^{(\tau)} = \frac{x_e^{(\tau)}}{\eta} \left(- \frac{\sum_{k=1}^{N_D} \lambda_k^{(\tau)} \dfrac{\partial d_k}{\partial x_e^{(\tau)}}}{\gamma_e L_e} - 1 \right) \qquad e = 1, 2, ..., N_E \tag{3.21}$$

Supposing that the kth behavioral constraint becomes active after the $(\tau + 1)$th iteration so that $(d_k^{(\tau+1)} = d_k^U)$, substituting (3.21) into (3.20) and rearranging gives [3.10, 3.8, 3.9, 3.11]:

$$\sum_{j=1}^{N_D} \lambda_j^{(\tau)} \sum_{e=1}^{N_E} \left(\frac{x_e^{(\tau)} \dfrac{\partial d_k}{\partial x_e^{(\tau)}} \dfrac{\partial d_j}{\partial x_e^{(\tau)}}}{\gamma_e L_e} \right) = - \sum_{e=1}^{N_E} x_e^{(\tau)} \frac{\partial d_k}{\partial x_e^{(\tau)}} - \eta (d_k^U - d_k^{(\tau)}) \quad k = 1, 2, ..., N_D \tag{3.22}$$

This represents a linear system in terms of the unknown vector of lagrangian multipliers $\boldsymbol{\lambda}^{(\tau)}$ of the τth step. This system is fully defined from the knowledge of $\mathbf{x}^{(\tau)}$ and the partial derivatives of the functions d_k evaluated in $\mathbf{x}^{(\tau)}$. The resolution of the system yields $\boldsymbol{\lambda}^{(\tau)}$ which can then be used to calculate $\mathbf{x}^{(\tau+1)}$ from equation (3.19)

Equation (3.19) for the sizing variables and equation (3.22) for Lagrange multipliers form the basis of the iterative OC method for the solution of the NLP problem of (3.6)÷(3.8). By successively applying the recursive optimization iteration until the convergence of $\mathbf{x}^{(\tau)}$ as well as $\boldsymbol{\lambda}^{(\tau)}$ occurs, a continuous optimal solution for (3.6)÷(3.8), is found.

3.4 Optimization under dynamic loads

The NLP problem of equations (3.6)÷(3.8) is set in a static environment. However, loads such as wind are obviously dynamic in nature. Not only that, but their frequency content can be similar to those of structures. This will result in a certain amount of dynamic amplification due to resonance between the two systems. Hence the structural response will be governed by equation (7.7). Traditionally the dependency on time of the response is eliminated through the definition of a number of idealized Equivalent Static Loads (ESLs) that account in some way for the dynamic nature of the problem. After the ESLs have been defined the structure can be optimized using the formulation so far presented. It should be appreciated that for a structural response with a resonant component the ESLs will depend on the dynamic properties of the system and will need updating during the optimization process. This is a fact nearly always overlooked during the optimization process.

Instead of defining ESLs, the NLP problem can be directly modeled in the time domain. The design problem outlined in equations (3.6)÷(3.8) would in this new setting be stated mathematically as:

$$\text{minimize} \qquad W = \sum_{e=1}^{N_E} \gamma_e L_e x_e \tag{3.23}$$

subject to:

$$d_k(\mathbf{x}, t) \leq d_k^U \qquad k = 1, 2, ..., N_D \tag{3.24}$$

$$\max(x_e^L, x_e^{bL}(t)) \leq x_e \leq x_e^U \qquad e = 1, 2, ..., N_E \tag{3.25}$$

In this new setting both the behavioral constraints and moveable lower limits depend on time. The potential advantage of this formulation over the equivalent static version is the elimination of the need to define any ESLs. For simple problems this may not give significant gains. However, for more complex problems, where the definition of appropriate ESLs becomes difficult, significant gains in both reliability and cost could be obtained, especially considering the sensitivity of the solution to a problem like that outlined in equations (3.6)÷(3.8) to the ESLs.

The problem stated in (3.23)÷(3.25) can be defined as a dynamic response optimization problem [3.3]. The difficulty of resolving this type of problem lays in the time dependent behavioral constrained functions, $d_k(\mathbf{x}, t)$.

3.4.1 Time dependent constraints

In treating the time dependent constraints the goal is to somehow eliminate the dependency on time therefore transforming the dynamic response optimization problem back into a standard NLP problem that can then be solved with an appropriate optimization algorithm [3.3, 3.33]. The exact approach adopted will depend, among other things, on the particular algorithm that is desired for the resolution of the resulting time independent problem. Excluding the heuristic search techniques, there

are two main categories of optimization algorithms that can be used to solve the general problem stated in equations (3.1)÷(3.3): primal methods and transformation methods [3.3, 3.4]. Primal methods work directly with the original problem while transformation methods convert the original constrained optimization problem into a series of unconstrained problems. OC methods fall under the umbrella of primal methods. Due to the extremely efficient nature of these methods for solving time independent problems of interest to this study, the method adopted for eliminating the time parameter must allow the resulting time independent problem to be resolved by a primal method.

There are two main methods for eliminating the time parameter from (3.24) [3.3, 3.33], namely: the method based on equivalent functionals [3.14, 3.38, 3.26, 3.27, 3.28] and the worst case approach based on replacing the original time dependent constraint with a number of static constraints derived from the time history of $d_k(\mathbf{x}, t)$ [3.26, 3.27, 3.28, 3.36, 3.41, 3.22, 3.13, 3.12, 3.62, 3.49, 3.16].

In the equivalent functional method the behavioral constrained function, $d_k(\mathbf{x}, t)$, is used to define an equivalent functional by integrating over the observation period of $d_k(\mathbf{x}, t)$ while setting its value to zero for moments in which the constraint is not violated. By considering the equivalent functional in place of $d_k(\mathbf{x}, t)$ the problem will converge to the same solution as the orginal problem. However, the convergence of the time independent problem is known to be slow and difficult. In particular it is noted that the equivalent functional is often numerically unstable [3.25, 3.33]. It should also be appreciated that finding an approximate explicit formulation of the implicit (in terms of the design variables) equivalent functional would not be an easy task.

In the worst case approach the behavioral constrained function $d_k(\mathbf{x}, t)$ is replaced by the maximum violated responses $\max(d_k(\mathbf{x}, t))$. While easy to implement, the time when the maximum violated response occurs generally varies as the optimization process proceeds. One of the local maximum responses, which is not the worst case in a previous iteration, can become the worst case in the next iteration. Thus, the convergence can be slow or the problem can diverge [3.3, 3.62, 3.33]. To improve the convergence, together with the maximum violated responses a number of local maximums can be taken as constraints or all time gird points derived from a discrete time representation of the functions $d_k(\mathbf{x}, t)$ may be considered [3.12, 3.49, 3.16]. However, this will cause the number of constraints to noticeably increase, hence causing a slowing of the OC optimization process at each redesign cycle.

As mentioned the formulation based on equivalent functionals is troublesome if an approximate explicit formulation of the resulting time independent problem is desired. Unfortunately, for large scale problems with implicit constraints, it is the possibility to define an approximate explicit formulation that guarantees a quick convergence at each redesign cycle. Therefore the only possible classical approach for eliminating time is based on the worst case approach. However, this formulation not only has the shortcomings already mentioned, but also suffers the fact that

it is the maximum response of a particular time history realization that is being optimized. This is not in general useful to the design of wind excited structures for which a probabilistic description of the response process $d_k(\mathbf{x}, t)$ is of far greater interest. While there is a number of studies in this direction [3.30, 3.31, 3.32], most of these concern relatively small scale systems subject to earthquake loading.

One of the goals of this thesis will be the definition of approaches, specifically for wind excited tall buildings, that efficiently solve the problem outlined in equations (3.23)÷(3.25) in terms of a probabilistic description of the peak of the time dependent constrained functions $d_k(\mathbf{x}, t)$.

Bibliography

[3.1] E. Aarts and J. Korst. *Simulated Annealing and Boltzmann Machines: A Stochastic Approach to Combinatorial Optimization and Neural Computing*. John Wiley and Sons, New York, 1989.

[3.2] J. S. Arora. *Introduction to optimum design*. McGraw-Hill, New York, 1989.

[3.3] J. S. Arora. Optimization of structures subjected to dynamic loads. In C. T. Leondes, editor, *Structural dynamic systems computational techniques and optimization*, pages 1–73. Gordon and Breach Science Publishers, 1999.

[3.4] A. D. Belegundu and J. S. Arora. A study of mathematical programming methods for structural optimization. *International journal for numerical methods in engineering*, 2(1):1583–1599, 1985.

[3.5] L. Berke. *An efficient approach to the minimum weight design of deflection limited structures*. Rep. Air Force Flight Dynamics Lab. AFFDL-TM-70-4, Ohio, USA, 1970.

[3.6] L. Berke and N. S. Knot. *Use of optimality criteria for large scale systems*. NATO AGARD-LS-70, NATO, 1974.

[3.7] K. U. Bletzinger, S. Kimmich, and E. Ramm. Efficient modelling in shape optimal design. *Computing Systems in Engineering*, 2(5):483–495, 1991.

[3.8] C. M. Chan. Optimal lateral stiffness design of tall buildings of mixed steel and concrete construction. *The Structural Design Of Tall Buildings, John Wiley Sons, Ltd.*, 10:155–177, 2001.

[3.9] C. M. Chan and J. K. L. Chui. Wind-induced response and serviceability design optimization of tall steel buildings. *Engineering Structures, Elsevier*, 28:503–513, 2006.

[3.10] C. M. Chan, D. E. Grierson, and A. N. Sherbourne. Automatic optimal design of tall steel building frameworks. *Journal of Structural Engineering, ASCE*, 121(5):838–847, 1995.

[3.11] C. M. Chan, M. F. Huang, and K. C. S. Kwok. Stiffness optimization for wind-induced dynamic serviceability design of tall buildings. *Journal of Structural Engineering*, 135(8):985–997, 2009.

[3.12] W. S. Choi and G. J. Park. Structural optimization using equivalent static loads at all time intervals. *Comput. Methods Appl. Mech. Engrg.*, 191:2077–2094, 20092.

[3.13] L. F. P. Etman and D. H. Van Campen. Design optimization of multibody systems by sequential approximation. *Multibody Syst. Dyn.*, 2:393–415, 1998.

[3.14] T. T. Feng, J. Arora, and E. J. Haug. Optimal structural design under dynamic loads. *Int. J. Numer. methods Eng.*, 11:39–52, 1977.

[3.15] C. Fleury. Structural weight optimization by dual methods of convex programming. *Int. Journal of Num. Meth. Engng*, 14:1761–1783, 1979.

[3.16] S. Gholizadeh and E. Salajegheh. Optimal design of structures subjected to time history loading by swarm intelligence and an advanced metamodel. *Comput. Methods Appl. Mech. Engrg.*, 198:2936–2949, 2009.

[3.17] P. E. Gill, W. Murray, and M. H. Wright. *Practical Optimization*. Academic Press., 1981.

[3.18] F. Glover and M. Laguna. *Modern heuristic techniques for combinatorial problems*. Halsted, New York, 1993.

[3.19] F. Glover and M. Laguna. *Tabu search*. Kluwer, Norwell, Mass., 1997.

[3.20] D. E. Goldberg. *Genetic Algorithms in Search, Optimization and Machine Learning*. Addison-Wesley Publishing, Reading, MA., 1989.

[3.21] R. T. Haftka and Z. Gurdal. *Elements of structural optimization*. Kluwer, Dordrecht, 1992.

[3.22] E. J. Haug and J. S. Arora. *Applied optimal design: mechanical and structural systems*. Wiley-Interscience, New York, 1979.

[3.23] F. S. Hillier and G. J. Lieberman. *Introduction to Mathematical Programming*. McGraw-Hill Publishing Company, New York, 1990.

[3.24] J. H. Holland. *Adaptation in Natural and Artificial Systems*. The University of Michigan Press, Ann Arbor, 1975.

[3.25] C. C. Hsieh and J. Arora. Design sensitivity analysis and optimization of dynamic response. *Comput. Methods Appl. Mech. Eng.*, 43:195–219, 1984.

[3.26] C. C. Hsieh and J. Arora. An efficient method for dynamic response optimization. *AIAA J.*, 23:1484–1486, 1985.

[3.27] C. C. Hsieh and J. Arora. A hybrid formulation for treatment of pointwise state variable constraints in dynamic response optimization. *Comput. Methods Appl. Mech. Eng.*, 48:171–189, 1985.

[3.28] C. C. Hsieh and J. Arora. Structural design sensitivity analysis with general boundary conditions-dynamic problem. *Int. J. Numer. Methods Eng.*, 21:267–283, 1985.

[3.29] S. L. Jacoby, J. S. Kowalik, and J. T. Pizzo. *Iterative methods for nonlinear optimization problems.* Prentice-Hill, 1972.

[3.30] H. A. Jensen. On the structural synthesis of uncertain systems subjected to environmenatal loads. *Struct. Multidisc. Optim.*, 20:37–48, 2000.

[3.31] H. A. Jensen, A. Marillanca, and O. Peñaloza. A computational procedure for response statistics-based optimization of stochastic non-linear FE-models. *Comput. Methods Appl. Mech. Engrg.*, 198:125–137, 2008.

[3.32] H. A. Jensen, M. A. Valdebenito, and G. I. Schuëller. An efficient reliability-based optimization scheme for uncertain linear systems subject to general gaussian excitation. *Comput. Methods Appl. Mech. Engrg.*, 198(1):7287, 2008.

[3.33] B. S. Kang, G. J. Park, and J. S. Arora. A review of optimization of structures subjected to transient loads. *Struct. Multidisc. Optim.*, 31:81–95, 2006.

[3.34] M. Kargahil and J. C. Anderson. Structural weight optimization of frames using tabu search. II: Evaluation and seismic performance. *Journal of Structural Engineering, ASCE*, 132(12):1869–1879, 2006.

[3.35] M. Kargahil, J. C. Anderson, and M. M. Dessouky. Structural weight optimization of frames using tabu search. I: Optimization procedure. *Journal of Structural Engineering, ASCE*, 132(12):1858–1868, 2006.

[3.36] M. R. Khan, W. A. Thornton, and K. D. Willmert. Optimality criterion techniques applied to mechanical design. *J. Mech. Des. Trans., ASME*, 100:319–327, 1978.

[3.37] N. S. Knot, L. Berke, and V. B. Venkayya. Comparison of optimality criteria algorithms for minimum weight design of structures. *AIAA Journal*, 17(2):182–190, 1979.

[3.38] F. Y. Kocer and J. Arora. Optimal design of latticed towers subjected to earthquake loading. *Journal of Structural Engineering, ASCE*, 128:197–204, 2002.

[3.39] L. S. Lasdon, A. D. Warren, A. Jain, and R. Ratner. Design and testing of a generalized reduced gradient code for nonlinear programming. *ACM Trans. Math. Soft.*, 4(1):34–50, 1978.

[3.40] G. L. Nemhauser and S. J. Wolsey. *Integer and Combinatorial Optimization.* John Wiley and Sons, New York, N.Y., 1988.

[3.41] S. Oral and S. K. Ider. Optimum design of high-speed flexible robotic arms with dynamic behavior constraints. *Computers and Structures, Elsevier Science Ltd.*, 65:255–259, 1997.

[3.42] M. Papadrakakis, Y. Tsompanakis, E. Hinton, and J. Sienz. Advanced solution methods in topology optimization and shape sensitivity analysis. *Journal of Engineering Computations*, 3(5):57–90, 1996.

[3.43] I. C. Parmee and P. Hajela. *Optimization in Industry.* Springer, Berlin, Heidelberg New York, 2002.

[3.44] S. N. Patnaik and D. A. Hopkins. *Optimality of a Fully Stressed Design.* NASA/TM1998-207411, Lewis Research Center, Cleveland, Ohio, 1998.

[3.45] R. Razani. Behavior of fully stressed design of structures and its relationship to minimum weight design. *AIAA Journal*, 3(14):2262–2268, 1965.

[3.46] I. Rechenberg. *Evolution Strategy: Optimization of Technical Systems according to the Principles of Biological Evolution.* Frommann-Holzboog, Stuttgart, 1973.

[3.47] G. I. N. Rozvany. *Structural design via optimality criteria.* Dordrecht, Kluwer, 1989.

[3.48] G. I. N. Rozvany, M. Zhou, and W. Gollub. Continuum-type optimality criteria methods for large finite element systems with a displacement constraint. part II. *Structural Optimization, Spinger-Verlag*, 2:77–104, 1990.

[3.49] E. Salajegheh, S. Gholizadeh, and M. Khatibinia. Optimal design of structures for earthquake loads by a hybrid RBFBPSO method. *Earthquake Engineering and Engineering Vibration*, 7(1):13–24, 2008.

[3.50] L. A. Schmit. Structural synthesis-its genesis and development. *AIAA Journal*, 19:1249–1264, 1981.

[3.51] H. P. Schwefel. *Numerical Optimization for Computer Models.* Wiley Sons, Chichester, 1981.

[3.52] K. Svanberg. The method of moving asymptotes, a new method for structural optimization. *Int. J. Num. Meth. Eng.*, 23:359–373, 1987.

[3.53] P. B. Thanedar, J. S. Arora, C. H. Tseng, O. K. Lim, and G. J. Park. Performance of some SQP methods on structural optimization problems. *Int. Journal of Num. Meth. Engng*, 23:2187–2203, 1986.

[3.54] G. N. Vanderplaats. *Numerical optimization techniques for engineering design.* McGraw-Hill, New York, 1984.

[3.55] G. N. Vanderplaats. 30 years of modern structural optimization. *Adv Eng Softw*, 16:8188, 1993.

[3.56] G. N. Vanderplaats. Structural design optimization status and direction. *J Aircr*, 36:1120, 1999.

[3.57] V. B. Venkayya, N. S. Knot, and L. Berke. Application of optimality criteria approaches on automated design of large practical structures. In *2nd Symp. Structure Optimization, AGARD CP-123*, pages 3.1–3.19. Milano, Italy, 1973.

[3.58] M. Zhou. An efficient DCOC algorithm based on high-quality approximations for problems including eigenvalue constraints. *Computer Methods in Applied Mechanics and Engineering, Elsevier Science S.A.*, 128:383–394, 1995.

[3.59] M. Zhou and G. I. N. Rozvany. DCOC: An optimality criteria method for large systems part I: theory. *Structural Optimization, Spinger-Verlag*, 5:12–25, 1992.

[3.60] M. Zhou and G. I. N. Rozvany. DCOC: An optimality criteria method for large systems part II: algorithm. *Structural Optimization, Spinger-Verlag*, 5:12–25, 1993.

[3.61] M. Zhou and G. I. N. Rozvany. An improved approximation technique for the dcoc method of sizing optimization. *Computers and Structures, Elsevier Science Ltd.*, 60(5):763–769, 1996.

[3.62] X. K. Zou and C. M. Chan. An optimal resizing technique for dynamic drift design of concrete buildings subjected to response spectrum and time history loadings. *Computers and Structures*, 83:1689–1704, 2005.

Chapter 4

Wind Tunnel Tests

The response of any dynamic system will obviously depend strongly on the nature of the forcing functions. In the case of wind excited tall buildings these will depend on the particular aerodynamic behavior of the structure under consideration and can be determined through specific experimental tests. In this chapter wind tunnel tests, carried out in the boundary layer wind tunnel of the CRIACIV-DIC[1], aimed at aerodynamically characterizing two tall buildings are described.

4.1 Test characteristics

4.1.1 Tunnel description

The CRIACIV - DIC Boundary Layer wind tunnel (figure 4.1) is an open circuit facility with a convergent nozzle for the flow acceleration and a T-shaped symmetric diffuser.

The tunnel has a total length of 27 m and cross-section that diverges from a 2.20 m width with 1.60 m height at the inlet to 2.40 m width and 1.60 m height at the working section allowing constant pressure along the axis. The total length of the developing fetch is 8 m while the length of the working section is 2.4 m. At the inlet the flow is regularized by a barrier consisting of a 5 cm thick honeycomb panel, followed by a squared mesh screen. The growth of the boundary layer is artificially accelerated by the spires-roughness technique [4.11, 4.10]. A general outline of the tunnel is reported in figure 4.2.

The models are mounted on a turntable which enables the incident wind direction to be changed. The flow is drawn in by an axial fan placed downstream of the working section ensuring that the turbulence generated by the fan does not contaminate the flow. The axial fan rotates at a constant speed. An elastic joint

[1]CRIACIV: Italian Inter-university Research Center in Aerodynamics of Constructions and Wind Engineering. DIC: Civil Engineering Department. University of Florence, Italy.

Figure 4.1: Wind tunnel.

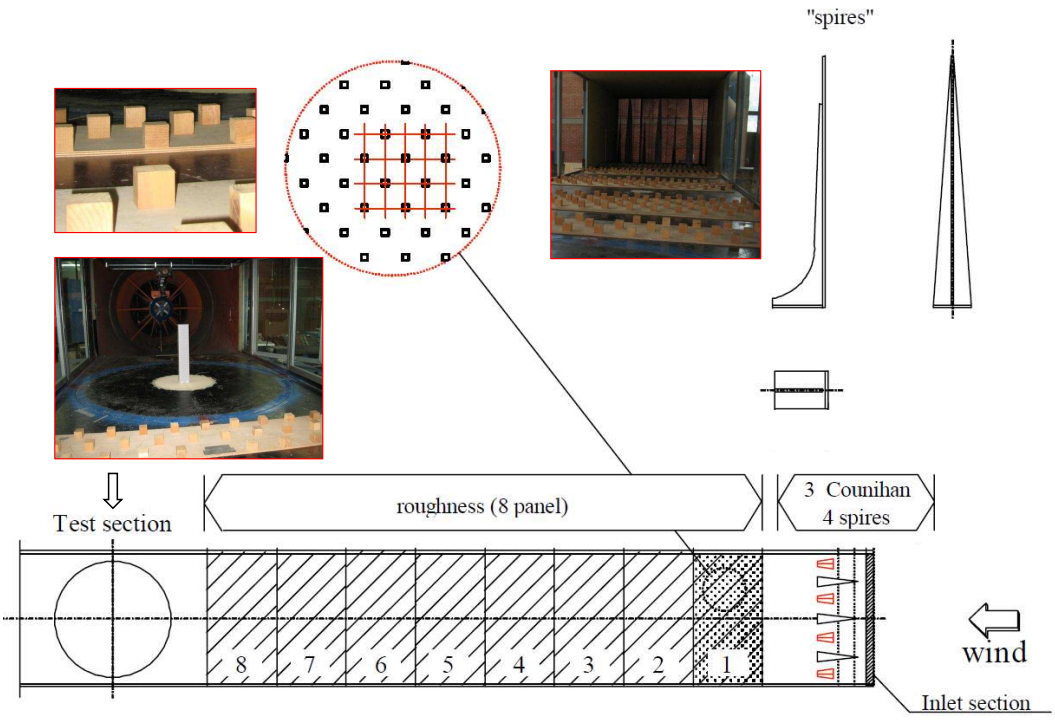

Figure 4.2: Tunnel outline.

is placed between the working section and the axial fan to isolate the former from the vibration produced by the propeller system. The velocity of the flow can be varied from 0 to 32 m/s by controlling the angle pitch of the 10 blades constituting the fan and by regulating the number of engine turns through an inverter. The fan has a power of 158 kW and is equipped with a servomotor to control the continuity of the flow. The exit of the flow is regularized by two diffusers which minimize the loss of pressure.

4.1.2 Measurement instrumentation

The instrumentation devices used during the wind tunnel tests were the hot wire anemometer for the dynamic measurements of the wind speed, the Pitot-Prandtl tube for the static pressure measurement and pressure transducers with synchronous acquisition, SMPSS set up, for measuring the local pressure field on the building surfaces.

Pressure transducers

Dynamic pressures can be measured with a sampling frequency up to 1 kHz. The number of acquisition channels used are inversely proportional to the sampling frequency. For example, for the maximum number of pressure signals that can be simultaneously measured (128), the sampling frequency decreases to 250 Hz per channel. Six peripheral scanners (figure 4.3), each with 16 or 32 miniaturized piezoelectric pressure transducers are controlled by a Pressure System unit, PSI 8400 (figure 4.4), for calibration, acquisition, and analogic-digital conversion of the data.

The pressure is indirectly determined by measuring the deformation of an elastic diaphragm, with a known area, caused by the pressure itself. As the pressure is not a fundamental quantity, it is measured indirectly from the ratio between the force and the area where the force is applied. The deformation is used to generate a voltage signal that is sampled by the acquisition board, KPC- 488.2AT.

Owing to their small dimensions (13 $\times$ 21.5 $\times$ 69 mm for the 16 channel type and 26 $\times$ 21.5 $\times$ 69 for the 32 channel type), the PSI scanners can also be located inside the models (figure 4.5). Before every measurement the transducers must be calibrated because the output depends on the wind tunnel's air density, namely the air pressure and temperature inside the working section. Once the measurement range is evaluated, the calibration is carried out by means of a pressure calibration unit, PCU. During the calibration, each of the transducers reads 5 reference pressure values generated by the PCU. These values can be changed by the operator depending on the required range which must be between 254 mm of water. The measured points are interpolated by a fourth order polynomial. The accuracy of the calibration procedure is $\pm 0.05\%$ of the maximum allowed pressure. The error of the pressure measurements is $\pm 0.2\%$ of the maximum allowed pressure.

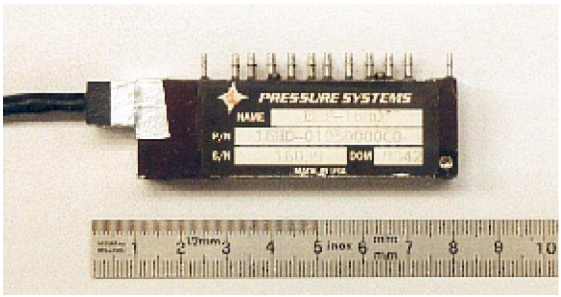

Figure 4.3: Pressure transducers.

Figure 4.4: Pressure acquisition system PSI 8400.

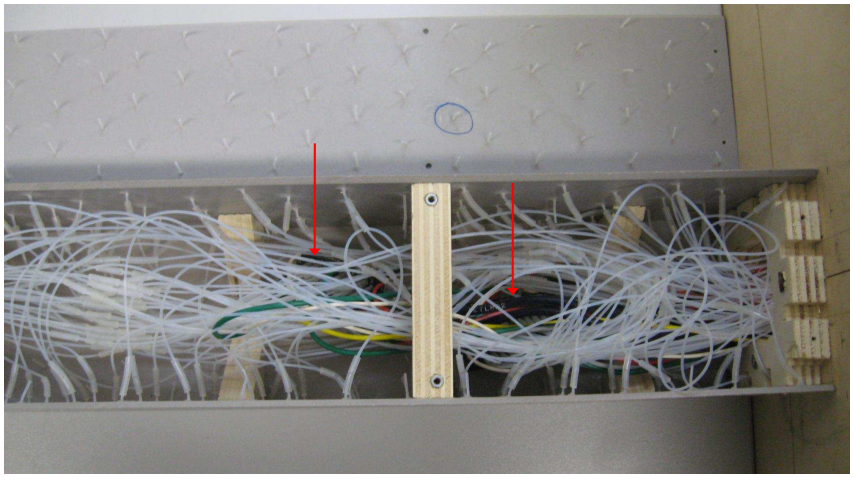

Figure 4.5: PSI placed inside the model.

The pressures acting on the model's surface must be transmitted to the sensor without distortions. The transmission is carried out through small highly flexible plastic tubes, manufactured in silicone or teflon. Inside the tubes are inserted one or more dampers, obtained by a contraction of the tube's diameter. The system constituted by tubes and dampers is properly calibrated so that its frequency response does not influence the measurements, figure 4.6.

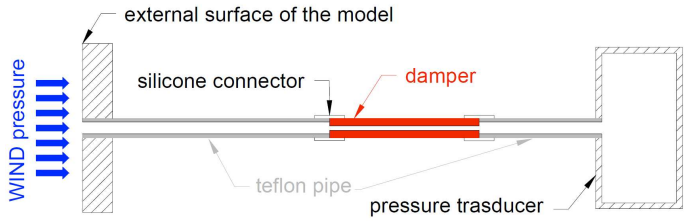

Figure 4.6: Tubing set up.

4.2 Experimental results

4.2.1 Wind simulation

The flow conditions that were simulated for this study correspond to suburban terrain. Prior to the pressure measurements, hot wire anemometer measurements using a single probe were carried out in order to evaluate the characteristics of the incoming wind flow. The measurement points were located along a vertical line at the center of the working section. The wind velocity was recorded for 60 seconds with a sampling frequency of 600 Hz.

Fitting the experimental data of the mean wind speed profiles, $\bar{V}(z)$, with the power law model an exponent of 2/9 is found (figure 4.7). The gradient height (boundary layer thickness) is estimated in the order of $h_g = 75$ cm. While for the logarithmic model a roughness length of $z_0 = 0.223$ is obtained (figure 4.7). The corresponding longitudinal turbulence intensities, $I_z = \sigma(z)/\bar{V}(z)$ [4.11, 4.9] at the test section are shown in figure 4.8. Figure 4.9 shows the estimated spectra of the simulated wind speed at height $h = 30$ cm compared with von Kármán's wind spectrum:

$$\frac{fS_{VV}(f)}{\sigma_V^2} = \frac{4f_r}{(1+70.8f_r^2)^{\frac{5}{6}}} \tag{4.1}$$

where $S_{VV}(f)$ is the power spectral density function of the longitudinal wind speed, σ_V is the standard deviation while f_r is the reduced frequency defined by $f_r = f_r L_{V_z}/\bar{V}_z$ where $\bar{V}_z$ is the mean wind speed and $L_{\bar{V}_z}$ is the integral length scale [4.3]. In figure 4.10 is shown $L_{\bar{V}_z}$ determined for each height, z, by fitting the estimated spectra at that height, $S_{VV}(f,z)$, with von Kármán's wind spectrum.

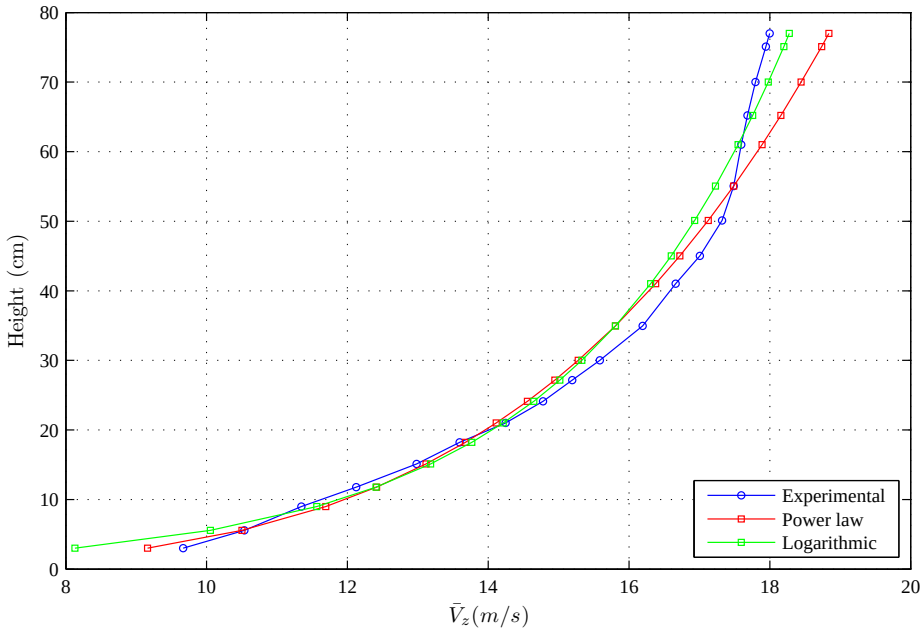

Figure 4.7: Mean wind speed profile.

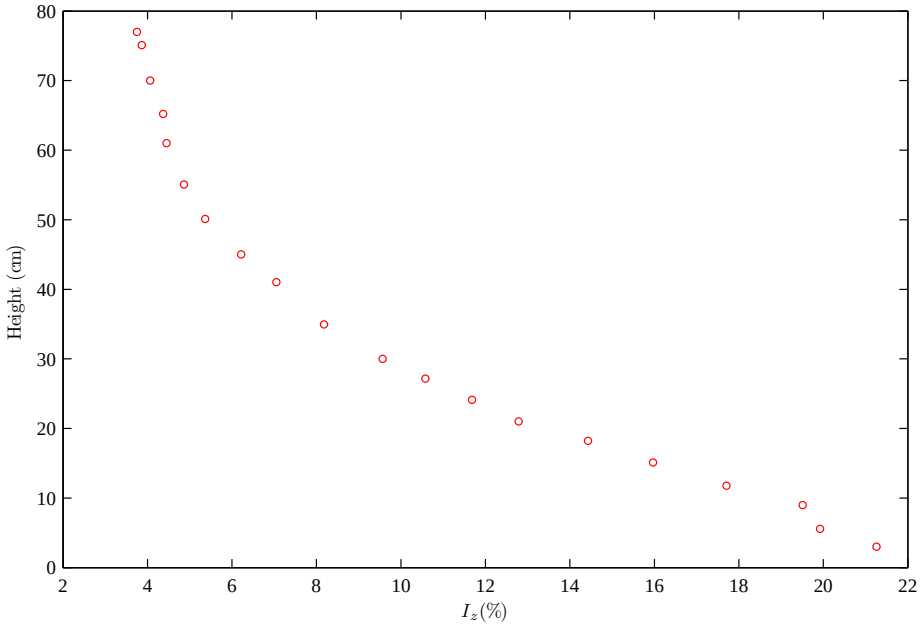

Figure 4.8: Turbulence intensity.

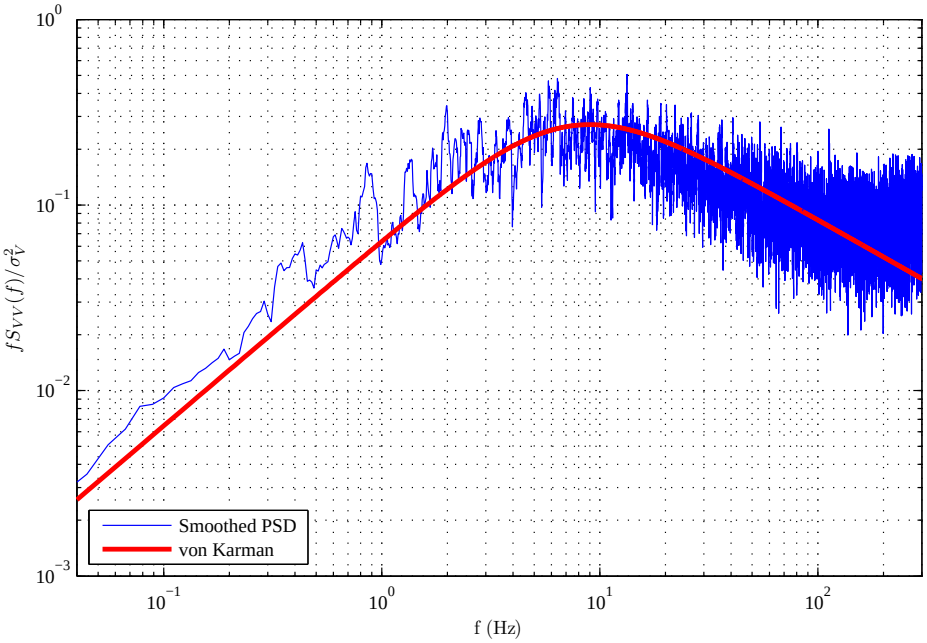

Figure 4.9: Wind velocity fluctuations spectra, Von Kármán fit.

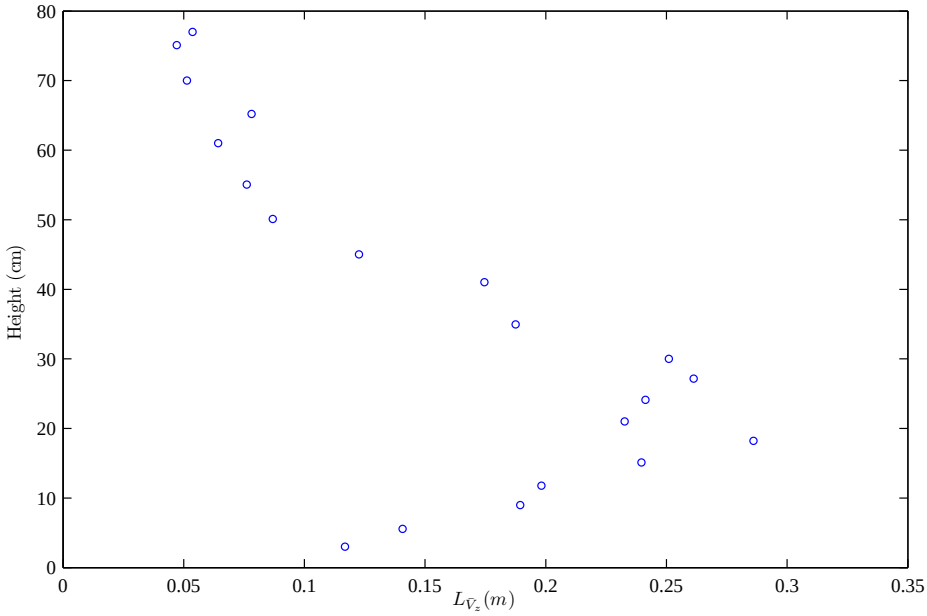

Figure 4.10: Integral length scale of the longitudinal turbulence.

4.2.2 Pressure measurements

The objective of the wind tunnel tests described in this chapter was the aerodynamic characterization of two tall buildings having the geometric profiles shown in figures 4.12 and 4.13. In particular one of the buildings has the geometric form of the Bank of China, situated in Hong Kong and design by I.M. Pei, while the other is characterized by having the same square footprint and height but is defined by a regular geometric form. In the following figures the Bank of China will be identified by the letter "B" while the regular building will be identified by the letter "R".

For both buildings pressure measurements were carried out on rigid 1/500 scale models equipped with 126 simultaneously measured pressure taps. The location of the taps and influence areas are shown in figures 4.14 and 4.15. The measurements were repeated with 10° increments from 0° to 360° for a total of 36 wind directions in the case of the Bank of China building, while for the regular building only increments from 0° to 90° were considered due to the buildings symmetry. The measurements commence with wind blowing as shown in figures 4.12 and 4.13. A sampling frequency, f_m, of 250 Hz was adopted and 30 s of data was recoded for each wind direction. The average wind speed at the top of the model $\bar{V}_m$ in the wind tunnel during the tests was 20 m/s. Sets of time varying pressure coefficients for each wind direction were evaluated. These coefficients are given by:

$$\mathcal{C}_p(t) = \frac{\mathcal{P}(t) - \mathcal{P}_H(t)}{\frac{1}{2}\rho_a \bar{V}_H^2} \tag{4.2}$$

were $\mathcal{P}(t)$ is the total pressure, H is the building model height, $\mathcal{P}_H(t)$ the static pressure at H, ρ_a the mass density of air, and $\bar{V}_H$ the mean wind velocity at H. The time history and PSD of an example pressure coefficient of the regular building for wind blowing at $\alpha = 0°$ are shown in figure 4.11.

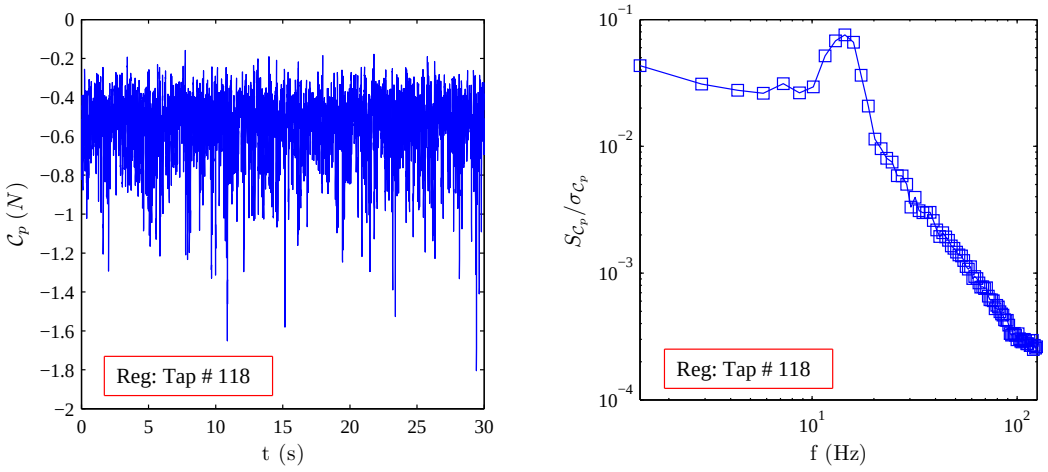

(a) (b)

Figure 4.11: Example pressure coefficient: (a) time history, (b) smoothed PSD.

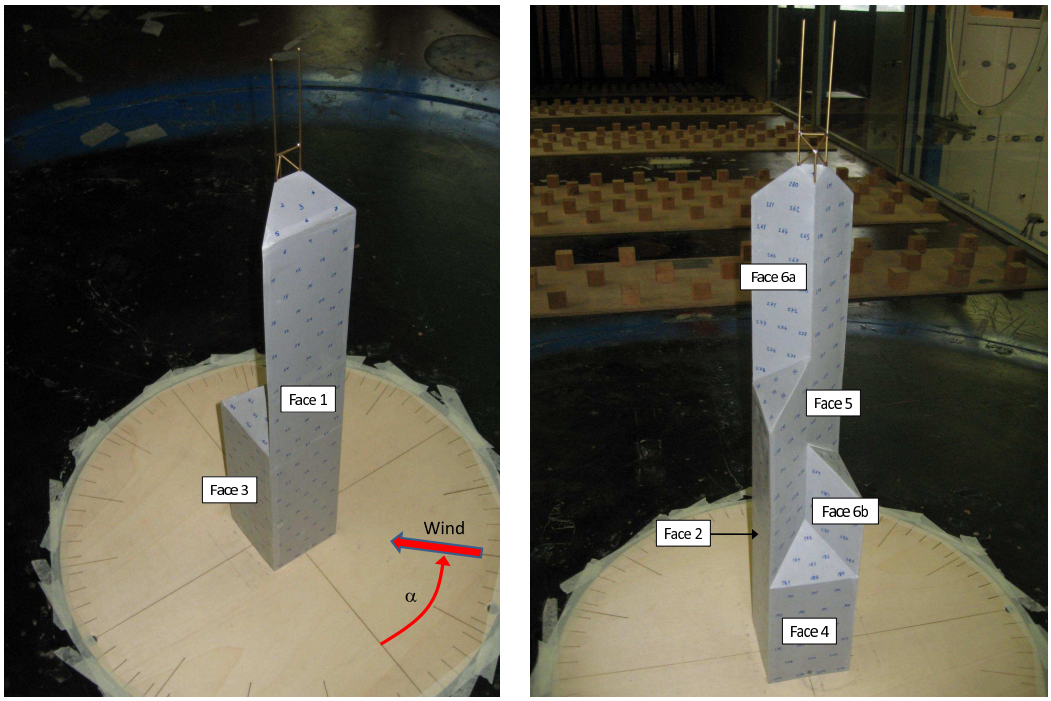

(a) (b)

Figure 4.12: Building's geometry and reference system for the Bank of China building: (a) faces 1 and 3, (b) faces 2 and 4 to 6b.

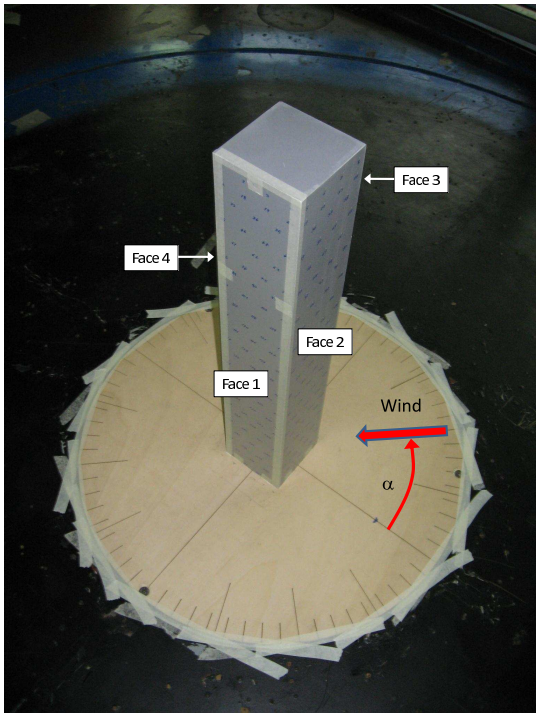

Figure 4.13: Regular building's geometry and reference system.

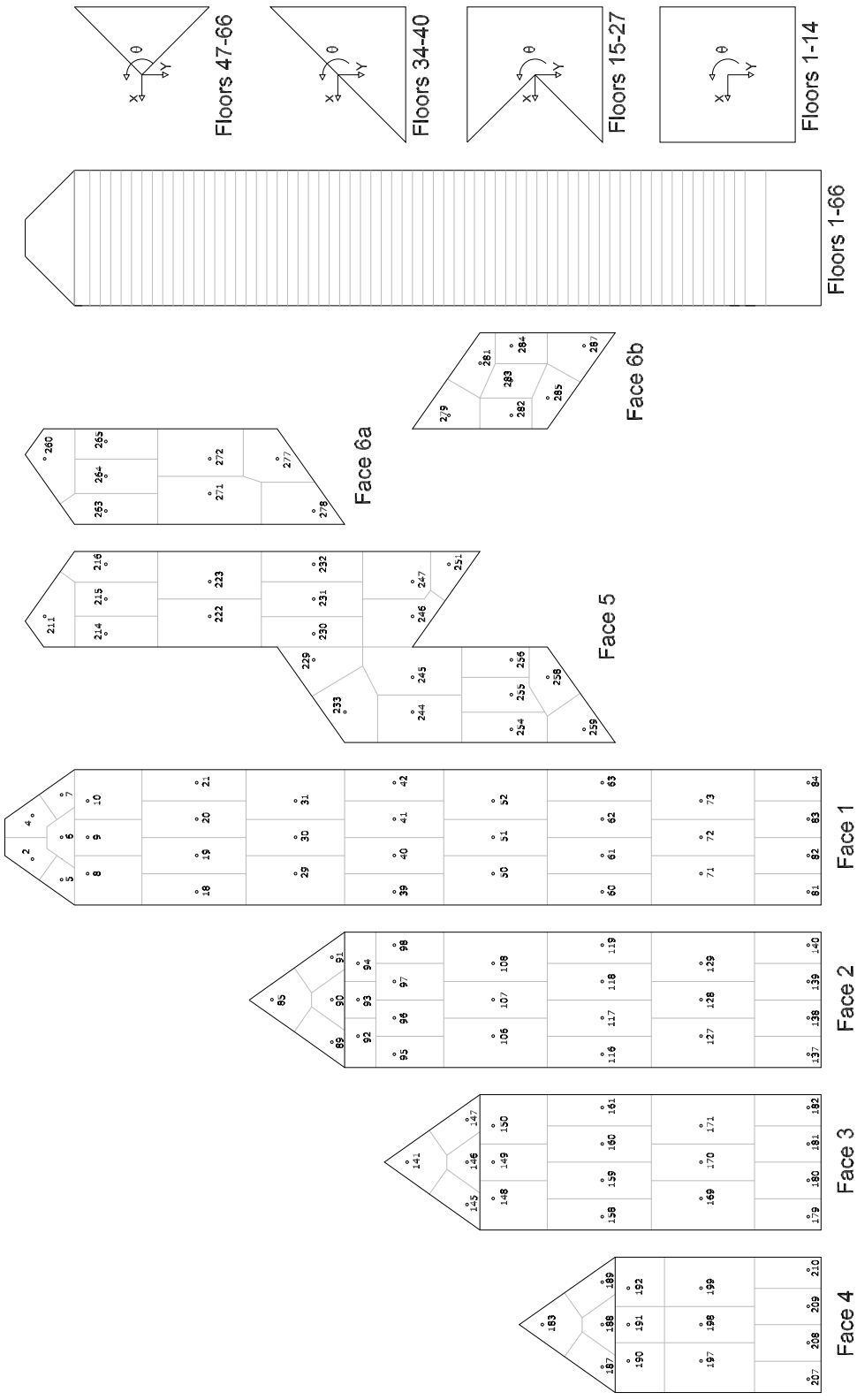

Figure 4.14: Pressure tap locations, Bank of China building.

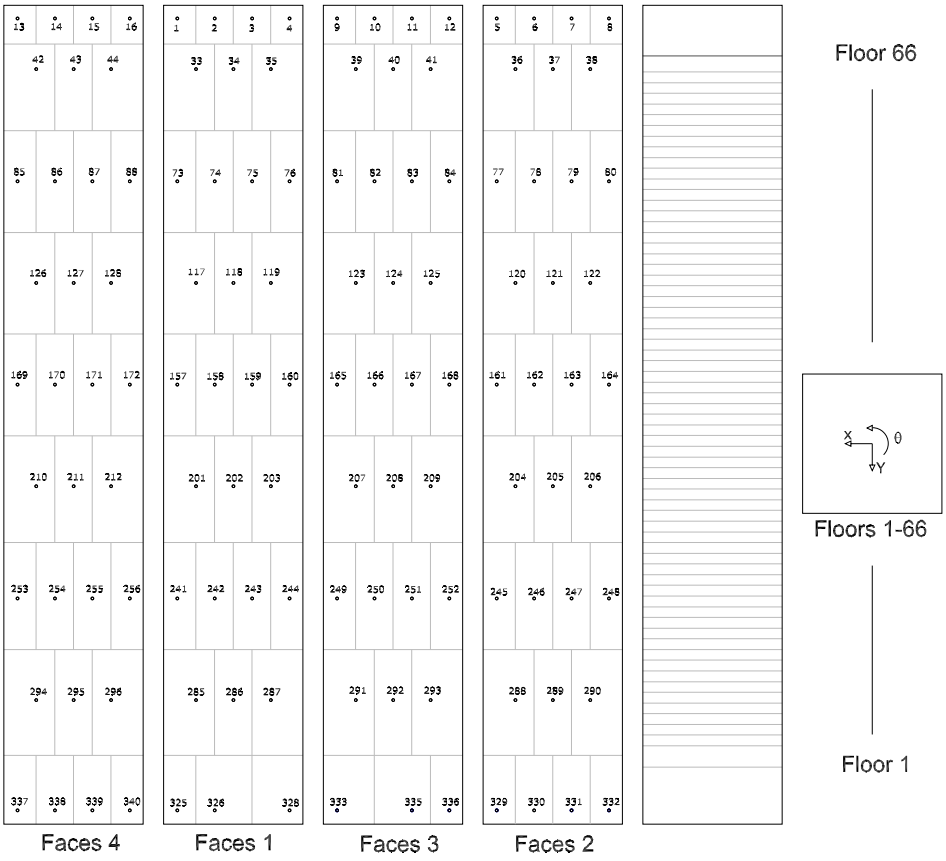

Figure 4.15: Pressure tap locations, regular building.

Skewness and kurtosis

In this paragraph the maximum and minimum skewness and kurtosis of the pressure coefficients are investigated. These give a particularly useful insight into the probabilistic nature of the external pressure field.

Figures 4.17 and 4.18 show the maximum and minimum skewness and kurtosis over all pressure coefficients for each wind direction while in tables 4.1 and 4.2 are reported the pressure taps where the maxima and minima occur over all wind directions. In figure 4.16 are shown the histograms of the pressure coefficients where the maximum kurtosis occurs for the two buildings. As mentioned the wind tunnel tests for the Regular building were carried out only for the wind directions comprised between 0° and 90°. By taking advantage of symmetry the results can be extended to other wind directions therefore allowing for an easy comparison with those of the Bank of China building. From figures 4.17 and 4.18 it is evident that in general the buildings display a similar behavior concerning both the skewness and kurtosis. In particular there seems to be a tendency towards high values of kurtosis indicating the importance of the tails of the marginal distributions of the

	Skewness	Kurtosis	α	Tap # n
Max B	1.27	5.01	40	278
Min B	-5.51	74.48	280	5
Max R	0.84	3.21	20	166
Min R	-3.44	37.42	60	286

Table 4.1: Maximum skewness of the external pressure field.

	Skewness	Kurtosis	α	Tap # n
Max B	-5.51	74.48	280	5
Min B	-1.28	0	80	7
Max R	-3.44	37.42	60	286
Min R	-0.8	-0.08	20	250

Table 4.2: Maximum kurtosis of the external pressure field.

pressure coefficients which is also seen in other studies [4.8, 4.6, 4.5]. In figures 4.19 to 4.26 the skewness and kurtosis maps for wind directions 60° and 280° are illustrated for both buildings. From figures 4.17 and 4.18 it is evident that for a wind direction of 280° a particular event occurs. By observing the skewness and kurtosis maps of figures 4.23 and 4.26 it is evident that there is a region of highly leptokurtic and skewed pressure coefficients towards the top of the building due to particularly strong vortex shedding. From the comparison with the maps of the regular building, figures 4.24 and 4.26 for a wind direction 80° comparable due to symmetry, the effects of the geometry on the external pressure field is clear.

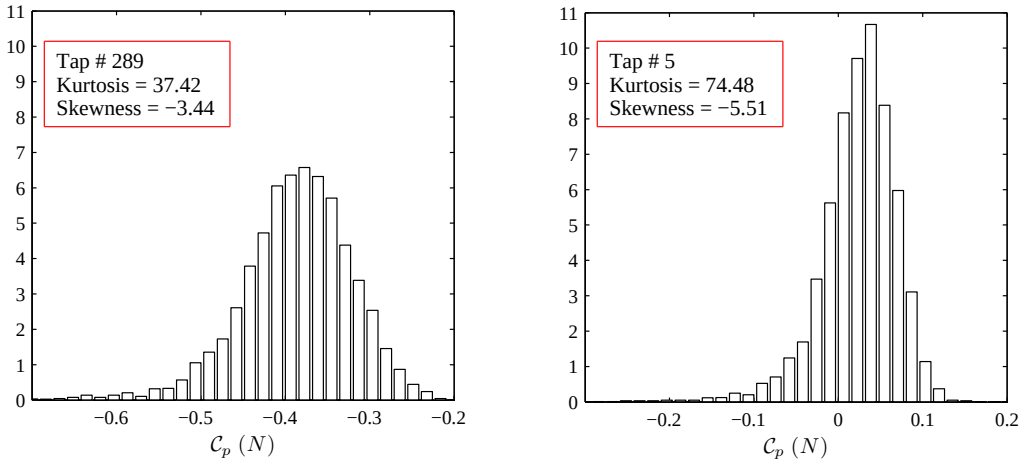

(a) (b)

Figure 4.16: Histograms of the pressure coefficients with maximum kurtosis: (a) regular building, (b) Bank of China building.

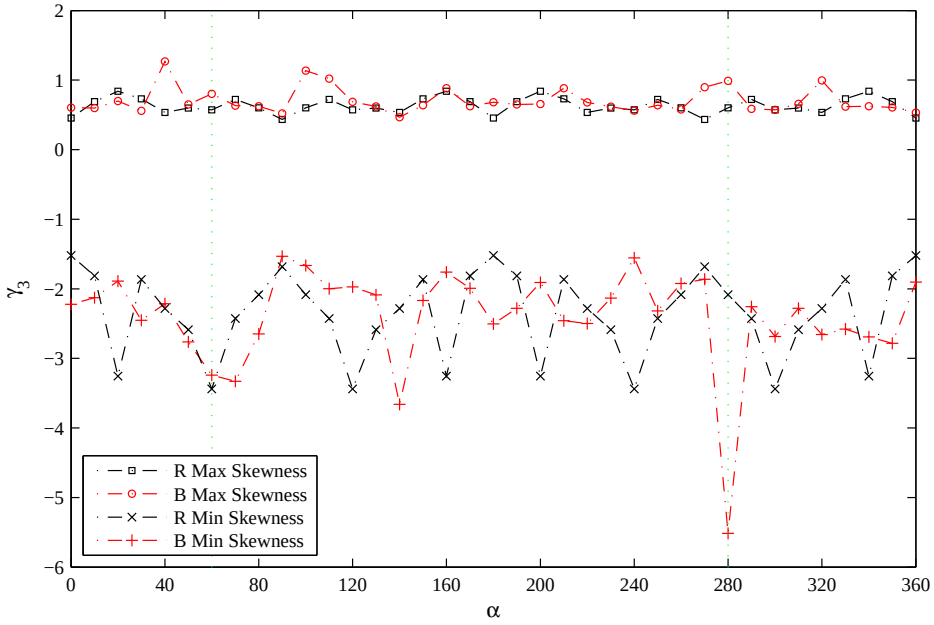

Figure 4.17: Maximum skewness of the external pressure field for each wind direction.

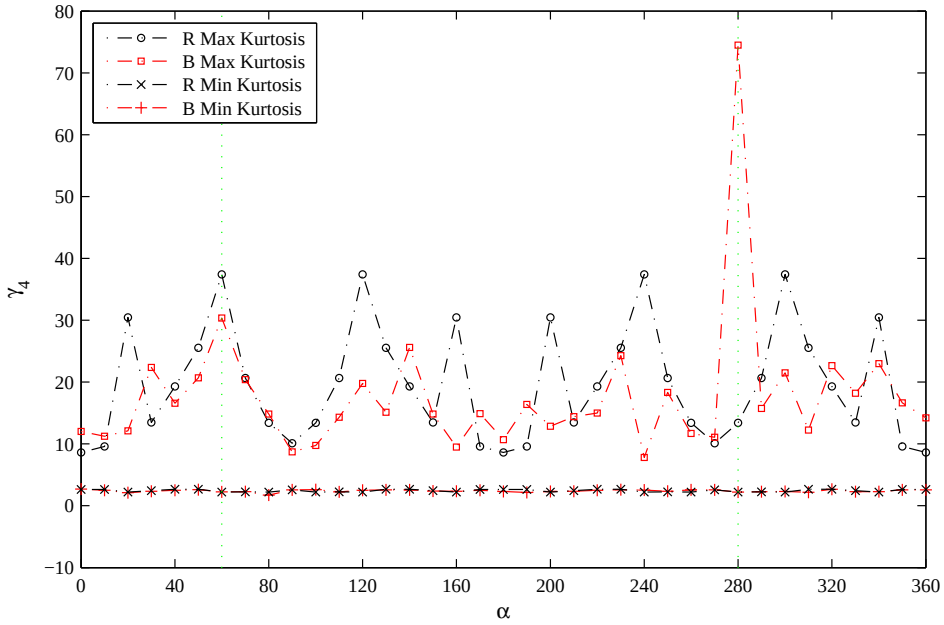

Figure 4.18: Maximum kurtosis of the external pressure field for each wind direction.

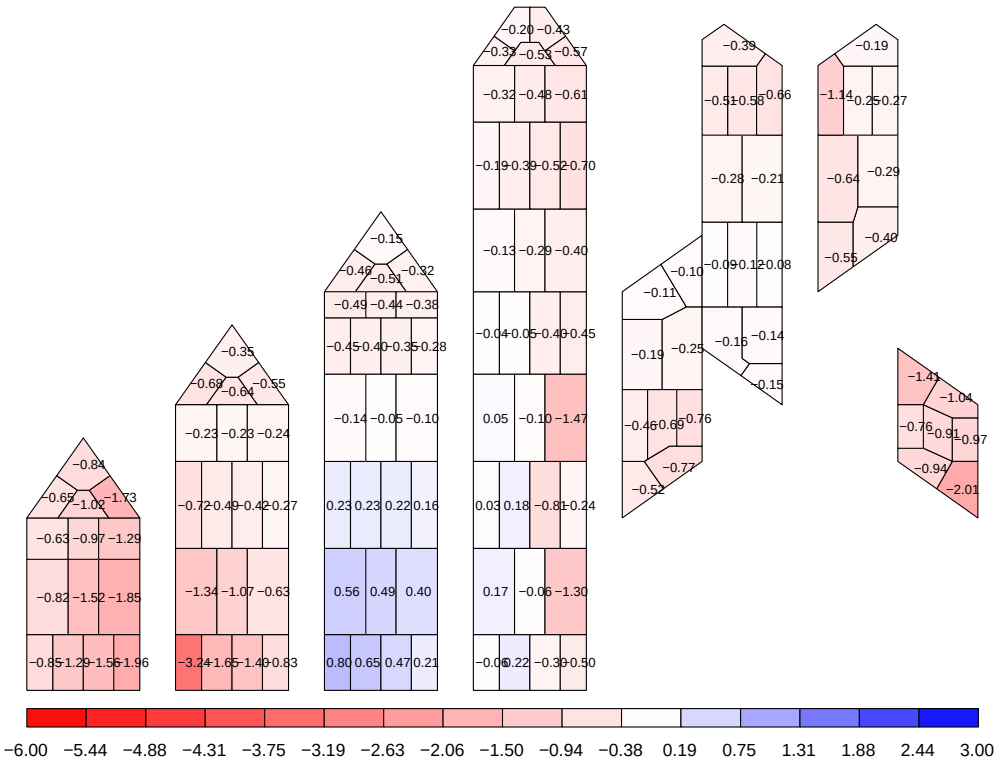

Figure 4.19: Skewness map for the Bank of China building, $\alpha = 60°$.

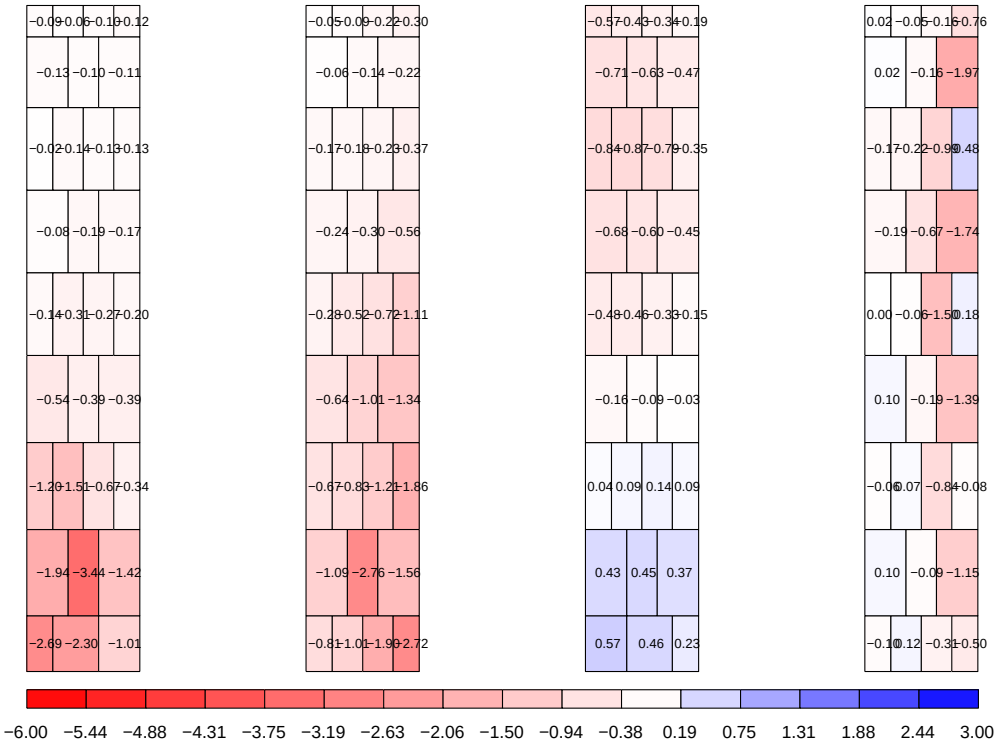

Figure 4.20: Skewness map for the regular building, $\alpha = 60°$.

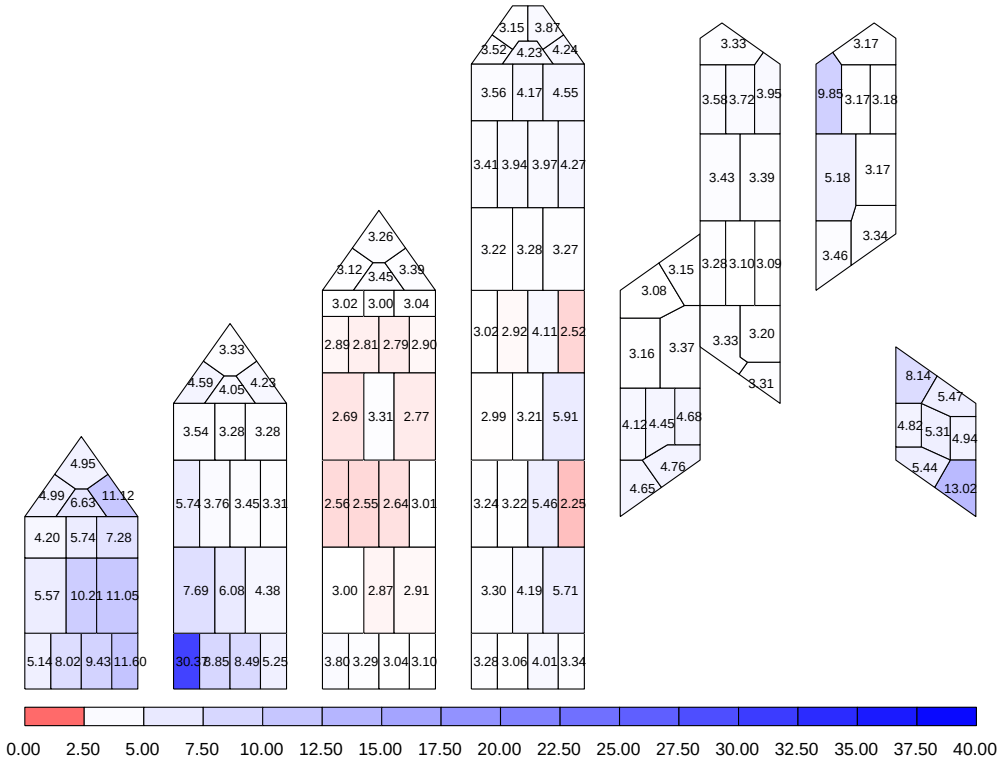

Figure 4.21: Kurtosis map for the Bank of China building, $\alpha = 60°$.

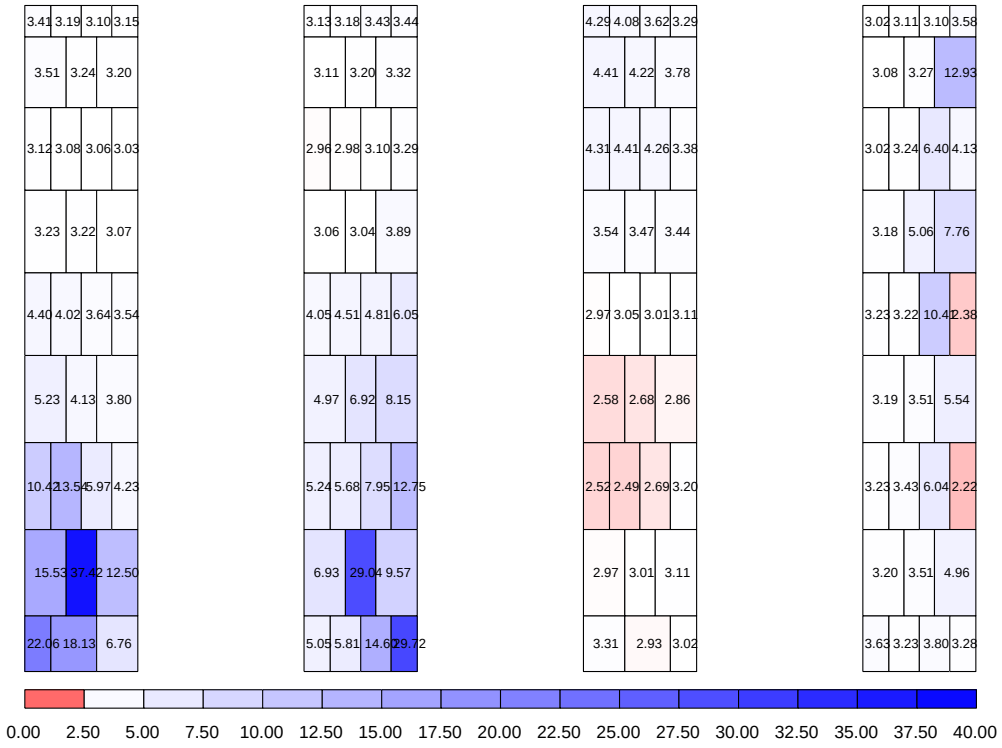

Figure 4.22: Kurtosis map for the regular building, $\alpha = 60°$.

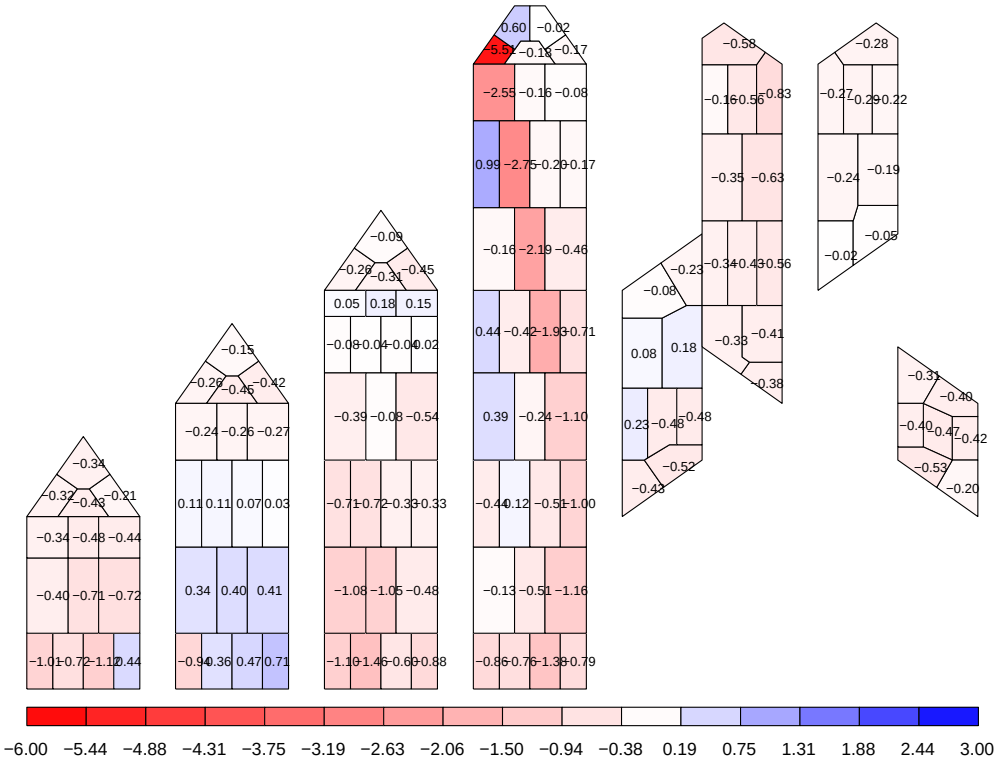

Figure 4.23: Skewness map for the Bank of China building, $\alpha = 280°$.

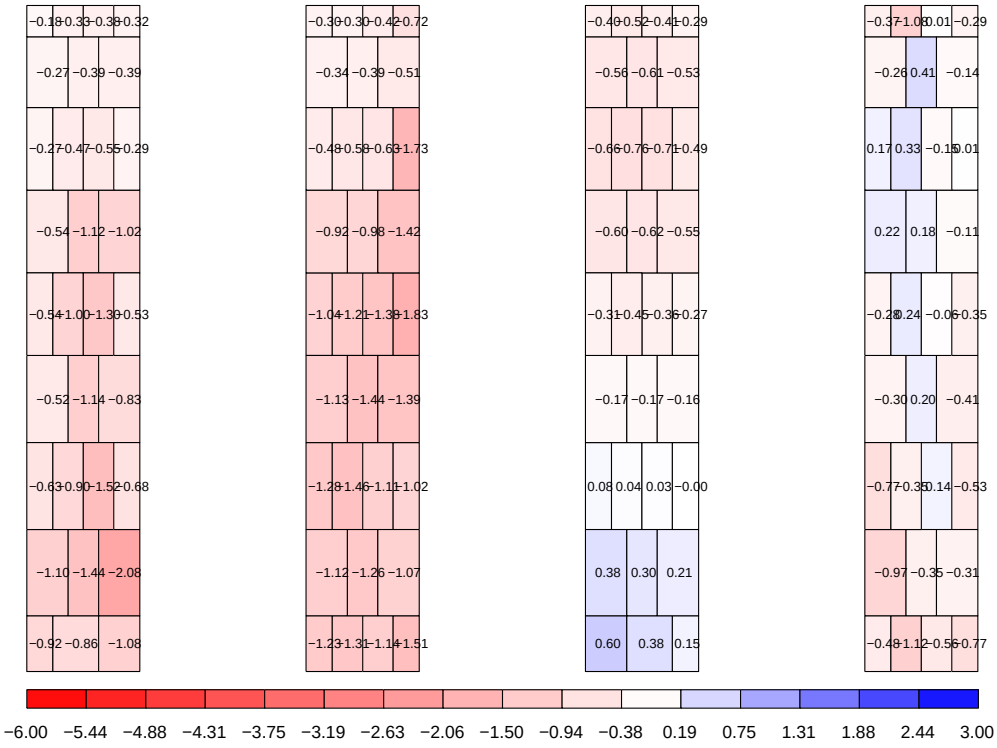

Figure 4.24: Skewness map for the regular building, $\alpha = 80°$.

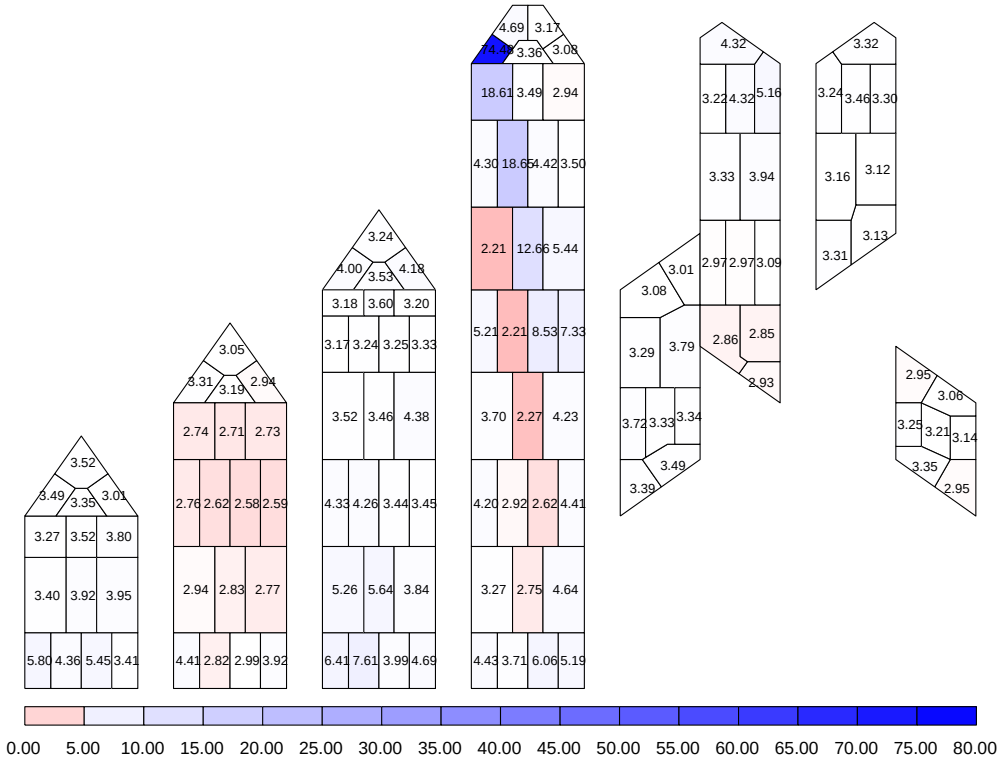

Figure 4.25: Kurtosis map for the Bank of China building, $\alpha = 280°$.

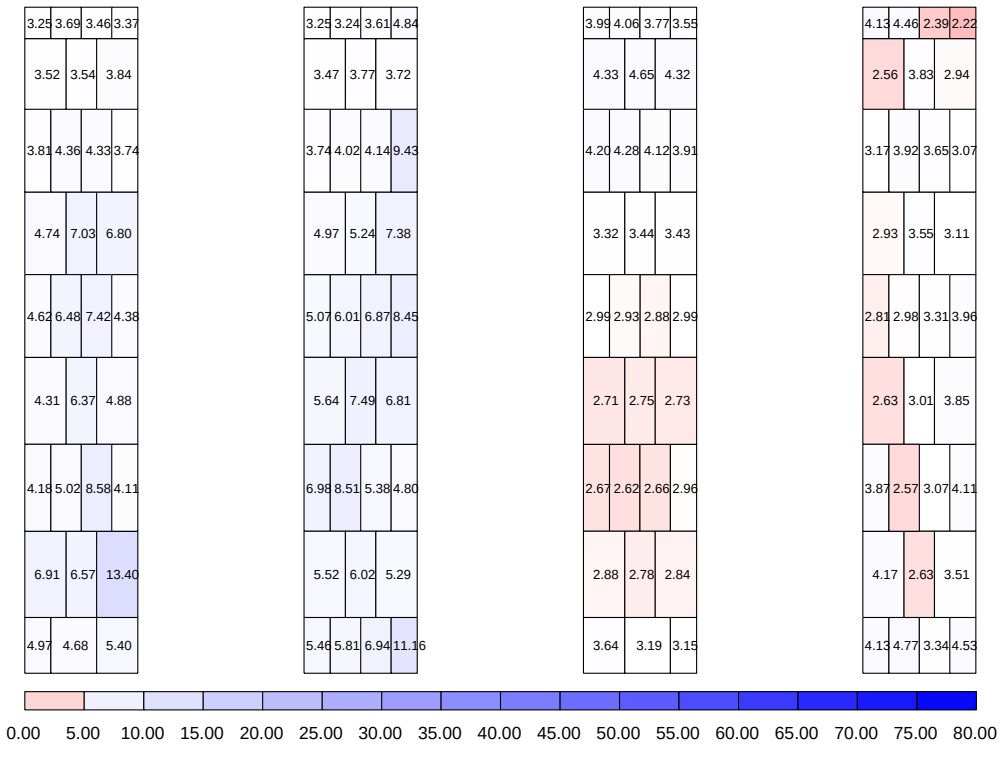

Figure 4.26: Kurtosis map for the regular building, $\alpha = 80°$.

4.2.3 The forcing functions

Wind tunnel tests are carried out on scale models. It is however the full scale or prototype scale that is of interest in the design of structures, and in particular for the studies that will be carried out in the next chapter. Therefore the model measurements must be opportunely modified.

Scaling

This can be achieved through the scaling laws first introduced by Jensen [4.7]. If the velocity $\bar{V}$, the pressure $\mathcal{P}$, the frequency f, the air density ρ_a and the dynamic viscosity μ_d are considered the six variables describing the flow around the structure then, from the Buckingham theorem, three independent non-dimensional parameters can be derived, namely the pressure coefficients $\mathcal{C}_p = \mathcal{P}/\frac{1}{2}\rho_a\bar{V}^2$, the Reynolds number $\mathrm{Re} = \rho_a\bar{V}D/\mu_d$ and the Strouhal number $\mathrm{St} = fD/\bar{V}$. These represent ratios of physical significance. The pressure coefficient, $\mathcal{C}_p$, is the ratio of the actual pressure to the ideal dynamic pressure. The Reynolds number, Re, is the ratio of fluid inertia forces to viscous forces. The Strouhal number, St, or reduced frequency, is the ratio of the transit period of the air flow to the period of an oscillation at the frequency f [4.4]. The scaling laws require that the non-dimensional parameters take the same values at both prototype and model scale. By defining the scaling factors as the ratio between the model and the prototype dimensions, it can be seen that this will be achieved only if all the scaling factors are unitary [4.2]. Therefore the choice has to be made to match exactly one parameter. The accuracy of the model depends on which of the non-dimensional parameters is matched, and on the significance of the others, which do not meet the scaling law requirements.

In wind tunnel tests on bluff bodies it is generally the Strouhal number defining the velocity scale factor which is matched. This is because of the frequency and time dependency of most of the parameters of interest to the aerodynamic description of civil structures.

By matching the Strouhal number while considering a mean wind speed at the top of the building four times that found in the wind tunnel tests, i.e. $\bar{V}_p = 80$ m/s, the following prototype sampling frequency is obtained:

$$f_p = \frac{\bar{V}_p D_m f_m}{\bar{V}_m D_p} = 2\,\mathrm{Hz} \tag{4.3}$$

where D_m and D_p are representative geometric dimensions in model and prototype scale respectively. From the Nyquist theorem [4.1], any response derived from the scaled measurements will have a cutoff frequency of 1 Hz.

It should be stated that the choice of a prototype wind speed velocity of 80 m/s is made purely to ensure a prototype sampling frequency high enough to allow the inclusion of any eventual natural frequencies below 1 Hz.

Prototype scale forcing functions

From the knowledge of the time histories of the pressure coefficients the forcing functions of (7.7) may be estimated by integrating the pressures within the tributary area of each floor. The pressure field, for each floor, will in this way be reduced to two translational forces in the global X- and Y-directions and a torque in the θ-direction, rotation around the Z-axis (figure 4.27). This was done for both buildings considering 66 floors located as shown in figures 4.14 and 4.15.

To investigate the energy content of the forcing function random vectors acting on the two systems, envelopes for all wind directions of the PSDs where considered for various equidistant points over the buildings height. For example in figure 4.28 are shown the maximum and minimum PSD envelopes for the Bank of China building for floors 11, 22 and 33, while in figure 4.29 are shown the identical quantities for floors 44, 55 and 66. Figures 4.30 and 4.31 show the equivalent spectral envelopes for the regular building. What is immediately evident for both buildings is the classical form of the PSDs typical of wind excited tall buildings. This validates the wind tunnel tests concerning the energy that will be transferred to the eventual vibration modes with natural frequencies inferior to 1 Hz.

In figures 4.32 to 4.35 are shown the enveloped second order characteristics of the forcing function random vectors for all incident wind directions. Strong non-gaussian features can be seen in both cases, figures 4.34 and 4.35. In general it is seen that the forcing functions of the Bank of China system tend to present a more pronounced non-gaussian nature.

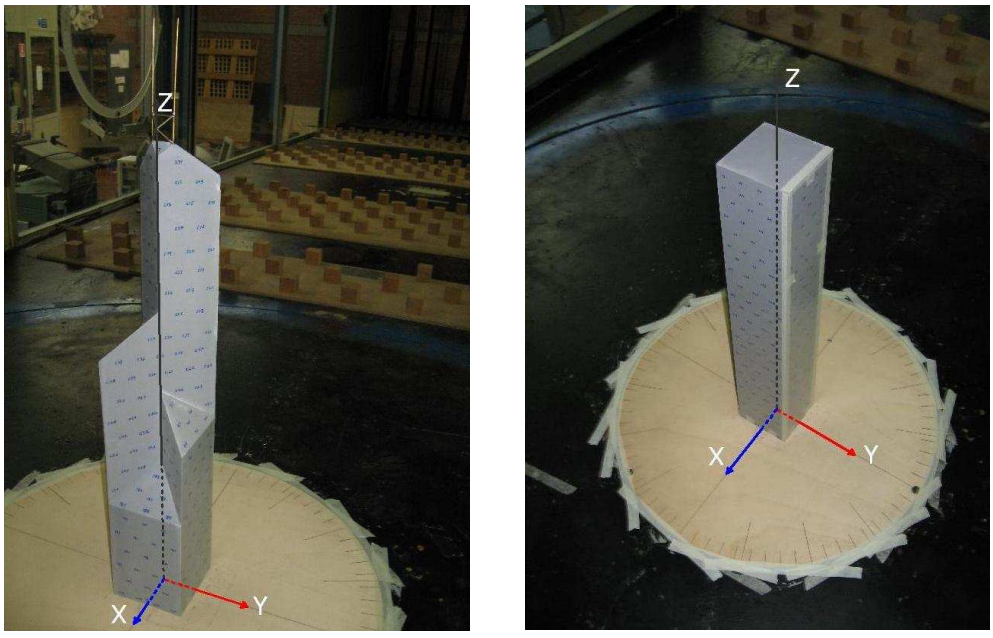

(a) (b)

Figure 4.27: Building model geometries and reference systems: (a) Bank of China building, (b) regular building.

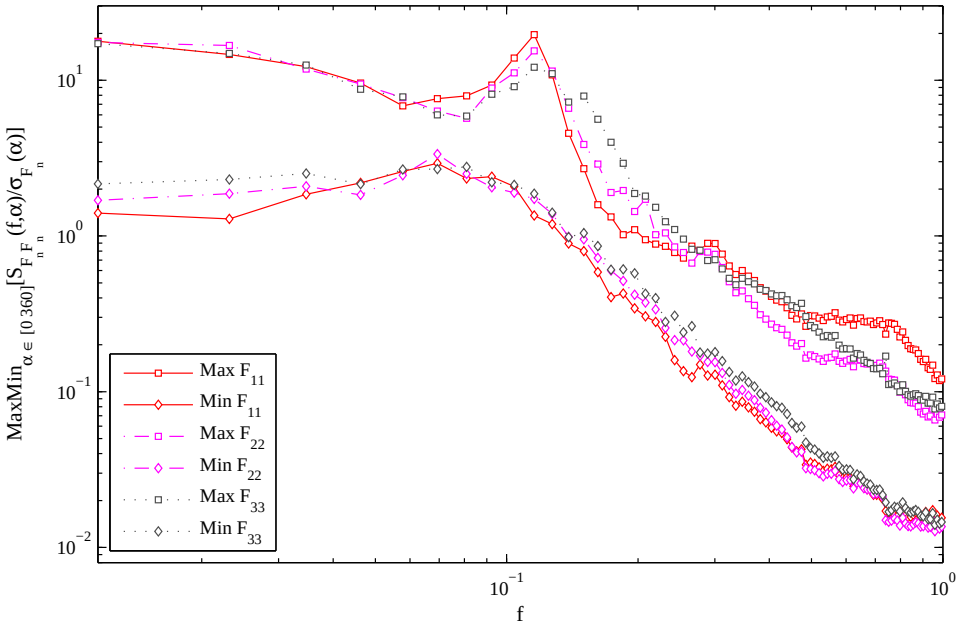

Figure 4.28: Forcing functions spectral envelopes for Bank of China building, lower half of the building.

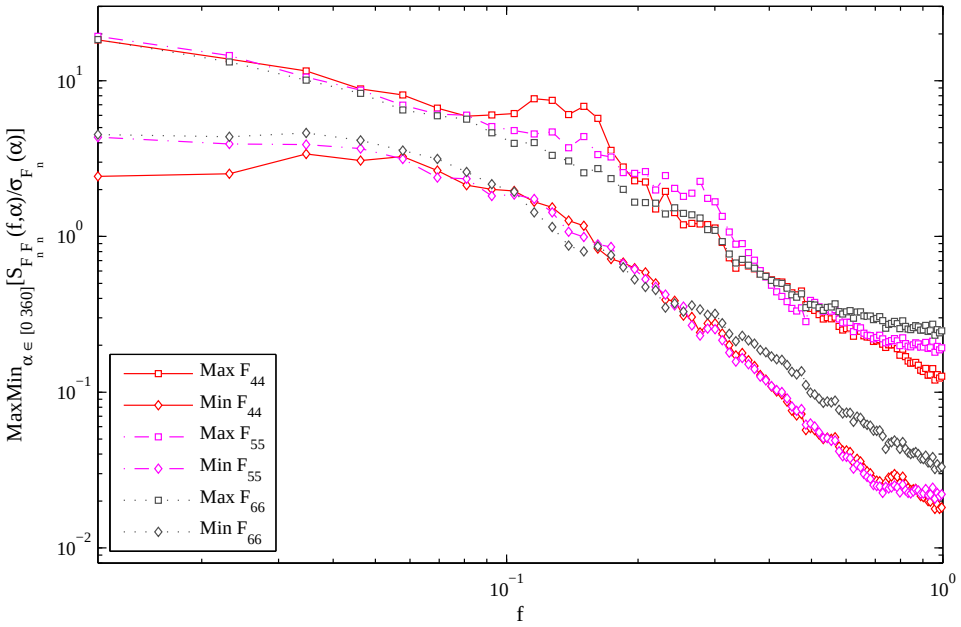

Figure 4.29: Forcing functions spectral envelopes for Bank of China building, higher half of the building.

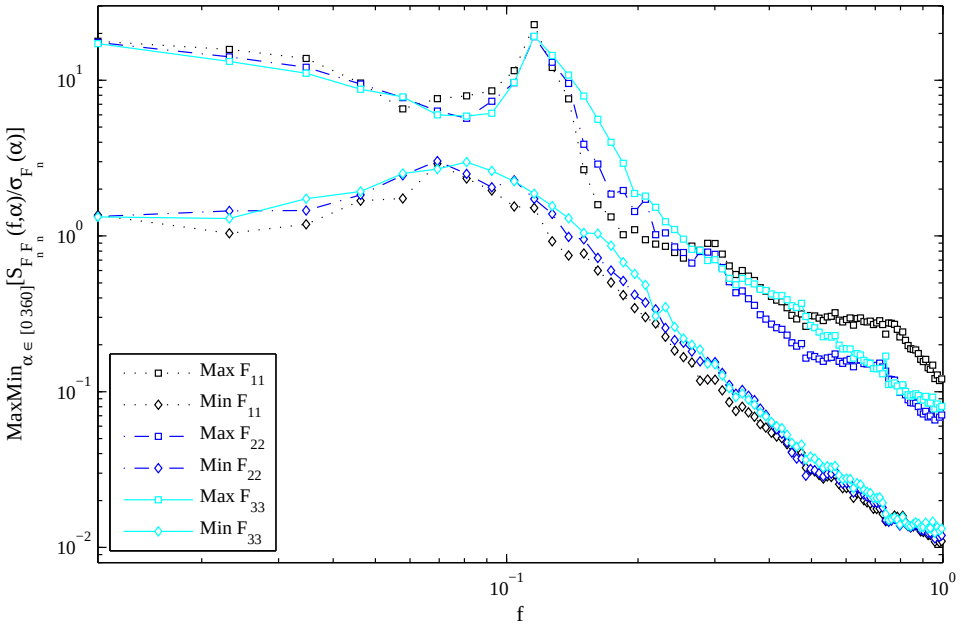

Figure 4.30: Forcing functions spectral envelopes for regular building, lower half of the building.

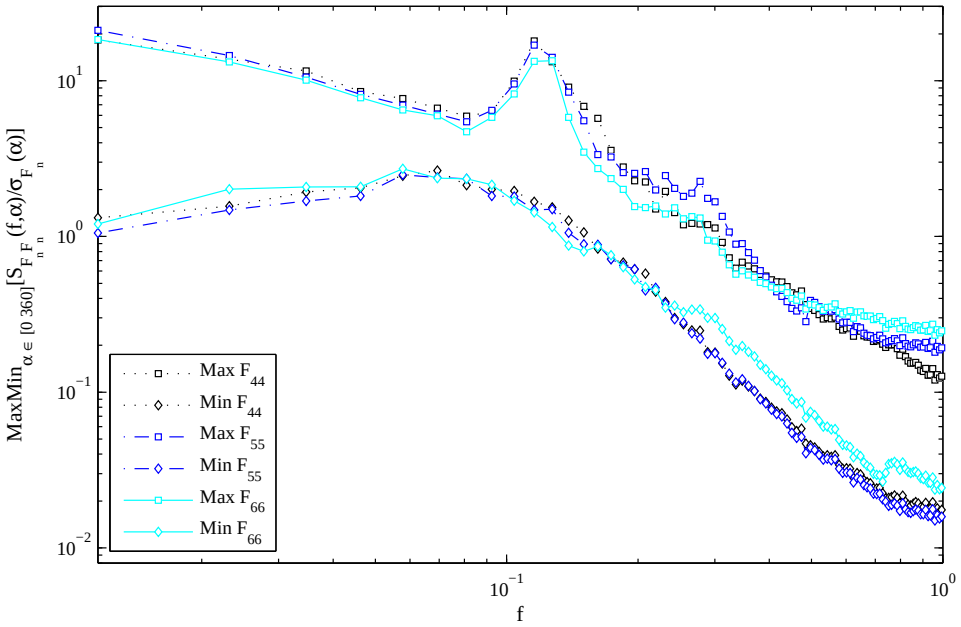

Figure 4.31: Forcing functions spectral envelopes for regular building, higher half of the building.

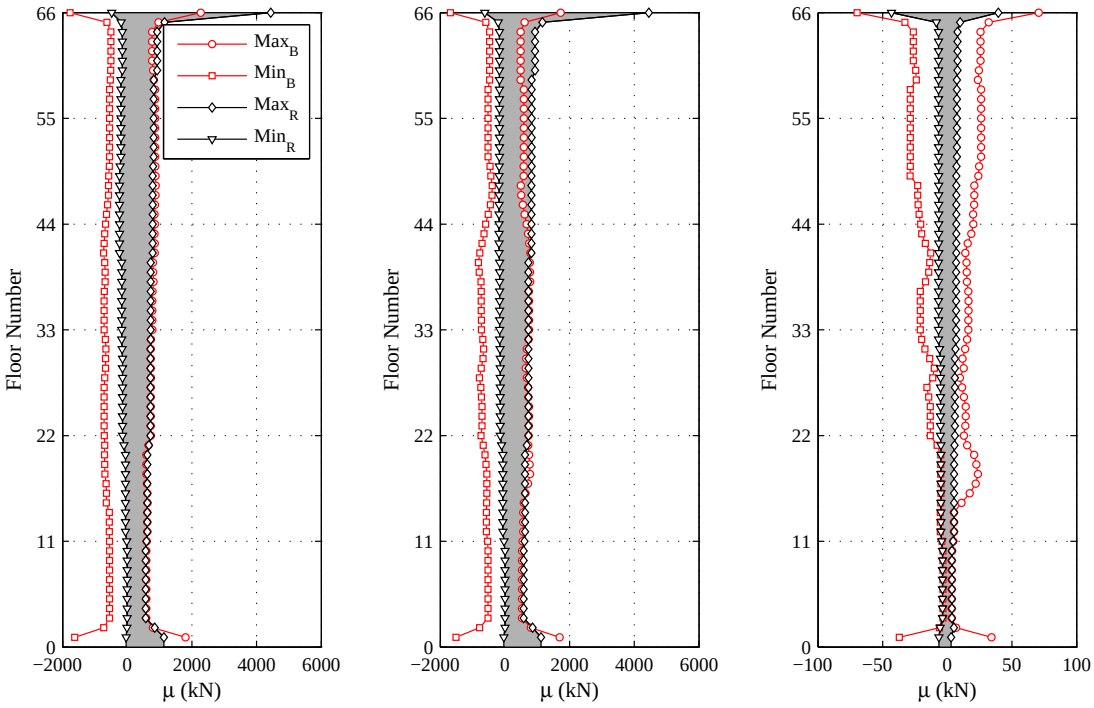

(a) (b) (c)

Figure 4.32: Mean values over all wind directions: (a) dir-X, (b) dir-Y, (c) dir-θ.

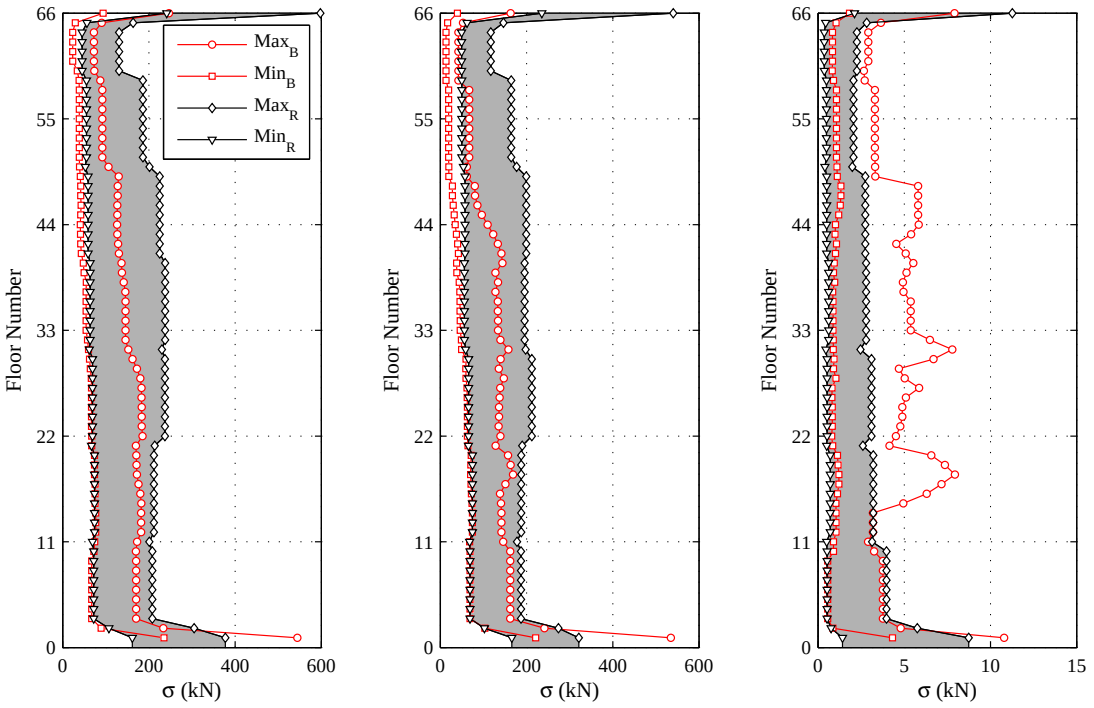

(a) (b) (c)

Figure 4.33: Standard deviation over all wind directions: (a) dir-X, (b) dir-Y, (c) dir-θ.

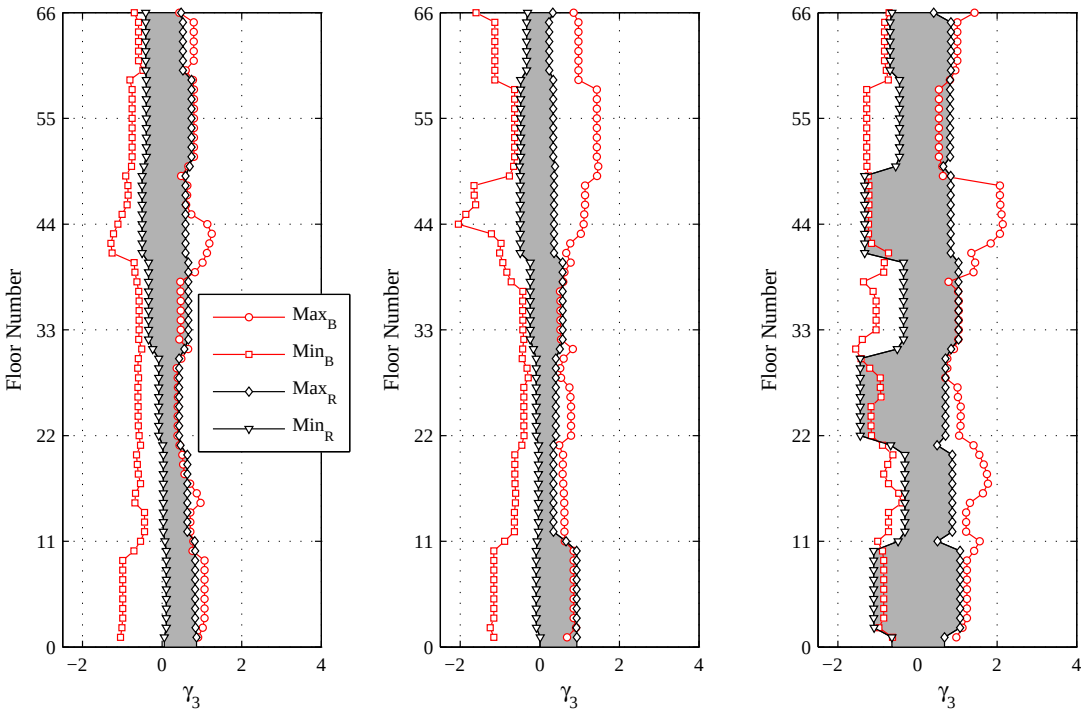

Figure 4.34: Skewness over all wind directions: (a) dir-X, (b) dir-Y, (c) dir-θ.

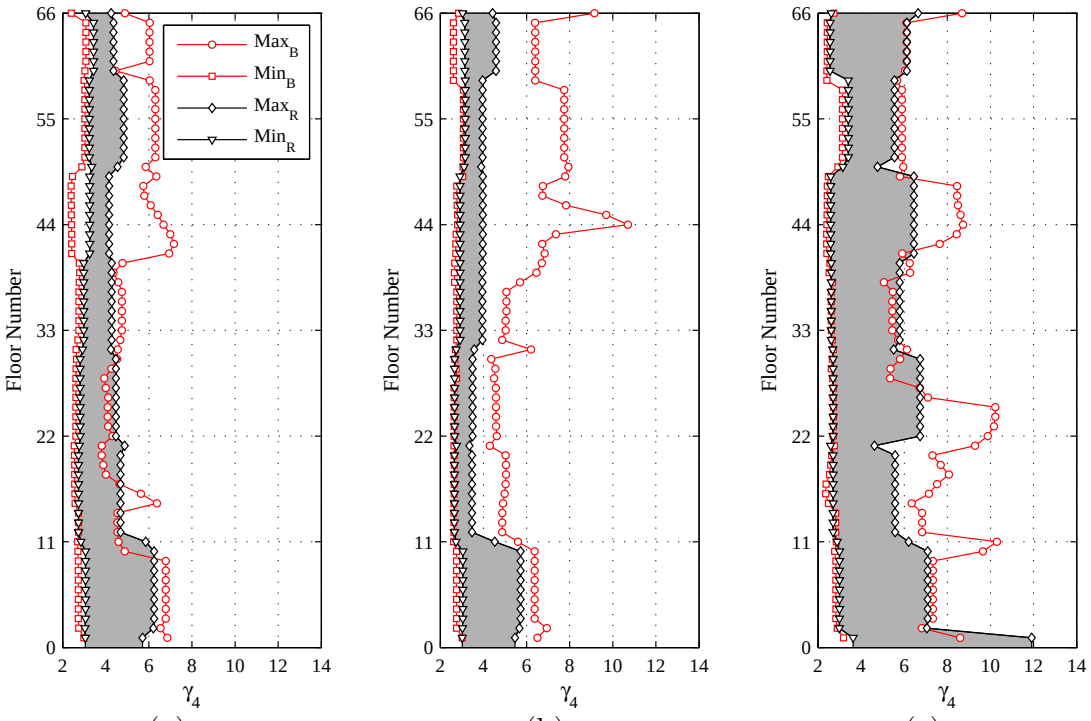

Figure 4.35: Kurtosis over all wind directions: (a) dir-X, (b) dir-Y, (c) dir-θ.

Bibliography

[4.1] R. B. Blackman and J. W. Tukey. *The measurement of power spectra.* Dover publications, Inc., New York, 1958.

[4.2] N. J. Cook. *The designers guide to wind loading of building structures Part 1: Background, Damage Survey, Wind Data and Structural Classification.* Butterworths, London, 1986.

[4.3] C. Dyrbye and S. O. Hansen. *Wind loads on structures.* J. Wiley Chichester, New York, 1997.

[4.4] M. Gioffrè. *Analysis and simulation of non-Gaussian processes with application to wind engineering and reliability.* PhD thesis, University of Florence, Florence, Italy, 1998.

[4.5] M. Gioffrè, V. Gusella, and M. Grigoriu. Non-gaussian wind pressure on prismatic buildings I: Stochastic field. *Journal of Structural Engineering, ASCE*, 127:981–989, 2001.

[4.6] A. Kareem. *Wind excited motion of tall buildings.* PhD thesis, Colorado State University, 1978.

[4.7] J. M. The model law for phenomena in natural wind. *Ingenioren, International edition*, 2(4), 1954.

[4.8] J. A. Peterka and J. E. Cermak. Wind pressure on buildings: probability densities. *Journal of the Structural Division, ASCE*, 127:1255–1267, 1975.

[4.9] E. Simiu and T. Miyata. *Design of Buildings and Bridges for Wind.* John Wiley Sons, Hoboken, New Jersey, 2006.

[4.10] E. Simiu and R. H. Scanlan. *Wind effects on structures: an introduction to wind engineering 1st Ed.* Wiley-Interscience, New York, 1986.

[4.11] E. Simiu and R. H. Scanlan. *Wind effects on structures: Fundamentals and applications to design 3rd Ed.* Wiley-Interscience, New York, 1996.

Chapter 5

Random Response Analysis of Uncoupled and Coupled Structural Systems

In this chapter the effect of higher mode truncation on the response of tall buildings with both regular and irregular geometric shapes in elevation is investigated together with the probabilistic nature of the global response. Commencing from the forcing functions evaluated in chapter 4, the importance of considering higher modes and wind direction when estimating the dynamic response of irregular tall buildings possessing complex 3D mode shapes is investigated and compared to the case of tall buildings with a regular geometric profile and uncoupled mode shapes. The role played by the background response on both root mean square and higher order probabilistic moments of global response is also investigated.

5.1 Introduction

Recent trends in tall building design have seen an ever increasing number of proposals for buildings with geometrically irregular shapes. However the methods adopted for estimating their response are generally based on theories that were developed considering buildings with regular geometric profiles and uncoupled fundamental mode shapes. As mentioned in chapter 2, while estimating the dynamic response it is generally deemed sufficient to consider only the first three modes of vibration, fundamental modes, and a global response characterized by being gaussian in nature. These hypotheses are particularly useful when the High Frequency Force Balance (HFFB) technique [5.19, 5.1] is adopted in conjunction with frequency domain dynamic analysis to ascertain the global loads and response of the structure.

Firstly, the estimate of the generalized forces associated with higher modes are not available from HFFB measurements. Secondly, in the case of non-linear coupled

fundamental mode shapes, the HFFB technique involves the use of complex mode corrections [5.20, 5.1, 5.21, 5.22, 5.23, 5.11, 5.14] which require the knowledge of the effective wind load distribution over the structure which is not available through HFFB measurements. Thirdly, by working in the frequency domain no knowledge of the probabilistic nature associated with the global response can be obtained. Therefore the peak factors used to estimate the maximum response are calculated considering a parent distribution given a priori.

Over the years studies have been carried out with the aim of quantifying the errors committed through mode truncation [5.18, 5.15, 5.12]. However these investigations are all concerned with alongwind and acrosswind response of regular tall buildings. In the case of irregular geometry, the presence of non-coincident centers of mass and stiffness leads to complex 3D mode shapes which, combined with an irregular geometric profile, can lead to a far greater sensitivity to wind direction.

In this chapter the dynamic wind induced response of the two tall buildings presented in chapter 4, namely the Bank of China building (figure 5.1) and a prismatic building of similar geometric size, are investigated. For both buildings direct integration of the equations of motion of an equivalent dynamical system is performed. In particular the equivalent dynamical system of the Bank of China building is calibrated in order to achieve the first three non linear coupled mode shapes and frequencies as determined experimentally for the actual building [5.17].

Figure 5.1: Bank of China building.

The regular building is modeled with the same vertical floor locations and densities as the irregular building. It is also calibrated so as to achieve the same frequencies with, however, quasi linear uncoupled mode shapes due to coincident and vertically aligned centers of mass and stiffness. Higher mode contributions, together with the probabilistic nature of various response quantities such as top displacements, shear forces, bending moments, torque and top accelerations, are investigated for a full range of wind directions revealing the high sensitivity of the results to the particular wind direction and the strongly non-gaussian nature of the global response. The relative importance of the background and resonant dynamic responses for dictating the probabilistic features of the global response and their sensitivity to higher mode contributions is also evaluated.

5.2 Analysis framework

5.2.1 Dynamic modeling

As discussed in chapter 2, the global behavior of tall buildings can be modeled by an equivalent dynamic system with three degrees of freedom (i.e. two orthogonal displacements relative to the ground and θ-rotation about a vertical axis) for each floor. Under these conditions a N-floor building will be governed by the equations of motion given in (7.7) and reported here for completeness:

$$\mathbf{M}\ddot{\mathbf{z}}(t) + \mathbf{C}\dot{\mathbf{z}}(t) + \mathbf{K}\mathbf{z}(t) = \mathbf{f}(t)$$

where $\mathbf{M}$ is the $3N \times 3N$ diagonal mass matrix, $\mathbf{C}$ is the $3N \times 3N$ damping matrix and $\mathbf{K}$ is the $3N \times 3N$ stiffness matrix while $\mathbf{f}(t)$ is the $3N \times 1$ time varying floor load vector given at the center of mass of each floor and $\mathbf{z}(t)$ is the $3N \times 1$ response vector.

Because of the linear nature of the structural systems under consideration a convenient setting in which to solve the above equations is in terms of modal analysis. In particular the system of equations in (7.7) are transformed into a system of $j = 1, ..., 3N$ uncoupled equations given by (2.14) and also reported for completeness:

$$\ddot{q}_j(t) + 2\zeta_j\omega_j\dot{q}_j(t) + \omega_j^2 q_j(t) = \frac{Q_j(t)}{\boldsymbol{\phi}_j^T\mathbf{M}\boldsymbol{\phi}_j}$$

where ζ_j, and ω_j are the jth generalized damping ratio and circular frequency respectively, $Q_j(t)$ is the generalized force while $\boldsymbol{\phi}_j$ is the jth $3N \times 1$ mode shape vector.

If the centers of mass and stiffness for each floor are coincident and lay on a vertical axis and the mode shape vectors $\boldsymbol{\phi}_j$ are referred to a reference system with vertical axis passing through the centers of mass, then the building will experience what is known as uncoupled vibration modes in three principal directions, two orthogonal translational directions and a rotational direction (see also chapter

2). Therefore if the system of equations (7.7) are organized such that the first N equations govern the response in one of the principal directions while the next N equations in one of the other principal directions and so forth, the first three mode shape vectors will be characterized by having non-zero terms only in correspondence of the Degrees Of Freedom (DOFs) associated with one of the principal directions. However if the centers of mass and stiffness do not comply to the above mentioned conditions the building will, in general, experience what is known as coupled modes, therefore the first three mode shapes characterized by non-zero terms for all principal DOFs. The first three natural modes of tall buildings are generally called the fundamental modes. The presence of coupled fundamental mode shapes will produce what is generally termed mechanical coupling.

By opportunely separating the response into quasi-static and resonant components, any response of interest R will be given by:

$$R(t) = R_r(t) + R_b(t) = \sum_{j=1}^{3N} \Lambda_{R,j} q_{jr}(t) + \sum_{j=1}^{3N} \Lambda_{R,j} q_{jb}(t) \tag{5.1}$$

where R_r is the resonant response component, R_b is the background response component, $q_{jb}(t) = Q_j(t)/k_j$ is the jth background (quasi-static) generalized displacement and $q_{jr}(t) = q_j(t) - q_{jb}(t)$ is the jth resonant generalized displacement, k_j is the jth generalized stiffness while $\Lambda_{R,j}$ is the modal participation coefficient for R (see chapter 2). Obviously, due to the very nature of modal analysis, a good approximation of the response may be achieved by considering a limited number of modal contributions. In particular by observing that the total maximum response, $\tilde{R}$, including the mean response, μ_R, may be written as:

$$\tilde{R} = \mu_R + g_R \sigma_R \tag{5.2}$$

where g_R is the peak factor while σ_R is the Root Mean Square (RMS) of the response R, the accuracy of the peak dynamic response will depend on the accurate estimate of the RMS response and of the peak factor. Therefore the appropriate number of modes required in order to efficiently predict the response in equation (5.7) can be and should be carried in terms of the peak factor and RMS.

5.2.2 The contribution of higher modes

The question of the appropriate number of modes to use in order accurately estimate the RMS of a particular response R depends on various factors including whether R is displacement-, velocity- or acceleration-based, the level of damping and the natural frequencies of the structure. For the general range in which the natural frequencies of tall buildings lay, the resonant response is normally considered to be acceptably estimated from the contribution of the first three fundamental modes. The background response, on the other hand, does not depend on the frequency content of the extreme wind event. Therefore, there is no logical reason that

the accurate description of the background response will be achieved through the exclusive consideration of the fundamental modes.

It should be appreciated that in most tall buildings the resonant response will be dominant over the background response which leads to the common assumption that the first three modes are adequate in predicting the dynamic response [5.18, 5.15, 5.12]. While this may be true for the acceleration, it is not necessarily true for displacement based responses. Another reason that in general the fundamental modes are considered adequate for estimating both the background as well as the resonant response is the use of the HFFB for directly determining the generalized forces. Indeed, as described in chapter 2, this method only allows for the inclusion of the first three modes in equation (2.22) and therefore in the eventual estimation of the RMS response. Another important consideration not covered in literature is the possible effect that complex geometry and 3D coupled mode shapes may have on the common assumption of dominate fundamental modes. Indeed complex geometric shapes often lead to situations where the distinction between alongwind and acrosswind response is meaningless; therefore, studies like [5.18, 5.15, 5.12] where regular geometric shapes define clear alongwind and acrosswind directions for which the response is known to be at its severest are not applicable.

The peak dynamic response of equation (5.2) not only depends on the RMS response but also on an appropriate value of the peak factor. Given that this will depend on a variety of choices, such as the exceedance probability, it will also depend on the probabilistic nature of the response. In particular during the analysis of tall buildings it is customary to consider the global response to be gaussian in nature. The root of this hypothesis lies in the fact that tall buildings are impinged by a large, generally non-gaussian, random pressure field [5.9] which has however a correlation structure that does not allow these non-gaussian features to be transferred to the global response due to the central limit theorem. This simplifies greatly the calculation of the peak response which can be estimated from the knowledge of the RMS gathered from frequency domain analysis.

The purpose of this chapter is to investigate not only the adequacy of considering only the fundamental modes in the estimate of the RMS response, but also the probabilistic nature of the response and the effects of mode truncation on the last.

5.3 Mechanical characteristics of the buildings

In this study the Bank of China building is considered because of its irregular external geometry. To obtain the same first three natural frequencies of vibration and associate mode shapes the effective number and position of the floors with a building density which varies from 200 kg/m^3 at the base to 170 kg/m^3 at the top were considered (figure 5.2), as reported in [5.17]. The first six mode shapes and associated frequencies of the Bank of China building are shown in figures 5.3 and 5.4, referred to the global reference system fixed at the geometric centre of the buildings

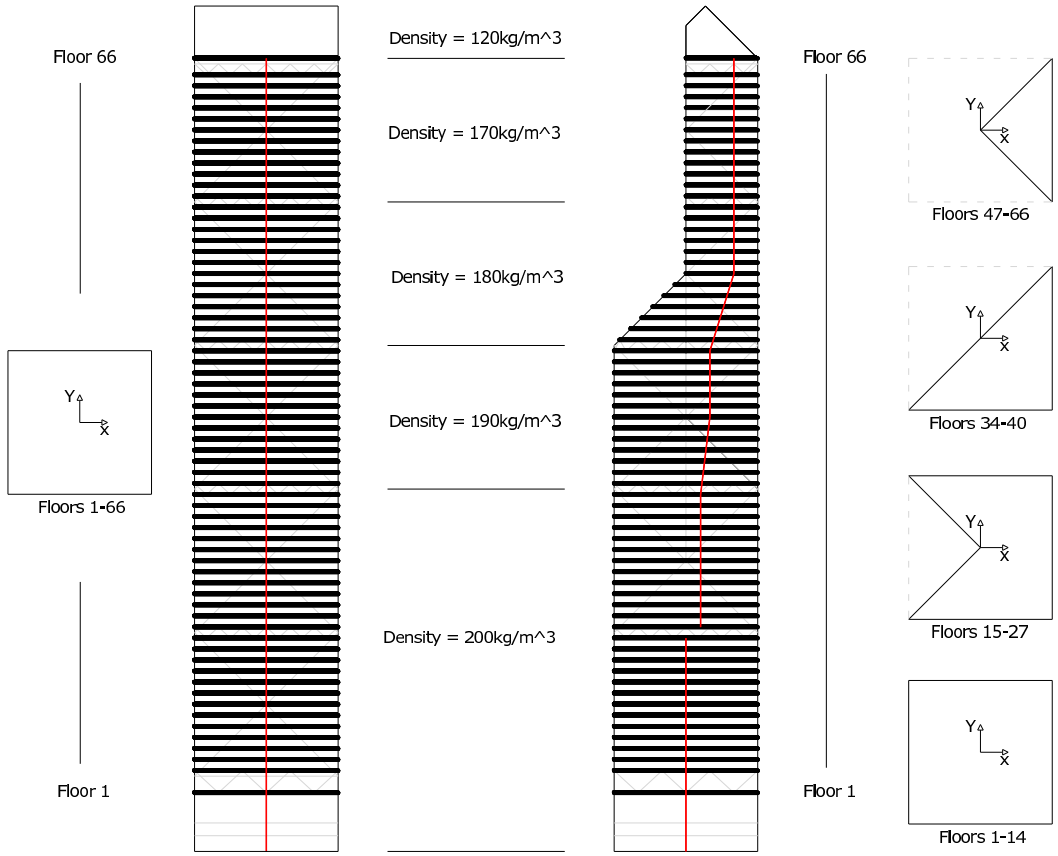

Figure 5.2: Mass densities and centers (shown as a red line) over the building height of the structural systems.

base and shown in figure 4.27. The centers of mass and stiffness of each floor are modeled as coincident, however, due to the building's irregular geometry, they do not lay on a vertical axis (figure 5.2), so causing coupled mode shapes. The regular building assumes the same floor locations and relative densities as the irregular building. However, due to the regular nature, it possesses coincident centers of mass and stiffness aligned on a vertical axis (figure 5.2), resulting in uncoupled fundamental mode shapes as shown in figures 5.5 and 5.6 with respect to the global reference system of figure 4.27. The stiffness matrix was calibrated in order to achieve the same natural frequencies as the irregular building. The buildings have the first two fundamental frequencies very closely spaced. This will cause the modal response correlation to play a significant role in the accurate prediction of the global response [5.4, 5.6, 5.5, 5.13]. The presence of closely spaced fundamental frequencies and therefore of important intermodal correlation is generally termed statistical coupling.

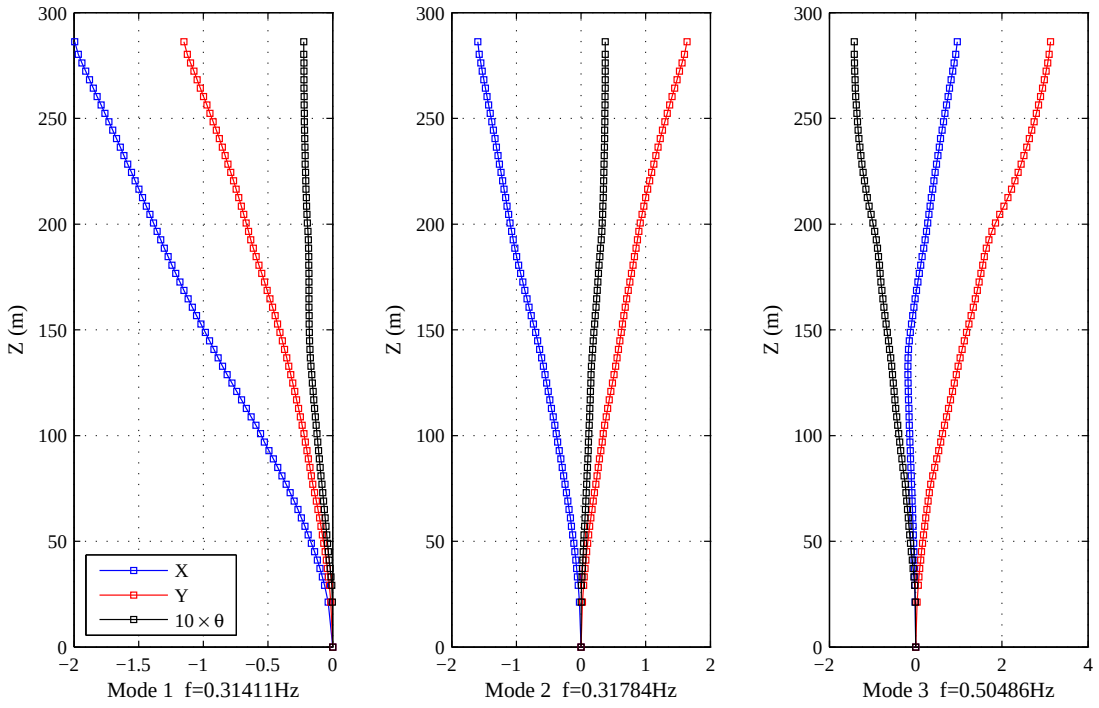

(a) (b) (c)

Figure 5.3: Mode shapes, Bank of China building: (a) mode 1, (b) mode 2, (c) mode 3

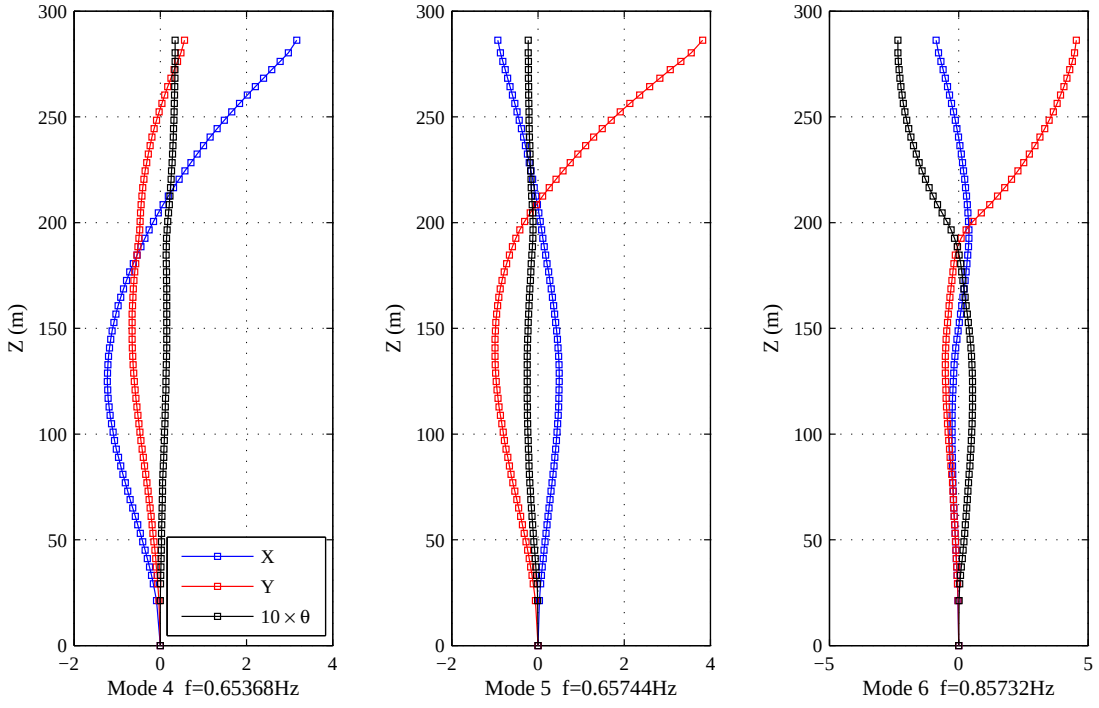

(a) (b) (c)

Figure 5.4: Mode shapes, Bank of China building: (a) mode 4, (b) mode 5, (c) mode 6.

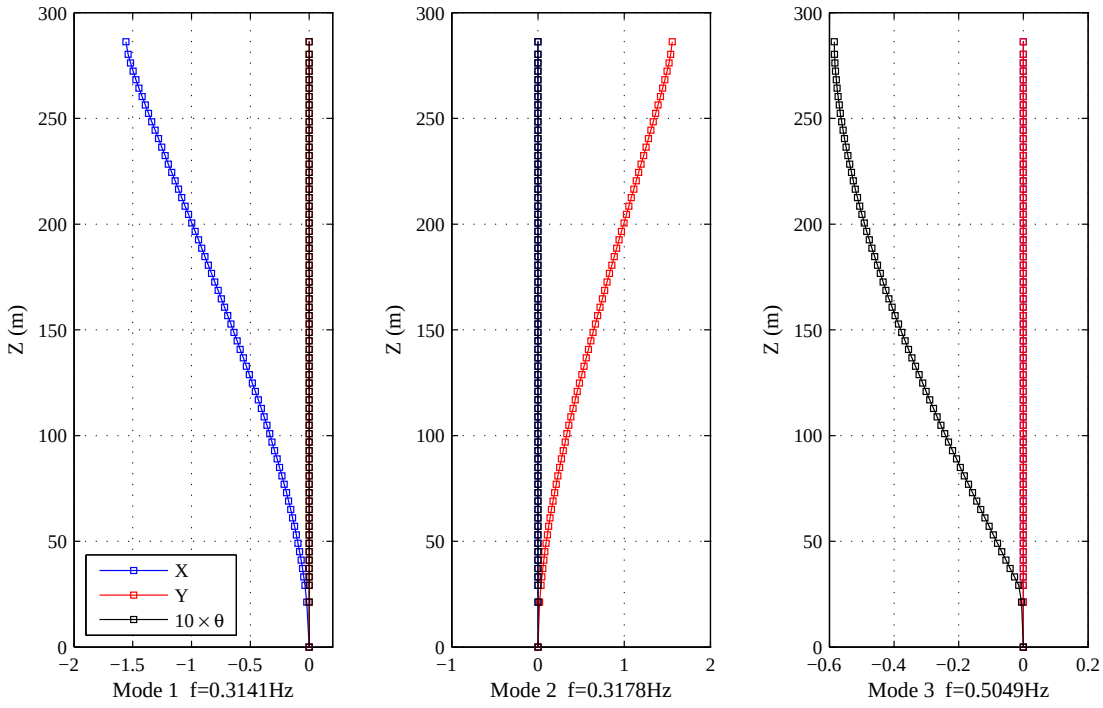

(a) (b) (c)

Figure 5.5: Mode shapes, regular building: (a) mode 1, (b) mode 2, (c) mode 3.

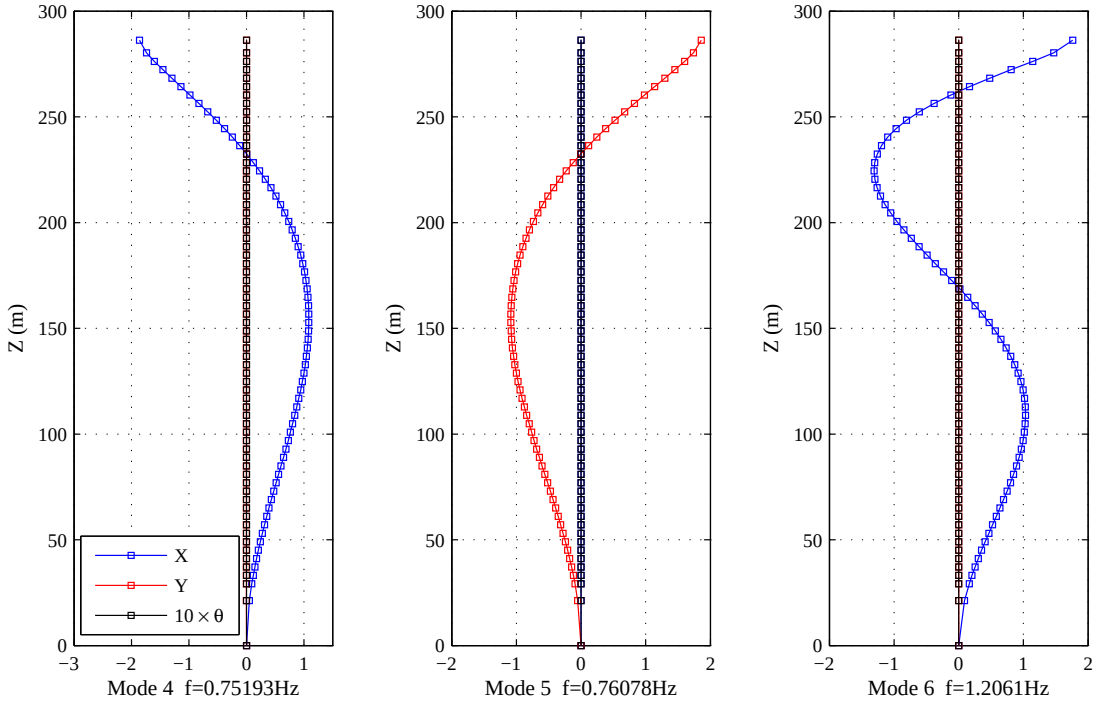

(a) (b) (c)

Figure 5.6: Mode shapes, regular building: (a) mode 4, (b) mode 5, (c) mode 6.

5.4 Response analysis

The response analysis carried out in this study was performed in the time domain, therefore allowing for the direct evaluation of the mechanically and statistically coupled response of the Bank of China building. The forcing functions are those determined at the end of chapter 4, in section 4.2.3. As described these last have a sampling frequency of 1 Hz, therefore the maximum number of natural modes that can be used for estimating the resonant response of equation (5.7) is governed by the condition of natural frequencies inferior to 1 Hz. Hence for the Bank of China building the first six modes can be used while for the regular the first five.

5.4.1 The generalized forces

In a modal analysis framework the forcing functions of equations (7.7) are transformed into the generalized forces by:

$$Q_j(t) = \boldsymbol{\phi}_j^T \mathbf{f}(t) \tag{5.3}$$

where $\boldsymbol{\phi}_j$ is the jth mode shape while $\mathbf{f}(t)$ is the vector of time varying floor loads.

In figures 5.7 to 5.10 are shown the second order probabilistic characteristics of the random vectors Q_j for $j = 1, 2, ..., 15$ of generalized forces exciting the Bank of China system. While in figures 5.11 to 5.14 are shown the analogous quantities for the regular building system. As can be seen from figures 5.9, 5.10 and 5.13, 5.14, the skewness and kurtosis are similar for both sets of forces. A fundamental difference between the two systems of forces is seen with respect to the means and standard deviations. Indeed, for the regular building, it is evident how the first two generalized forces are dominant (figures 5.11 and 5.12). This is not seen at all for the Bank of China system where significant values of both the mean and standard deviation are seen for a number of higher modes.

Figures 5.15 to 5.18 show the enveloped and smoothed PSDs over all wind directions for the first six generalized forces acting on the Bank of China building and the first five exciting the regular building. It is immediately evident from the form of the enveloped PSDs that most of the energy of the generalized forces is concentrated between 0.1 Hz and 0.2 Hz as is expected for the generalized forces of wind excited tall buildings [5.12]. In the same figures are also reported the natural frequencies of the first six modes concerning the Bank of China building while in turn for the regular the first five. It is interesting to observe that the energy that will excite modes four and five of the Bank of China is not that different from the energy finding its way onto mode three. The enveloped PSDs for the fourth and fifth generalized forces of both systems are very similar concerning their energy distribution over the frequency range of interest. However, the associated natural frequencies of the Bank of China building are somewhat lower compared to those of the regular building. This will decrease the significance of the resonant response component associated with these generalized forces for the regular building.

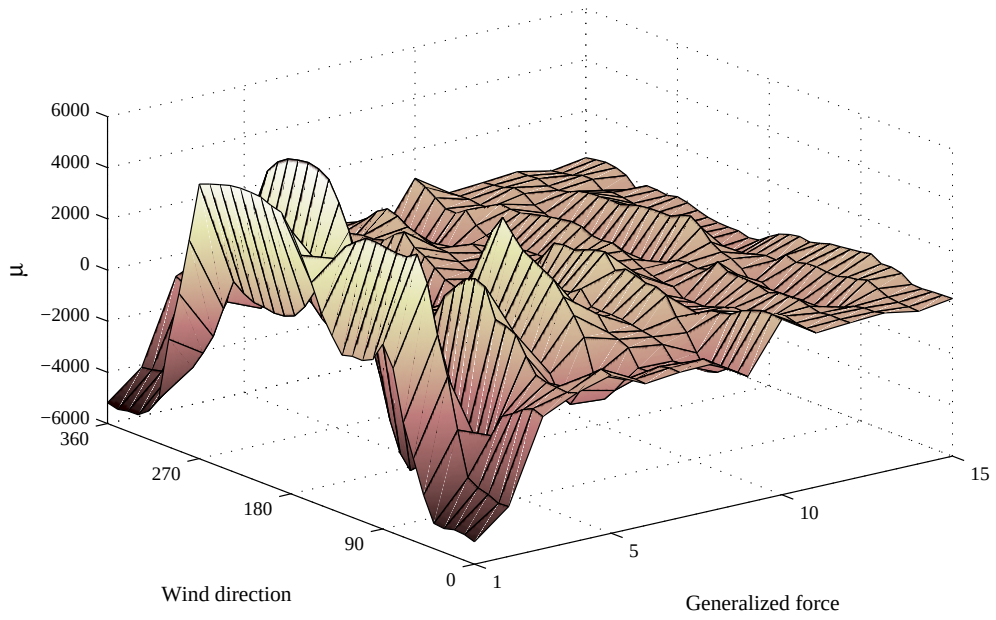

Figure 5.7: Mean values of the generalized forces, Bank of China building.

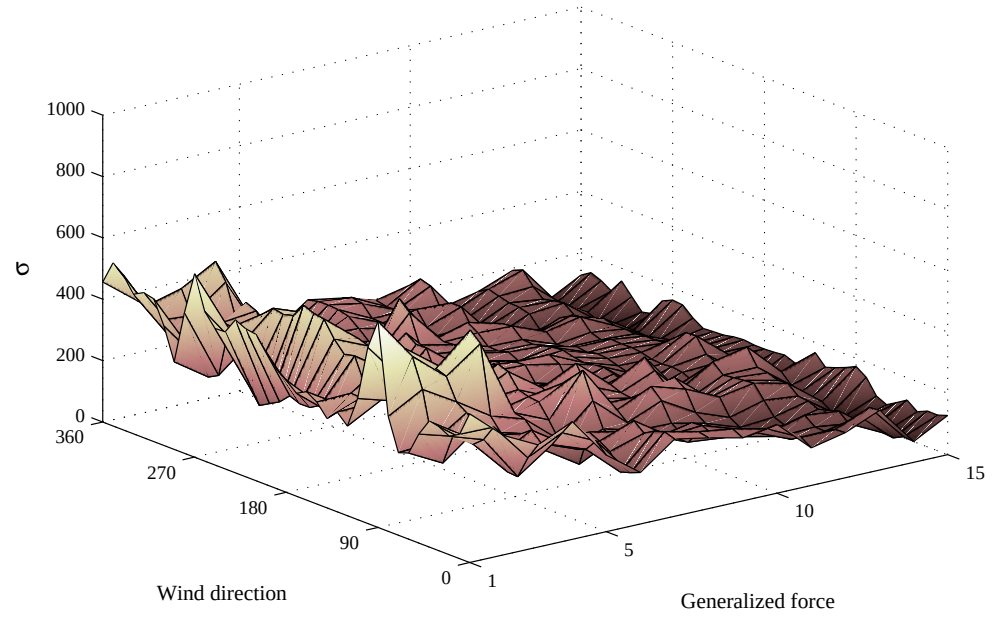

Figure 5.8: Standard deviation of the generalized forces, Bank of China building.

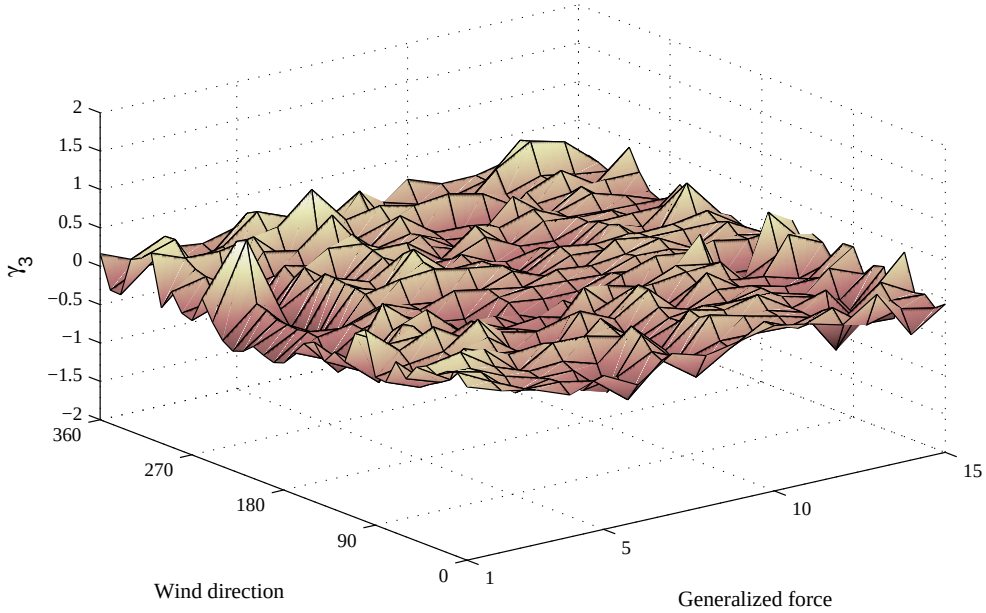

Figure 5.9: Skewness of the generalized forces, Bank of China building.

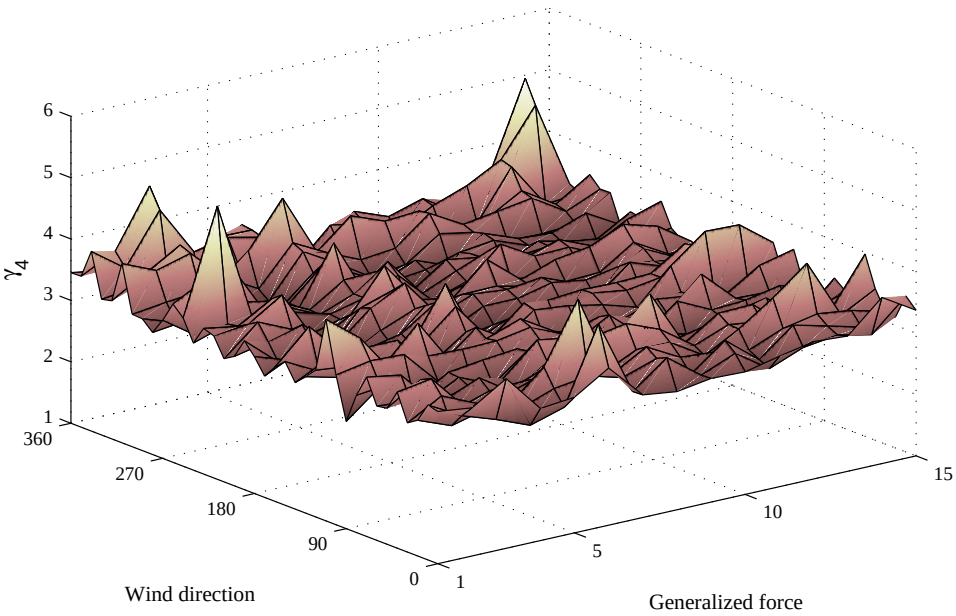

Figure 5.10: Kurtosis of the generalized forces, Bank of China building.

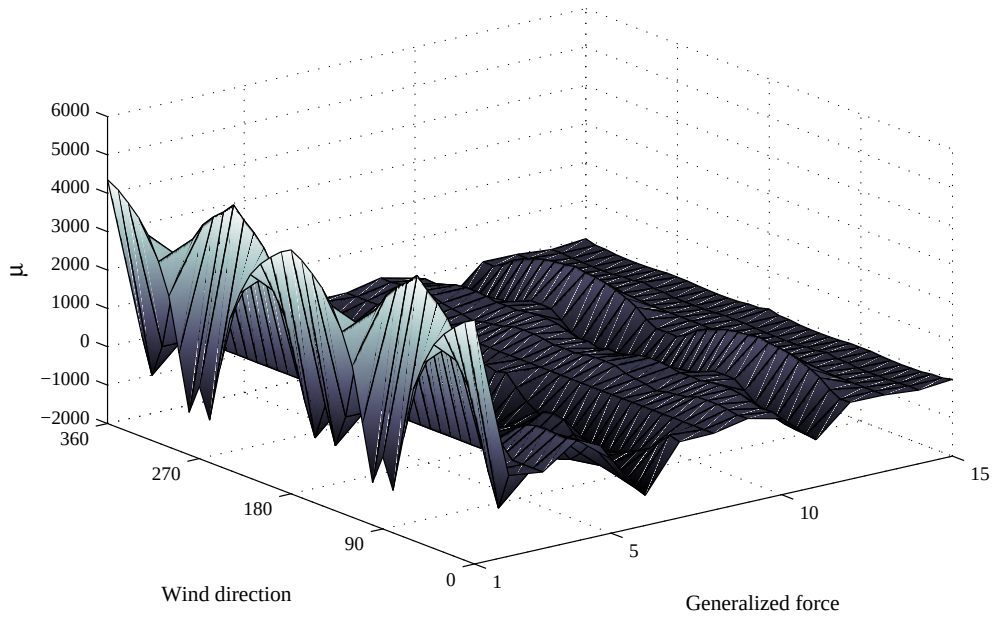

Figure 5.11: Mean values of the generalized forces, regular building.

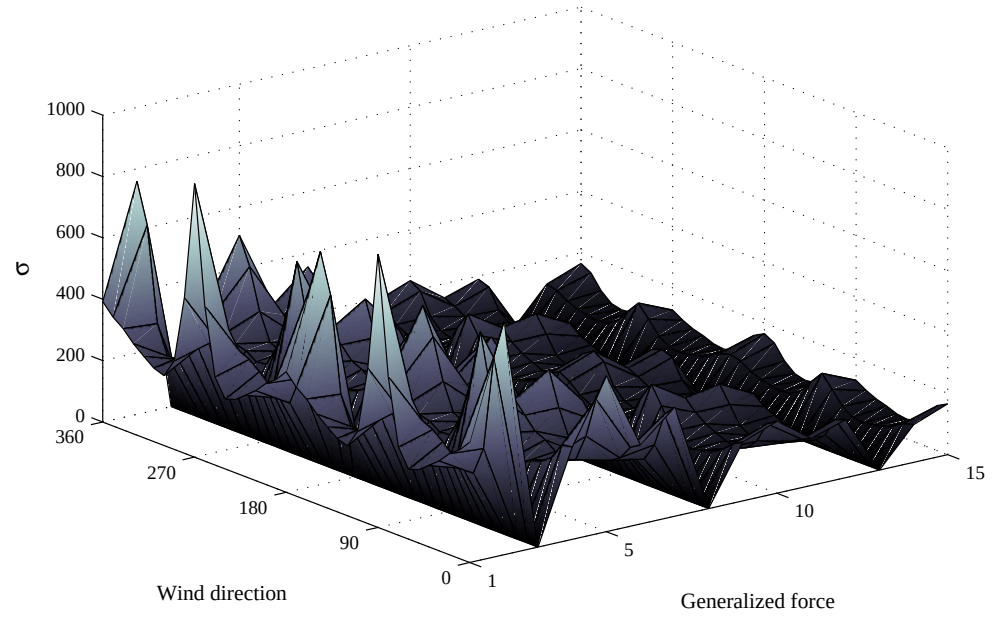

Figure 5.12: Standard deviation of the generalized forces, regular building.

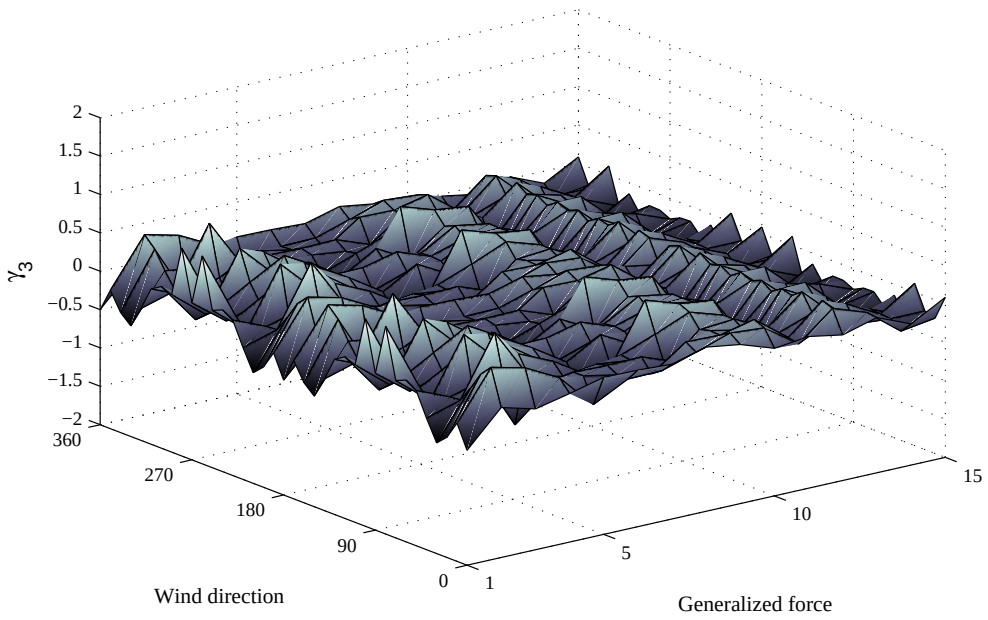

Figure 5.13: Skewness of the generalized forces, regular building.

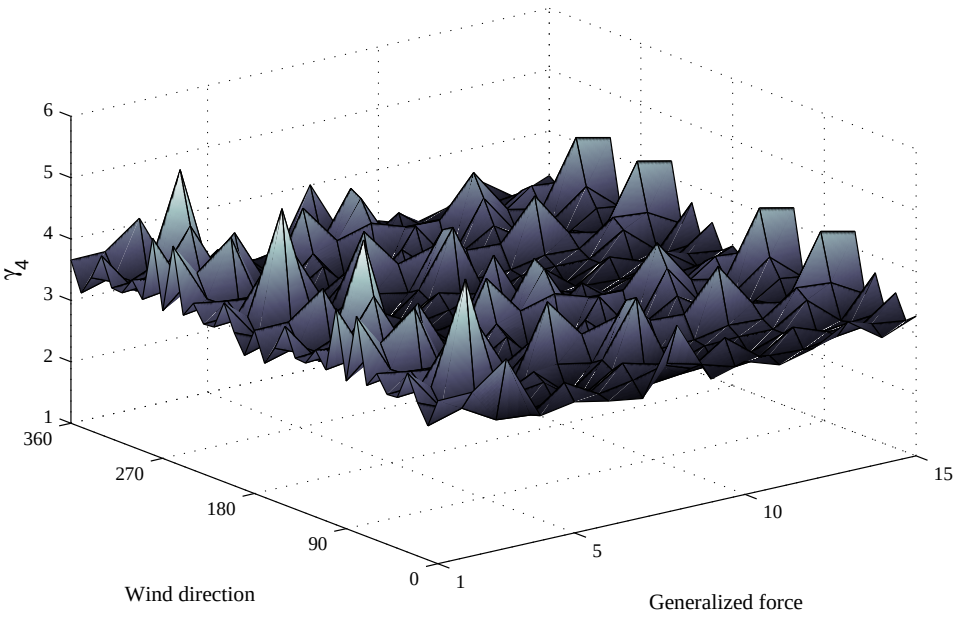

Figure 5.14: Kurtosis of the generalized forces, regular building.

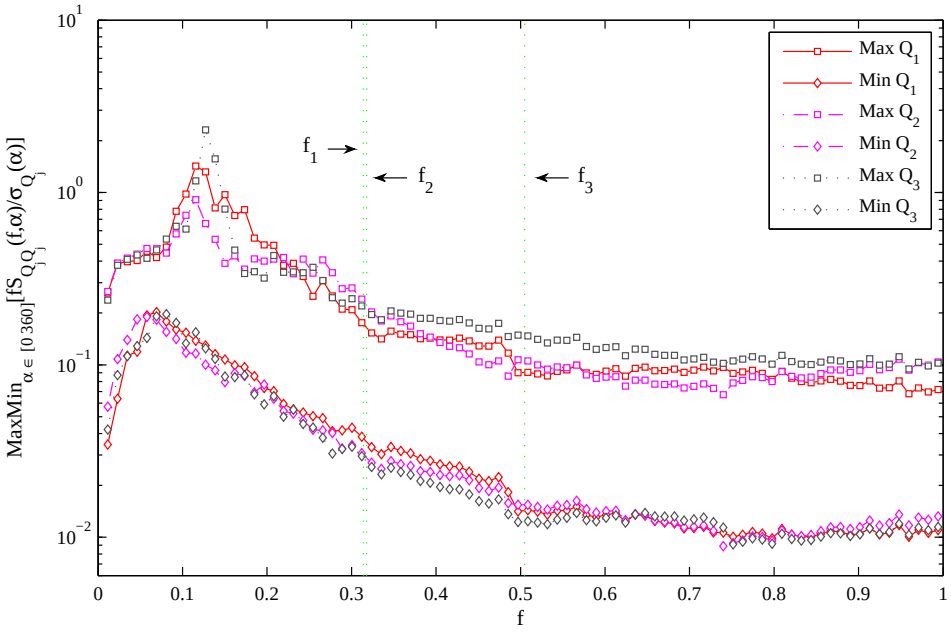

Figure 5.15: Generalized force spectral envelopes over all wind directions for the Bank of China building, forces one to three.

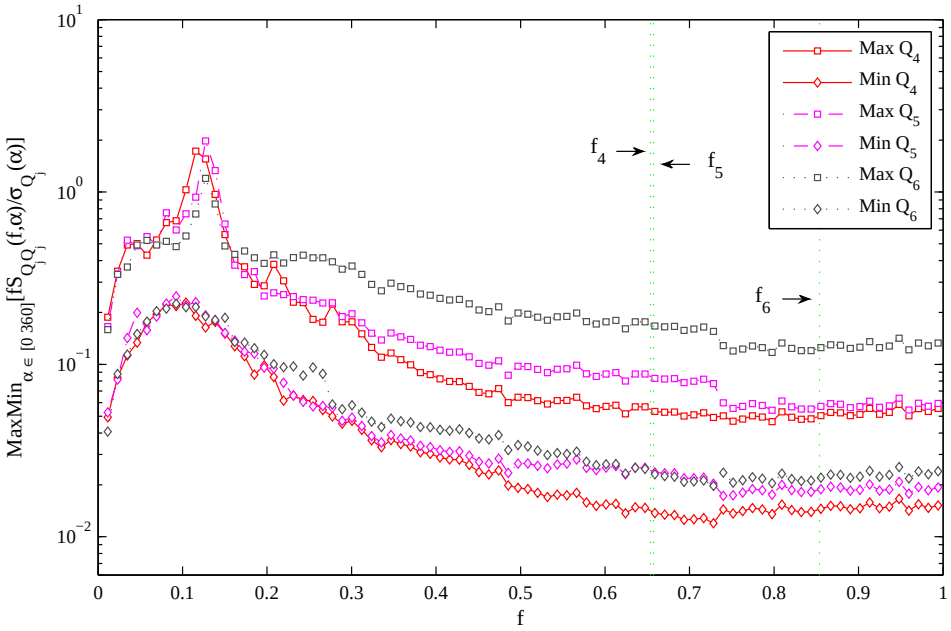

Figure 5.16: Generalized force spectral envelopes over all wind directions for the Bank of China building, forces four to six.

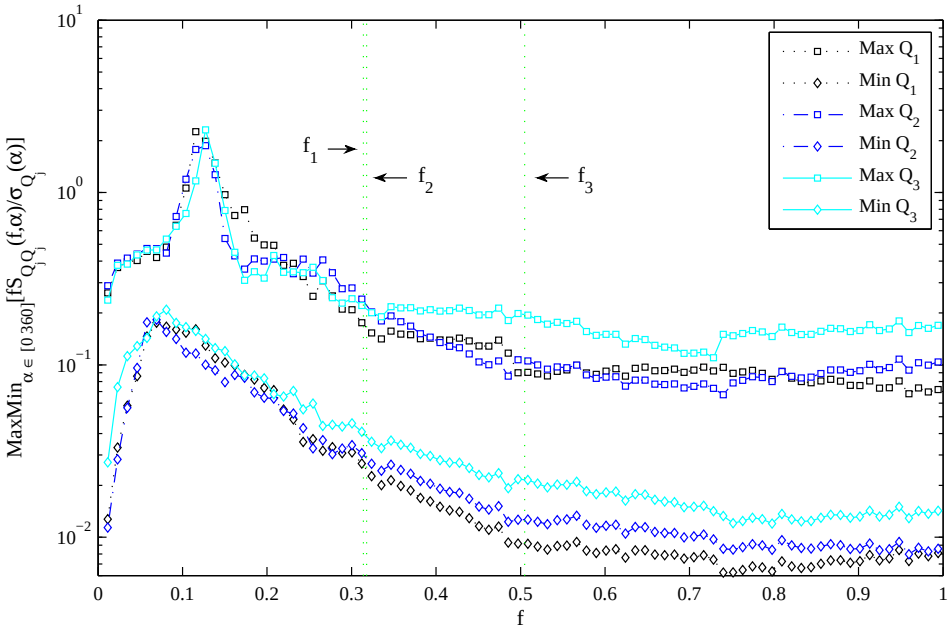

Figure 5.17: Generalized force spectral envelopes over all wind directions for the regular building, forces one to three.

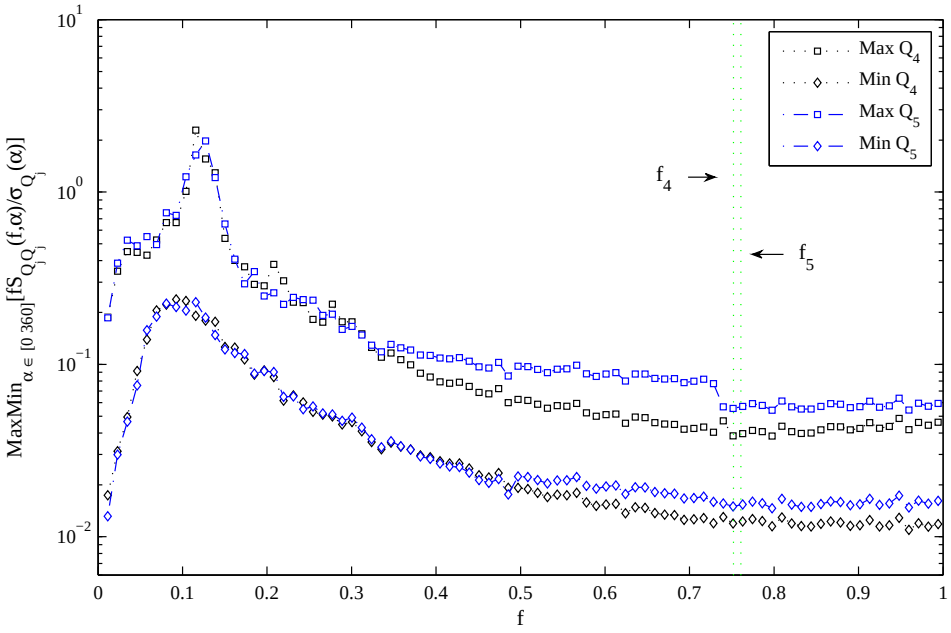

Figure 5.18: Generalized force spectral envelopes over all wind directions for the regular building, forces four to five.

5.5 Mode truncation and the RMS response

In order to investigate the effects of mode truncation on the RMS response the following parameter was considered:

$$\kappa_1 = \frac{\sigma_{R_{HFFB}}(\alpha)}{\sigma_{R_{Tot}}(\alpha)} \tag{5.4}$$

where $\sigma_{R_{HFFB}}(\alpha)$ is the RMS of the generic response component R considering only the resonant and background contribution of the first three modes therefore simulating the estimate obtainable from HFFB measurements for a wind direction α, while $\sigma_{R_{Tot}}(\alpha)$ is the estimate of the RMS response of R given by:

$$R_{Tot}(t) = \sum_{j=1}^{N_r} \Lambda_{j,R} q_{jr}(t) + \sum_{i=1}^{3N} \eta_{i,R} f_i(t) \tag{5.5}$$

where $\Lambda_{R,j}$ are the modal participation coefficients of R, N_r is the number of natural modes used to estimate the resonant response (equal to six for the Bank of China building and five for the regular building), $\eta_{R,i}$ is the influence function of the response R given by the static response caused by a unit load acting in the direction of the ith DOF while f_i are the time varying floor loads. R_{Tot} represents the most complete estimate of the response R available from the experimental data and will be considered as the baseline against which the adequacy of all other methods will be tested.

In figures 5.19 to 5.22 the variation of κ_1 for the top floor acceleration, top floor displacement, top and base bending moments, torque and shears are shown and compared for both the regular system (R) and Bank of China system (B). The results of this study clearly show the importance of considering the contribution of higher modes to the dynamic response of tall buildings with an irregular geometric profile and complex 3D mode shapes. Indeed, as can be seen the effects of mode truncation for all the response components is far greater in the case of a complex system (B) if compared to a regular tall building system (R).

In the particular case of the top floor acceleration (figure 5.19(c) and 5.20(a)) errors of up to 40% can be seen which is over four times what is observed for the regular building. Similar results can be seen for all the other response components except the base moments which seem quite insensitive to the contribution of higher modes. The variable nature of the coupled systems response components demonstrates the sensitivity of the effects of mode truncation to wind direction. It is worth noting that for a regular tall building the response is more uniform with the wind direction and that the acrosswind and alongwind responses seem to represent the extremes of κ_1, see for example figure 5.21(a).

It is observed that the higher mode contributions have different effects on different response components. Indeed considering only the first three fundamental modes does not necessarily mean that a response of interest is underestimated, as

can be seen for the base torque of the coupled building system (figure 5.22), which shows a modest overestimate. This difference in behavior is due to the various modal correlations that exist between the response components and points out the importance of properly describing the modal response correlation for tall buildings with complex 3D mode shapes. It is clear however that in general modal truncation can cause significant underestimates of the RMS response of mechanically and statistically coupled systems.

Figures 5.23 to 5.26 show the variation with height of the maximum and minimum of $\kappa_1(\alpha)$ over all wind directions. In general, the difference between the responses of the two buildings tends to decrease towards the base of the structures. However, this is not seen for the rotational acceleration where far greater errors can be observed for all floors (figure 5.24(c)).

The existence of a vertical coordinate somewhere over the buildings' height where the error due to mode truncation seems to vanish, or at least become negligible, seems clearly evident. In particular this point will in general be located around $0.75H$, where H is the buildings height. An important exception to this can be seen for the base moments (figure 5.25), which seem to present an error vanishing point at the base of the structure. This is true for both the regular building and the irregular building and highlights the adequacy of the base bending moments in describing the dynamic response of tall buildings. A final observation should be made about the far greater sensitivity of the coupled system in the global Y-direction. This can be explained by observing that the building exhibits a far greater geometric variation in this direction compared to the global X-direction due to the presence of a flat vertical regular face (figure 4.27).

These results show the importance of considering higher mode contributions for properly describing the RMS response of tall buildings with an irregular geometric profile and statistically and mechanically coupled systems. The adequacy of considering only the first three vibration modes in the case of regular geometry is clear and confirms what can be found in literature [5.18, 5.15, 5.12].

5.5.1 RMS and the background response

The first part of section 5.5 clearly demonstrated the adverse effects of mode truncation on the RMS response of statistically and mechanically coupled building systems. This was in relative contrast to what can be seen for the regular uncoupled system where mode truncation will in general bring significantly smaller errors confirming the validity of loading schemes based on HFFB measurements where the resonant and background contribution of only the first three generalized forces can be estimated [5.6]. The aim of this section is to quantify the importance of the background response for statistically and mechanically coupled systems as well as for uncoupled systems. To this end the following parameter was considered:

$$\kappa_2 = \frac{\sigma_{R_{3r+Back}}(\alpha)}{\sigma_{R_{Tot}}(\alpha)} \tag{5.6}$$

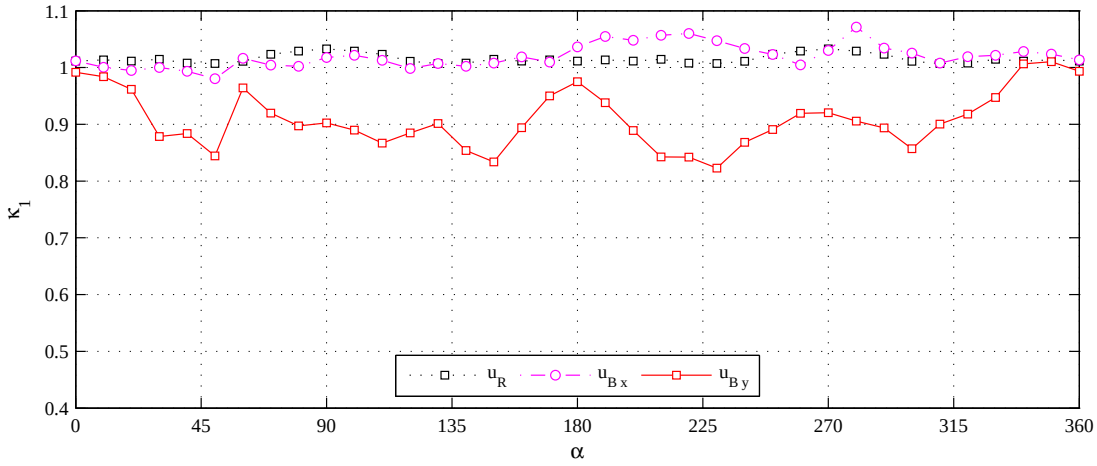

(a)

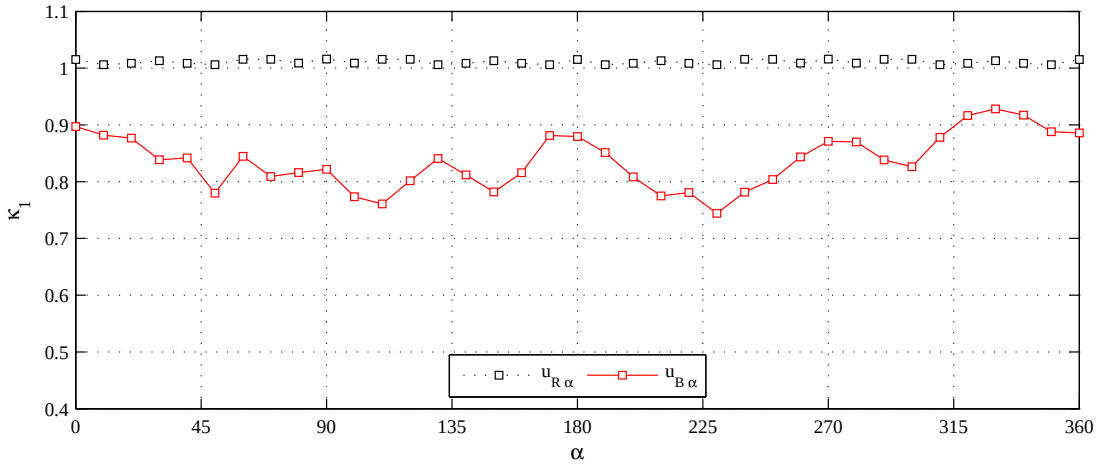

(b)

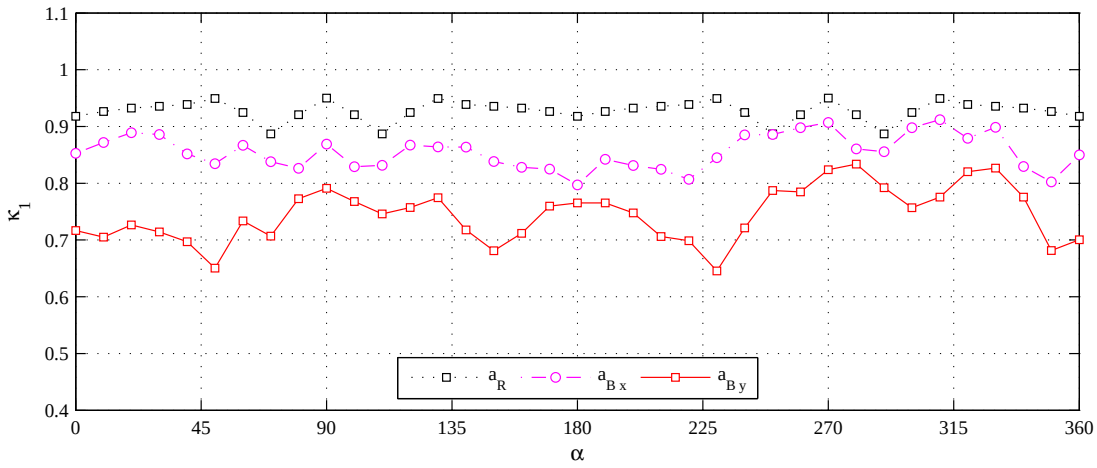

(c)

Figure 5.19: κ_1 for: (a) top floor displacement, (b) top floor rotation, (c) top floor acceleration.

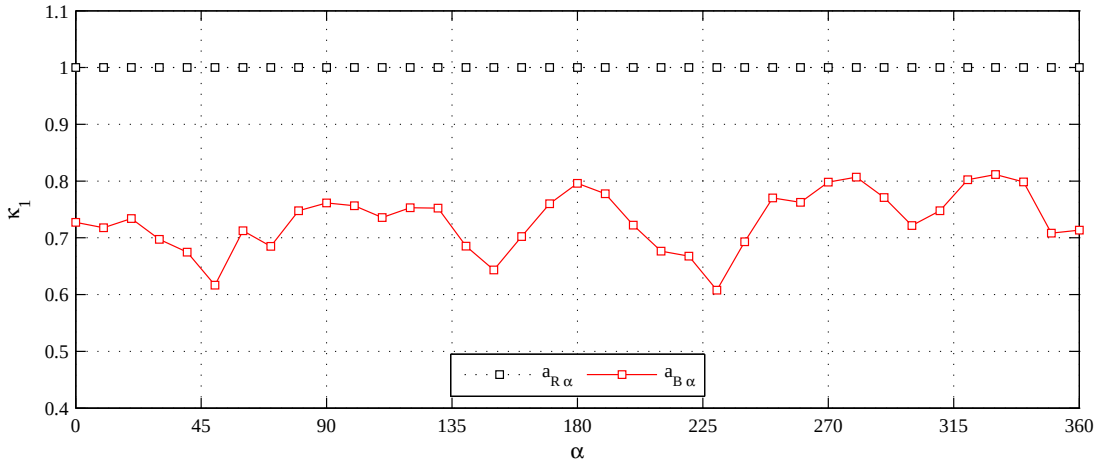

(a)

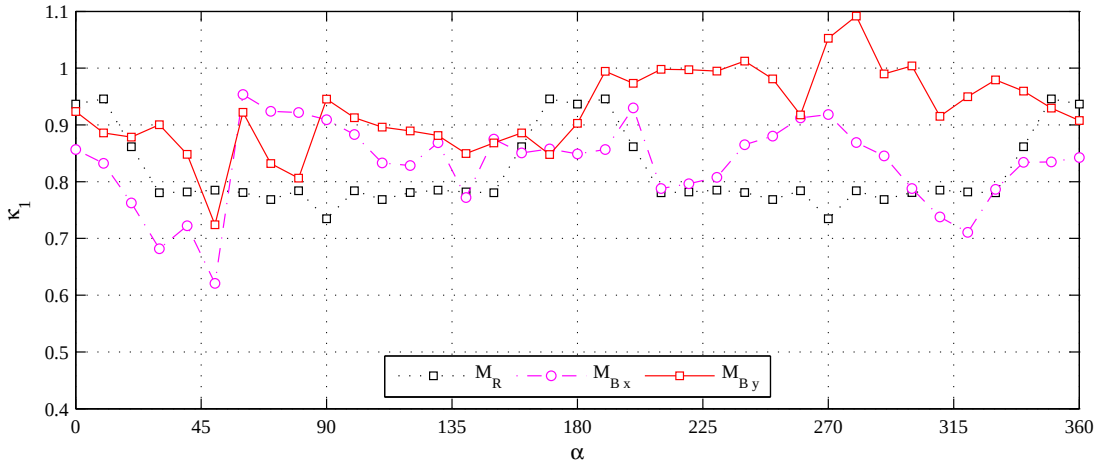

(b)

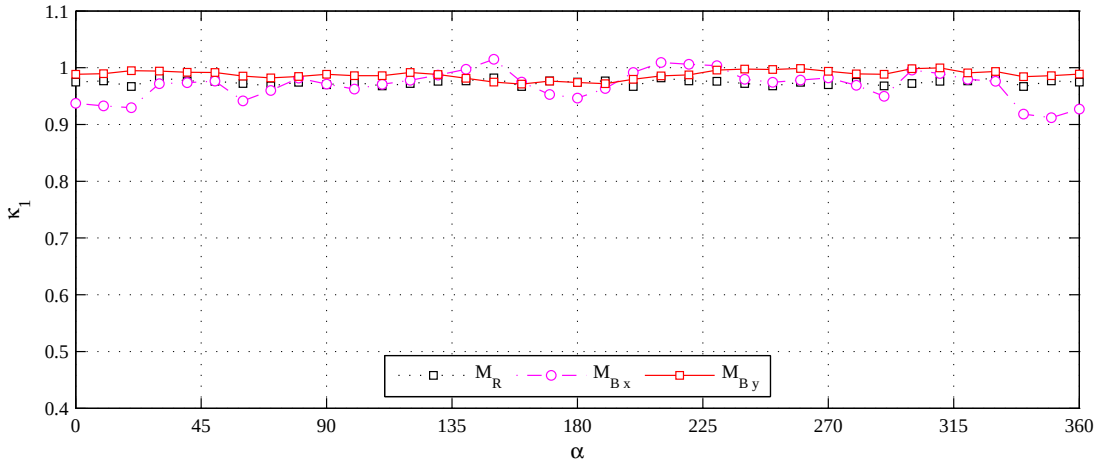

(c)

Figure 5.20: κ_1 for: (a) top floor angular acceleration, (b) top floor bending moments, (c) base bending moments.

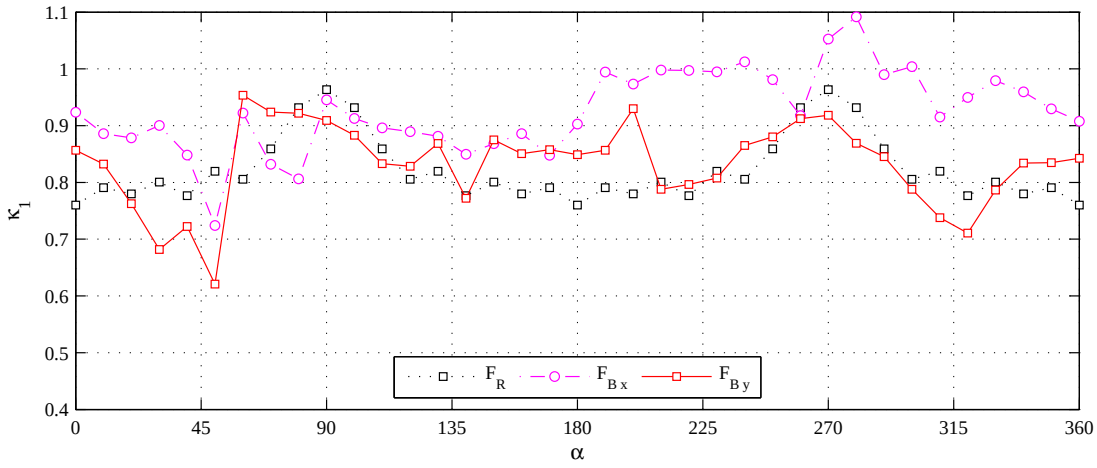

(a)

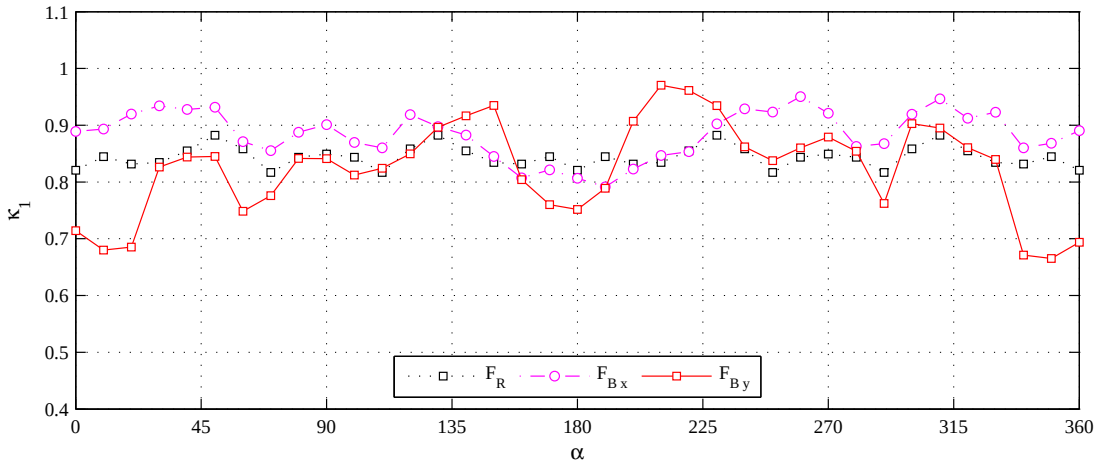

(b)

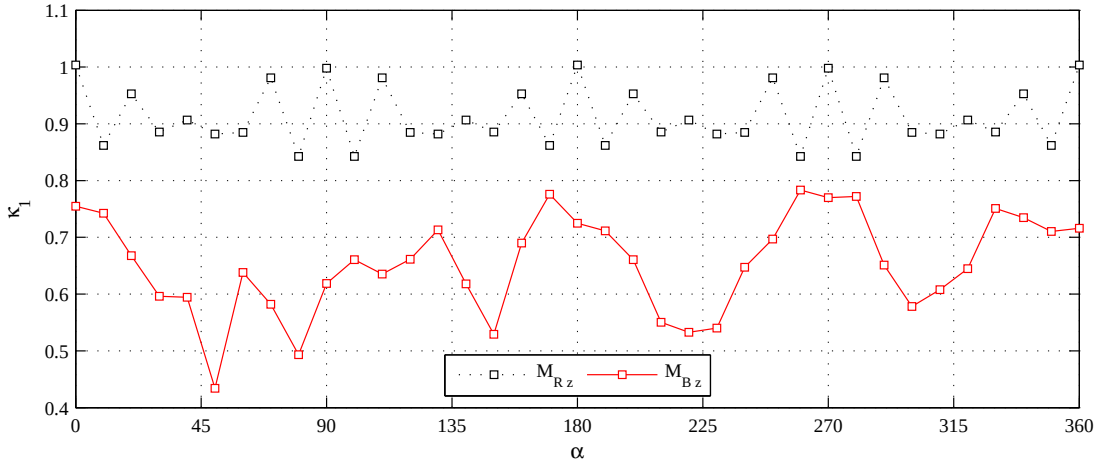

(c)

Figure 5.21: κ_1 for: (a) top floor shear, (b) base shear, (c) top floor torque.

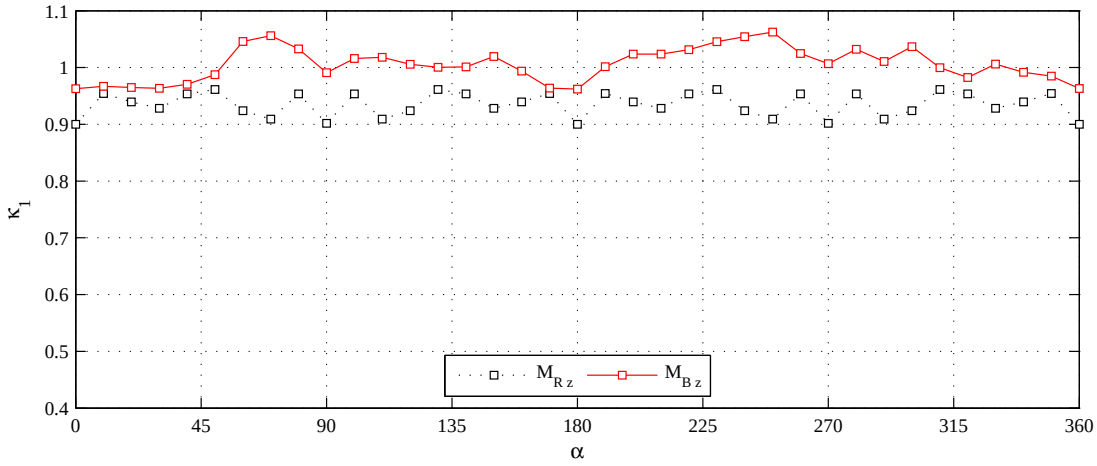

Figure 5.22: base torque

where $\sigma_{R_{3r+Back}}(\alpha)$ is the RMS of a particular response component R considering the resonant response of the first three modes for a wind direction α with however a complete background representation. Therefore $R_{3r+Back}$ can be written as:

$$R_{3r+Back}(t) = \sum_{j=1}^{3} \Lambda_{j,R} q_{jr}(t) + \sum_{i=1}^{3N} \eta_{i,R} f_i(t) \tag{5.7}$$

where $\Lambda_{j,R}$ are the modal participation coefficients of R, $\eta_{i,R}$ is the influence function of the response R given by the static response caused by a unit load acting in the direction of the ith DOF while f_i are the time varying floor loads. Obviously $\sigma_{R_{Tot}}(\alpha)$ is defined as in equation (5.5). κ_2 will give an indication of the importance of a complete background representation.

The influence of the background response is significant. Indeed by considering a full background representation the errors in the estimation of the dynamic response are significantly decreased for all response components except the acceleration which has a negligible background contribution [5.12]. Examples of this behavior for the Bank of China building are shown in figures 5.27 and 5.28 for the top floor displacements, top and base bending moments, top floor and base torque, top floor and base shear forces. This observation is further highlighted by figures 5.29 to 5.31 showing the maxima and minima of the ratios κ_2 and κ_1 over all wind directions. The advantages in a complete background representation are clearly seen. However, while this is uniformly true for the regular uncoupled building system, (see figures 5.32 to 5.34), for the coupled system significant resonant contributions of the higher modes to the shear, moments and torque towards the top of the structure are evident (figures 5.30 and 5.31). This is again visible in terms of the wind direction θ at the top floor, as can be seen in figure 5.27(b) for the top bending moments, figure 5.28(a) for the top floor torque and figure 5.28(b) for the floor top shear.

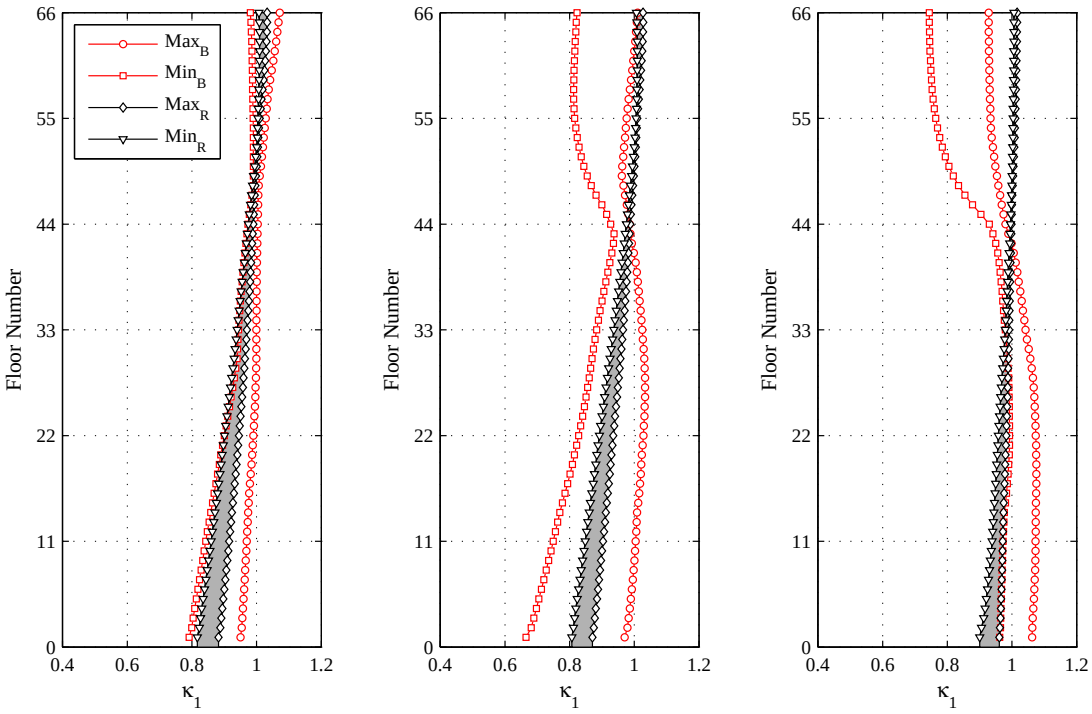

Figure 5.23: Extremes of κ_1: (a) displacement X, (b) displacement Y, (c) rotation θ.

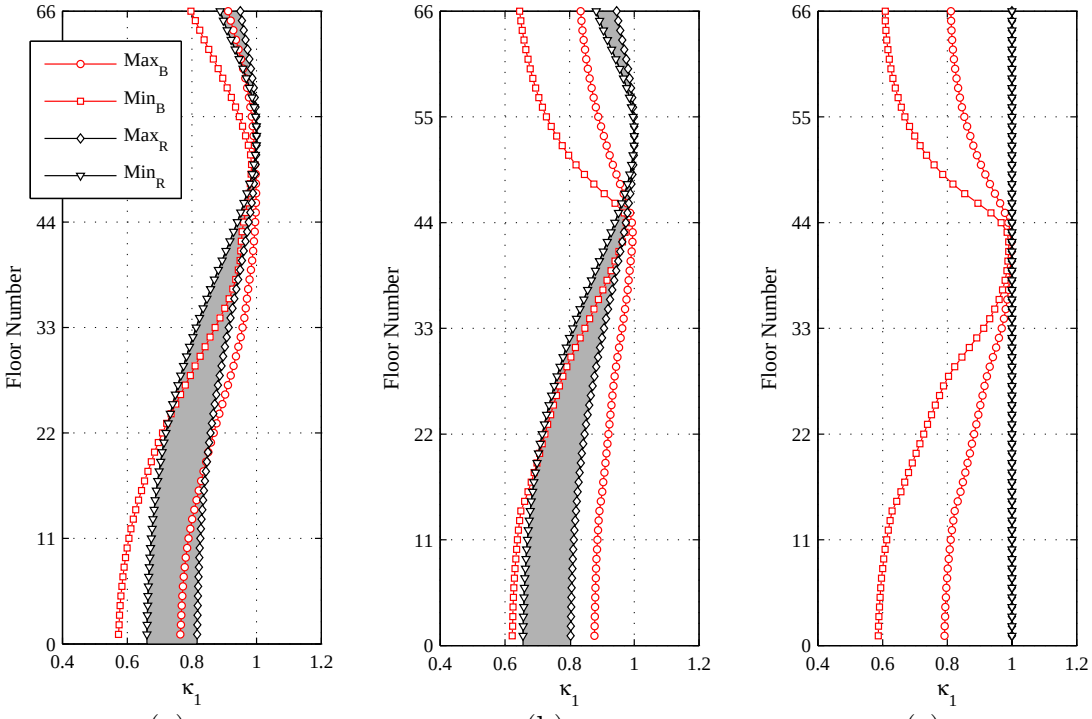

Figure 5.24: Extremes of κ_1: (a) acceleration X, (b) acceleration Y, (c) acceleration θ.

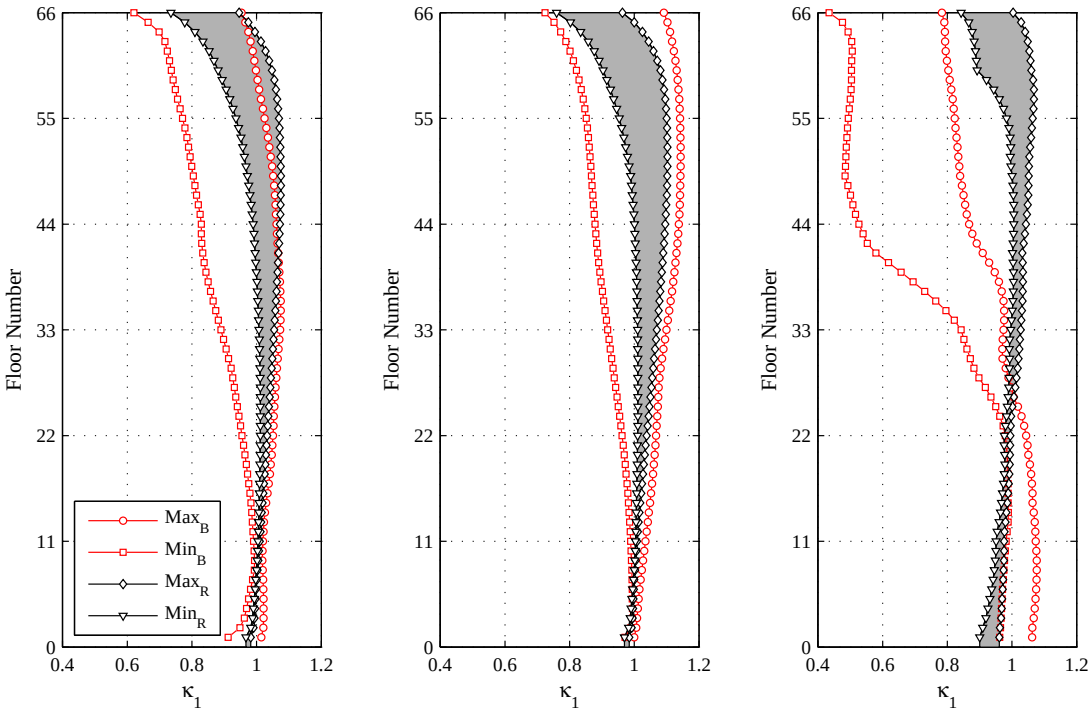

Figure 5.25: Extremes of κ_1: (a) bending moment X, (b) bending moment Y, (c) torque.

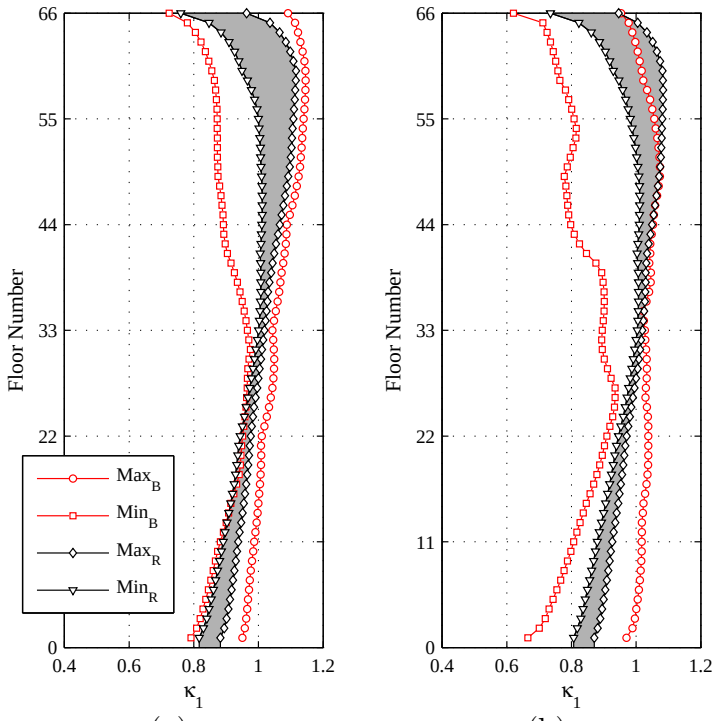

Figure 5.26: Extremes of κ_1: (a) shear X, (b) shear Y.

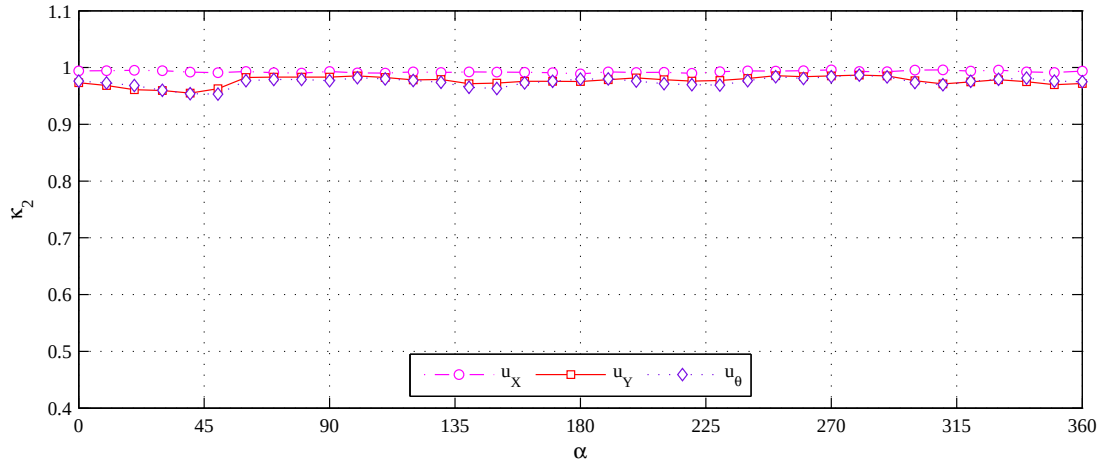

(a)

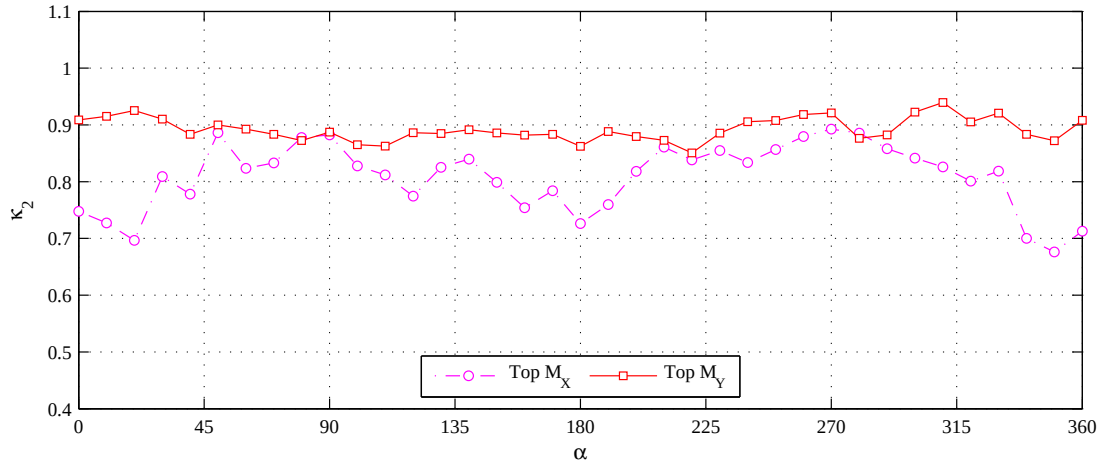

(b)

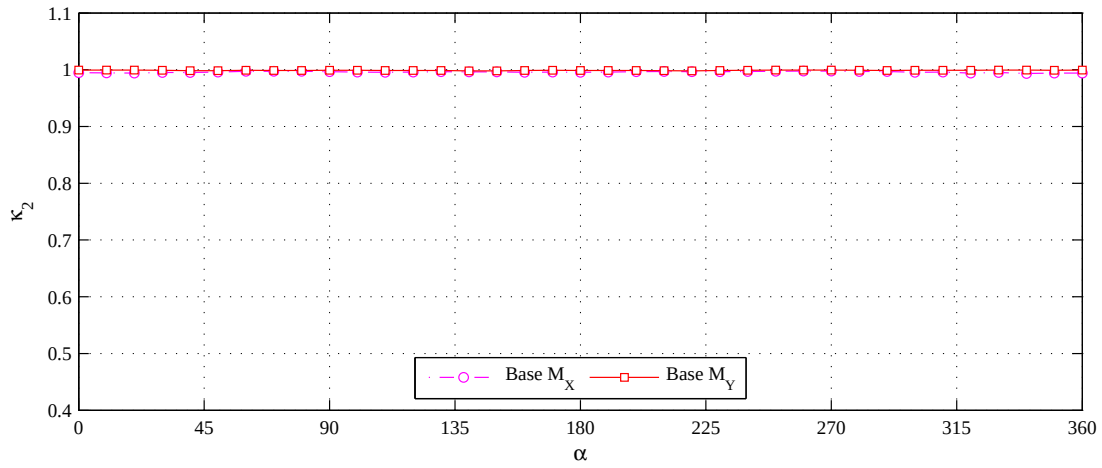

(c)

Figure 5.27: Extremes of κ_2: (a) top floor displacement, (b) top floor bending moments, (c) base bending moments, Bank of China building.

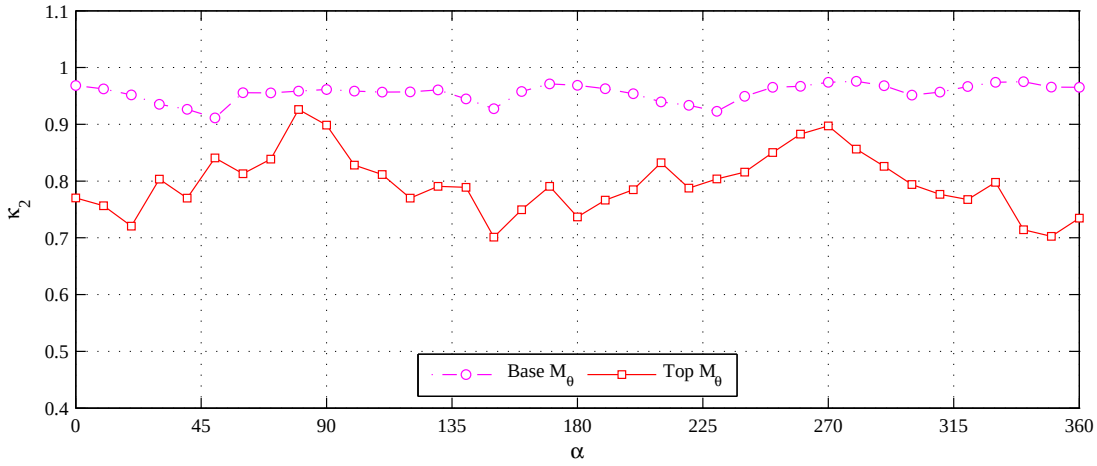

(a)

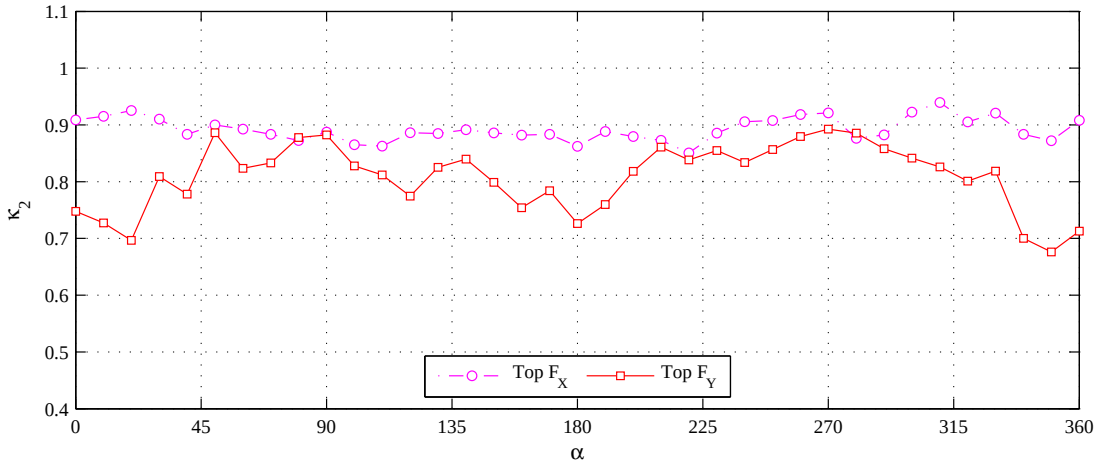

(b)

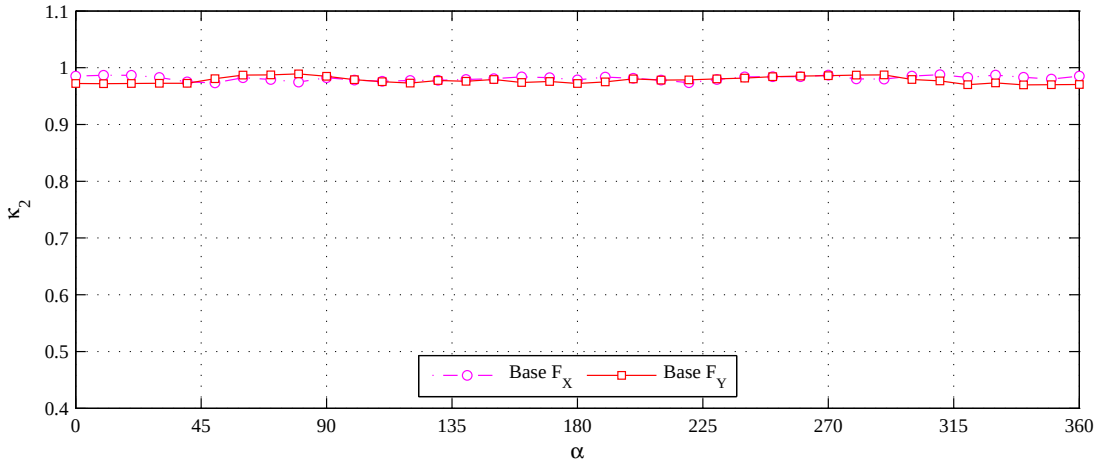

(c)

Figure 5.28: Extremes of κ_2: (a) top floor and base torque, (b) top floor shear forces, (c) base floor shear forces, Bank of China building.

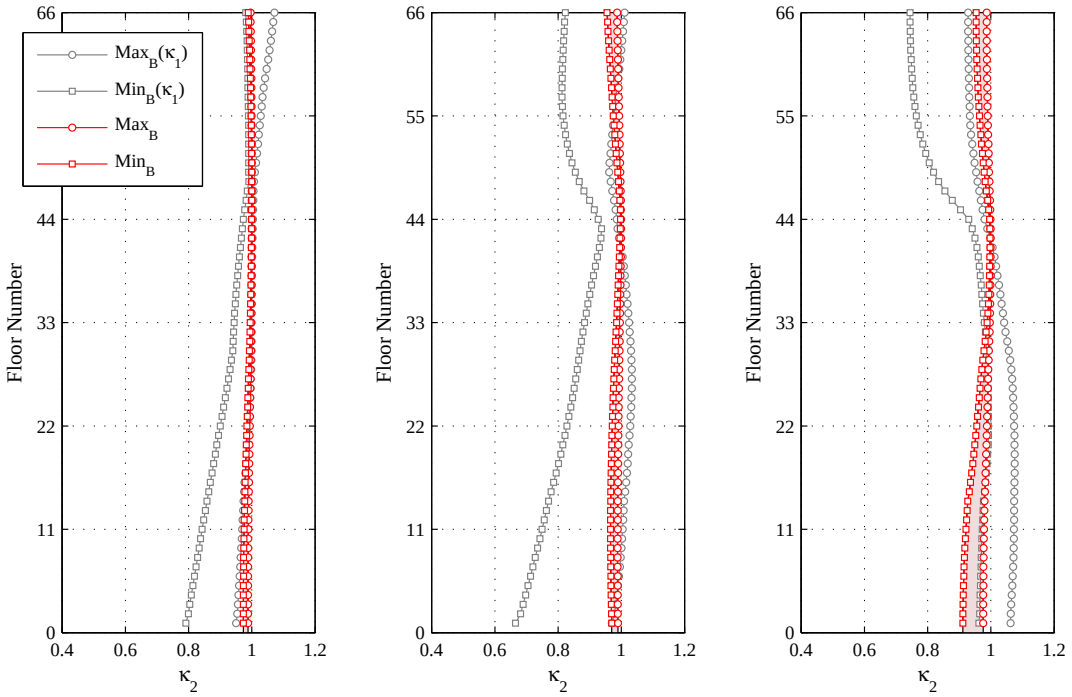

Figure 5.29: Extremes of κ_2: (a) displacement X, (b) displacement Y, (c) rotation θ, Bank of China building.

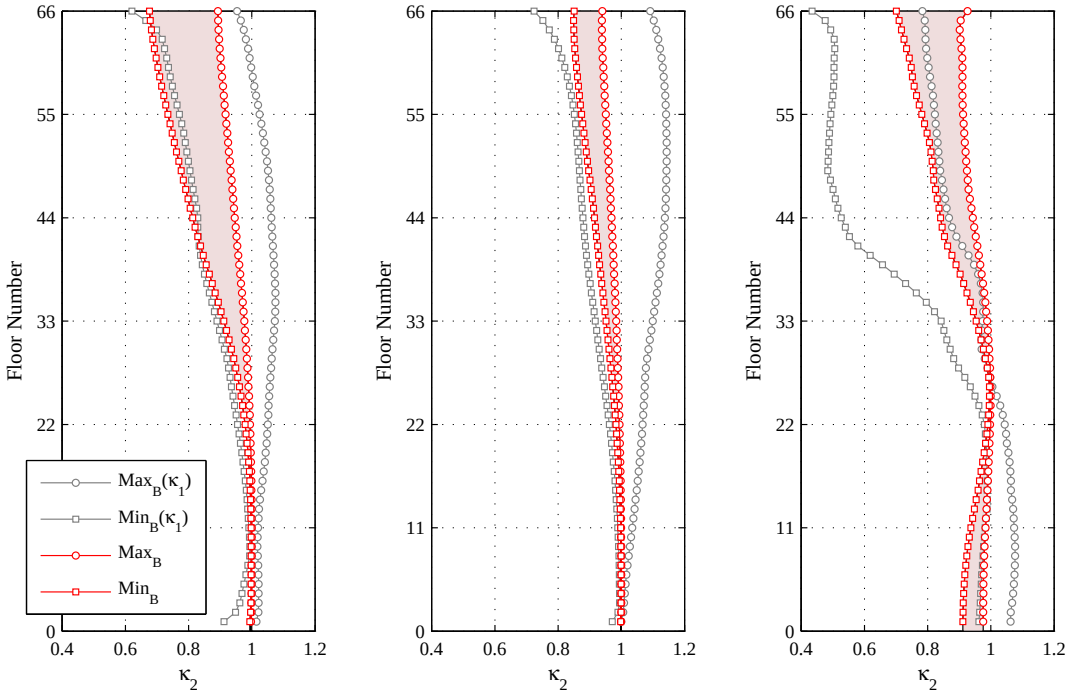

Figure 5.30: Extremes of κ_2: (a) bending moments X, (b) bending moments Y, (c) torque θ, Bank of China building.

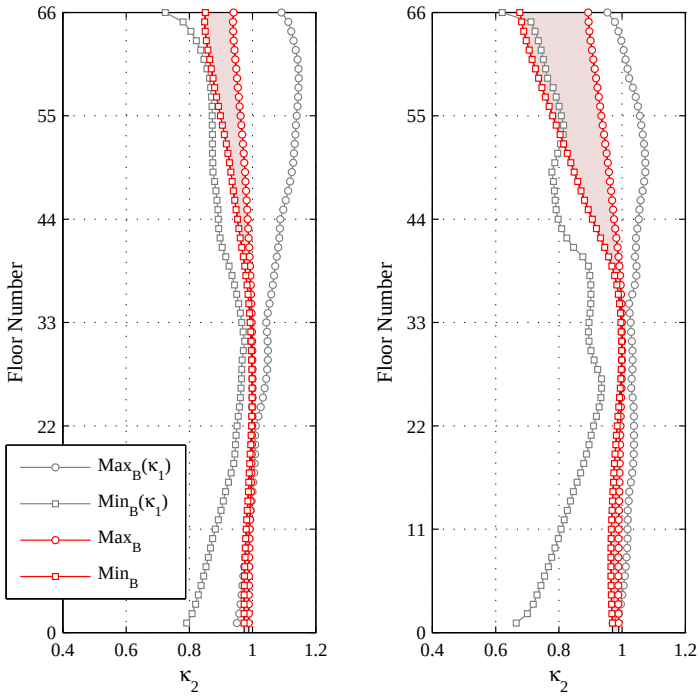

Figure 5.31: Extremes of κ_2: (a) shear X, (b) shear Y, Bank of China building.

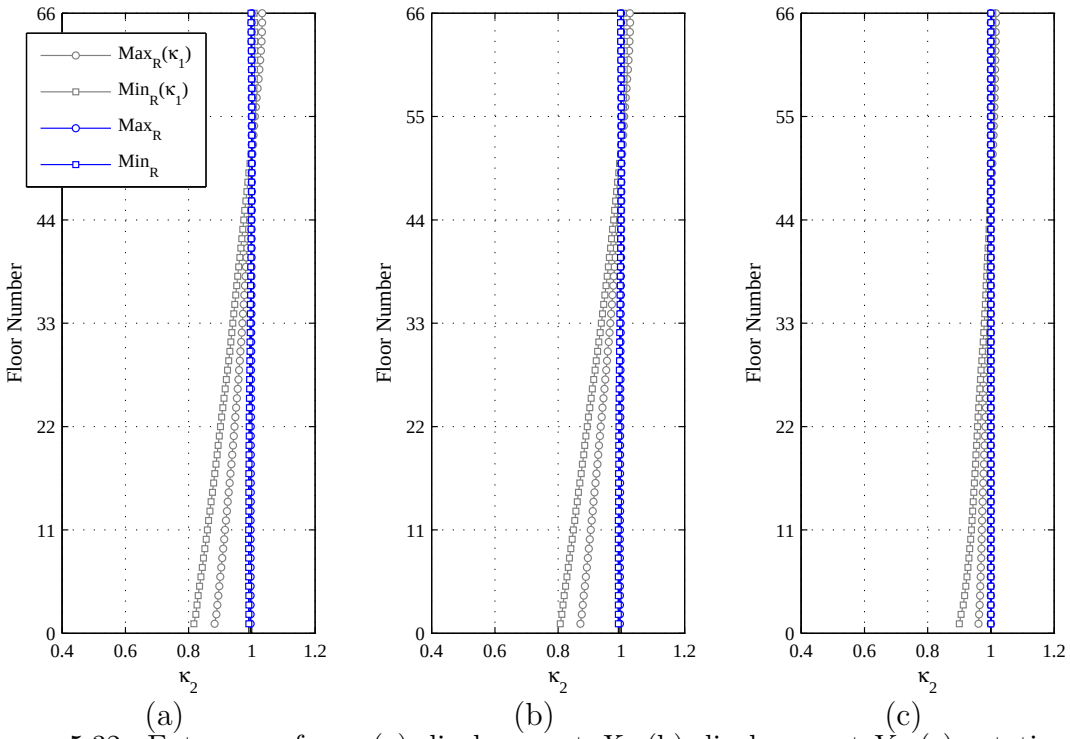

Figure 5.32: Extremes of κ_2: (a) displacement X, (b) displacement Y, (c) rotation θ, regular building.

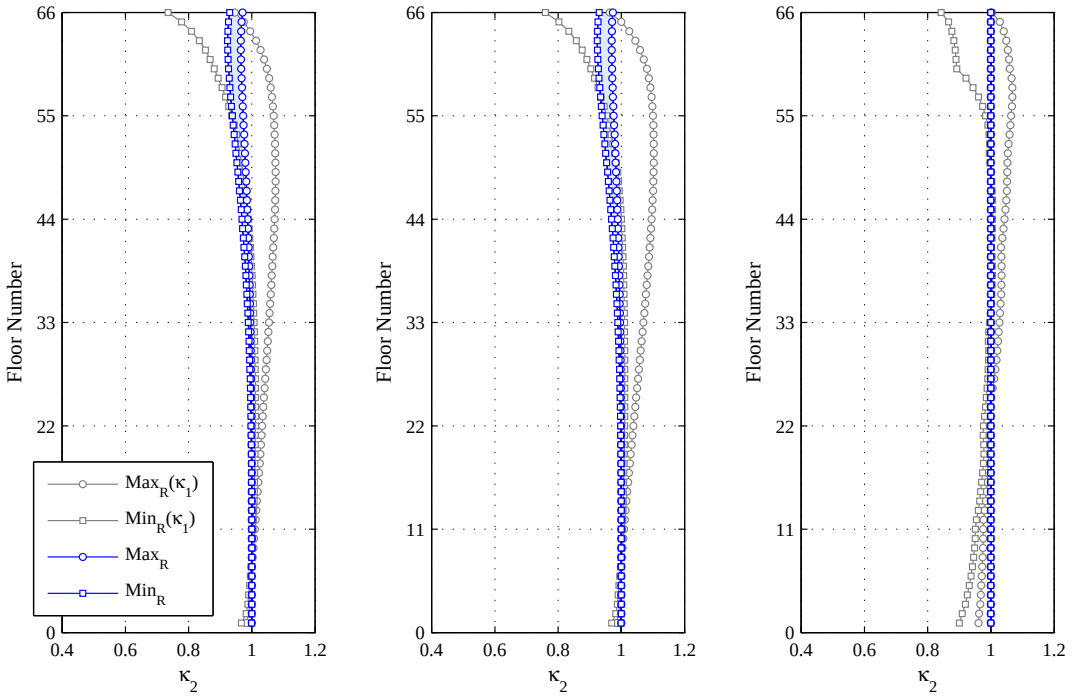

Figure 5.33: Extremes of κ_2: (a) bending moments X, (b) bending moments Y, (c) torque θ, regular building.

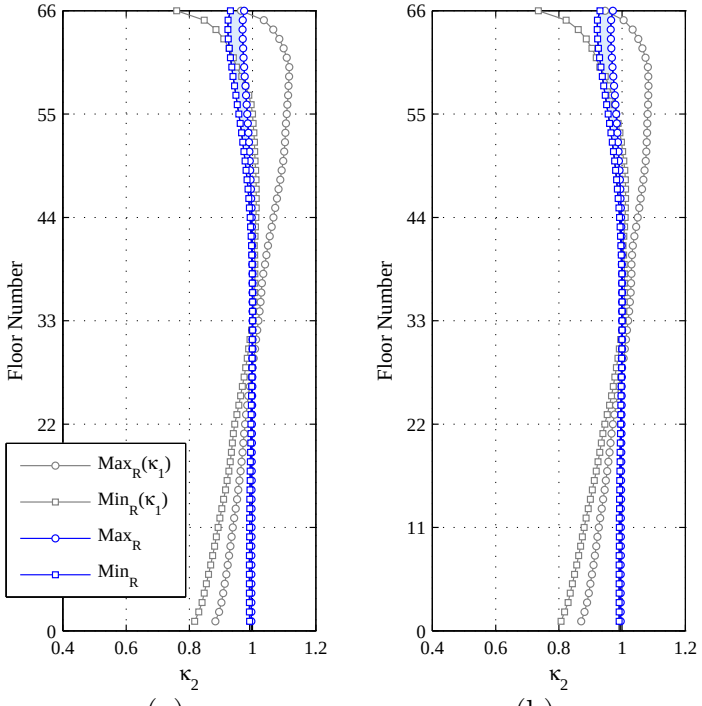

Figure 5.34: Extremes of κ_2: (a) shear X, (b) shear Y, regular building.

5.6 Skewness and kurtosis and mode truncation

As previously mentioned it is customary in the design and analysis of tall buildings to consider the response gaussian in nature even though the forcing functions show strong non-gaussian features, section 4.2.3. This section has the twofold objective of firstly verifying whether this is true and if there is any influence on this result caused by the particular system under consideration, and secondly to investigate the effects of mode truncation on the probabilistic nature of the response.

Figures 5.35 to 5.42 show the maximum and minimum skewness and kurtosis coefficients over all wind directions for the shears, displacements, accelerations and moments occurring at each floor level. The calculations are carried out for wind directions 0° to 360° in the case of the Bank of China building and for symmetry reasons from 0° to 90° in the case of the regular building.

It is immediately clear from the values of the skewness and kurtosis that the global response of both the coupled and uncoupled systems is strongly non-gaussian. This holds not only for the response parameters shown in figures 5.35 to 5.42, but also for parameters such as interstory drift not reported here for a question of brevity. It also seems evident that the irregular and coupled systems present a more pronounced tendency towards the conservation of non-gaussian response features. This can be seen in figures 5.35 to 5.42 by the fact that the skewness and kurtosis values associated with this system tend to be outside the shaded region representing the range of variability of the skewness and kurtosis for the regular uncoupled system.

The effect of higher modes on the maximum and minimum values of skewness and kurtosis does not so much influence the maxima or minima as it affects the regularity of the values seen over the height of the building. Indeed, by considering an increased number of modes the response will be influenced by a larger number of generalized forces each of which has a particular probabilistic nature, contributing more or less, depending on the associated mode shape. It is interesting to note from figure 5.39 that the skewness of the acceleration takes on values indicating a gaussian distribution which however is not confirmed by the kurtosis (figure 5.40). This peculiar behavior is due to the relative importance of the resonant part of the acceleration.

Figures 5.43 to 5.50 show the variation of skewness and kurtosis for the X component of the acceleration and bending moments of both systems. What can clearly be seen is the sensitivity of these parameters to the incident wind direction and the relatively lower non-gaussian features of the regular uncoupled system. Indeed, the highly non-gaussian features seen in figures 5.35 to 5.42 will tend to manifest themselves for certain wind directions. For instance the X component of bending moment of the irregular coupled system shows strong non-gaussian features for an incident wind direction of 350° (figure 5.46). A similar behavior can be seen for the other response components. It is interesting to notice how sensitive the coupled system with complex geometric profile is to wind direction. This is clearly

seen for the acceleration in direction X of figure 5.44 where a number of wind directions will cause strong non-gaussian features to manifest.

These non-gaussian features are in stark contrast to the common hypothesis of gaussianity when calculating the peak factors for the estimation of the maximum response and design loads of tall buildings [5.6, 5.5, 5.3, 5.24, 5.16, 5.2]. This study would seem to indicate that the non-gaussian response features are by no means negligible. This obviously has a direct effect on the most appropriate peak factors to consider in the design of tall buildings.

Various models have been proposed in literature to account for non-gaussian features in the definition of the peak factor. In particular the application of models based on translation processes [5.10, 5.7, 5.8] would seem to offer an interesting possibility due to their simplicity and capability of capturing non-gaussian features of an extremely wide variety of processes.

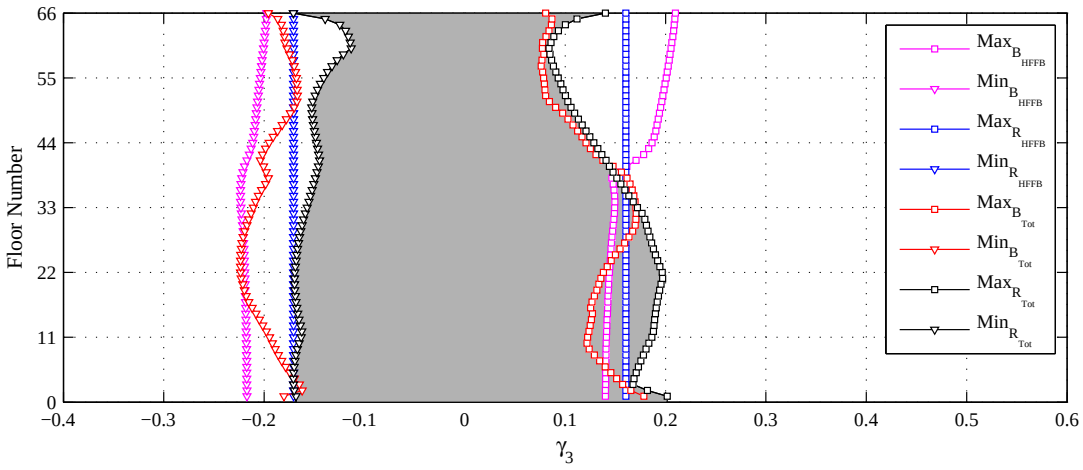

(a)

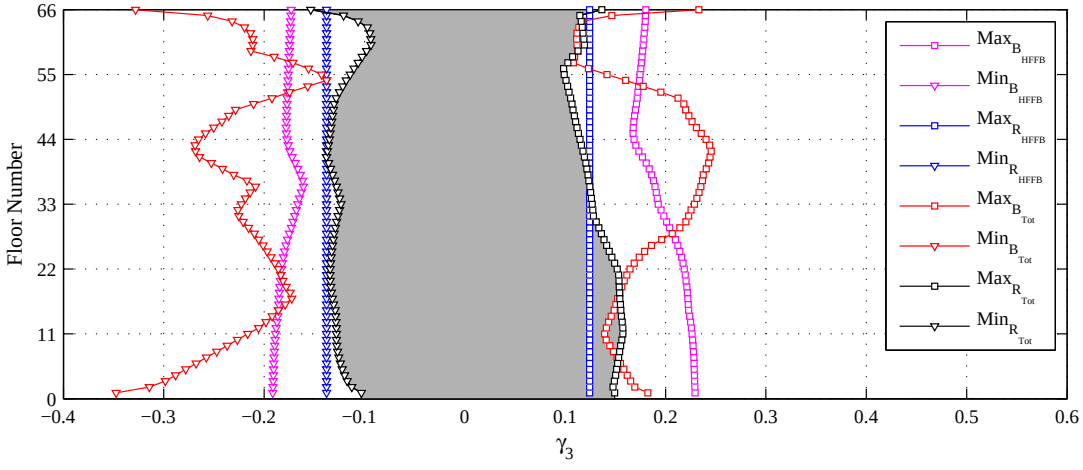

(b)

Figure 5.35: Extreme skewness over all wind directions: (a) shear X, (b) shear Y.

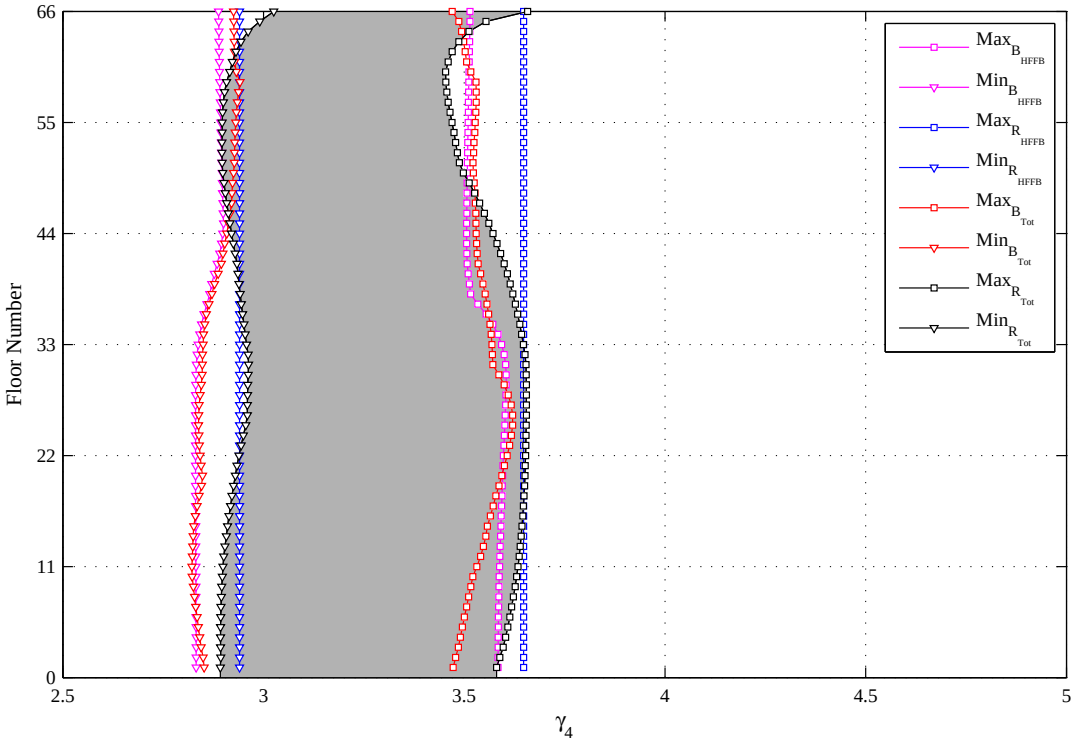

(a)

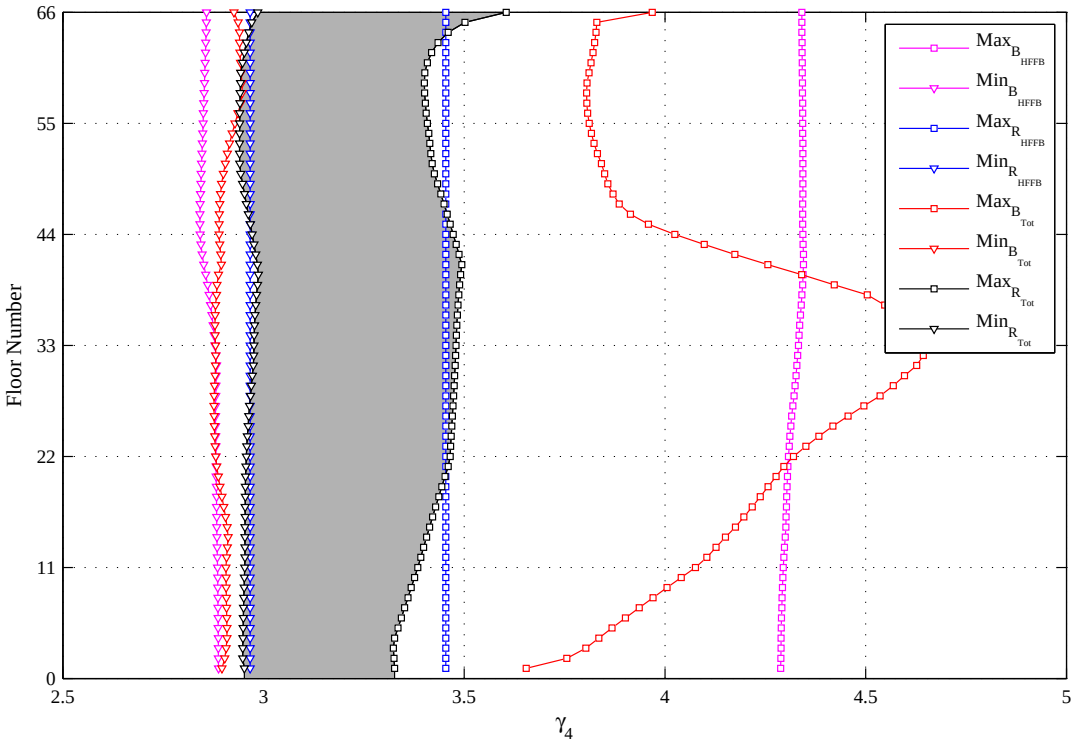

(b)

Figure 5.36: Extreme kurtosis over all wind directions: (a) shear X, (b) shear Y.

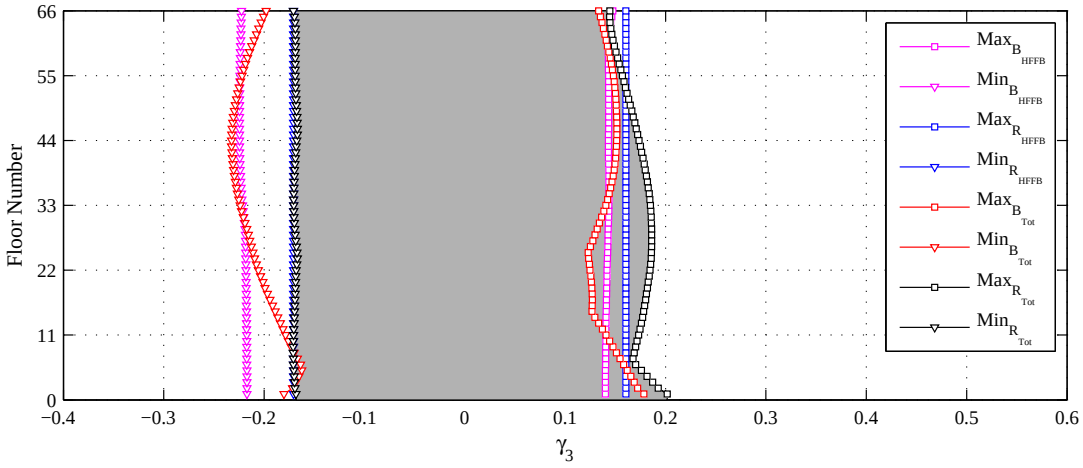

(a)

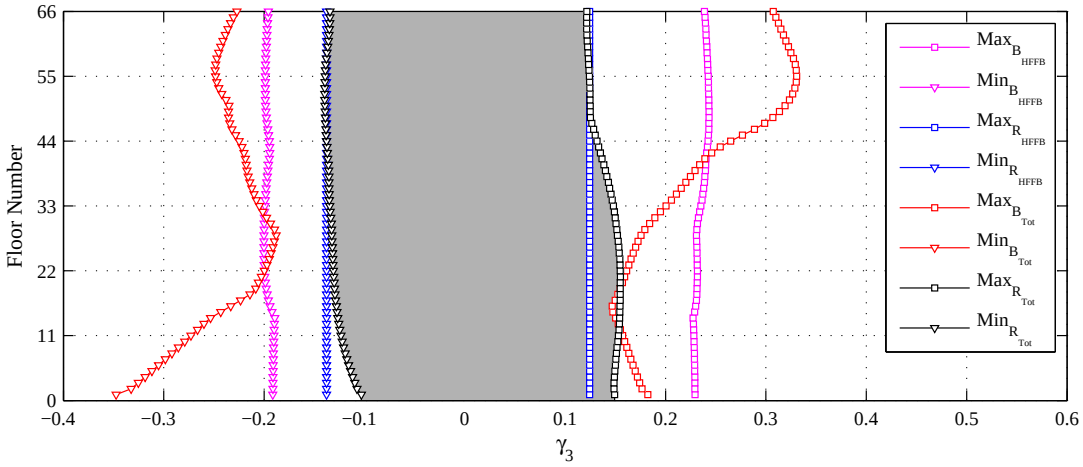

(b)

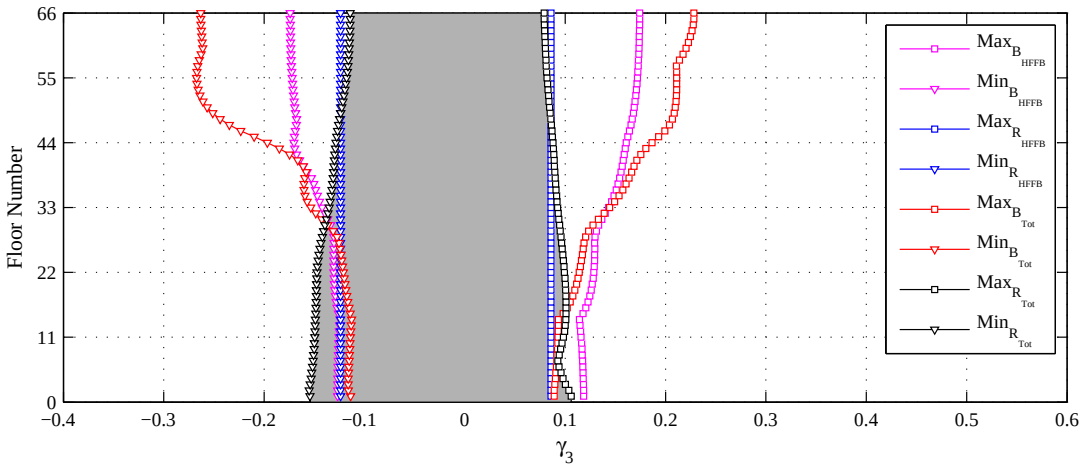

(c)

Figure 5.37: Extreme skewness over all wind directions: (a) displacement X, (b) displacement Y, (c) rotation θ.

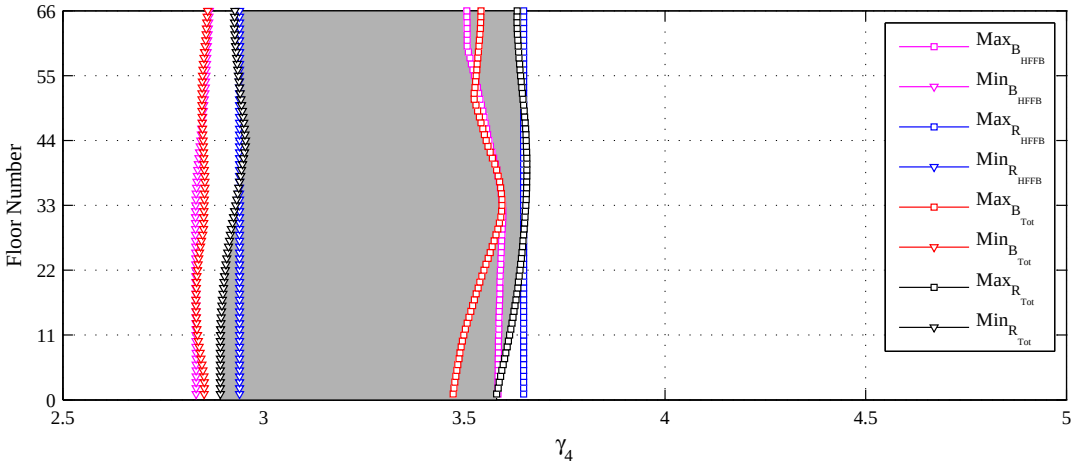

(a)

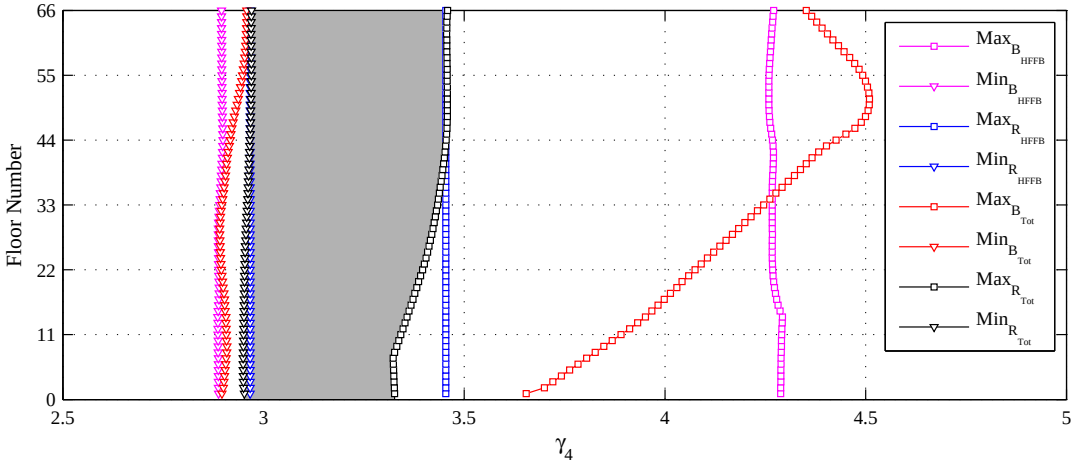

(b)

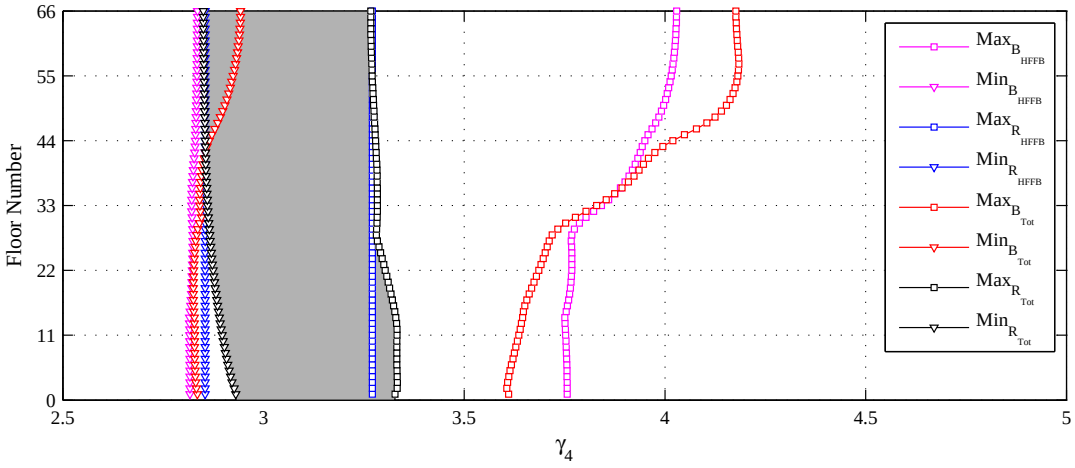

(c)

Figure 5.38: Extreme kurtosis over all wind directions: (a) displacement X, (b) displacement Y, (c) rotation θ.

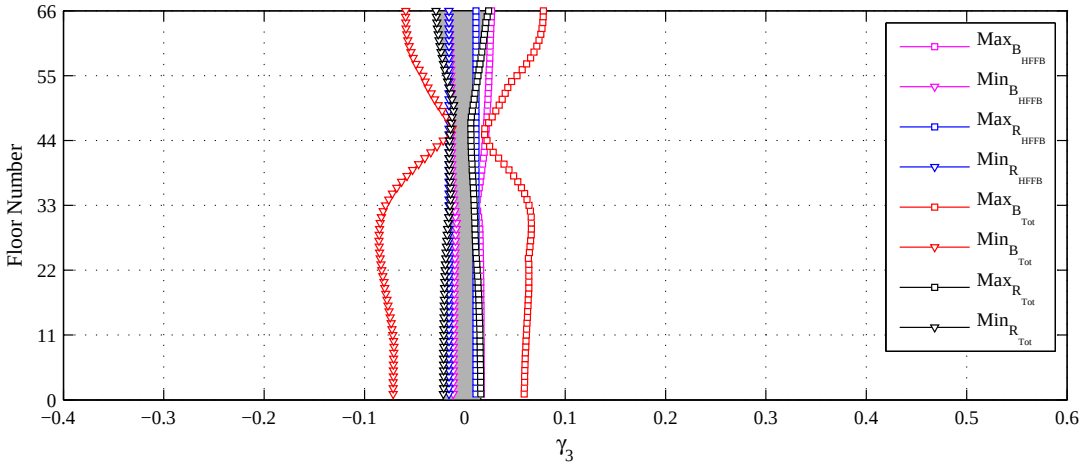

(a)

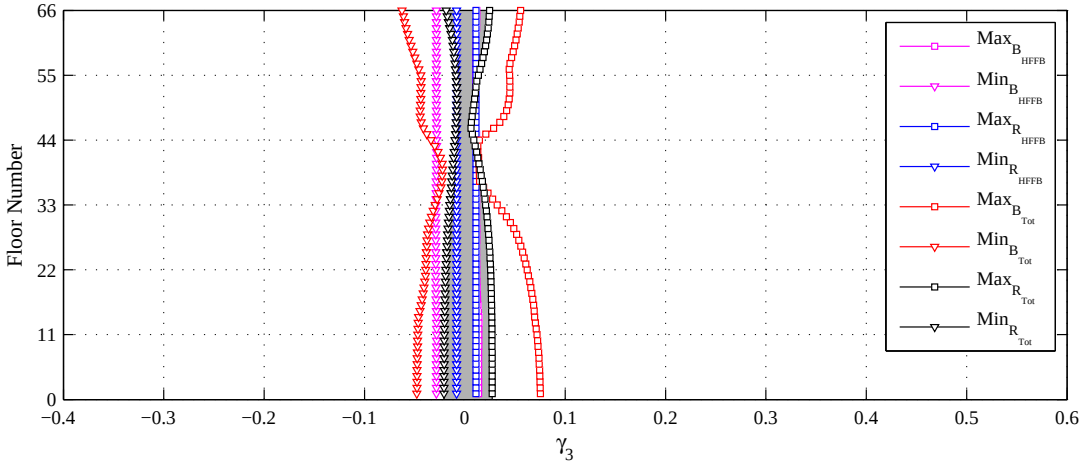

(b)

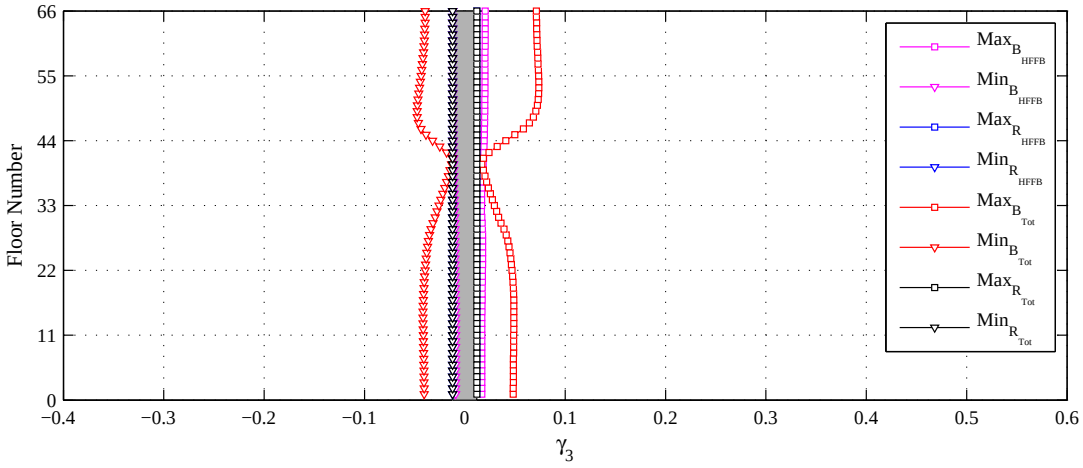

(c)

Figure 5.39: Extreme skewness over all wind directions: (a) acceleration X, (b) acceleration Y, (c) angular acceleration θ.

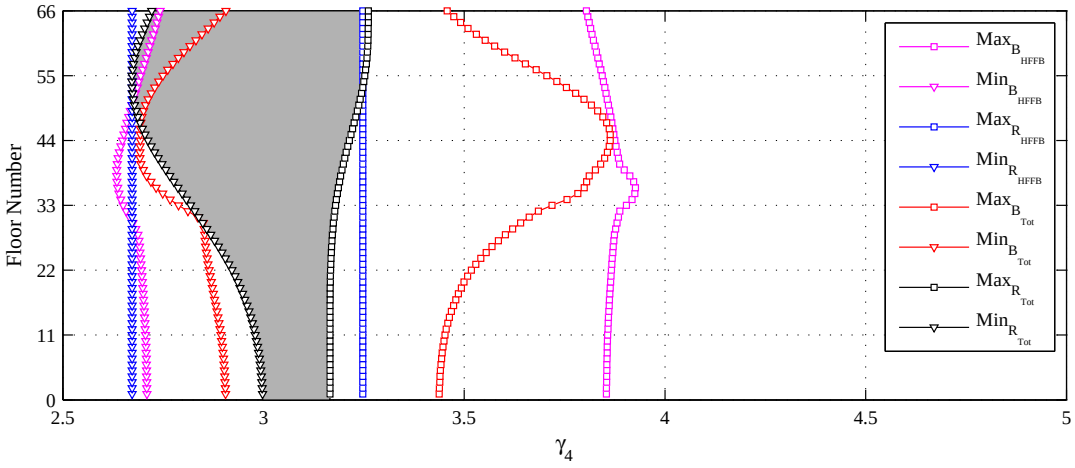

(a)

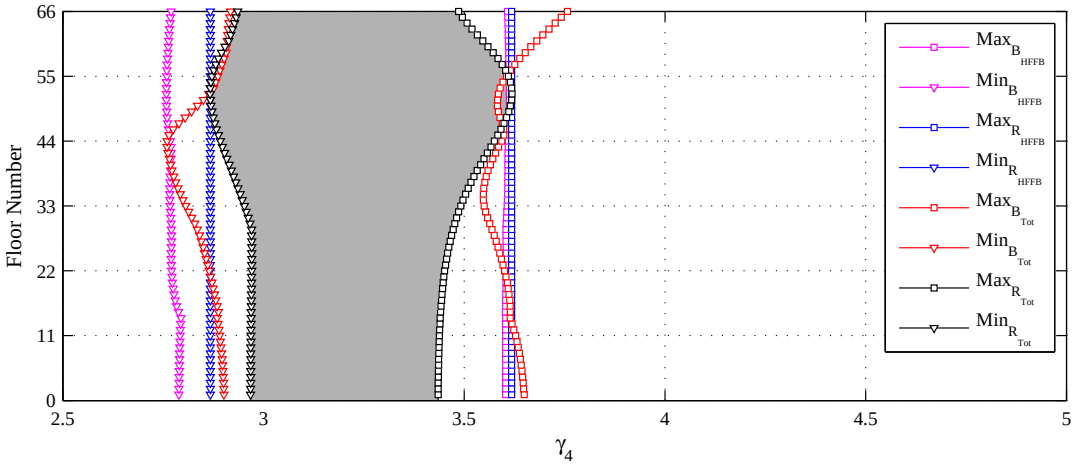

(b)

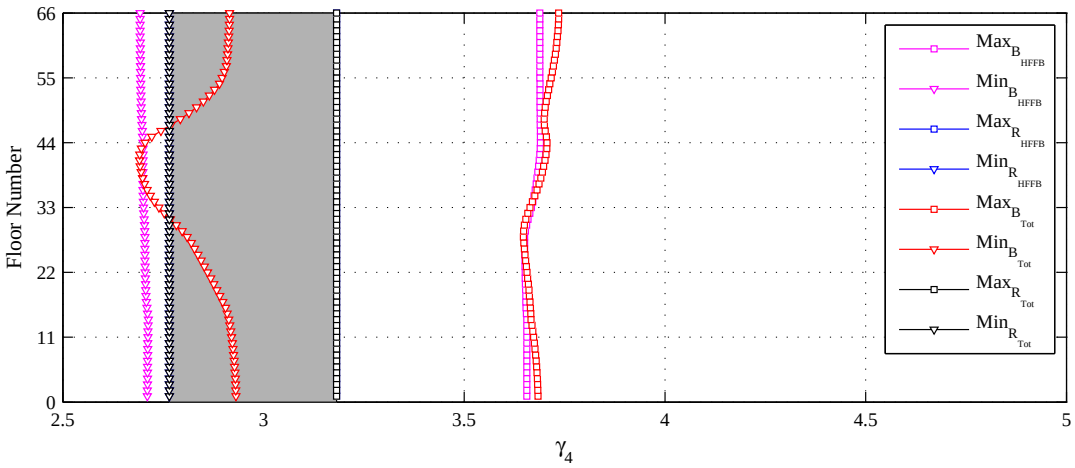

(c)

Figure 5.40: Extreme kurtosis over all wind directions: (a) acceleration X, (b) acceleration Y, (c) angular acceleration θ.

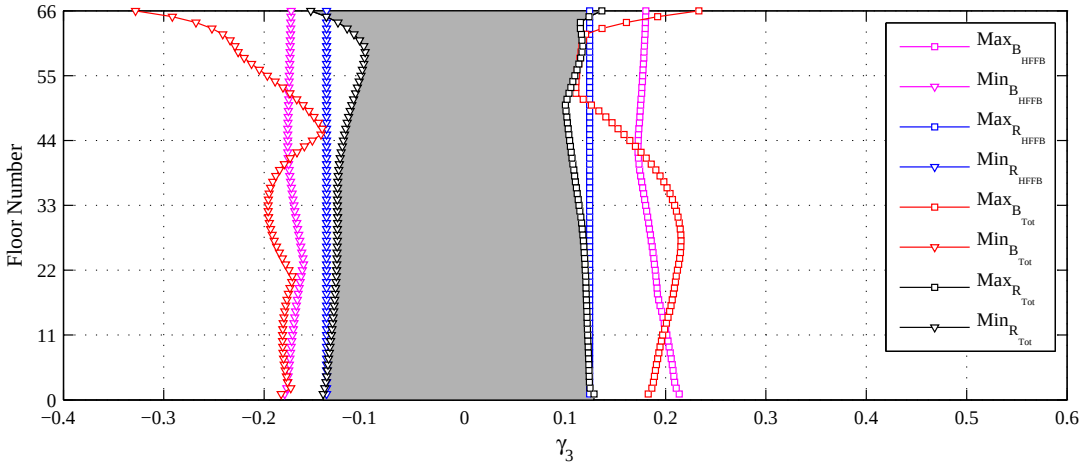

(a)

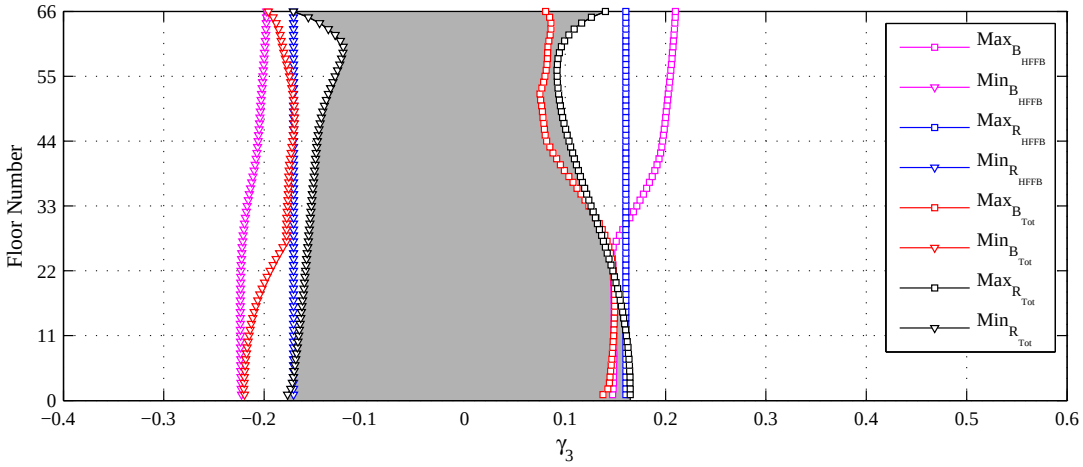

(b)

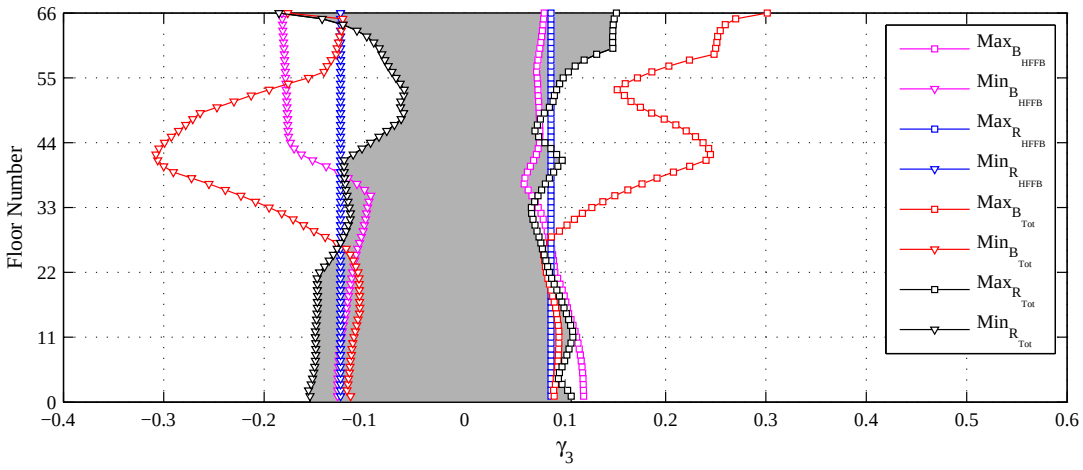

(c)

Figure 5.41: Extreme skewness over all wind directions: (a) bending moment X, (b) bending moment Y, (c) torque θ.

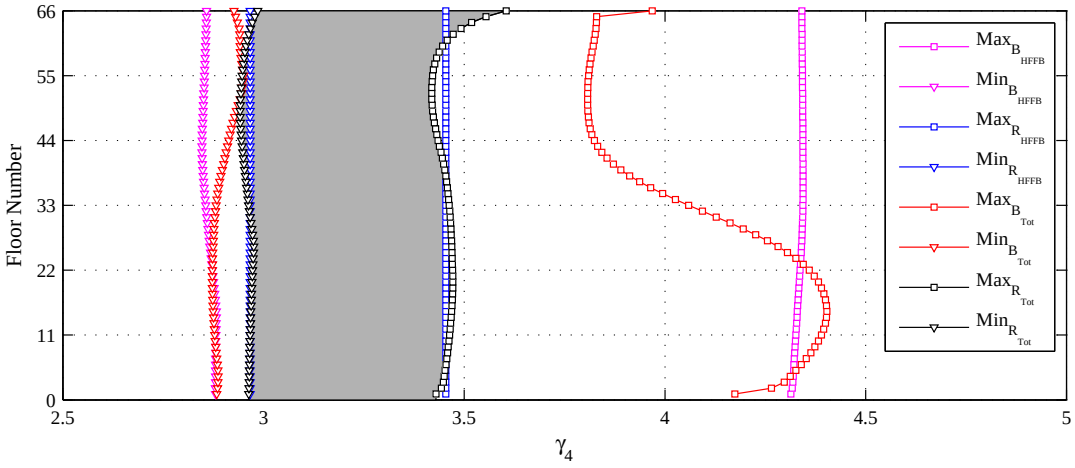

(a)

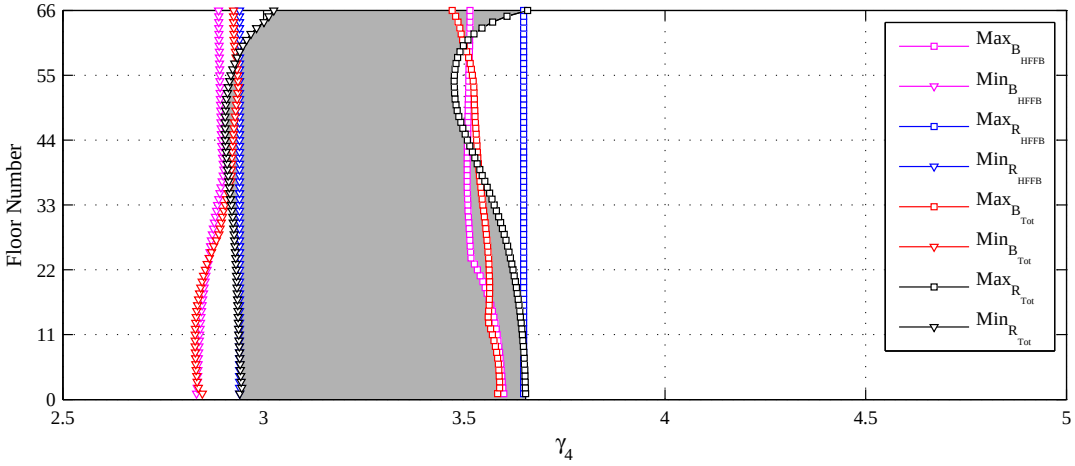

(b)

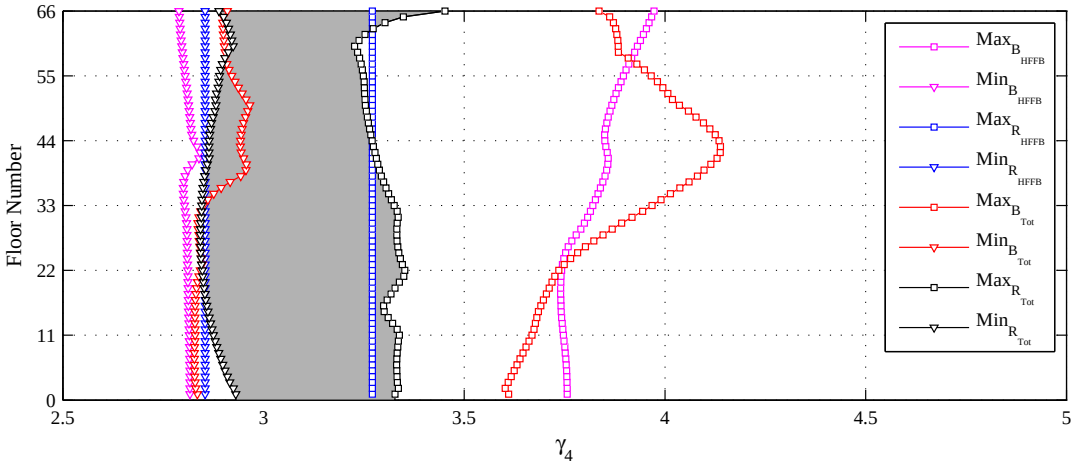

(c)

Figure 5.42: Extreme kurtosis over all wind directions: (a) bending moment X, (b) bending moment Y, (c) torque θ.

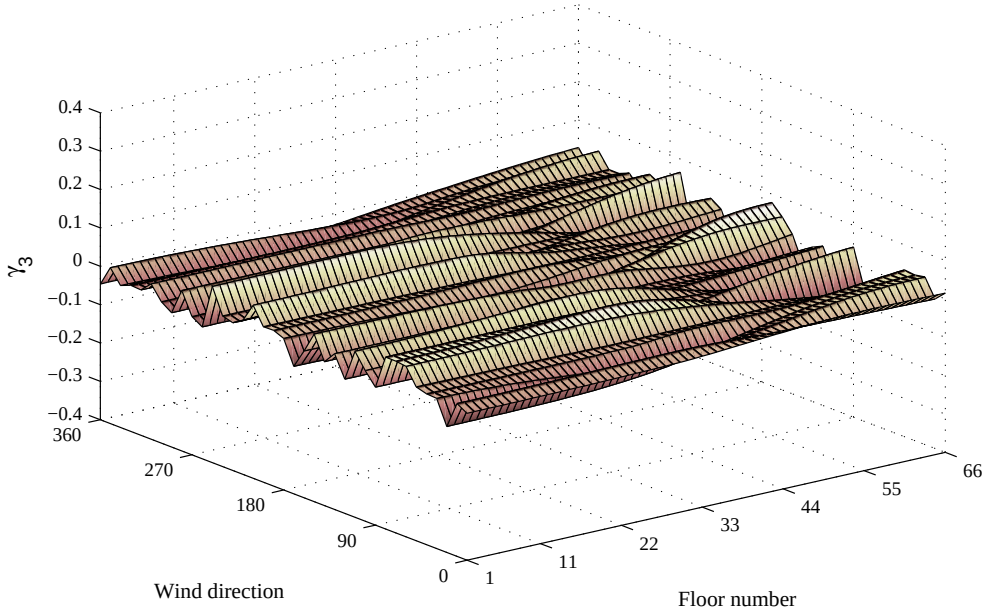

Figure 5.43: Skewness of the acceleration in direction X, Bank of China building.

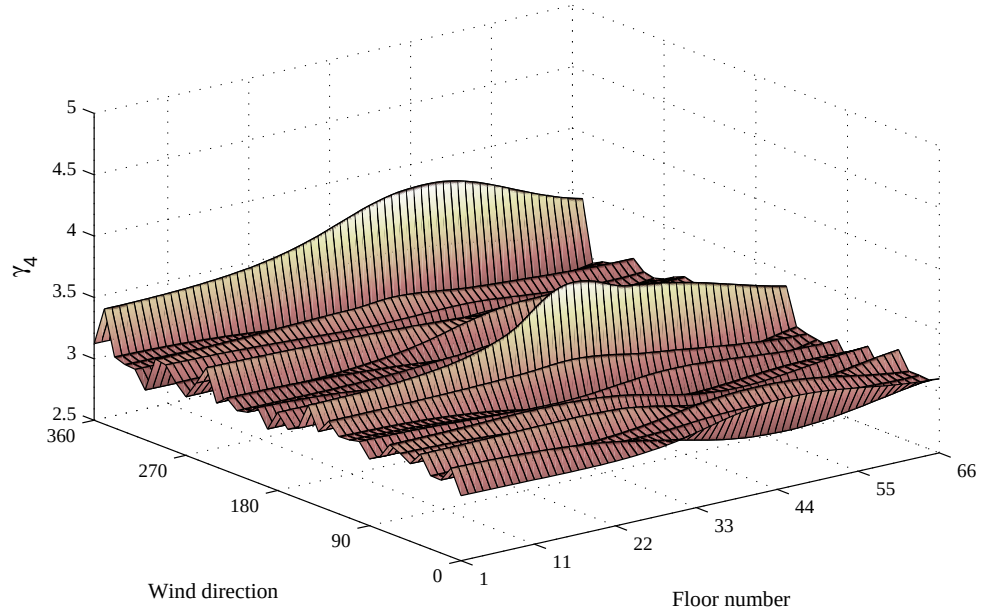

Figure 5.44: Kurtosis of the acceleration in direction X, Bank of China building.

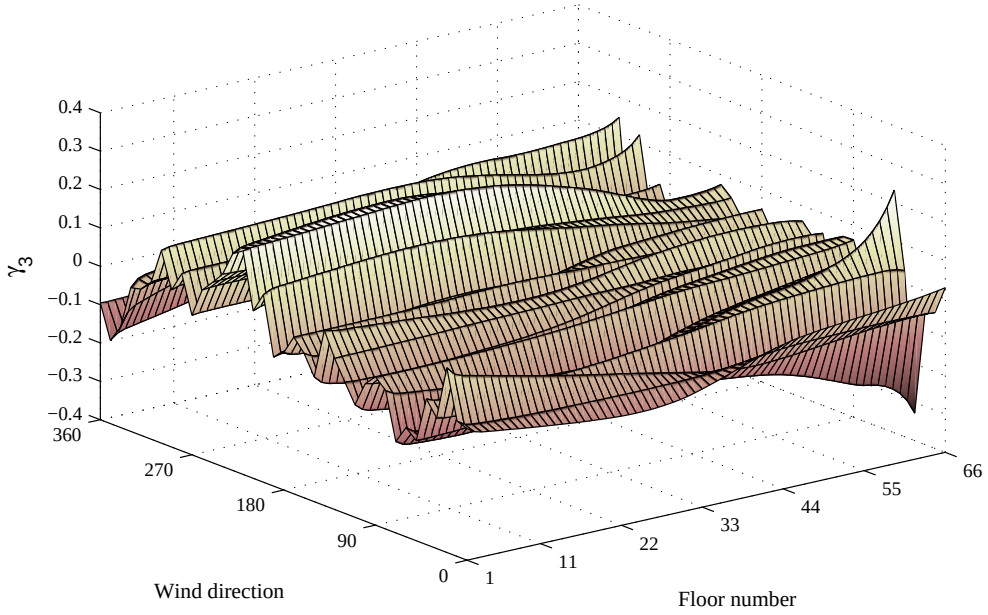

Figure 5.45: Skewness of the bending moment in direction X, Bank of China building.

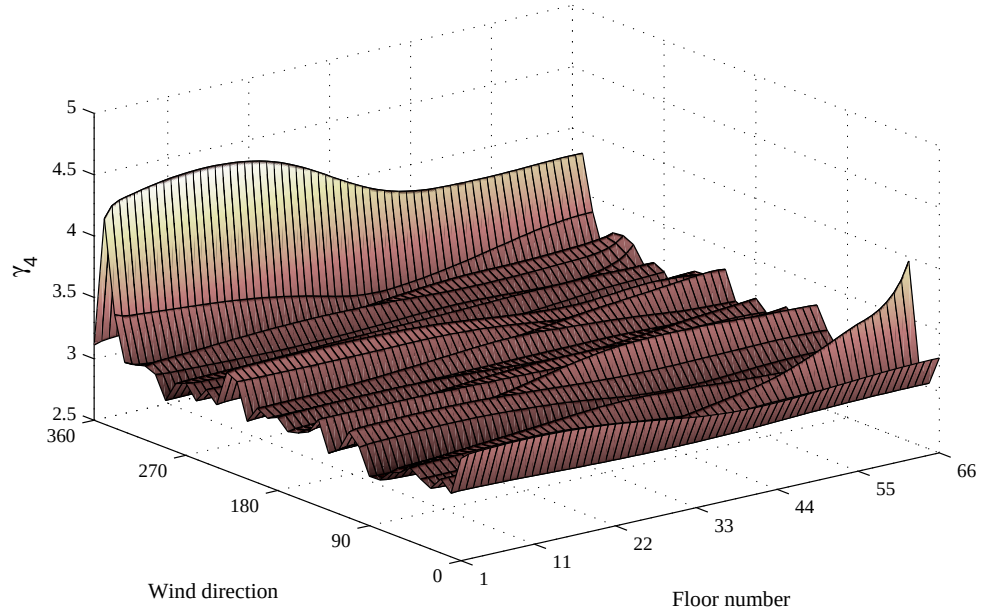

Figure 5.46: Kurtosis of the bending moment in direction X, Bank of China building.

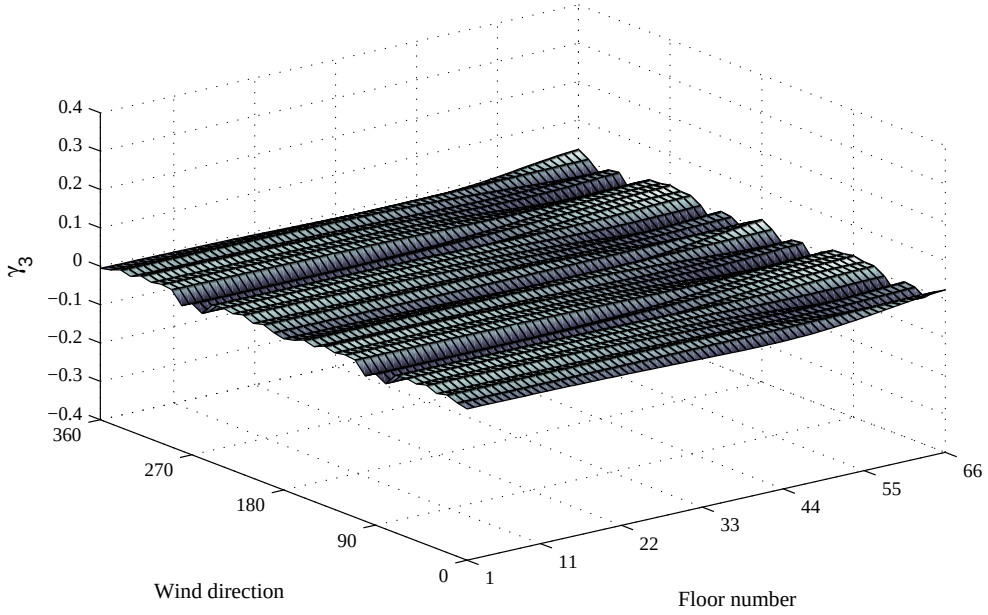

Figure 5.47: Skewness of the acceleration in direction X, regular building.

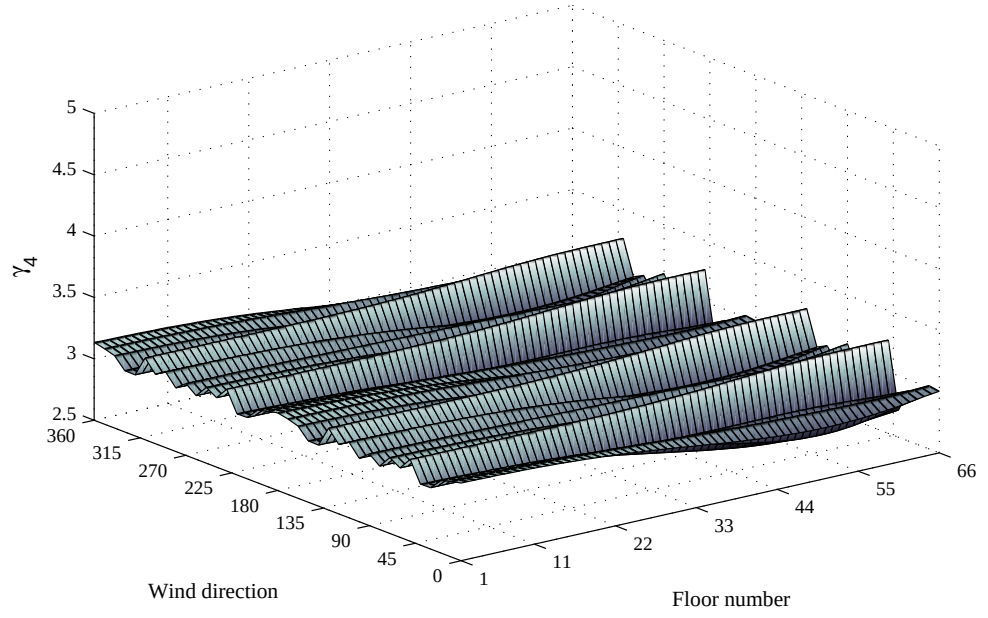

Figure 5.48: Kurtosis of the acceleration in direction X, regular building.

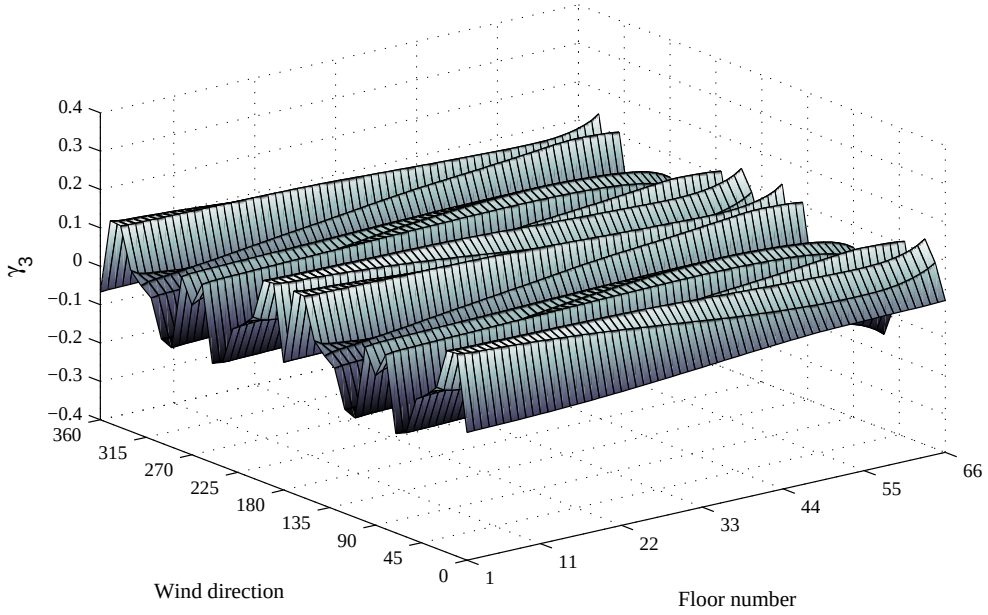

Figure 5.49: Skewness of the bending moment in direction X, regular building.

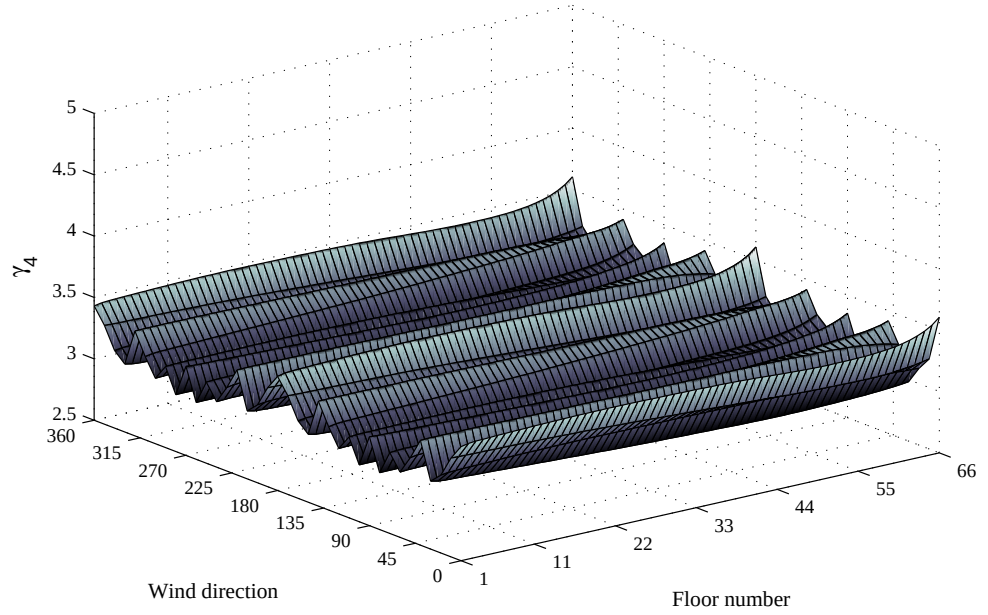

Figure 5.50: Kurtosis of the bending moment in direction X, regular building.

5.6.1 The background response and higher order moments

Figures 5.51 to 5.56 show the maximum and minimum skewness and kurtosis over all wind directions at each floor height for both systems. In particular the probabilistic nature of the total response, R_{Tot}, is compared to that obtained by considering only the resonant contribution of the fundamental modes, $R_{3r+Back}$. The responses considered are those of the previous section with the exception of the acceleration as this is a response dominated by contribution of the resonant component. What is clearly evident for both systems and all response components is that the inclusion of a complete background representation is fundamental if an accurate estimation of the true probabilistic response features is to be obtained. It is worth noting how once again the response of the uncoupled regular system is particularly well estimated from three resonant modes and a full background representation.

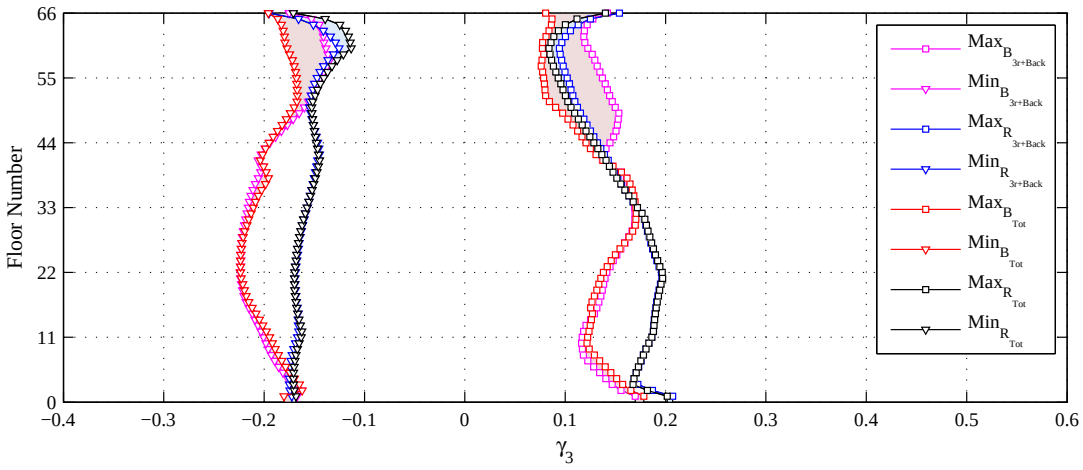

(a)

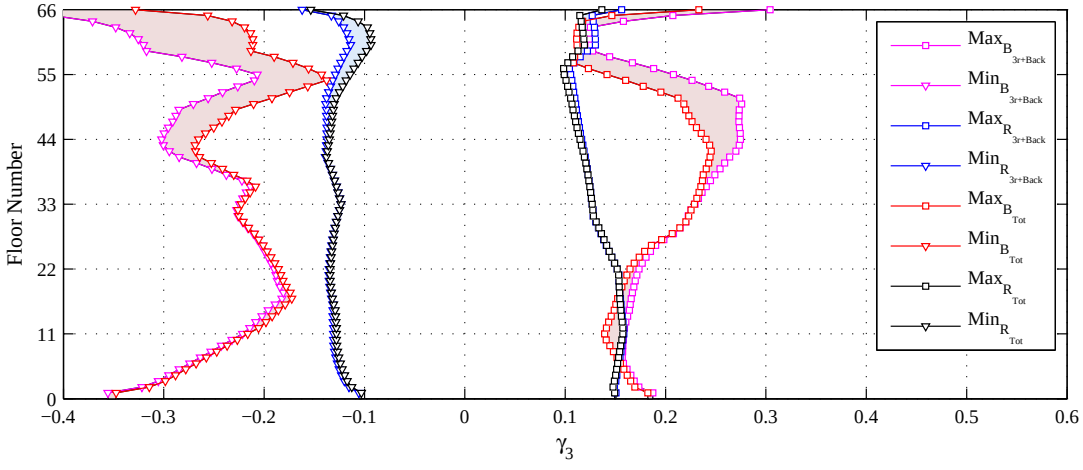

(b)

Figure 5.51: Extreme skewness over all wind directions: (a) shear X, (b) shear Y.

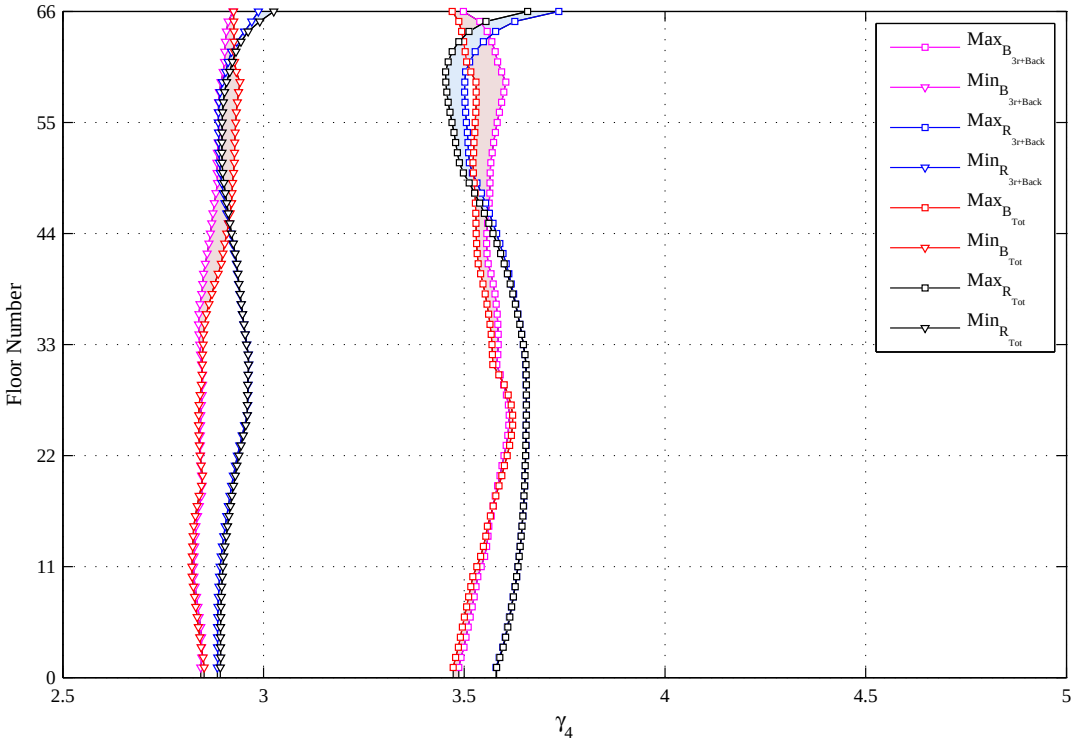

(a)

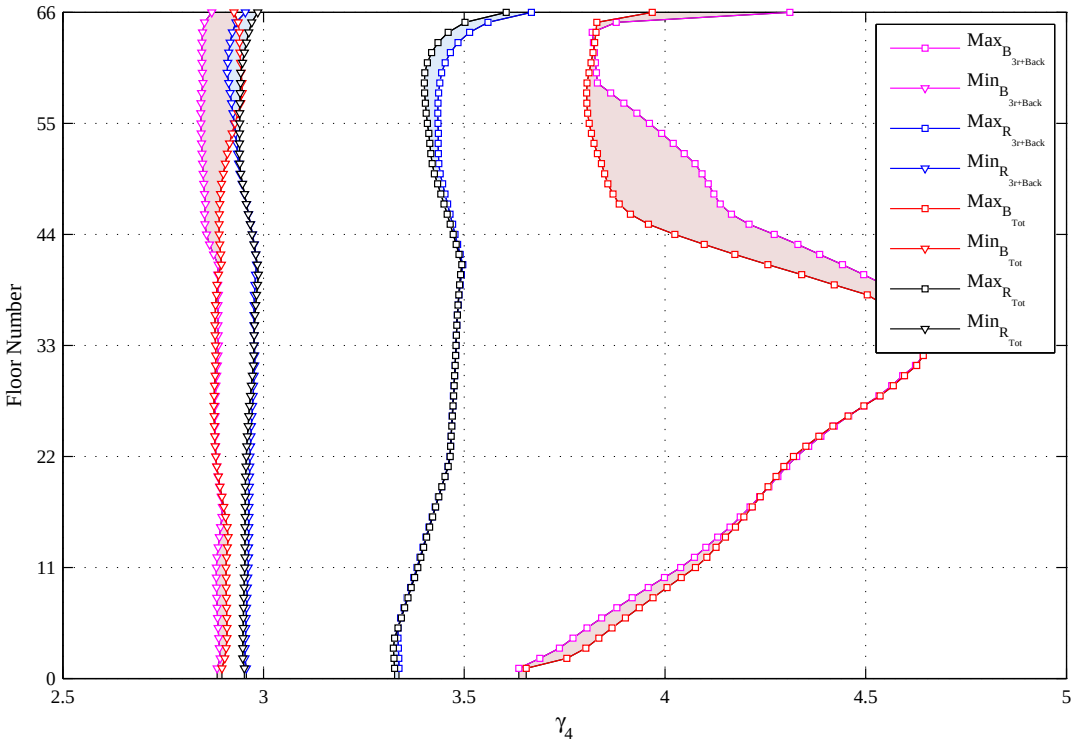

(b)

Figure 5.52: Extreme kurtosis over all wind directions: (a) shear X, (b) shear Y.

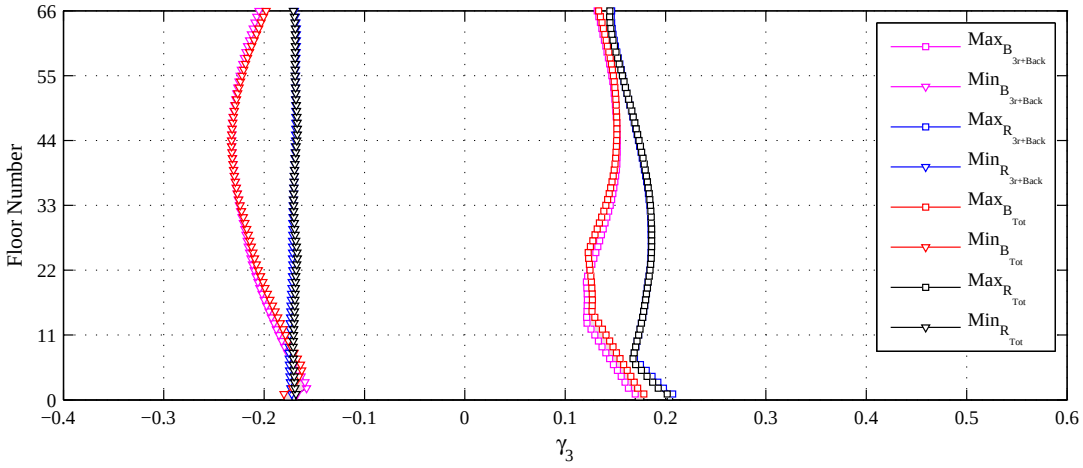

(a)

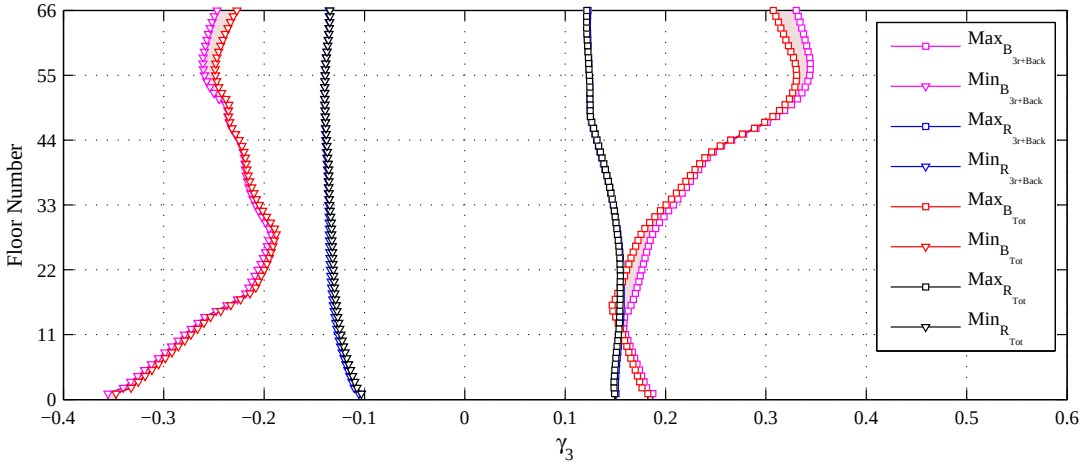

(b)

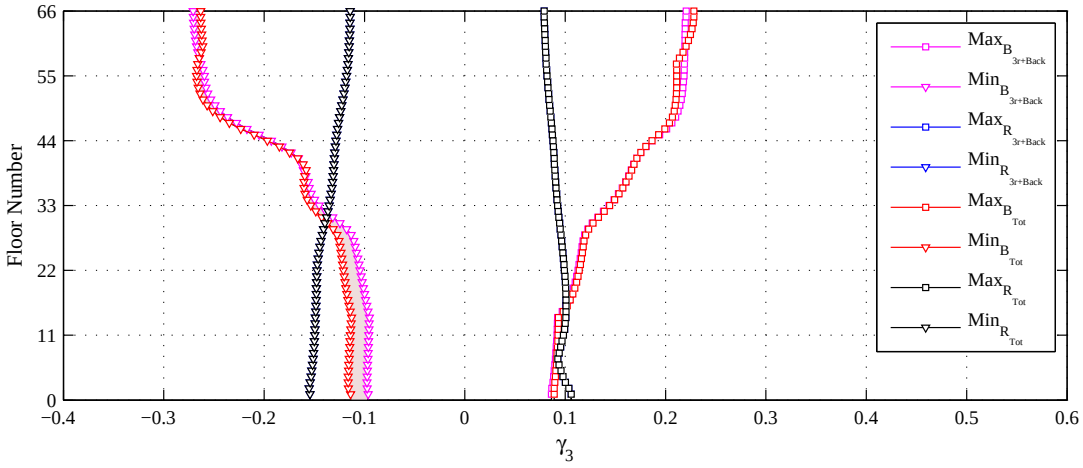

(c)

Figure 5.53: Extreme skewness over all wind directions: (a) displacement X, (b) displacement Y, (c) rotation θ.

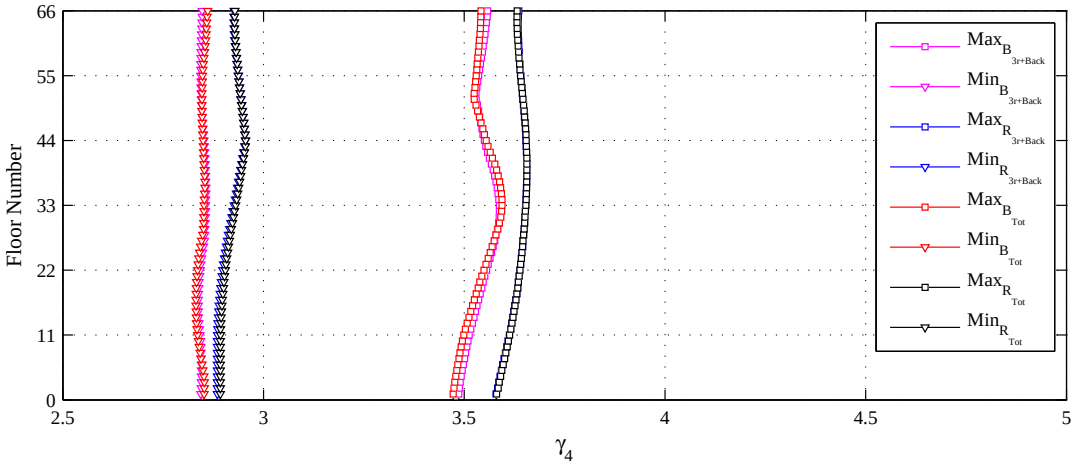

(a)

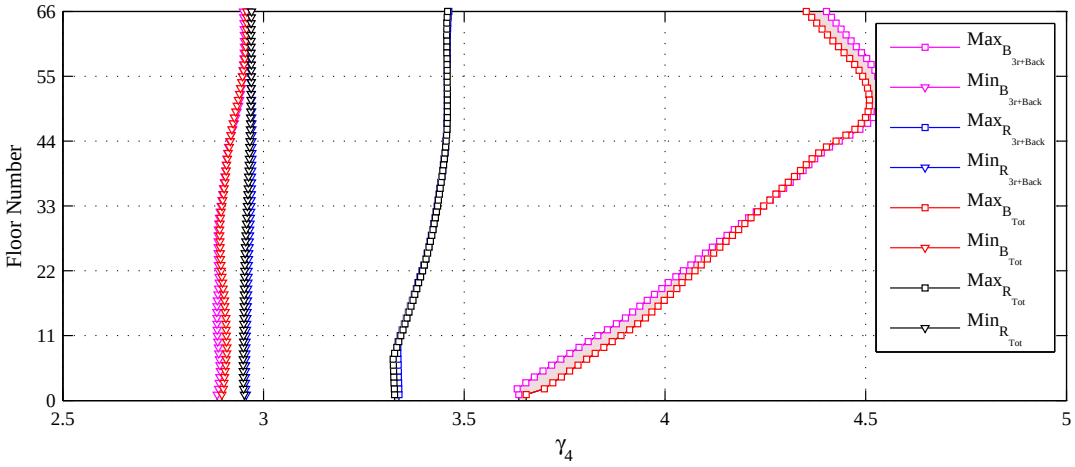

(b)

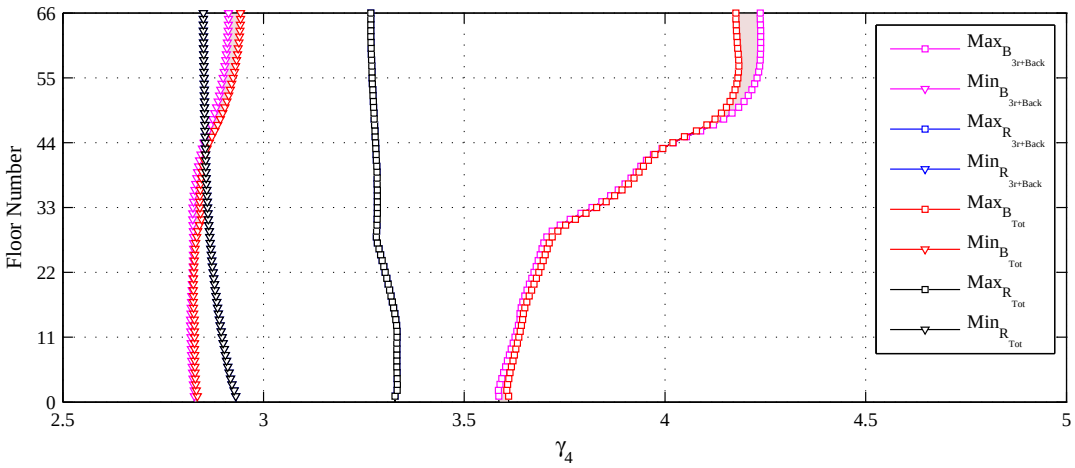

(c)

Figure 5.54: Extreme kurtosis over all wind directions: (a) displacement X, (b) displacement Y, (c) rotation θ.

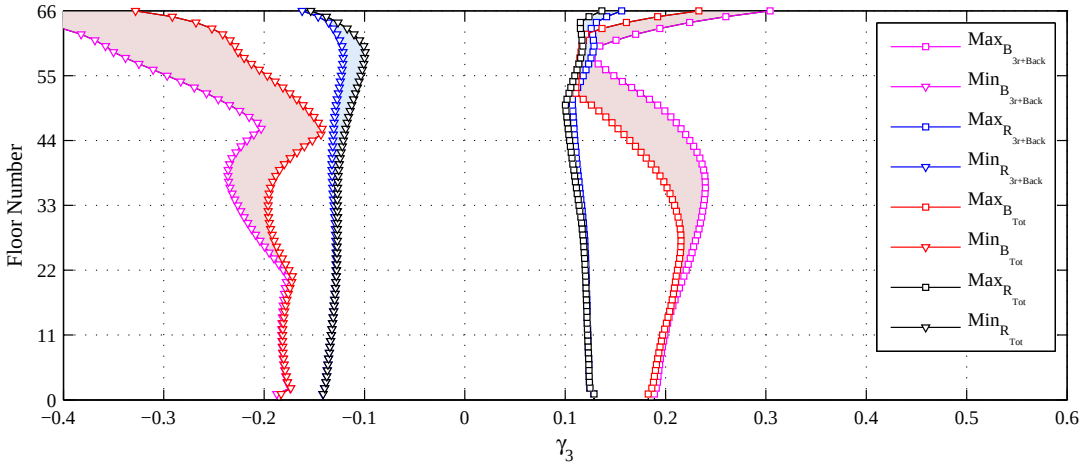

(a)

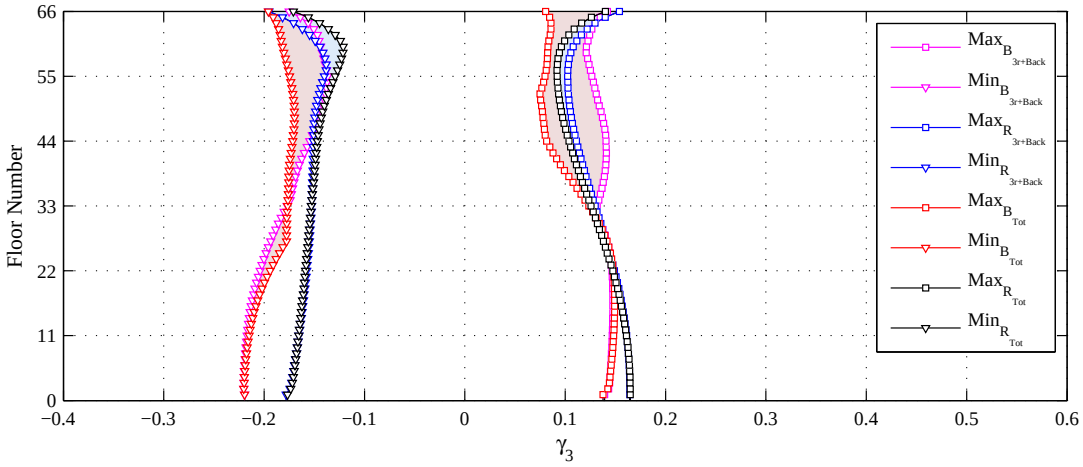

(b)

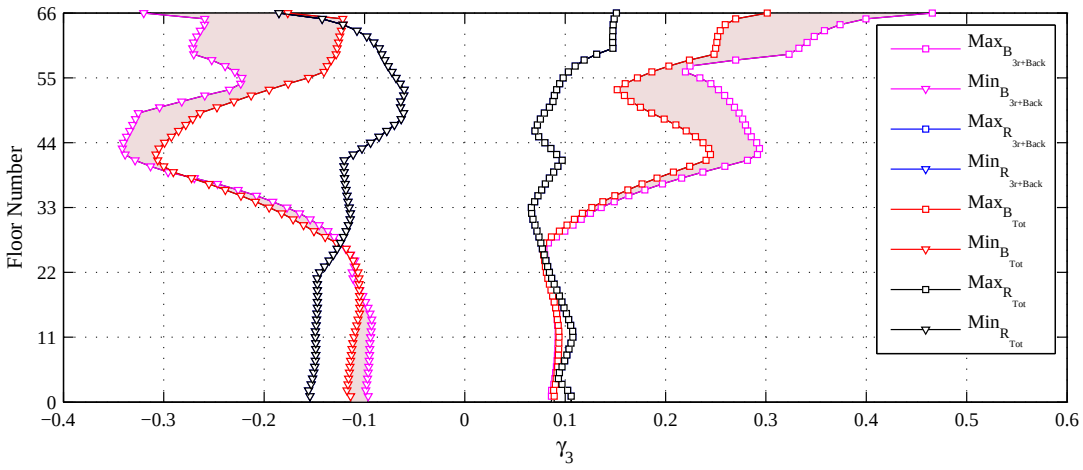

(c)

Figure 5.55: Extreme skewness over all wind directions: (a) bending moment X, (b) bending moment Y, (c) torque θ.

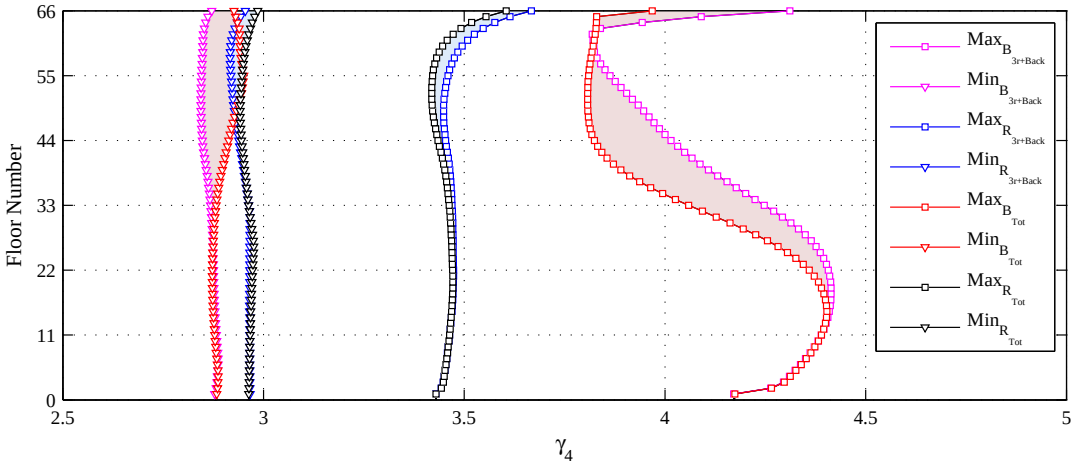

(a)

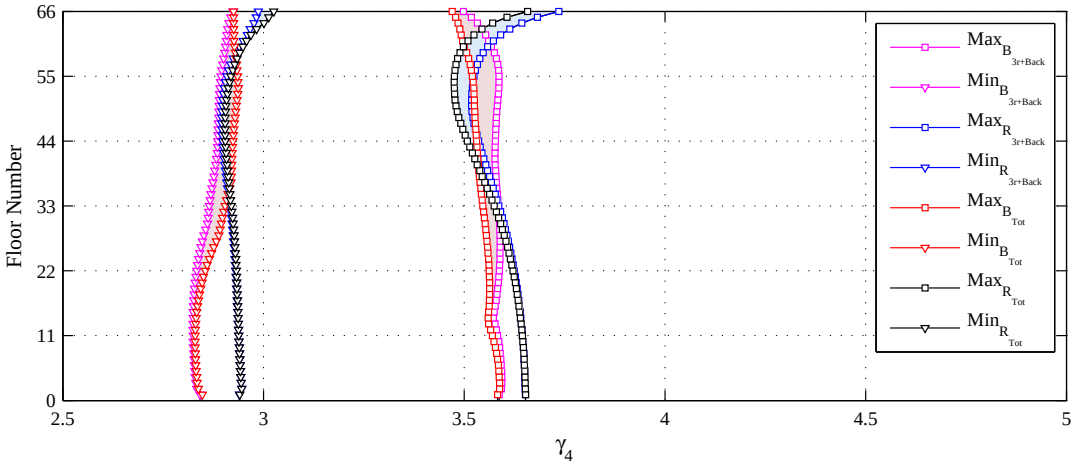

(b)

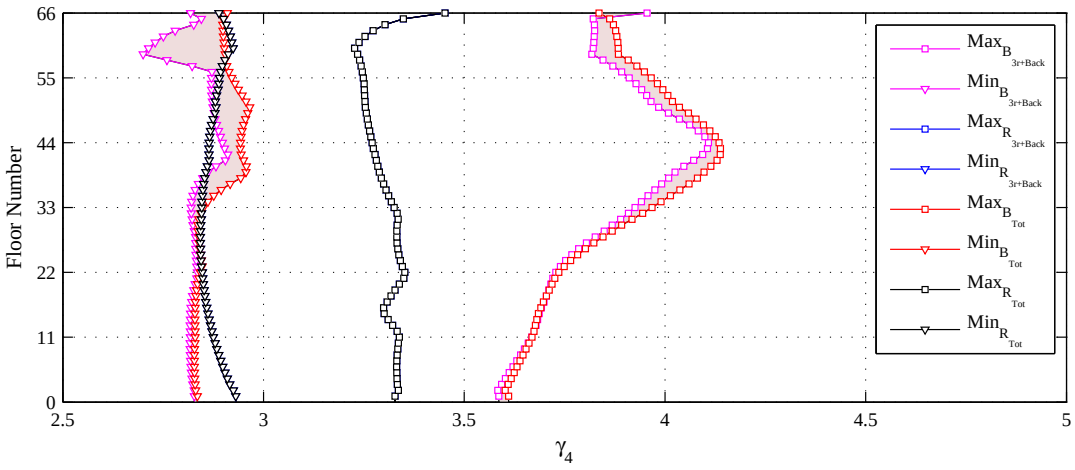

(c)

Figure 5.56: Extreme kurtosis over all wind directions: (a) bending moment X, (b) bending moment Y, (c) torque θ.

5.7 Concluding remarks

In this chapter it was shown that the global response of both regular tall buildings with uncoupled dynamic systems and irregular tall buildings with coupled dynamic systems are non-gaussian in nature. This behavior was observed for all important response components including the top floor acceleration, top floor displacements, bending moments, torque and shear forces. Values of the skewness were seen to vary between -0.5 and 0.5 while values of over 4.5 were seen in the case of the kurtosis. It was seen that these results are affected by higher modes which tend to increase the variability of the maximum and minimum skewness and kurtosis experienced over the height of the structure. It was also observed how a full background representation of the response, together with the resonant contribution of the fundamental modes, will guarantee a good representation of the non-gaussian response features. The non-gaussian nature of the response is particularly significant in light of the well established habit of considering the response of these types of structures gaussian while estimating the peak factors. This study would seem to indicate the necessity of adopting peak factor models capable of modeling non-gaussian processes.

This study also demonstrated the susceptibility of irregular tall buildings to the influence of higher modes on their response. In particular the top floor acceleration was seen to be very sensitive where errors were tripled if compared to the regular building. Also the importance of wind directionality on the errors committed by mode truncation was seen for all response components, with the exception of the base bending moments. The important role played by the correlation of the modal response was observed by the presence of both over- and underestimates sometimes occurring for the same response component by simply varying the incident wind direction or the floor at which the response was being calculated. The particular sensitivity of the torsional response to higher modes was significant with errors of up to 60% in the estimation of the RMS of the top floor torque. The importance of a complete background response representation in the case of a mechanically coupled building system was clearly seen. In particular, this result conveys an important consideration. While for traditional mechanically uncoupled and geometrically regular tall buildings the background response may be, to a certain extent, adequately estimated from fundamental modes, this is definitely not true for coupled geometrically irregular buildings. This result is particularly significant within the context of HFFB measurements where only the first three generalized forces can be estimated.

Bibliography

[5.1] D. W. Boggs and J. A. Peterka. Aerodynamic model tests of tall buildings. *Journal of Engineering Mechanics*, 115(3):618–635, 1985.

[5.2] C. M. Chan, J. K. L. Chui, and M. F. Huang. Integrated aerodynamic load determination and stiffness design optimization of tall buildings. *Struct. Design Tall Spec. Build.*, 2007.

[5.3] C. M. Chan, M. F. Huang, and K. C. S. Kwok. Stiffness optimization for wind-induced dynamic serviceability design of tall buildings. *Journal of Structural Engineering*, 135(8):985–997, 2009.

[5.4] X. Chen and A. Kareem. Coupled building response analysis using HFFB: Some new insights. In *Proc., 5th Bluff Body Aerodynamics and Applications (BBAAV)*. Ottawa, 2004.

[5.5] X. Chen and A. Kareem. Coupled dynamic analysis and equivalent static wind loads on buildings with three-dimensional modes. *Journal of Structural Engineering*, 131(7):1071–1082, 2005.

[5.6] X. Chen and A. Kareem. Dynamic wind effects on buildings with 3D coupled modes: Application of high frequency force balance measurements. *Journal of Engineering Mechanics*, 131(11):1115–1125, 2005.

[5.7] M. Gioffrè, M. Grigoriu, M. Kasperski, and E. Simiu. Wind-induced peak bending moments in low-rise building frames. *Journal of Engineering Mechanics*, 126(8):879–881, 2000.

[5.8] M. Gioffrè and V. Gusella. Peak response of a nonlinear beam. *Journal of Engineering Mechanics*, 133(9):963–969, 2007.

[5.9] M. Gioffrè, V. Gusella, and M. Grigoriu. Non-gaussian wind pressure on prismatic buildings I: Stochastic field. *Journal of Structural Engineering, ASCE*, 127:981–989, 2001.

[5.10] M. Grigoriu. Crossing of non-gaussian translation process. *Journal of Engineering Mechanics*, 110(4):610–620, 1984.

[5.11] J. D. Holmes, A. Rofail, and L. Aurelius. High frequency base balance methodologies for tall buildings with torsional and coupled resonant modes. In *Proceedings of the 11th International Conference on wind engineering*, pages 2381–2388. Texas Tech Univ., Lubbock, Texas, 2003.

[5.12] G. Huang and X. Chen. Wind load effects and equivalent static wind loads of tall buildings based on synchronous pressure measurements. *Engineering Structures*, 29:2641–2653, 2007.

[5.13] M. F. Huang, C. M. Chan, K. C. S. Kwok, and P. A. Hitchcock. Cross correlations of modal responses of tall buildings in wind-induced lateral-torsional motion. *Journal of Engineering Mechanics*, 135(8):802–812, 2009.

[5.14] P. A. Irwin and J. Xie. Wind loading and serviceability of tall buildings in tropical cyclone regions. In *Proc., 3rd AsiaPacific Symp. on Wind Engineering*. Univ. of Hong Kong, Hong Kong, 1993.

[5.15] A. Kareem. Wind-excited response of buildings in higher modes. *Journal of Structural Division, ASCE*, 107:701–706, 1981.

[5.16] D. K. Kwon, T. Kijewski, and A. Kareem. e-analysis of high-rise buildings subjected to wind loads. *Journal of Structural Engineering*, 134(7):1139–1153, 2008.

[5.17] Q. S. Li, K. Yang, C. K. Wong, and A. P. Jeary. The effect of amplitude-dependent damping on wind-induced vibrations of a super tall building. *Journal of Wind Engineering and Industrial Aerodynamics*, 91:1175–1198, 2003.

[5.18] E. Simiu. Equivalent static wind loads for tall building design. *Journal of Structural Division, ASCE*, 104:719–737, 1976.

[5.19] T. Tschanz. Measurement of total aerodynamic loads using elastic models with high natural frequencies. In *International Workshop on Wind Tunnel Modeling Criteria and Techniques in Civil Engineering Applications*. Gaithersburg, Maryland, 1982.

[5.20] P. J. Vickery, S. C. Steckley, N. Isyumov, and B. J. Vickery. The effect of mode shape on the wind induced response of tall buildings. In *Proceedings of the 5th United States National Conference on wind engineering*, pages 1B–41–1B–48. Lubbock, Texas, 1985.

[5.21] Y. L. Xu and K. C. S. Kwok. Mode shape corrections for wind tunnel tests of tall buildings. *Engineering Structures*, 15:618–635, 1993.

[5.22] D. Y. N. Yip and R. G. J. Flay. A new force balance data analysis method for wind response predictions of tall buildings. *Wind. Eng. Ind. Aerodyn.*, 54/55:457–471, 1995.

[5.23] Y. Zhou, A. Kareem, and M. Gu. Mode shape corrections for wind load effects. *Journal of Engineering Mechanics*, 128(1):15–23, 2002.

[5.24] Y. Zhou, T. Kijewski, and A. Kareem. Aerodynamic loads on tall buildings: Interactive database. *Journal of Structural Engineering*, 129(3):394–404, 2003.

Chapter 6

A Framework for Accurate Combination of Directional Aerodynamics and Wind Climatological Information

In this chapter a framework is presented that rigorously combines the directional characteristics of both the extreme wind climate and buildings aerodynamics in a component-wise reliability model that ensures consistent estimates of responses with specified mean recurrence intervals. In particular the proposed reliability model introduces limit state functions with specified vulnerability levels. This allows for the identification of limit states, in terms of the maximum mean wind speeds for each wind direction, that allow for the rigorous estimation of the response levels with specified mean recurrence intervals through the resolution of time-invariant reliability integrals.

The proposed model is compared to traditional methods commonly adopted in the wind analysis of tall buildings. In particular both non directional and directional methods are compared to the proposed approach for a 74 floor planar frame analyzed in a fully three dimensional extreme wind environment. The results seem to highlight the inadequacy of traditional approaches for accurately estimating responses with specified mean recurrence intervals.

6.1 Introduction

In the wind induced analysis of tall buildings it is common to assume that the Mean Recurrence Interval (MRI) or inverse of the annual probability of failure of a critical load effect may be estimated as the MRI of the mean wind speed causing

the response level [6.23, 6.14, 6.4, 6.5, 6.6]. This assumption neglects the inherently directional characteristics of wind climate even though it is a known fact that wind climates often have strong directional properties [6.19, 6.17, 6.8, 6.20]. Indeed, the non directional assumption becomes problematic during the combination of directional aerodynamics with what is actually a directional wind climate. The simplest way around this is to consider the most severe aerodynamic direction alongside the non directional climate model and define a directional factor that accounts for the improbable occurrence of such an event (see chapter 1 and [6.2]). While this procedure could be considered adequate for most structures, it is generally not acceptable for dynamically sensitive structures, such as tall buildings, which are far more sensitive to wind direction [6.22]. For this reason, during the wind analysis of such structures, wind direction must be accounted for in some way. A common procedure often adopted is the sector-by-sector approach (see chapter 1 and [6.20]). However, this method has been demonstrated to strictly underestimate the response with a Mean Recurrence Interval of interest [6.18].

In this chapter a framework is presented for the rigorous estimation of all critical wind induced responses. In particular a component wise-reliability model is adopted [6.16]. The method rigorously combines the directional characteristics of both the wind climate and the building aerodynamics through the introduction of limit state functions with specified vulnerability levels for each critical load effect. This yields limit states in terms of level cut sets of response surfaces with prescribed vulnerability containing the mean wind speeds that cause a specific critical response to assume a level with specified MRI. Moreover, from the application of the proposed model to a full scale tall building situated in an extreme wind climate, it is seen how the actual mean wind speeds causing a response with specified MRI bear very little resemblance to the directional/non directional wind speeds with the same MRI. The results of this chapter would seem to imply the insufficiency of commonly adopted models for the estimation of wind induced responses of tall buildings with specified MRIs.

6.2 Wind and reliability models

6.2.1 Directional wind model

As described earlier, a shortcoming of the traditional approach to the definition of an extreme wind climate is the neglection of its directional characteristics. Therefore an appropriate directional model is required.

In this work the model described in [6.12, 6.13] is adopted. This model is based on assuming the random arrival times, $T_1 < T_2 < ...$, of the extreme wind storms at a particular location to be jump times of an homogeneous Poisson process, $N(t), t > 0$, of intensity $\upsilon > 0$, where the intensity υ of the Poisson process N is directly estimated from the data and represents the average number of extreme events expected

during the epoch of a year. Therefore the average number of extreme wind events during a time, $t > 0$, is equal to the expectation $E[N(t)] = \upsilon t$. Each event, and therefore point of the Poisson process, is defined by a W_d-dimensional wind speed vector, $\mathbf{V}(k)$, whose coordinates, $V_{k,i}, i = 1, 2, ...Ws_d$, are the maximum mean wind speeds, for a certain averaging time, recorded in W_d directions during the kth extreme wind event. In this way the model rigorously accounts for the directional characteristics of the extreme wind climate. If K extreme events are recorded for the location of interest the wind climate will be defined by the wind speed vectors $\mathbf{V}(k)$, $k = 1, 2, ...K$. From these wind vectors a directional extreme joint probability density function, $p(\bar{V}, \alpha)$, can be fitted.

6.2.2 Vulnerability model

Vulnerability may be defined as the sensitivity of a building to an extreme event in terms of damage [6.3]. In other words it expresses the probability of having structural damage once a hazardous event has occurred with a given energy content. Vulnerability is an integral part of the Performance-Based Design (PBD) philosophy commonly adopted in seismic design and analysis of buildings but sparingly used in the design of wind excited structures. The PBD philosophy may be effectively synthesized through the following equation [6.15]:

$$P(DV) = \int\int\int P(DV|DM)|dP(DM|EDP)||dP(EDP|IM)|dP(IM) \quad (6.1)$$

where IM (Intensity Measure) is an appropriate measure of the magnitude of the extreme wind event; EDP (Engineering Design Parameter) is a parameter representing the structural response; DM (Damage Measure) is a parameter denoting the level of damage; DV (Decision Variable) represents a parameter that determines the design decisions (for example a limit state); $P(*)$ denotes a probability of exceedance while $P(*|*)$ denotes a conditional probability of exceedance.

In equation 6.1 the term $P(EDP|IM)$ represents the probability of exceedance of a given limit state or performance objective while the term $P(DM|EDP)$ represents the probability of exceedance of a certain damage level given a response level. Their product may be identified as a measure of vulnerability and therefore:

$$\text{Vulnerability} = P(DM|EDP)P(EDP|IM) \quad (6.2)$$

By taking a damage measure coincident with an EDP the vulnerability is simply given by:

$$\text{Vulnerability} = P(EDP|IM) \quad (6.3)$$

and therefore the conditional probability of exceeding a particular structural response level given a certain hazard level. It is therefore this conditional probability that is of interest if the vulnerability of the system is to be evaluated.

In particular, concerning wind excited structures, the external pressure wind field acting on the surface of a tall building of height H may be characterized by the following pressure coefficients (see chapter 4):

$$\mathcal{C}_p(t) = \frac{\mathcal{P}(t, \bar{V}_H, \alpha) - \mathcal{P}_H(t, \bar{V}_H, \alpha)}{\frac{1}{2}\rho_a \bar{V}_H^2} \tag{6.4}$$

were $\mathcal{P}(t)$ is the total pressure, $\mathcal{P}_H(t)$ the static pressure at H, ρ_a the mass density of air, V_H the mean wind velocity at H while α is the incident wind direction. Through integration the pressure coefficients the forcing functions, $\mathbf{f}$, acting on the structural system can be estimated (see chapter 4) yielding the following dynamic equilibrium problem:

$$\mathbf{M}\ddot{\mathbf{z}}(t) + \mathbf{C}\dot{\mathbf{z}}(t) + \mathbf{K}\mathbf{z}(t) = \mathbf{f}(t, \bar{V}_H, \alpha) \tag{6.5}$$

where $\mathbf{z}$ is the response vector while $\mathbf{M}$, $\mathbf{C}$ and $\mathbf{K}$ are the mass, damping and stiffness matrices respectively. The dependency of $\mathbf{f}(t, \bar{V}_H, \alpha)$ on the maximum mean wind speed and wind direction implies the dependency of the response vector on these last. Therefore, given a generic response of interest R and associated performance objective in terms of a limit state, LS_R, the following limit state function, G_R, may be defined:

$$G_R = LS_R - R(\bar{V}_H, \alpha, \mathbf{z}, \dot{\mathbf{z}}, \ddot{\mathbf{z}}, t) \tag{6.6}$$

Obviously $\bar{V}_H$ and α are time independent random variables that can be used to define the intensity measure (IM) of the extreme wind event. Under this hypothesis the conditional probability of equation 6.3 defining the vulnerability of the structural system is given by the resolution of the following time-variant reliability problem:

$$G_R(\mathbf{z}, \dot{\mathbf{z}}, \ddot{\mathbf{z}}, t)|_{\bar{V}_H, \alpha} < 0 \quad \forall t \in [0, T] \tag{6.7}$$

where T is the time interval in which the probability of failure is to be evaluated conditional on $(\bar{V}_H, \alpha)$. An upper bound on this failure probability, first excursion probability, can be estimated through the calculation of the mean crossing rate through the threshold level LS_R of the stochastic process $R(t)$ and therefore from the resolution of the Rice's formula:

$$\nu(LS_R; t) = \int_{-\infty}^{\infty} |x| p_{R\dot{R}}(LS_R, x; t) dx \tag{6.8}$$

where $p_{R\dot{R}}(LS_R, x; t)$ is the joint probability density function of $\{R(t), \dot{R}(t)\}$ while $\nu(LS_R; t)$ is the mean crossing rate. It should be observed that this will give a good approximation of the probability failure only if the threshold is relatively high [6.16] which is the case of most practical applications including the structural systems of interest to this work. Because the stochastic process $R(t)$ may be considered stationary for wind induced responses, from the knowledge of the crossing rate, the

peak factor with specified failure probability, $g_{\%}$, may be calculated, as can the associated response level from:

$$R_{\text{peak},\%}|_{\bar{V}_H,\alpha} = \mu_R + g_{\%}\sigma_R \tag{6.9}$$

where μ_R is the mean response while σ_R is the standard deviation of $R(t)$. Equation 6.9 represents the response level associated with the vulnerability level specified through the failure probability of the peak factor $g_{\%}$. Of particular interest are the limit state functions, $G_{R,\%}(\bar{V}_H, \alpha)$, with specified vulnerability levels. It should be observed that any non gaussian response features may be included by considering appropriate peak factor models such as those reported in [6.11, 6.9, 6.10].

6.2.3 Global time invariant model

As mentioned, vulnerability represents the probability of failure conditional on a given hazard level. However, for the design of structures, once an acceptable vulnerability level has been fixed, it is the probability of failure over all hazard levels that is of interest. By fixing a vulnerability level, indicated by the symbol $\tilde{}$, the limit state function of equation 6.7 may be written as:

$$\tilde{G}_R(\mathbf{v}, \mathbf{x}) = LS_{\tilde{R}} - \tilde{R}(\mathbf{v}, \mathbf{x}) \tag{6.10}$$

where $\mathbf{v} = (\bar{V}_H, \alpha)$ is the vector of random variables indicating the hazard intensity while $\mathbf{x} = (x_1, x_2, ...)$ is the vector of deterministic variables. Having fixed the vulnerability level this is now simply a time invariant component reliability problem, the solution of which is given by [6.16]:

$$P_{f,\tilde{R}}(\mathbf{x}) = \int_{\tilde{G}_R(\mathbf{v},\mathbf{x})<0} p_{\mathbf{v}}(\mathbf{v}) d\mathbf{v} \tag{6.11}$$

where $\tilde{P}_{f,R}(\mathbf{x})$ is the searched after failure probability of the response component R while $p_{\mathbf{v}}(\mathbf{v})$ is the joint probability density function of $\mathbf{v}$. This may be written in function of the MRI, $y_{LS_{\tilde{R}}}$, associated with the exceedance of the limit state $LS_{\tilde{R}}$ of the response R with assigned vulnerability as:

$$P(\tilde{R} > LS_{\tilde{R}}) = 1 - \left[\int_0^{\bar{V}_H^{LS_{\tilde{R}}}} \int_0^{2\pi} p(\bar{V}_H, \alpha) d\bar{V}_H d\alpha \right]^{\upsilon} = \frac{1}{y_{LS_{\tilde{R}}}} \tag{6.12}$$

where $p(\bar{V}_H, \alpha)$ is the joint probability density function of the directional extreme wind climate of section 6.2.1 with intensity υ while $\bar{V}_H^{LS_{\tilde{R}}}$ is the level cut set containing all those wind speeds associated with the limit state $LS_{\tilde{R}}$ and shown in Figure 7.1. The geometric meaning of the double-fold integral of equation 6.12 is shown in Figure 6.2.

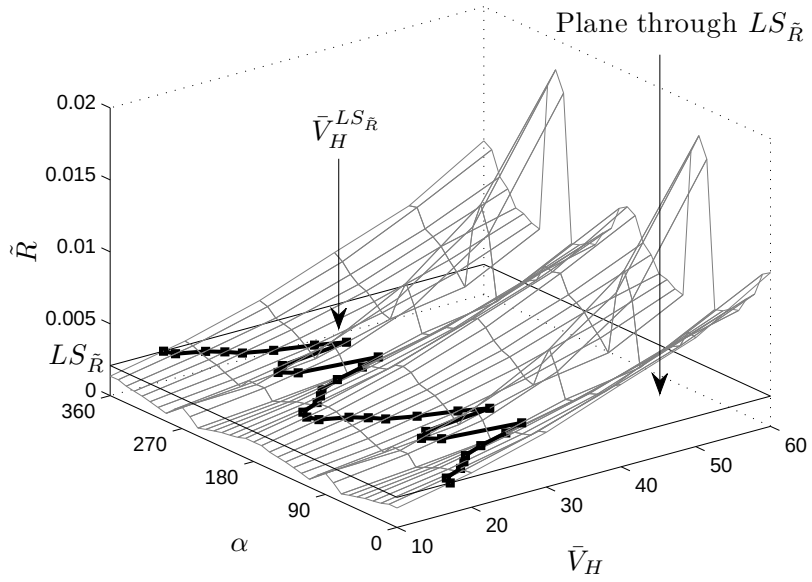

Figure 6.1: $\tilde{R}(\mathbf{v}, \mathbf{x})$ with prescribed vulnerability and the associated limit state.

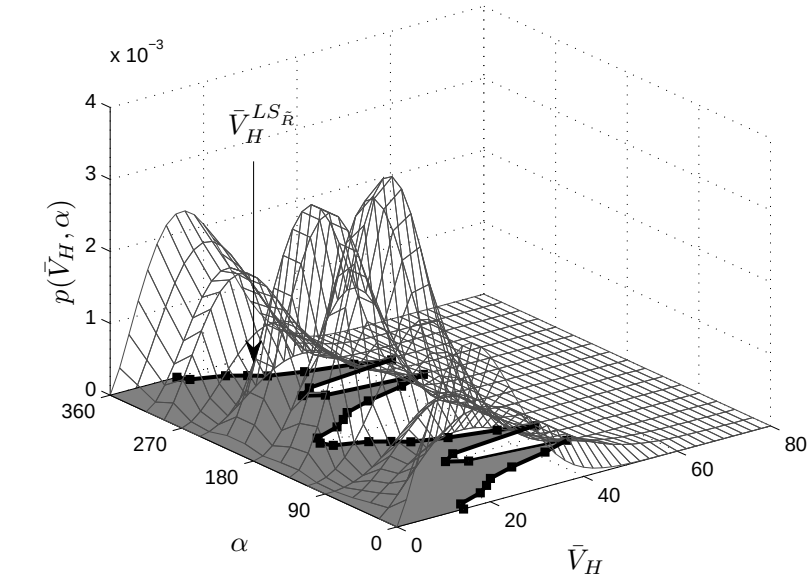

Figure 6.2: Extreme joint probability density function, $p(\bar{V}_H, \alpha)$, and the integration domain.

6.2.4 Algorithm

In this section an efficient algorithm is presented for the calculation of the failure probability distribution of equation 6.12.

After appropriate scaling [6.21, 6.20], the wind speed vectors can be represented as a $K \times W_d$ matrix $\bar{\mathbf{V}}_H$ of hourly averaged wind speeds at the top of the building. Given the response R, for each extreme wind event k, it is then necessary to evaluate the peak of the response with specified vulnerability or first excursion probability over all wind directions, $\tilde{R}_k^{max} = \max_{i=1,2...W_d}[\tilde{R}_k(\bar{V}_{H,k}, i)]$ where $\tilde{R}_k$ can be derived from the knowledge of the response surface of R with prescribed vulnerability,˜, see figure 7.1. Obviously the response surfaces will be calculated in a discrete number of points and then interpolated for other values. Therefore the resolution of the surfaces is important for obtaining accurate estimates of $\tilde{R}_k$.

From the maximum response, $\tilde{R}_k^{max}$, the time series of maximum values of the response $\tilde{R}$ in each extreme wind event can be expressed as a $1 \times K$ vector $\tilde{\mathbf{R}}_{max}$. Let the elements of this vector be sorted in descending order, so that $\tilde{R}_1^{max} = \max(\tilde{\mathbf{R}}^{max})$. The probability that the response $\tilde{R}$ will exceed the nth ranked value in any given extreme wind event can then be estimated as follows:

$$P(\tilde{R} > \tilde{R}_n^{max} | \text{ 1 event}) = \frac{n}{1+K} \tag{6.13}$$

As mentioned the wind speed model is based on the assumption that the frequency of the extreme wind events are governed by a Poisson process with constant occurrence rate. It is therefore consistent to make the same assumption in computing the annual probability of exceedance of $\tilde{R}_n^{max}$ based on the probability of exceedance per extreme wind event given in (6.13), whereby the following result is obtained [6.21]:

$$P(\tilde{R} > \tilde{R}_n^{max} | \text{ 1 year}) = 1 - \exp\left(\frac{-\upsilon n}{1+K}\right) \tag{6.14}$$

The MRI, $y_{\tilde{R}_n^{max}}$, associated with the exceedance of $\tilde{R}_n^{max}$ is then given by the inverse of this annual probability

$$y_{\tilde{R}_n^{max}} = \left[1 - \exp\left(\frac{-\upsilon n}{1+K}\right)\right]^{-1} \tag{6.15}$$

Through interpolation it is then possible to estimate the response or limit state, $LS_{\tilde{R}}$, corresponding to any MRI, $y_{LS_{\tilde{R}}}$, of interest. To get a good estimation of $LS_{\tilde{R}}$ a large number of wind speed vectors $\mathbf{V}(k)$ $k = 1, 2, ...K$ are needed. Historical data for most sites is unlikely to be sufficient. To overcome this the wind speed vectors can be increased through simulation and therefore the calibration appropriate probabilistic models. Methods for this purpose have been proposed for various extreme wind climates [6.12, 6.13].

6.3 Case study

6.3.1 Building description

The planar frame considered in this application is taken from a full 3D model of a regular 74 story tall building with a typical story height of 3.98 m. The original structure is a steel outrigger framework. The planar frame considered is one of the inner frames, part of the steel core and connected to the external tube through three outriggers placed at 1/3 and 2/3 of the height as well as at the top of the building (figure 6.3). The central frame is stiffened through a series of diagonals. All beams are rigidly connected to the columns while the diagonals and K-bracing are simply connected. The outriggers are also simply connected. The beams and diagonals are American AISC standard wide-flange W sections [6.1]. The initial beam sizes are W24 $\times$ 176 while the diagonals are W14 $\times$ 370. The columns and outriggers are steel box sections of flange thickness 1/20 of the mid-line diameter. The frame is analyzed in the vertical plane parallel to the global x-direction. The nodes at each floor level of the frame are rigidly connected concerning translations in the global x-direction simulating the presence of the rigid floor diaphragms. The rigid connections do not apply to z-direction translations or rotations around the y-axis.

The directional aerodynamic wind induced translational forces at the geometrical center of each floor are estimated from the wind tunnel tests of chapter 4. In particular the forcing functions derived in section 4.2.3 for the regular building are considered. The intensity of the loads acting on the frame are taken as 1/3 of the x-direction loading. Appropriate scaling is considered during the construction of the response surfaces.

6.3.2 Limit state functions

Inter-story drift ratio

The global response of interest in the design of the frame is the inter-story drift ratio d_{jx}, where $j = 1, ..., 74$ floor number, defined as the relative displacement in the global x-direction (figure 6.3) between two adjacent floors normalized with respect to their distance.

The limit state function of the inter-story drift $G_{d_{jx}}(\mathbf{v}, T)$ will assume the following form:

$$G_{d_{jx}}(\mathbf{v}, T) = LS_{d_j} - \left(\mu_{d_{jx}}(\mathbf{v}) + g_{d_{jx}}(\mathbf{v}, T)\sigma_{d_{jx}}(\mathbf{v})\right) \tag{6.16}$$

where $LS_{d_j} = 1/400$ is the limit state, $\mu_{d_{jx}}$, $\sigma_{d_{jx}}$ and $g_{d_{jx}}$ is the mean, standard deviation and peak factor, with specified first excursion probabilities or prescribed vulnerability for an observation period T, of the response processes $d_{jx}(t)$ and $\mathbf{v} = (\bar{V}_H, \alpha)$. In this example the inter-story drift ratio response processes $d_{jx}(t)$ may be calculated directly from the response at the geometrical centre of each floor.

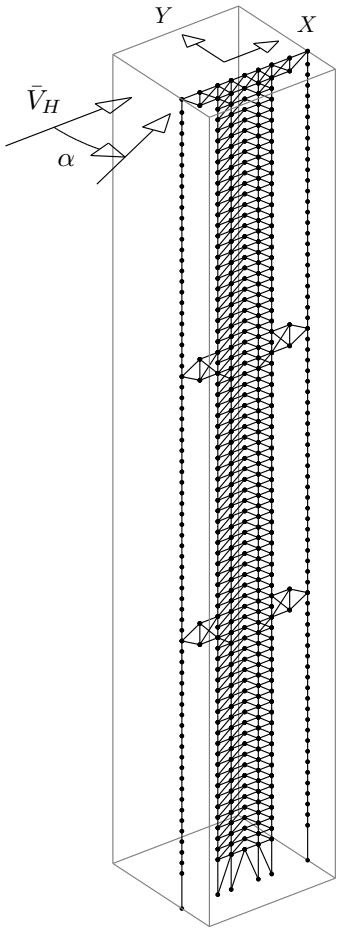

Figure 6.3: Planar frame as set in the 3D wind environment.

Capacity ratios

Concerning the local member level response the following capacity ratios, suggested by the American institute of steel construction [6.1] were considered:

$$\begin{aligned} \frac{N_{il}(\mathbf{v},t)}{\phi N_{ni}} \geq 0.2 \quad &\Rightarrow \quad b_{il}(\mathbf{v},t) = \frac{N_{il}(\mathbf{v},t)}{\phi N_{ni}} + \frac{8}{9}\left(\frac{M_{Xil}(\mathbf{v},t)}{\phi_b M_{Xni}}\right) \leq 1 \\ \frac{N_{il}(\mathbf{v},t)}{\phi N_{ni}} < 0.2 \quad &\Rightarrow \quad b_{il}(\mathbf{v},t) = \frac{N_{il}(\mathbf{v},t)}{2\phi N_{ni}} + \frac{M_{Xil}(\mathbf{v},t)}{\phi_b M_{Xni}} \leq 1 \end{aligned} \tag{6.17}$$

where N_{ni} and M_{Xni} are the nominal axial and flexural strengths of member i, ϕ and ϕ_b are axial and flexural resistance factors while $N_{il}(\mathbf{v},t)$ and $M_{Xil}(\mathbf{v},t)$ are the total internal forces due to specified factored combinations $l = 1, ..., L$.

From the capacity ratios the following local level limit state functions may be defined:

$$G_{b_{il}}(\mathbf{v},T) = LS_{b_{il}} - (\mu_{b_{il}}(\mathbf{v}) + g_{b_{il}}(\mathbf{v},T)\sigma_{b_{il}}(\mathbf{v})) \tag{6.18}$$

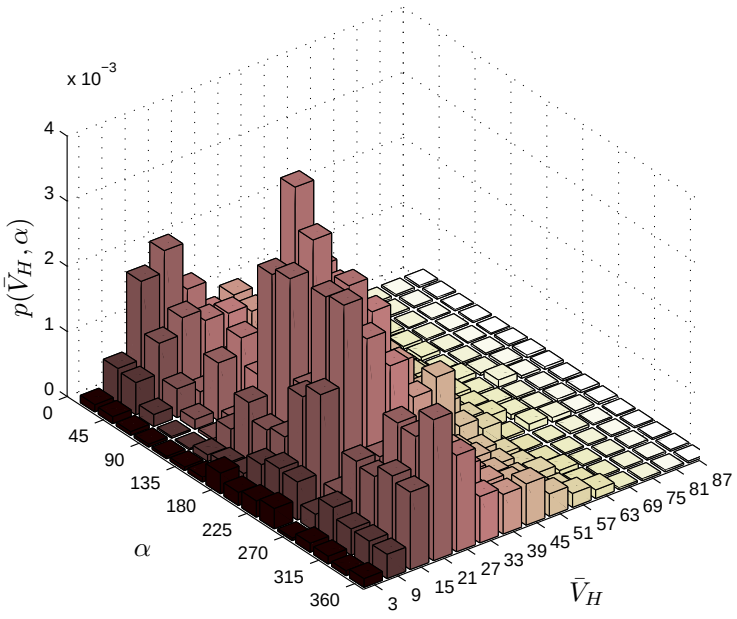

Figure 6.4: Extreme joint probability density function of the wind climate.

where $LS_{b_{il}} = 1$ is the limit state level while T is the observation period for which the first excursion probability is calculated concerning $b_{il}(t)$. It should be observed that the peak response functions $(\mu_{b_{il}} + g_{b_{il}}(T)\sigma_{b_{il}})$ are evaluated for both the axial force ratios of equation (7.26). The governing peak response is then chosen on the basis of the maximum and minimum axial force occurring in the member. The procedure is repeated for a number of control sections over the length of the member. The governing peak response function is that yielding the most sever response over all control sections and all load combinations.

6.3.3 The wind hazard

The extreme wind climate is described by the directional model of section 6.2.1. In particular the directional wind speeds used for creating the simulated hurricane databases come from the National Institute of Standards and Technology (NIST). For various mileposts situated on the US cost line, 999 simulated extreme wind events are created. Every event is defined by 16 maximum sectorial wind speeds occurring during the hurricane. Each location is assigned an intensity, υ, derived from the Poisson model. The building is considered in the Miami area of Florida. Therefore milepost 1500 was considered. The wind speeds are represented as mean hourly speeds at the building's top by using the power law in a suburban setting.

The extreme joint probability density function of the wind climate is shown in Figure 6.4 illustrating the directional characteristics of the wind climate.

6.4 Results and discussion

6.4.1 Traditional directional and non directional methods

There are two methods commonly adopted for combining a building's aerodynamics with the sites' wind climatological information for obtaining estimates of the MRIs of various response components of interest. The first approach is based on a non directional model that simply takes the maximum response induced by the non directional maximum mean wind speed, with specified MRI, blown from all wind directions. The MRI of the maximum response is then simply taken as that of the non directional wind speed. This method is the most commonly adopted by international codes and standards (see section 1.3.1). Because this will in general overestimate the response some codes, such as the ASCE 7-05 [6.2] will prescribe a directional factor K_d that reduces the non directional maximum mean wind speed to account for the improbable event of having both the most severe aerodynamic direction coincident with the most severe wind direction of the inherently, but neglected, directional extreme wind climate. The second approach is a directional method based on the assumption that the sectorial maximum mean wind speed with MRI of interest will produce a response with the same MRI (see section 1.3.2). Therefore the maximum response with specified MRI is simply taken as the maximum of all the sectorial responses. This intuitive approach is strictly correct only in the case that the sectorial wind speeds are fully correlated, a physically un-meaningful case, while in all other cases it can be shown to strictly underestimate the response with MRI of interest [6.18, 6.20]. To implement these methods the directionless and sectorial maximum mean wind speeds are required for the site of interest. For the wind climate of section 6.3.3 the directionless mean hourly wind speed with 50 year MRI was calculated as 57.75m/s. The sectorial wind speeds with 50 year MRIs are shown in table 6.1.

Sector	$\bar{V}_H$ (m/s)	Sector	$\bar{V}_H$ (m/s)
1	43.94	9	45.75
2	44.46	10	45.38
3	47.99	11	45.36
4	47.81	12	45.74
5	45.88	13	43.31
6	47.24	14	41.34
7	47.94	15	40.77
8	46.60	16	41.13

Table 6.1: Sectorial wind speeds with 50 year MRIs.

6.4.2 Comparison with proposed model

In the following, the 50 year inter-story drift response and factored 50 year member capacity ratios, both with assigned vulnerability, are calculated with the proposed model and compared to estimates obtained considering traditional approaches.

In particular the vulnerability of the frame outlined in section 6.3 is taken as the expected value of equation (6.3) and therefore as $E[EDP|IM]$ while the response processes are considered gaussian in nature. Therefore response surfaces with assigned vulnerability may be obtained by considering the following peak factor [6.7]:

$$g_{\tilde{R}} = \sqrt{2\mathrm{In}(\nu_0 T)} + \frac{0.5772}{\sqrt{2\mathrm{In}(\nu_0 T)}} \tag{6.19}$$

where ν_0 is the mean 0-level up-crossing rate which for tall buildings may be taken equal to the first natural frequency of the building while T is the observation period equal to 3600 s. The load combination used in conjunction with the local capacity requirements of section 6.3.2 was the following [6.2]:

$$1.2(\mathrm{DL}) + 1.0(\mathrm{LL}) + 1.6(\text{Wind Load}) \tag{6.20}$$

where DL is the dead load and LL is the static live load. The members are gathered into a number of design groups. In particular beams and columns were grouped two levels at a time. The outriggers are considered member by member ensuring however symmetry about the central vertical axis. The final number of design groups is 287.

In figures 6.5 and 6.6 the limit states for the drift responses of the 74th and 37th floors compared to those that would be obtained by considering a non directional or sector-by-sector model is reported. The strong dependency of the limit state on the model adopted is immediately evident as is the non linear nature of the limit states associated with the more rigorous proposed approach. Similar behavior can be seen for the limit states of the member capacities as seen in figure 6.7, for a diagonal member between the 72nd and 73rd floor, and for a box column member between the 58th and 59th floor of the core, figure 6.8. For both the drift and member capacity response the sector-by-sector approach is seen to significantly underestimate the mean hourly wind speeds that produce a response with the desired MRI. This is seen for all responses and demonstrates the inadequacy of the sector-by-sector approach.

The non directional method seems to quite accurately estimate the response with specified MRI for certain wind directions while for others severe underestimates can be seen. This is demonstrated by the significant difference in the 50 year non directional mean wind speed compared to the limit state mean speeds, figures 6.5 to 6.8. Because the non directional approach is based on considering the maximum response over all wind directions as the design value, in this example it can be seen to overestimate the 50 year design value of the inter-story drift over the building's height figure 6.9(a).

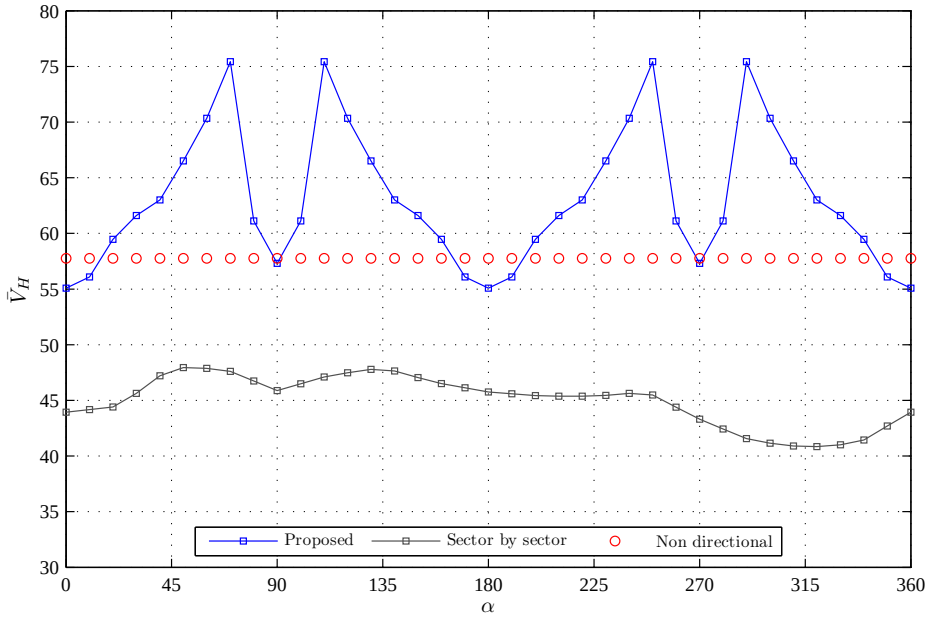

Figure 6.5: Limit state, $\bar{V}_H^{LS_{\tilde{d_{74x}}}}$, for the 50 year non factored inter-story drift response of the 74th floor.

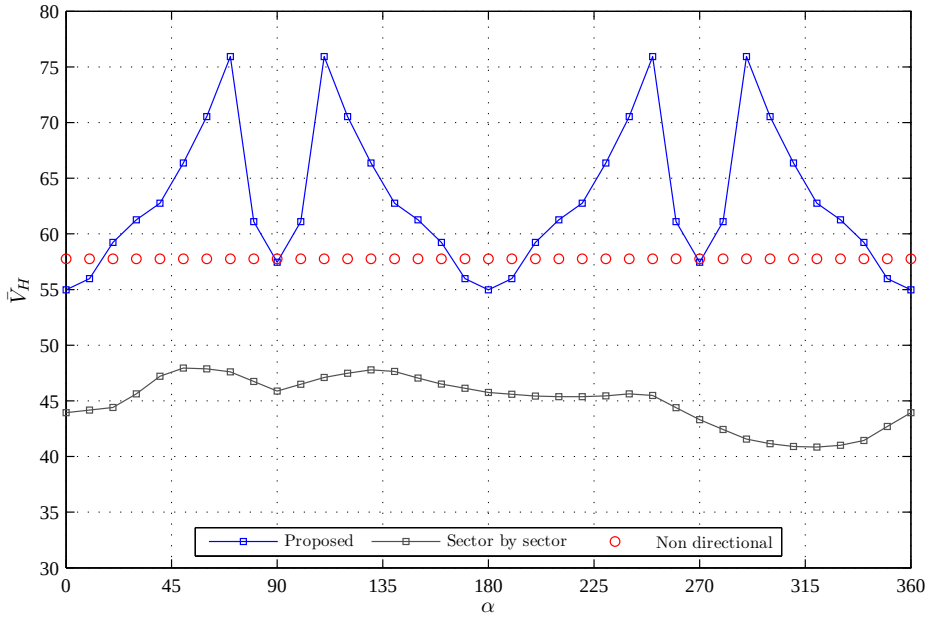

Figure 6.6: Limit state, $\bar{V}_H^{LS_{\tilde{d_{74x}}}}$, for the 50 year non factored inter-story drift response of the 37th floor.

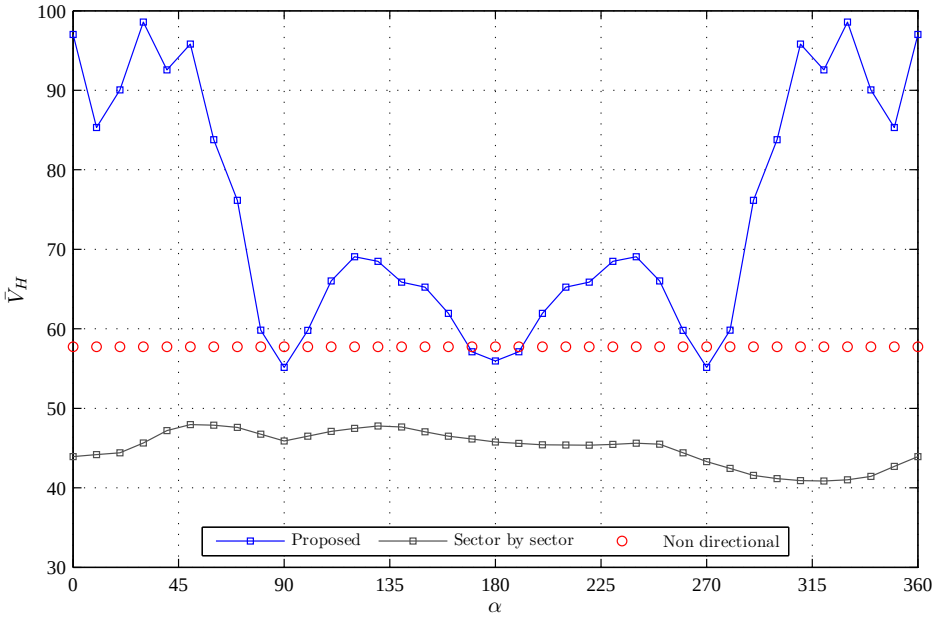

Figure 6.7: Limit state, $\bar{V}_H^{LS_{\tilde{b}_{133l}}}$, for the 50 year factored capacity response of member 133.

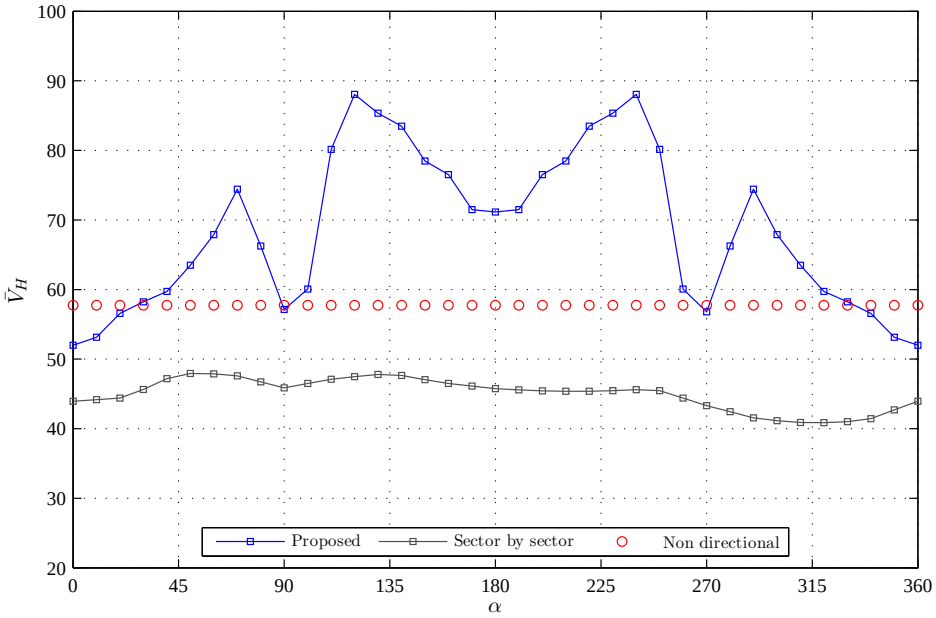

Figure 6.8: Limit state, $\bar{V}_H^{LS_{\tilde{b}_{295l}}}$, for the 50 year factored capacity response of member 295.

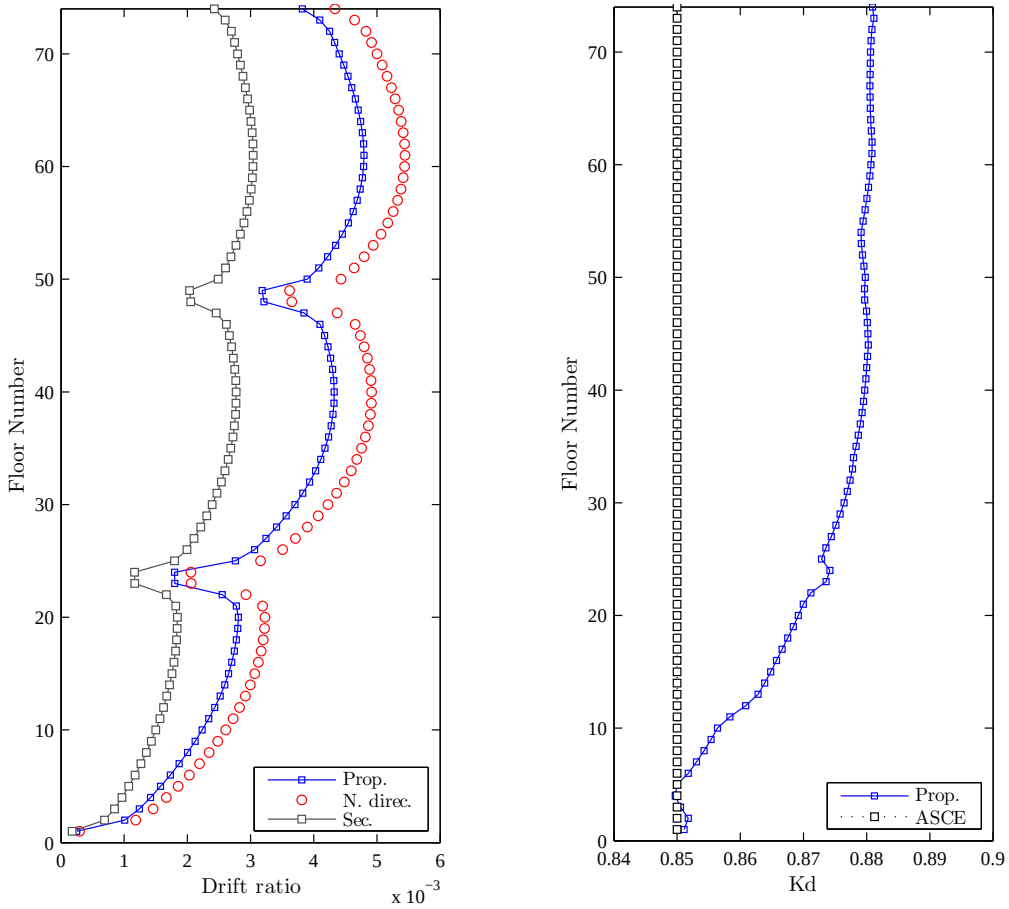

(a) (b)

Figure 6.9: (a) 50 year inter-story drift response: comparison between proposed model and traditional approaches, (b) Wind directionality factor, K_d, for the 50 year inter-story drift response.

Figure 6.9(b) reports the wind directionality factor, K_d, for the inter-story drift calculated as:

$$K_d = \frac{\tilde{R}_{\text{Proposed}}}{\tilde{R}_{\text{Non direc.}}} \tag{6.21}$$

This is compared to the value proposed in ASCE 7-05 [6.2] of 0.85. As can be seen the value of 0.85 seems un conservative. Figures 6.10 and 6.11 report the analogous quantities concerning the member capacity ratios. In this case the situation is more complicated. Indeed, in this case, K_d may assume a wide range of values including a number significantly greater than one, figure 6.11. The reason for this may be traced back to the discontinuous nature of the AISC [6.1] capacity ratios adopted in this example. This result does not however lose in generality as most code prescribed member capacity ratios will be discontinuous in order to account for the interaction between the various internal forces.

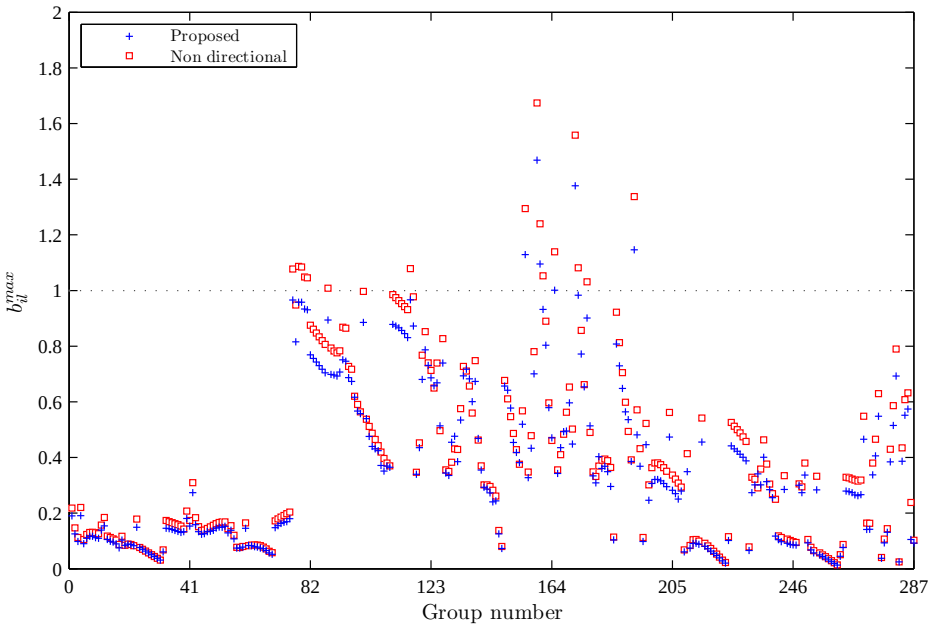

Figure 6.10: 50 year factored capacity response: comparison between proposed model and non directional approaches.

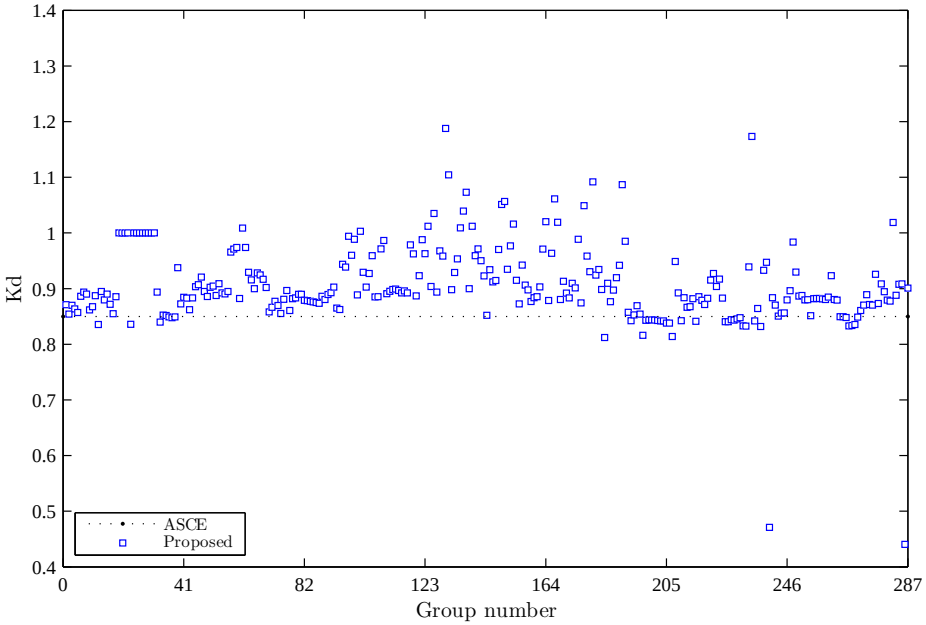

Figure 6.11: Wind directionality factor, K_d, for the 50 year factored capacity response.

6.5 Concluding remarks

In this chapter a component wise reliability based model is proposed that rigorously combines the experimentally determined directional aerodynamics with a directional wind climate defined through the extreme joint probability density function of the maximum mean hourly wind speed and direction occurring during a given epoch. The proposed model indentifies the maximum mean wind speeds that will cause a response to assume a specified MRI. In particular the model demonstrates how for any response level with specified MRI there exists a level cut set containing the maximum mean wind speeds and directions that will cause this response level. From the application of the proposed model to an illustrative tall building a considerable difference is observed between the directional/non-directional wind speeds with specified MRIs and the actual wind speeds causing a critical response to assume a level with specified MRI. The inadequacy of flat directionality factors when applied to this type of structure seems to be apparent from the large underestimates caused by applying these approaches to the test case.

Bibliography

[6.1] AISC. *Manual of steel construction: load and resistance factor design, 3rd Edition*. Chicago, IL, 2001.

[6.2] ASCE. *ASCE 7-05 Minimum design loads for buildings and other structures*. Reston, VA, 2005.

[6.3] G. Augusti, C. Borri, and H. J. Niemann. Is aeolian risk as significant as other environmental risks? *Reliability Engineering and System Safety*, 74:227–237, 2001.

[6.4] C. M. Chan and J. K. L. Chui. Wind-induced response and serviceability design optimization of tall steel buildings. *Engineering Structures, Elsevier*, 28:503–513, 2006.

[6.5] C. M. Chan, J. K. L. Chui, and M. F. Huang. Integrated aerodynamic load determination and stiffness design optimization of tall buildings. *Struct. Design Tall Spec. Build.*, 2007.

[6.6] C. M. Chan, M. F. Huang, and K. C. S. Kwok. Stiffness optimization for wind-induced dynamic serviceability design of tall buildings. *Journal of Structural Engineering*, 135(8):985–997, 2009.

[6.7] A. G. Davenport. Note on the distribution of the largest value of a random function with application to gust loading. *INPROCEEDINGS Institution of Civil Engineering*, 28:187–196, 1964.

[6.8] W. P. Fritz and E. Simiu. Probabilistic description of tall building response to wind: Database-assisted design, dynamics, and wind directionality effects. In *9th Int. Conf. on Structural Safety and Reliability CD-ROM*, 2005.

[6.9] M. Gioffrè, M. Grigoriu, M. Kasperski, and E. Simiu. Wind-induced peak bending moments in low-rise building frames. *Journal of Engineering Mechanics*, 126(8):879–881, 2000.

[6.10] M. Gioffrè and V. Gusella. Peak response of a nonlinear beam. *Journal of Engineering Mechanics*, 133(9):963–969, 2007.

[6.11] M. Grigoriu. Crossing of non-gaussian translation process. *Journal of Engineering Mechanics*, 110(4):610–620, 1984.

[6.12] M. Grigoriu. A model for directional hurricane wind speeds. *NIST Government Contractor Report*, 06-905, 2006.

[6.13] M. Grigoriu. Algorithms for generating large sets of synthetic directional wind speed data for hurricane, thunderstorm, and synoptic winds. *NIST Technical Note*, 1626, 2009.

[6.14] D. K. Kwon, T. Kijewski, and A. Kareem. e-analysis of high-rise buildings subjected to wind loads. *Journal of Structural Engineering*, 134(7):1139–1153, 2008.

[6.15] C. Paulotto, M. Ciampoli, and G. Augusti. Some proposals for a first step towards a performance based wind engineering. In *Forum in Engineering Decision Making (IFED)*, Stoos, 2004.

[6.16] P. E. Pinto, R. Giannini, and P. Franchin. *Seismic Reliability Analysis of Strucutures*. IUSS Press, Pavia, Italy, 2004.

[6.17] A. Rigato, P. C. Chang, and E. Simiu. Data-based design and wind directionality effects. In *Bluff Body Aerodynamics and Applications, 4th International colloquium*, pages 213–216, Ruhr-University Bochum, September 11-14, 2000.

[6.18] E. Simiu and J. Filliben. Wind tunnel testing and the sector-by-sector approach to wind directionality effects. *Journal of Structural Engineering, ASCE*, 137(7):1043–1045, 2005.

[6.19] E. Simiu and N. Heckert. Wind direction and hurricane-induced ultimate wind loads. *Journal of Wind Engineering and Industrial Aerodynamics*, 74-76:1037–1046, 1998.

[6.20] E. Simiu and T. Miyata. *Design of Buildings and Bridges for Wind*. John Wiley Sons, Hoboken, New Jersey, 2006.

[6.21] E. Simiu and R. H. Scanlan. *Wind effects on structures: Fundamentals and applications to design 3rd Ed.* Wiley-Interscience, New York, 1996.

[6.22] S. M. J. Spence, M. Gioffrè, and V. Gusella. Influence of higher modes on the dynamic response of irregular and regular tall buildings. In *6th International Colloquium on Bluff Bodies Aerodynamics and Applications (BBAA VI)*, Milano, Italy, July 20-24, 2008.

[6.23] Y. Zhou, T. Kijewski, and A. Kareem. Aerodynamic loads on tall buildings: Interactive database. *Journal of Structural Engineering*, 129(3):394–404, 2003.

Chapter 7

An Efficient RBDO Procedure for Tall Buildings

Modern tall buildings are often characterized by statistically and mechanically coupled dynamic systems. For these buildings traditional least weight optimization procedures based on a few idealized equivalent static wind loads derived from directionless wind models may be inadequate. This is especially true considering traditional models used for combining aerodynamics and site specific climatological information. Indeed these methods were developed for buildings with statistically and mechanically uncoupled systems exhibiting strong preferential behavior for certain wind directions. Using these models during a traditional deterministic optimization may lead to unsafe designs.

In this chapter the component-wise reliability model of chapter 6 is used to rigorously combine the directional building aerodynamics and climatological information. An efficient reliability-based design optimization scheme is then proposed based on decoupling the traditionally nested optimization loop from the reliability analysis. The decoupling is achieved by assuming the level cut sets containing the mean wind speeds generating a response with specified exceedance probability independent of changes in the design variable vector. This hypothesis results in a series of conservative designs during convergence. The decoupled optimization problem is solved by defining a series of approximate explicit sub-problems in terms of the second order response statistics of the constrained functions.

7.1 Introduction

The member size optimization of tall buildings is a well established field of application for large scale optimization algorithms. This is easily explained through the obvious economic advantages that can be had through this type of application due

to the high initial costs of such constructions. Research into this area has been vigorously explored since the early Nineties. While size and scope of problems examined have grown over the years, the basic approach to solve these problems has remained unaltered. In particular they are based on the resolution of a static response optimization problem and therefore the definition of an adequate number of idealized Equivalent Static Wind Loads (ESWLs) [7.5, 7.12, 7.33, 7.28, 7.29, 7.11, 7.31]. However the process of transforming an inherently dynamic phenomenon, such as the response of wind sensitive tall buildings, into a static response problem is not an easy task especially considering modern tall buildings which tend to be characterized by a coupled response [7.23, 7.14, 7.13]. Traditional methods for treating the wind hazard through the definition of an appropriate number of ESWLs are based on several simplifications including: the combination of the directional aerodynamics and wind climate information through approximate, often directionless, models; the definition of the ESWLs that reproduce the maximum value of a limited number of critical load effects, often the base bending moments or top floor displacements [7.38]; the assignment of the occurrence probability of a generic load effect equal to the occurrence probability of the wind speed that produces the maximum response of one of the critical load effects. These simplifications introduce a number of shortcomings in the response estimation among which are the choice of the critical load effects and the inaccurate estimation of the occurrence probabilities of both the critical and non critical load effects. This last is due to the fact that the mean hourly wind speed with a certain occurrence probability will not in general produce a load effect with the same occurrence probability due to the inherently directional nature of both the wind climate and building aerodynamics. Considering the computational power now available, the investigation of more thorough approaches based on reliability models, such as that proposed in chapter 6, that rigorously account for problems concerning the accurate combination of directional aerodynamic and climatological information is overdue. From an optimization viewpoint this implies the definition of appropriate Reliability-Based Design Optimization (RBDO) algorithms [7.32, 7.18] that must be capable of handling the sheer size of modern tall buildings. Indeed the inherent computational effort necessary for solving such large scale (thousands of probabilistic constraints) RBDO problems implies the need for defining efficient algorithms that overcome the coupled or nested nature of traditional RBDO algorithms.

In this chapter an efficient RBDO procedure is proposed for the member size optimization of tall buildings subject to multiple loading conditions and time variant experimentally determined wind loads. In particular the algorithm is based on the concept of decoupling the reliability analysis from the optimization loop [7.16, 7.35, 7.17, 7.39, 7.26]. This allows the reliability analysis to be performed separately from the successive deterministic optimization loop, guaranteeing far greater efficiency than traditional approaches. The reliability of the system is guaranteed through the component-wise strategy proposed in chapter 6 that fully accounts for the non linear nature of the limit state functions. The results of the reliability

analysis are then used to define a deterministic optimization problem in terms of the second order response statistics. This problem is characterized by the replacement of the reliability constraints of the original optimization problem with response constraints evaluated in the level cut sets of the component response surfaces with prescribed vulnerability. An efficient algorithm is then developed for implementing the proposed RBDO procedure for tall frameworks. The applicability of the proposed algorithm is then demonstrated on a full scale planar frame set in a 3D wind environment.

7.2 The RBDO procedure

7.2.1 Problem formulation

Consider a tall building with $j = 1, ..., N$ floors and $i = 1, ..., M$ members making up the structural system and consider $k = 1, ..., K$ sets of N geometrical points, one for each floor. Considering the kth set, the inter-story drift ratio d_{jks}, defined as the relative displacement between two points of two adjacent floors normalized with respect to their distance, has to be controlled in two orthogonal directions $(s = x, y)$. With the objective of minimizing the weight of the structure, W, in terms of a vector of deterministic design variables, $\mathbf{x} = \{x_1, ..., x_n\}^T$, while ensuring the structural integrity of the system through component-wise reliability constraints on the inter-story drift and member capacity ratios, b_{il}, under $l = 1, 2, ..., L$ static loading conditions, the following time invariant RBDO problem may be posed:

$$\text{Find} \qquad \mathbf{x} = \{x_1, ..., x_n\}^T \tag{7.1}$$

$$\text{to minimize} \qquad W = f(\mathbf{x}) \tag{7.2}$$

subject to:

$$\begin{aligned} &P_{f,d_{jks}}(\mathbf{x}) = \int_{G_{d_{jks}}(\mathbf{x},\mathbf{v},\mathbf{z},T)\leq 0} f_{\mathbf{v}}(\mathbf{v})d\mathbf{v} \leq P_{f,d_{jks}}^{accept} \\ &(j = 1, ..., N)(k = 1, ..., K)(s = x, y) \end{aligned} \tag{7.3}$$

$$\begin{aligned} &P_{f,b_{ip}}(\mathbf{x}) = \int_{G_{b_{il}}(\mathbf{x},\mathbf{v},\mathbf{z},T)\leq 0} f_{\mathbf{v}}(\mathbf{v})d\mathbf{v} \leq P_{f,b_{il}}^{accept} \\ &(i = 1, ..., M)(l = 1, ..., L) \end{aligned} \tag{7.4}$$

where $G_{d_{jks}}(\mathbf{x}, \mathbf{v}, \mathbf{z}, T)$ and $G_{b_{il}}(\mathbf{x}, \mathbf{v}, \mathbf{z}, T)$ are the limit state functions with specified first excursion probabilities; $\mathbf{z}$ is the response vector calculated from the dynamic equilibrium problem governing the response of the structural system; T is the observation period for which the first excursion probabilities are calculated; $\mathbf{v}$ is a vector of random variables defining the intensity of the wind hazard taken as $(\bar{V}_H, \alpha)$ where $\bar{V}_H$ is the maximum mean wind speed at the building top H blowing from direction

α; f is the objective function; $P_{f,d_{jks}}(\mathbf{x})$ and $P_{f,b_{il}}(\mathbf{x})$ are the failure probabilities associated with the drift and capacity ratios while $P^{accept}_{f,d_{jks}}$ and $P^{accept}_{f,b_{il}}$ are their acceptable values respectively; $f_{\mathbf{v}}$ is the joint probability density function between $\bar{V}_H$ and α; $l = 1, ..., L$ are the static loading conditions.

The optimization problem outlined in equations (7.1)÷(7.4) is characterized by the limit state functions $G_{d_{jks}}(\mathbf{x}, \mathbf{v}, \mathbf{z}, T)$ and $G_{b_{il}}(\mathbf{x}, \mathbf{v}, \mathbf{z}, T)$ that assume the following form:

$$G_{d_{jks}}(\mathbf{x}, \mathbf{v}, \mathbf{z}, T) = LS_{d_{jks}} - (\mu_d(\mathbf{z}(\mathbf{x}, \mathbf{v})) + g_d(\mathbf{z}(\mathbf{x}, \mathbf{v}), T)\sigma_d(\mathbf{z}(\mathbf{x}, \mathbf{v}))_{jks} \tag{7.5}$$

$$G_{b_{il}}(\mathbf{x}, \mathbf{v}, \mathbf{z}, T) = LS_{b_{il}} - (\mu_b(x_i, \mathbf{z}(\mathbf{x}, \mathbf{v})) + g_b(\mathbf{z}(\mathbf{x}, \mathbf{v}), T)\sigma_b(x_i, \mathbf{z}(\mathbf{x}, \mathbf{v}))_{il} \tag{7.6}$$

where $LS_{d_{jks}}$ and $LS_{b_{il}}$ are the limit states, μ_d, μ_b, σ_d, σ_b, g_d and g_b are the means, standard deviations and peak factors, with specified first excursion probabilities, of the response processes $d_{jks}(t)$ and $b_{il}(t)$ calculated from the following dynamic equilibrium problem:

$$\mathbf{M}\ddot{\mathbf{z}}(t) + \mathbf{C}\dot{\mathbf{z}}(t) + \mathbf{K}\mathbf{z}(t) = \mathbf{f}(t, \mathbf{v}) \tag{7.7}$$

where $\mathbf{M}$, $\mathbf{C}$ and $\mathbf{K}$ are the mass, damping and stiffness matrices respectively while $\mathbf{f}(t, \mathbf{v})$ is the vector of the time varying forcing functions evaluated for the hazard intensity $\mathbf{v} = (\bar{V}_H, \alpha)$ and considered stationary. It should be observed that the limit state functions of equations (7.5) and (7.6) are implict functions of the design variables $\mathbf{x}$ because of their dependency on the response vector $\mathbf{z}$ which can be shown to be an implicit function of the design variables [7.2].

The peak factors g_d and g_b are of fundamental importance for the present formulation. Indeed the solutions of the following time-variant reliability problems:

$$G_{d_{jks}}(\mathbf{x}, \mathbf{z}(t))|_{\mathbf{v}} \text{ or } G_{b_{il}}(\mathbf{x}, \mathbf{z}(t))|_{\mathbf{v}} < 0 \qquad \forall t \in [0, T] \tag{7.8}$$

may be estimated as the first excursion probabilities passed the limit state levels $LS_{d_{jks}}$ and $LS_{b_{il}}$ of the response processes $d_{jks}(t)$ and $b_{il}(t)$. These probabilities obviously coincide with the exceedance probabilities associated with the peak factors that give response levels equal to the relevant limit states [7.34]. In particular by defining the component vulnerability as the conditional probability of exceedance $p(LS_{d_{jks}}|\mathbf{v})$ or $p(LS_{b_{il}}|\mathbf{v})$ (see chapter 6), the fixing of acceptable excursion probabilities for the limit state functions is equivalent to the fixing of acceptable vulnerability levels for the various response components that are to be constrained in the optimization problem. Therefore the accurate estimation of peak factors with specified excursion probabilities is central to this formulation. As mentioned in chapter 6 any non gaussian response feature seen in $d_{jks}(t)$ and $b_{il}(t)$ may be accounted for through appropriate peak factor models.

7.2.2 Proposed resolution setting

The main difficulty solving the RBDO problem outlined in equations (7.1)÷(7.4) is posed by the non linear nature of the limit states (section 6.4.2) and by the large scale, thousands of probabilistic constraints, of the problems that are of practical interest. This is particularly true for traditional general purpose RBDO algorithms which are in general coupled, or nested, implying the fact that the reliability analysis is carried out simultaneously with the optimization causing the procedures to be extremely computationally cumbersome [7.22]. To overcome this problem, various methods have been developed [7.37]. In particular methods based on decoupling the optimization loops for the reliability analysis have received considerable attention [7.16, 7.35, 7.17, 7.39, 7.26], as they allow the adoption of efficient deterministic optimization algorithms to be applied to the results of the reliability analysis.

In the following a method is proposed that decouples the optimization problem of equations (7.1)÷(7.4) from the reliability analysis which is carried out using the model proposed in chapter 6 and therefore rigorously accounting for the non linear nature of the limit state functions. The method is based on firstly expanding the constraints in equations (7.3) and (7.4) in the following form:

$$P_{f,d_{jks}}(d_{jks} > LS_{d_{jks}}) = 1 - \left[\int_0^{\bar{V}_H^{LS_{d_{jks}}}} \int_0^{2\pi} p(\bar{V}_H, \alpha) d\bar{V}_H d\alpha\right]^{\upsilon} \leq P_{f,d_{jks}}^{accept} \tag{7.9}$$

$$P_{f,b_{il}}(b_{il} > LS_{b_{il}}) = 1 - \left[\int_0^{\bar{V}_H^{LS_{b_{il}}}} \int_0^{2\pi} p(\bar{V}_H, \alpha) d\bar{V}_H d\alpha\right]^{\upsilon} \leq P_{f,b_{il}}^{accept} \tag{7.10}$$

where $p(\bar{V}_H, \alpha)$ is the joint probability density function of the directional extreme wind climate with intensity υ [7.19, 7.20], while $\bar{V}_H^{LS_{d_{jks}}}$ and $\bar{V}_H^{LS_{b_{il}}}$ are the level cut sets of the response surfaces with prescribed vulnerability containing all those wind speeds associated with the limit states $LS_{d_{jks}}$ and $LS_{b_{il}}$. The geometric meaning of the level cut sets is shown in figure 7.1 for a generic response R. If in equations (7.9) and (7.10) the probability of exceedance is fixed coincident to $P_{f,d_{jks}}^{accept}$ and $P_{f,b_{il}}^{accept}$ respectively, then the corresponding level cut sets $\bar{V}_H^{d_{jks}}$ and $\bar{V}_H^{b_{il}}$ give the wind speeds over all wind directions that will give the response levels, d_{jks} and b_{il} associated with $P_{f,d_{jks}}^{accept}$ and $P_{f,b_{il}}^{accept}$. The knowledge of the level cut sets $\bar{V}_H^{d_{jks}}$ and $\bar{V}_H^{b_{il}}$ allow for the definition of the following alternative optimization problem:

$$\text{Find} \qquad \mathbf{x} = \{x_1, ..., x_n\}^T \tag{7.11}$$

$$\text{to minimize} \qquad W = f(\mathbf{x}) \tag{7.12}$$

subject to:

$$\underbrace{\left(\mu_d(\mathbf{z}(\mathbf{x}, \mathbf{v})) + g_d(\mathbf{z}(\mathbf{x}, \mathbf{v}), T)\sigma_d(\mathbf{z}(\mathbf{x}, \mathbf{v}))\right)_{jks}}_{\bar{V}_H^{d_{jks}}} - LS_{d_{jks}} \leq 0 \tag{7.13}$$

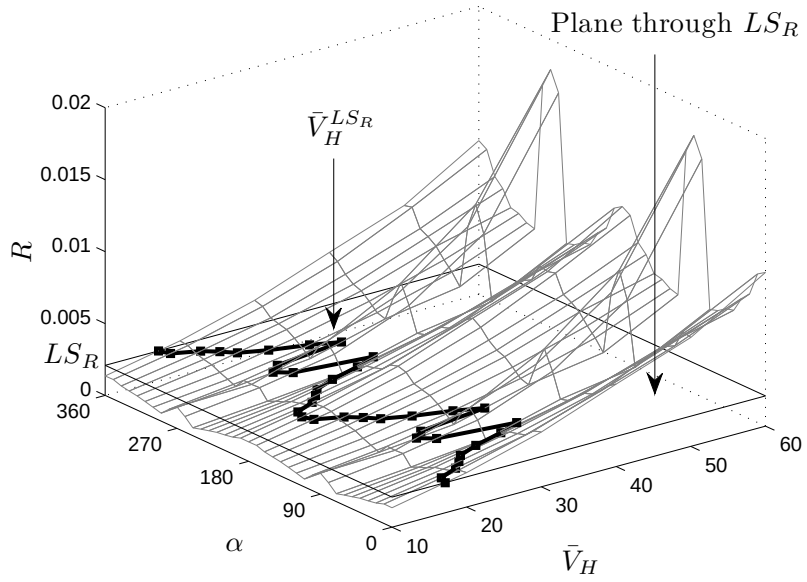

Figure 7.1: Level cut set, $\bar{V}_H^R$, through the response surface of R with prescribed vulnerability.

$$\underbrace{(\mu_b(x_i, \mathbf{z}(\mathbf{x}, \mathbf{v})) + g_b(\mathbf{z}(\mathbf{x}, \mathbf{v}), T)\sigma_b(x_i, \mathbf{z}(\mathbf{x}, \mathbf{v}))_{il}}_{\bar{V}_H^{b_{il}}} - LS_{b_{il}} \leq 0 \tag{7.14}$$

The solution of this optimization problem formulated in the level cut sets will at convergence give the same solution as the original problem. In particular if a constraint is active at the optimum this implies that the corresponding limit state function is in the limit state.

The problem outlined in equations (7.11)÷(7.14) is still coupled, as a variation in the design variable vector $\mathbf{x}$ will cause a change in the level cut set causing the responses d_{jks} and b_{il}. Therefore during the optimization the reliability model has to be updated. To decouple the process it is proposed to consider the level cut sets, $\bar{V}_H^{d_{jks}}$ and $\bar{V}_H^{b_{il}}$, independent of the design vector. This makes the process iterative as at the end of an optimization loop the reliability model must be updated therefore yielding the new level cut sets. It should be observed that at the convergence of each optimization problem the failure probability will be strictly overestimated if the limit state functions of equations (7.5) and (7.6) are considered strictly monotonically increasing functions of $\bar{V}_H$ which is to be expected for the systems under consideration in this work. This is a highly desirable condition as the optimization may be terminated at any point yielding a conservative outcome.

By decoupling the optimization, the problem of equations (7.11)÷(7.14) may be solved by any appropriate deterministic algorithm while, as mentioned, the reliability analysis may be carried out using the method proposed in 6 therefore rigorously

accounting for wind directionality effects and any non linearity in the limit states.

7.2.3 Optimization procedure

For practical applications the size of the problem outlined in equations (7.11)÷(7.14) implies the need for optimization algorithms with high convergence rates. These will in general be achieved by adopting gradient-based algorithms [7.2, 7.21]. However, these methods require design sensitivity analysis which in light of the high number of implicit non linear probabilistic constraints, second order nature of the governing equations and onerous reanalysis can require excessive computational effort [7.27, 7.3]. Various methods have been developed for increasing the overall efficiency of the optimization process. Among these are those based on the concept of defining a sequence of approximate explicit sub-problems in terms of the design variables around the current design points [7.36, 7.24, 7.6, 7.25, 7.26]. The approximate problems are solved by conventional optimization algorithms without the need to perform any additional structural analyses due to the explicit nature of sub-problem. Convergence is reached when the magnitude of change in the objective function or optimality conditions is below a fixed level. The next section will present an algorithm for implementing the proposed RBDO procedure for tall frameworks.

7.3 Proposed procedure for tall frameworks

7.3.1 Drift constraints

In this section an approximate explicit probabilistic expression for the constraints of equation (7.13) on the inter-story drift ratios will be presented based on the Principle of Virtual Work (PVW). Numerically the constraints of equation (7.13) are imposed in a discrete number of points, $q = 1, ..., Q$, belonging to the level cut set $\bar{V}_H^{d_{jks}}$ evaluated in the current design point $\mathbf{x}_0$. The problem is therefore to find an explicit approximate expression in terms of the design variables around the current design point, $\mathbf{x}_0$, of the following peak response function of the response process $d_{jksq}(\mathbf{x}_0, \mathbf{z}(t))$:

$$\begin{aligned} &\hat{d}_{jksq} = \mu_d(\mathbf{z}(\mathbf{x}_0)) + g_d(\mathbf{z}(\mathbf{x}_0, T))\sigma_d(\mathbf{z}(\mathbf{x}_0)|_{jksq} \\ &(j = 1, ..., N)(k = 1, ..., K)(q = 1, ..., Q)(s = x, y) \end{aligned} \tag{7.15}$$

For the sake of clarity the approximate expression will be derived considering the case of a 2D structure acting in the xz plane with $i = 1, ..., M$ members and $j = 1, ..., N$ floors. The extension to the third dimension is immediate. With the aim of finding the explicit approximate expression of (7.15) consider the following

expression of the response process $d_{jkxq}(\mathbf{x}_0, \mathbf{z}(t))$ in terms of the PVW:

$$\begin{aligned} d_{jkxq}(\mathbf{x}_0, \mathbf{z}(t)) = \sum_{i=1}^{M} \int_0^{L_i} \Bigg(& \frac{1}{A_i} f_{1i}^*(\mathbf{x}_0) N_i(\mathbf{x}_0, \mathbf{z}(t)) \\ & + \frac{1}{A_{Yi}} f_{2i}^*(\mathbf{x}_0) V_{Yi}(\mathbf{x}_0, \mathbf{z}(t)) + \frac{1}{I_{Xi}} f_{4i}^*(\mathbf{x}_0) M_{Xi}(\mathbf{x}_0, \mathbf{z}(t)) \Bigg) \, dl \end{aligned} \tag{7.16}$$

where the functions f_{1i}^*, f_{2i}^* and f_{3i}^* are given by:

$$\begin{aligned} f_{1i}^*(\mathbf{x}_0) &= \frac{n_{ji}^*(\mathbf{x}_0) - n_{j-1i}^*(\mathbf{x}_0)}{Eh_j} \\ f_{2i}^*(\mathbf{x}_0) &= \frac{v_{Yji}^*(\mathbf{x}_0) - v_{Yj-1i}^*(\mathbf{x}_0)}{Gh_j} \\ f_{3i}^*(\mathbf{x}_0) &= \frac{m_{Xji}^*(\mathbf{x}_0) - m_{Xj-1i}^*(\mathbf{x}_0)}{Eh_j} \end{aligned} \tag{7.17}$$

in which the quantities n_{ji}^*, v_{Yji}^*, and m_{Xji}^* are the axial force, shear and bending moments in the local reference system (X, Y) of member i due to a unit force acting in the x-direction of the degree of freedom of the jth point of the kth inter-story set, while m_{Xj-1i}^*, v_{Yj-1i}^*, and n_{j-1i}^* are the analogous quantities for the $(j-1)$th point of the kth set. $N_i(\mathbf{x}_0, \mathbf{z}(t))$, $V_{Yi}(\mathbf{x}_0, \mathbf{z}(t))$, and $M_{Xi}(\mathbf{x}_0, \mathbf{z}(t))$ are the time varying axial force, shear and bending moments while A_i and A_{Yi} are the axial and shear areas of member i while I_{Xi} is the flexural moment of inertia. E and G are the axial and shear material moduli while L_i is the length of the ith member. Equation (7.16) in the case of structures consisting of beams, columns and trusses may be written as:

$$\begin{aligned} d_{jkxq}(\mathbf{x}_0, \mathbf{z}(t)) = \sum_{i=1}^{M} & \frac{1}{A_i} F_{1i}^* N_i(\mathbf{x}_0, \mathbf{z}(t)) + \frac{1}{A_{Yi}} F_{2i}^* V_{Yi}(\mathbf{x}_0, \mathbf{z}(t)) \\ & + \frac{1}{I_{Xi}} \left(F^{*(1)}_{3i} M_{Xi}^{(1)}(\mathbf{x}_0, \mathbf{z}(t)) + F^{*(2)}_{3i} M_{Xi}^{(2)}(\mathbf{x}_0, \mathbf{z}(t)) \right) \end{aligned} \tag{7.18}$$

where the constants $F_{1i}^*, F_{2i}^*, F^{*(1)}_{3i}$ and $F^{*(2)}_{3i}$ are given by:

$$\begin{aligned} F_{1i}^* &= L_i f_{1i}^*(\mathbf{x}_0) \\ F_{2i}^* &= L_i f_{2i}^*(\mathbf{x}_0) \\ F^{*(1)}_{3i} &= \frac{L_i}{6} (2 f_{3i}^{*(1)}(\mathbf{x}_0) + f_{3i}^{*(2)}(\mathbf{x}_0)) \\ F^{*(2)}_{3i} &= \frac{L_i}{6} (2 f_{3i}^{*(2)}(\mathbf{x}_0) + f_{3i}^{*(1)}(\mathbf{x}_0)) \end{aligned} \tag{7.19}$$

in which the apexes (1) and (2) indicate that the internal forces have be evaluated in the initial and final cross sections of the ith member. No apex simply implies that the internal forces are constant along the member.

In equation (7.16) the inter-story drift depends on three variables A_i, A_{Yi} and I_{Xi} for each element. It is these variables that govern the stiffness of the structural system. In general, in the sizing optimization the design variable vector, $\mathbf{x} = \{x_1, ..., x_M\}$ will be closely related to these variables. In particular, by appropriately choosing the design variables, it is relatively easy to define three functions, χ_{1i}, χ_{2i} and χ_{3i} that explicitly link the design variables to A_i, A_{Yi} and I_{Xi} such that:

$$\begin{aligned} \frac{1}{A_i} &= \chi_{1i}(x_i) \\ \frac{1}{A_{Yi}} &= \chi_{2i}(x_i) \\ \frac{1}{I_{Xi}} &= \chi_{3i}(x_i) \end{aligned} \tag{7.20}$$

This type of formulation is also possible in the case of standard steel sections [7.9]. Substituting equations (7.20) into equation (7.18) the following expression is obtained for the inter-story drift:

$$d_{jkxq}(\mathbf{x}_0, \mathbf{z}(t)) = \sum_{i=1}^{M} \sum_{p=1}^{3} \chi_{pi}(x_i) \Gamma_{pi}(\mathbf{x}_0, \mathbf{z}(t)) \tag{7.21}$$

where the functions $\Gamma_{pi}(\mathbf{x}_0, \mathbf{z}(t))$ are given by:

$$\begin{aligned} \Gamma_{1i}(\mathbf{x}_0, \mathbf{z}(t)) &= F^*_{1i}(\mathbf{x}_0) N_i(\mathbf{x}_0, \mathbf{z}(t)) \\ \Gamma_{2i}(\mathbf{x}_0, \mathbf{z}(t)) &= F^*_{2i}(\mathbf{x}_0) V_{Yi}(\mathbf{x}_0, \mathbf{z}(t)) \\ \Gamma_{3i}(\mathbf{x}_0, \mathbf{z}(t)) &= {F^*}^{(1)}_{3i}(\mathbf{x}_0) M^{(1)}_{Xi}(\mathbf{x}_0, \mathbf{z}(t)) \\ &\quad + {F^*}^{(2)}_{3i}(\mathbf{x}_0) M^{(2)}_{Xi}(\mathbf{x}_0, \mathbf{z}(t)) \end{aligned} \tag{7.22}$$

Equation (7.21) defines an implicit relationship between $\mathbf{x}$ and $d_{jkxq}(\mathbf{x}, \mathbf{z}(t))$ because of the implicit dependency of $\mathbf{z}(t)$ on $\mathbf{x}$. However, if both the static and dynamic internal forces are assumed insensitive for small changes in the section sizes, because the functions $\Gamma_{1i}(\mathbf{x}_0, \mathbf{z}(t))$ depend only on the internal force distribution, equation (7.21) becomes an approximate time varying explicit function of the design variables $\mathbf{x}$. The hypothesis of constant internal forces in defining approximate explicit relationships between the design variables and constraints gives particularly good results for statically loaded tall buildings [7.12, 7.10] due to their close similarity, from a global point of view, to a vertical beam fixed at the base, therefore simulating a statically determinate structure. In this work this method is extended to the dynamic internal forces which include a significant resonant contribution.

Under these hypotheses, while assigning each design variable, x_i, to a set of members making up a number of design groups $i = 1, ..., DG$, for small changes of the design variables around the current design point, $\mathbf{x}_0$, the inter-story drift ratio

may be explicitly approximated by:

$$d_{jkxq}(\mathbf{x}, \mathbf{z}(t)) \approx \sum_{i=1}^{DG} \sum_{p=1}^{3} \chi_{pi}(x_i) \Gamma_{pi}(\mathbf{x}_0, t) \tag{7.23}$$

where $\mathbf{x} = \mathbf{x}_0 + \Delta\mathbf{x}$. From this explicit approximate expression for the time varying drift ratio the first and second order response statistics must be estimated. In particular if the peak factor, $g_d(\mathbf{z}(\mathbf{x}_0, \mathbf{v}), T)$, is also considered relatively insensitive to moderate changes in the design variables, the problem becomes expressing the mean and standard deviation of equation (7.23) explicitly in terms of the design variables. In particular by taking the external wind load as stationary the standard deviation of the right hand side of equation (7.23) may be written in terms of the zero lag covariance matrix of the Γ_{pi} functions therefore yielding the following approximate explicit expression for the standard deviation:

$$\sigma_{d_{jkxq}} = \sqrt{\sum_{i=1}^{DG} \sum_{w=1}^{DG} \sum_{p=1}^{3} \sum_{m=1}^{3} \chi_{pi}(x_i) \chi_{mw}(x_i) \underbrace{C_{\Gamma_{pi}\Gamma_{mw}}}_{jkxq}} \tag{7.24}$$

where $C_{\Gamma_{pi}\Gamma_{mw}}$ are the zero lag covariance coefficients between Γ_{pi} and Γ_{mw} The explicit formulation of the mean response, which is also needed, can easily be calculated through the mean values of the functions Γ_{pi}.

The extension of equation (7.24) to the third dimension simply implies that the functions Γ_{pi} will be six corresponding to the relevant internal forces as will the functions $\chi_{pi}(x_i)$ with correspondence to the six mechanical properties of each member. This allows the definition of the following approximate explicit representation of the inter-story drift peak response function around the point $\mathbf{x}_0$:

$$\begin{aligned} \hat{d}_{jksq} &= \mu_d(\mathbf{z}(\mathbf{x})) + g_d(\mathbf{z}(\mathbf{x}, T)) \sigma_d(\mathbf{z}(\mathbf{x}))|_{jksq} \\ &\approx \sum_{i=1}^{DG} \sum_{p=1}^{6} \chi_{pi}(x_i) \underbrace{\mu_{\Gamma_{1i}}(\mathbf{x}_0)}_{jksq} \\ &\quad + \underbrace{g_d(\mathbf{z}(\mathbf{x}_0, T))}_{jksq} \sqrt{\sum_{i=1}^{DG} \sum_{w=1}^{DG} \sum_{p=1}^{6} \sum_{m=1}^{6} \chi_{pi}(x_i) \chi_{mw}(x_i) \underbrace{C_{\Gamma_{pi}\Gamma_{mw}}(\mathbf{x}_0)}_{jksq}} \end{aligned} \tag{7.25}$$

where $\mathbf{x} = \mathbf{x}_0 + \Delta\mathbf{x}$.

It should be observed that the hypothesis on the stationary nature of the functions $\Gamma_{pi}(t)$ does not represent anything unusual for the analysis of the wind response of structures. It is also worth observing that the functions $\chi_{1i}, ..., \chi_{6i}$ define generalized reciprocal variables while equation (7.25) represents an expansion in terms of these variables around the current design point $\mathbf{x}_0$ capable of capturing the non linear nature of the peak response function and therefore non linear constraints.

7.3.2 Member capacity constraints

Capacity ratios

The capacity ratios considered in this study take a general form which has as particular cases the specific ratios proposed by the Eurocodes [7.7, 7.8] and AISC instructions [7.1]. Therefore, while considering a point q indentifying a specific vector $\mathbf{v}$ and so a couple $(\bar{V}_H, \alpha)$, the non-dimensional capacity ratios may be written as:

$$b_{ilq}(x_i, \mathbf{z}(t)) = \frac{|N_{ilq}(x_i, \mathbf{z}(t))|}{\alpha\phi N_{ni}(x_i)} + \beta\left(\frac{|M_{Xilq}(x_i, \mathbf{z}(t))|}{\phi_b M_{Xni}(x_i)} + \frac{|M_{Yilq}(x_i, \mathbf{z}(t))|}{\phi_b M_{Yni}(x_i)}\right) \tag{7.26}$$

subject to the conditions:

$$\begin{cases} \dfrac{|N_{ilq}(x_i, \mathbf{z}(t))|}{\phi N_{ni}(x_i)} \geq \tilde{N} & \Rightarrow & \begin{cases} \alpha = \alpha_1 \\ \beta = \beta_1 \end{cases} \\ \dfrac{|N_{ilq}(x_i, \mathbf{z}(t))|}{\phi N_{ni}(x_i)} < \tilde{N} & \Rightarrow & \begin{cases} \alpha = \alpha_2 \\ \beta = \beta_2 \end{cases} \\ N_{ilq}(x_i, \mathbf{z}(t)) \geq 0 & \Rightarrow & \phi = \phi_t \\ N_{ilq}(x_i, \mathbf{z}(t)) < 0 & \Rightarrow & \phi = \phi_c \end{cases} \tag{7.27}$$

where N_{ni}, M_{Xni} and M_{Yni} are the nominal axial and flexural capacities of member i, ϕ and ϕ_b are axial and flexural resistance factors, $N_{ilq}(x_i, \mathbf{z}(t))$, $M_{Xil}(x_i, \mathbf{z}(t))$ and $M_{Yil}(x_i, \mathbf{z}(t))$ are the total internal forces due to specified factored load combination l, $\tilde{N}$ represents the axial force ratio for which the bending capacity is reduced while α_1, α_2, β_1 and β_2 are the coefficients that define this reduction. Equation (7.26) represents a 3D normalized capacity domain for member i in terms of the axial, X-moment and Y-moment capacities.

For the development of the capacity constraints of the following paragraph it is convenient to interpret the conditions in equation (7.27) as identifying four capacity ratios for each set of indexes ilq depending on whether the member is in traction t:

$$\begin{cases} \alpha = \alpha_1 \\ \beta = \beta_1 \\ \phi = \phi_t \end{cases} \Rightarrow \quad b_{ilq}^{(1t)}(x_i, \mathbf{z}(t))$$
$$\begin{cases} \alpha = \alpha_2 \\ \beta = \beta_2 \\ \phi = \phi_t \end{cases} \Rightarrow \quad b_{ilq}^{(2t)}(x_i, \mathbf{z}(t)) \tag{7.28}$$

or in compression c:

$$\begin{cases} \alpha = \alpha_1 \\ \beta = \beta_1 \\ \phi = \phi_c \end{cases} \Rightarrow \quad b_{ilq}^{(1c)}(x_i, \mathbf{z}(t)) \qquad \begin{cases} \alpha = \alpha_2 \\ \beta = \beta_2 \\ \phi = \phi_c \end{cases} \Rightarrow \quad b_{ilq}^{(2c)}(x_i, \mathbf{z}(t)) \tag{7.29}$$

and on the value of the axial force. Obviously for a specific instant the capacity ratio $b_{ilq}(x_i, \mathbf{z}(t))$ will assume the value of one of the capacity ratios defined in equation (7.28) and equation (7.29).

Capacity constraints

The capacity constraints of equation (7.14) are defined by the peak response function, calculated in a discrete number of points Q belonging to the level cut set $\bar{V}_H^{b_{ilq}}$ and given by the following:

$$\begin{aligned} &\hat{b}_{ilq} = \mu_b(x_i, \mathbf{z}) + g_b(\mathbf{z}, T)\sigma_b(x_i, \mathbf{z})|_{ilq} \\ &(i = 1, ..., M)(l = 1, ..., L)(q = 1, ..., Q) \end{aligned} \tag{7.30}$$

Equation (7.30) may be evaluated in two steps. Firstly the peak response functions of the capacity ratios, $b_{ilq}^{(1t)}$, $b_{ilq}^{(2t)}$, $b_{ilq}^{(1c)}$ and $b_{ilq}^{(2c)}$, are calculated through the following expression:

$$\hat{b}_{ilq}^{(id)} = \sum_{i=1}^{3} I_i(x_i)|\mu_{IF}(x_i, \mathbf{z})| + g_b(\mathbf{z}, T)\sqrt{\sum_{j=1}^{3}\sum_{k=1}^{3} I_j(x_i)I_k(x_i)|C_{IF_jIF_k}(x_i, \mathbf{z})|} \tag{7.31}$$

where $IF_1 = N_{ilq}(\mathbf{x}, \mathbf{z}(t))$, $IF_2 = M_{Xilq}(\mathbf{x}, \mathbf{z}(t))$ and $IF_3 = M_{Yilq}(\mathbf{x}, \mathbf{z}(t))$ while $C_{IF_jIF_k}(x_i, \mathbf{z})$ is the zero lag covariance coefficient between the internal forces IF_j and IF_k with $id = 1t, 2t, 1c, 2c$ function identification index and I_j for $j = 1, 2, 3$ given by:

$$\begin{aligned} I_1 &= \frac{1}{\alpha\phi N_{ni}(\chi_{1i}(x_i))} \\ I_2 &= \frac{1}{\phi_b M_{Xni}(\chi_{3i}(x_i))} \\ I_3 &= \frac{1}{\phi_b M_{Yni}(\chi_{4i}(x_i))} \end{aligned} \tag{7.32}$$

where $\chi_{4i}(x_i)$ is the explict function linking the design variable x_i to the moment of inertia I_{Yi}. The second step consists in identifying which of the four capacity ratios

is governing. This may be determined from the maximum and minimum axial force occurring in the member given by:

$$\begin{cases} N^{+}_{ilq}(x_i, \mathbf{z}) = \mu_N(x_i, \mathbf{z}) + g^{+}_N \sigma_N(x_i, \mathbf{z}) \\ N^{-}_{ilq}(x_i, \mathbf{z}) = \mu_N(x_i, \mathbf{z}) + g^{-}_N \sigma_N(x_i, \mathbf{z}) \end{cases} \tag{7.33}$$

where g^{+}_N and g^{-}_N are the peak factors giving the maximum and minimumo axial force calculated for an observation period T and first excursion probability equal to that specified for g_b.

For the optimization loop the gradient of equation (7.30) must be defined. This is not straightforward as firstly, equation (7.30), and consequently equation (7.31), are implicit functions of the design variable vector, $\mathbf{x}$, due to the implicit relationship that exists between $\mathbf{z}$ and $\mathbf{x}$, and secondly, equation (7.30) is a discontinuous function of $\mathbf{x}$ due to the conditions in equation (7.27). However, by observing that it is the inter-story drift requirements that in general govern the design of tall structures [7.12, 7.10], an alternative approach can be defined that does not require the calculation of any gradients. The method is based on the Fully Stressed Design (FSD) concept [7.21] and therefore movable lower limits on the design variables, $\mathbf{x}^L = \{x^L_1, ..., x^L_n\}$, that maximize the utilization of member, or design group, i. The direct application of this method to equation (7.30) would be computationally extremely cumbersome as the identification of $\mathbf{x}^L = \{x^L_1, ..., x^L_n\}$ would require the repeated evaluation of the second order response statistics which, considering the number of capacity constraints of a typical tall building system, would become prohibitive.

In this study it is proposed to approximate equation (7.30) by the following expression:

$$\hat{b}_{ilq} \approx \sum_{i=1}^{3} I_i(x_i)|\mu_{IF}(\mathbf{x}_0)| + g_b(\mathbf{x}_0, T)\sqrt{\sum_{j=1}^{3}\sum_{k=1}^{3} I_j(x_i)I_k(x_i)|C_{IF_jIF_k}(\mathbf{x}_0)|} \tag{7.34}$$

where $\mathbf{x} = \mathbf{x}_0 + \Delta\mathbf{x}$. Equation (7.34) is again based on assuming the internal forces relatively insensitive to small changes in the design vector around the current design point. By defining similar approximations for the expressions in equation (7.33) it is possible to define an approximate lower limit vector on the design variables. This is achieved by simply placing the approximate expressions of $\hat{b}^{(1t)}_{ilq}$, $\hat{b}^{(2t)}_{ilq}$, $\hat{b}^{(1c)}_{ilq}$ and $\hat{b}^{(2c)}_{ilq}$ to their limiting values, solving for the relevant design variable, and then identifying which capacity ratio is governing through the approximations of the expressions in equation (7.33). By repeating the process over the loading conditions $l = 1, ..., L$, all points of the level cut set $q = 1, ..., Q$, and all control sections of the design group i the final approximate lower limit vector, $\tilde{\mathbf{x}}^L = \{\tilde{x}^L_1, ..., \tilde{x}^L_n\}$,is defined.

The proposed method for dealing with the capacity constraints will not in general guarantee an optimum final design as the internal force redistribution is not taken into account. However, due to the expected low level of active capacity constraints, at the optimum, this method should guarantee an extremely good suboptimum.

7.3.3 Explicit sub-problem

Given an initial design point $\mathbf{x}_0$ and the level cut sets $\bar{V}_H^{d_{jks}}$ and $\bar{V}_H^{b_{il}}$ derived from the reliability model, the approximate expressions so far formulated allow for the definition of the following static sub-problem:

$$\text{Find} \qquad \mathbf{x} = \{x_1, x_2, ..., x_{DG}\} \tag{7.35}$$

$$\text{to minimize} \qquad W(\mathbf{x}) = \sum_{i=1}^{DG} \gamma \frac{L_i}{\chi_{i1}(x_i)} \tag{7.36}$$

$$\begin{aligned} &\hat{d}_{jksq} \approx \sum_{i=1}^{DG} \sum_{p=1}^{6} \chi_{pi}(x_i) \underbrace{\mu_{\Gamma_{1i}}(\mathbf{x}_0)}_{jksq} \\ &+ \underbrace{g_d(\mathbf{z}(\mathbf{x}_0, T))}_{jksq} \sqrt{\sum_{i=1}^{DG} \sum_{w=1}^{DG} \sum_{p=1}^{6} \sum_{m=1}^{6} \chi_{pi}(x_i) \chi_{mw}(x_i) \underbrace{C_{\Gamma_{pi}\Gamma_{mw}}(\mathbf{x}_0)}_{jksq}} - LS_{d_{jks}} \leq 0 \\ &(j = 1, ..., N)(k = 1, ..., K)(q = 1, ..., Q)(s = x, y) \end{aligned} \tag{7.37}$$

$$\begin{aligned} &\max\left[\tilde{x}_i^L, \breve{x}_i^L\right] \leq x_i \leq x_i^U \\ &(q = 1, ..., Q)(i = 1, ..., DG) \end{aligned} \tag{7.38}$$

where γ is the specific weight of the material and the lower limits on the design variables are taken as the maximum between the lower limit due to construction issues, $\breve{x}_i^L$, and that evaluated from the results of the reliability model $\tilde{x}_i^L$. Once the sub-problem has converged it is reformulated in the new design point $\mathbf{x}_0^{DC\geq 1}$ and the optimization repeated. Each reformulation is termed a Design Cycle (DC). After a number of redesigns the problem will converge and the optimization process will terminate. A flowchart illustrating the process is shown in figure 7.2. Being a static response problem with explicit representation, any gradient-based optimization algorithm can be used to find its solution.

7.3.4 Sub-problem optimization algorithm

The resolution of the sub-problem outlined in equations (7.35)÷(7.38) may be performed by numerous algorithms. In this work an optimality criteria algorithm is implemented. This may be derived by temporarily omitting the side constraints of equation (7.38) and considering the following unconstrained lagrangian function:

$$\begin{aligned} &L(\mathbf{x}, \boldsymbol{\lambda}) = W(\mathbf{x}) + \sum_j \sum_k \sum_s \sum_q \lambda_{jksq} \hat{d}_{jksq}(\mathbf{x}) \\ &(j = 1, ..., N)(k = 1, ..., K)(s = x, y)(q = 1, ..., Q) \end{aligned} \tag{7.39}$$

where λ_{jksq} are the Lagrange multipliers while $\boldsymbol{\lambda} = \{\lambda_1, ..., \lambda_{N_h}\}$ is the vector containing the multipliers and $h = 1, ..., N_h)$ is the single subscript converting the

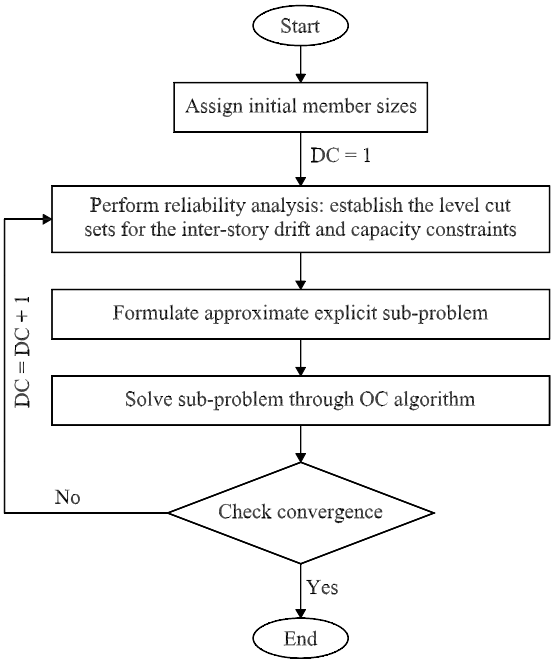

Figure 7.2: Flowchart of proposed RBDO algorithm.

subscripts (j, k, s, q), where N_h is the total number of drift constraints given by $(N \times K \times Q \times 2)$. For the sake of clarity, the rest of this paragraph will be developed in terms of h. The necessary condition for a stationary point of equation (7.39) is given by:

$$\nabla L(\mathbf{x}, \boldsymbol{\lambda}) = \mathbf{0} \Rightarrow \nabla W(\mathbf{x}) + \sum_{h=1}^{N_h} \lambda_h \nabla \hat{d}_h(\mathbf{x}) = \mathbf{0} \qquad (h = 1, ..., N_h) \tag{7.40}$$

where ∇ is the gradient operator. In addition, by imposing that all lagrangian multipliers must be non-negative and that if a constraint is not active then the corresponding multiplier must be zero, the solution of equation (7.40) will give necessary optimality criteria for the constrained sub-problem defined by equations (7.35)÷(7.37). From equation (7.40) it is possible to find the following recursive relationship for the design vector (see chapter 3 [7.30, 7.12]):

$$x_i^{\tau+1} = x_i^{\tau} \left[1 + \frac{1}{\eta} \left(- \frac{\sum_{h=1}^{N_h} \lambda_h \dfrac{\partial \hat{d}_h}{\partial x_i}}{\dfrac{\partial W}{\partial x_i}} - 1 \right) \right]_{\tau} \tag{7.41}$$

where τ indicates the iteration number. Equation (7.41) represent linear recursive relations. To use these relations for finding $\mathbf{x} = \{x_1, x_2, ..., x_{DG}\}$, the Lagrange

multipliers, λ_h, must be determined. These can be found by resolving the following set of simultaneous linear equations [7.30, 7.12]:

$$\sum_{h=1}^{N_h} \lambda_h^\tau \sum_{i=1}^{DG} \left(\frac{x_i \frac{\partial \hat{d}_h}{\partial x_i} \frac{\partial \hat{d}_m}{\partial x_i}}{\frac{\partial W}{\partial x_i}} \right)_\tau = -\sum_{i=1}^{DG} \left(x_i \frac{\partial \hat{d}_m}{\partial x_i} \right)_\tau - \eta(d_m^U - d_m^\tau) \quad (m = 1, ..., N_h) \tag{7.42}$$

In finding the solution to these equations the non negative conditions on the Lagrange multipliers must be satisfied. This may be achieved through applying the Gauss-Seidel iterative scheme with the following recursive formula:

$$\lambda_h^{\tau+1} = \frac{1}{a_{hh}} \left(b_h - \sum_{s=1}^{h-1} a_{hs} \lambda_s^{\tau+1} - \sum_{s=h+1}^{N_h} a_{hs} \lambda_s^\tau \right) \quad (m = 1, ..., N_h) \tag{7.43}$$

where:

$$a_{hh} = \sum_{i=1}^{DG} \left(\frac{x_i \frac{\partial \hat{d}_h}{\partial x_i} \frac{\partial \hat{d}_h}{\partial x_i}}{\frac{\partial W}{\partial x_i}} \right)_\tau \tag{7.44}$$

$$a_{hs} = \sum_{i=1}^{DG} \left(\frac{x_i \frac{\partial \hat{d}_h}{\partial x_i} \frac{\partial \hat{d}_s}{\partial x_i}}{\frac{\partial W}{\partial x_i}} \right)_\tau \tag{7.45}$$

$$b_h = -\sum_{i=1}^{DG} \left(x_i \frac{\partial \hat{d}_h}{\partial x_i} \right)_\tau - \eta(d_h^U - d_h^\tau) \tag{7.46}$$

Equation (7.41) for the sizing variables and equation (7.42) for Lagrange multipliers form the basis of the iterative OC method for the solution of each sub-problem. The side constraints, omitted during the derivation of the algorithm can be easily accounted for by only considering active design variables during each iteration, τ, of the OC algorithm [7.12].

7.4 Case study

The case study on which the proposed RBDO algorithm will be tested is that of section 6.3. Therefore a 74 story planar frame analyzed in a fully 3D wind environment (figure 6.3). A validation example for the procedure can be found in appendix A.

7.4.1 Initial performance

The initial performance of the inter-story drift ratios and factored member capacity ratios is estimated from the reliability model proposed in chapter 6 while assigning an acceptable failure probability of $P_{f,d_{jx}}^{accept} = P_{f,b_{il}}^{accept} = 0.02$ for an epoch of one year. These failure probabilities obviously coincide with Mean Recurrence Intervals (MRIs) of 50 years. As in chapter 6 the acceptable vulnerability/first excursion probability of the frame components is taken as the expected value of the conditional probabilities of exceedance $p(d_{jx}|\mathbf{v})$ or $p(b_{il}|\mathbf{v})$ where d_{jks} obviously becomes d_{jx} in the case of the planar frame. The response processes are considered gaussian in nature. Therefore response surfaces with assigned vulnerability may be obtained by considering the following peak factor [7.15]:

$$g = \sqrt{2\text{In}(\nu_0 T)} + \frac{0.5772}{\sqrt{2\text{In}(\nu_0 T)}} \tag{7.47}$$

where ν_0 is the mean 0-level up-crossing rate which for tall buildings may be taken equal to the first natural frequency while T is the observation period equal to 3600 s. Once again the load combination used was the following [7.4]:

$$1.2(\text{DL}) + 1.0(\text{LL}) + 1.6(\text{Wind Load}) \tag{7.48}$$

where DL is the dead load and LL is the static live load. Figure 7.3 shows the initial drift performance of the frame against the limit state $LS_{d_{jx}}$ set at 1/400 while figure 7.4 shows the initial factored member capacity ratios against the limit state $LS_{b_{il}}$ set at unity. In figure 7.5 are shown the failure distributions, $P_{f,d_{jx}}$, for the inter-story drift ratios highlighting the non feasible design region imposed by the limit state $LS_{d_{jx}} = 1/400$ while in figure 7.6 are shown the analogous distributions, $P_{f,b_{il}}$, for the factored capacity ratios and feasible design region for $LS_{b_{il}} = 1$.

7.5 Optimization

The calibration of the optimization algorithm is achieved through the definition of the design variable vector, $\mathbf{x}$, and therefore the functions $\chi_{1i}(x_i)$, $\chi_{2i}(x_i)$ and $\chi_{3i}(x_i)$. By choosing for the members with standard AISC sections their cross sectional areas as design variables, $x_i = A_i$, it can be shown that the functons χ_{1i}, χ_{2i} and χ_{3i} are given by:

$$\begin{cases} \chi_{1i}(A_i) = A_i \\ \chi_{2i}(A_i) = c_{A_X}/A_i + \grave{c}_{A_X} \\ \chi_{3i}(A_i) = c_{I_X}/A_i + \grave{c}_{I_X} \end{cases} \tag{7.49}$$

where c and $\grave{c}$ are the regressional constants derived under the assumption that the cross section maintains within a constant shape group as it changes size [7.12]. For

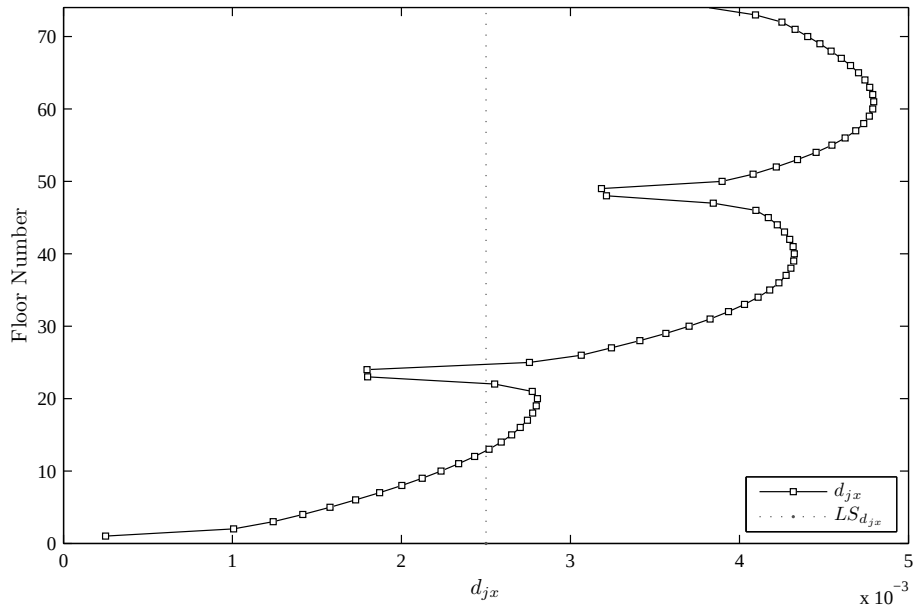

Figure 7.3: Initial drift performance for $P_{f,d_{jx}}^{accept} = 0.02$

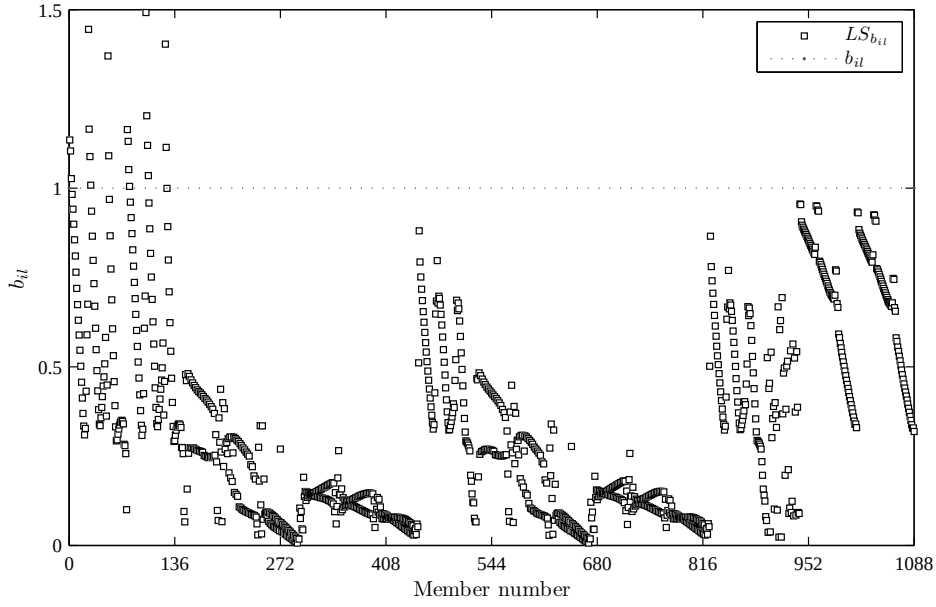

Figure 7.4: Initial factored member capacity performance for $P_{f,b_{il}}^{accept} = 0.02$

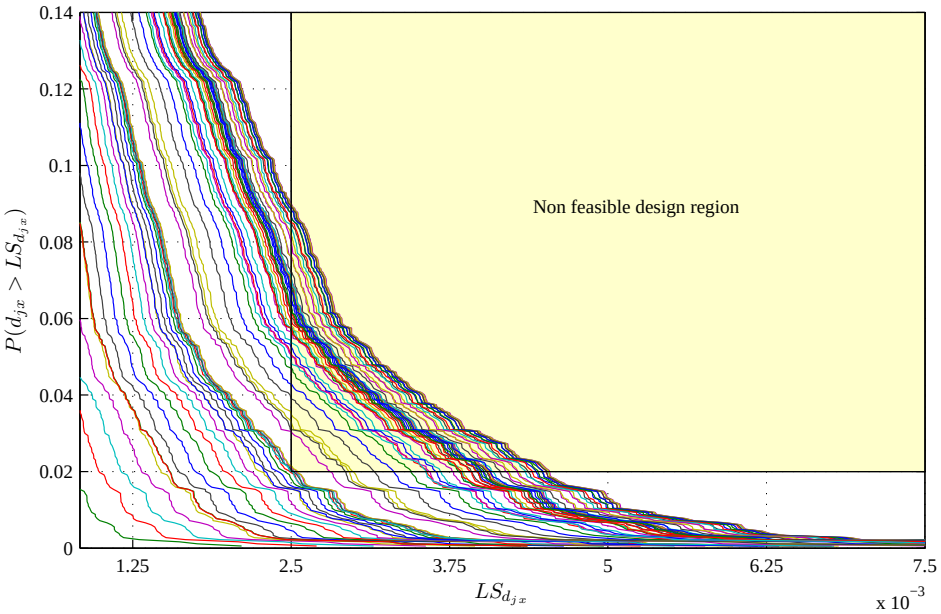

Figure 7.5: Failure distributions, $P_{f,d_{jx}}$, of the inter-story drift ratios

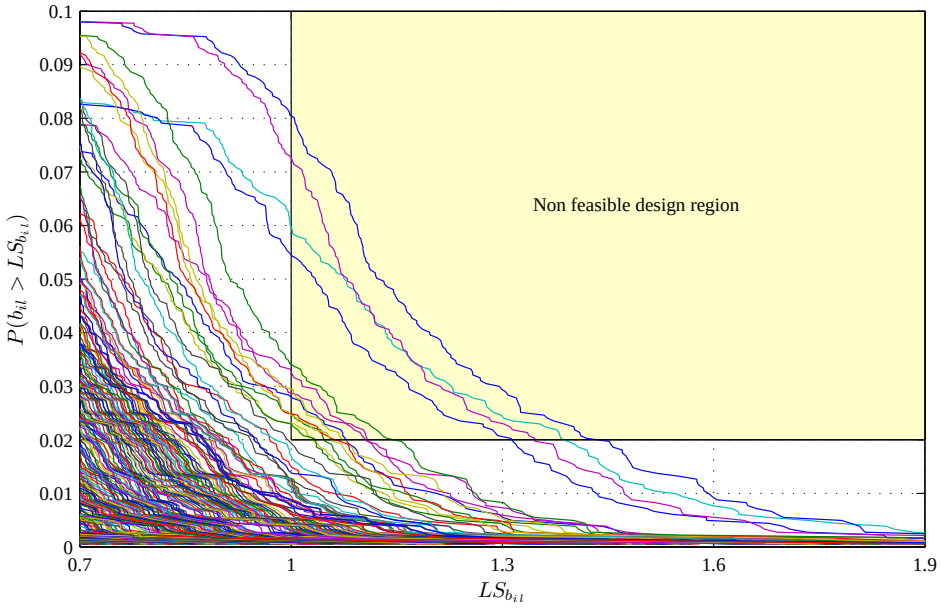

Figure 7.6: Failure distributions, $P_{f,b_{il}}$, of the capacity ratios

this example the beams and diagonals are allowed to vary within the groups W24 and W14 respectively.

The columns and outriggers are defined as steel box sections with a flange thickness 1/20 of the mid-line diameter. If these sections are kept as boxes while also keeping constant the flange to diameter ratio, the functions $\chi_{1i}(x_i)$, $\chi_{2i}(x_i)$ and $\chi_{3i}(x_i)$ may be written in terms of the mid-line diameter, D_i, as:

$$\begin{cases} \chi_{1i}(D_i) = 5/D_i^2 \\ \chi_{2i}(D_i) = 19/2D_i^2 \\ \chi_{3i}(D_i) = 30/D_i^4 \end{cases} \tag{7.50}$$

The lower limit on these design variables was fixed at $D_i = 0.3$ m while the upper limit was fixed at $D_i = 1.8$ m.

The design variables were then gathered into a number of design groups. In particular the symmetry of the frame was guaranteed by grouping symmetrically with respect to the central vertical axis. Also beams and columns were grouped two levels at a time. The outriggers were designed member by member ensuring, however, symmetry. The final number of independent design variables is 287.

7.5.1 Results

As mentioned in section 7.3.1 the constraints of equations (7.13) and (7.14) will be imposed in a discrete number of points Q. The exact number of points to consider, and therefore additional constraints, should take into account the fact that a change in the structural behaviour due to a change in the design vector $\mathbf{x}$ for a specific wind direction and response is likely to positively affect the same response for another wind direction. Therefore it is unlikely a large number for Q is necessary. It should be appreciated that the choice of Q can only affect eventual convergence of the optimization loop, and not the accuracy of the reliability estimation as this is carried out for all wind directions and passed to the optimization loop through the level cut sets $\bar{V}_H^{d_{jx}}$ and $\bar{V}_H^{b_{il}}$. In particular, for the frame of this example due to its simplicity, $Q = 1$ is considered. To investigate the effect on the results due to the choice of Q, the optimization was performed for two separate wind directions. That is, two separate optimization problems were solved considering the constraints constructed for a wind directions of 0° and 90°.

In figure 7.7 the optimized drift performance for $P_{f,d_{jx}}^{accept} = 0.02$ is shown. The high quality of the approximate sub-problem is clearly visible from the number of active or near active constraints at the optimum design. This is again seen in figure 7.8 from the rapid and steady convergence of proposed RBDO algorithm. The limited number of design cycles is very encouraging as it is the updating of the reliability model which represents the most time-consuming part of the proposed algorithm. The difference between the two optimuma seen in figure 7.8 is mainly due to the difference in the resolution of the response surfaces with prescribed

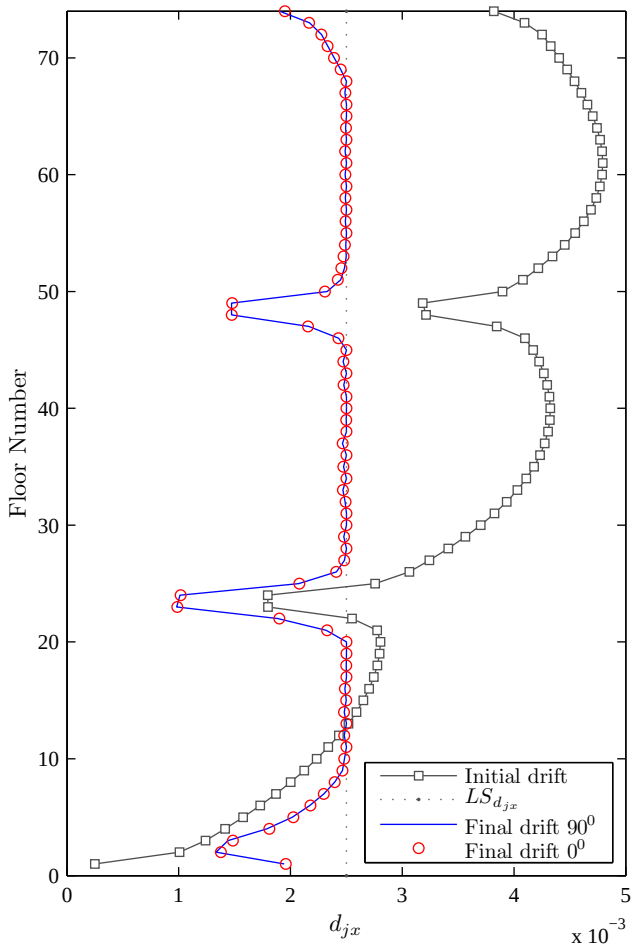

Figure 7.7: Optimized drift ratio performance for $P^{accept}_{f,d_{jx}} = 0.02$

vulnerability curves. Indeed the two optimuma seem to coincide as can be seen from figure 7.7 for the optimized drift ratios and from figure 7.9 for the optimized capacity ratios. From figure 7.9 the small number of active capacity ratios is evident, further justifying the use of probabilistic movable lower limits for the constraints on the capacity ratios. Figures 7.10 to 7.11 show the failure distributions of the inter-story drift ratios, $P_{f,d_{jx}}$, and of the capacity ratios, $P_{f,b_{il}}$, after the proposed optimization algorithm has been applied. It should be appreciated that the failure distributions rigorously account for the site specific directional aerodynamics and climatological information. Finally, in figures 7.12 to 7.14 are shown some example level cut sets $\bar{V}_H^{d_{jx}}$ and $\bar{V}_H^{b_{il}}$ for the drift and capacity ratios. In particular, from figure 7.12 for the 60th floor drift ratio, the level cut set seems to be quite insensitive to the optimization process. This result will obviously depend on the structure. For the 2D frame, this result was to be expected. It is interesting to observe, however, that this is not always true even for this simple example as can be seen for member 295, figure 7.14.

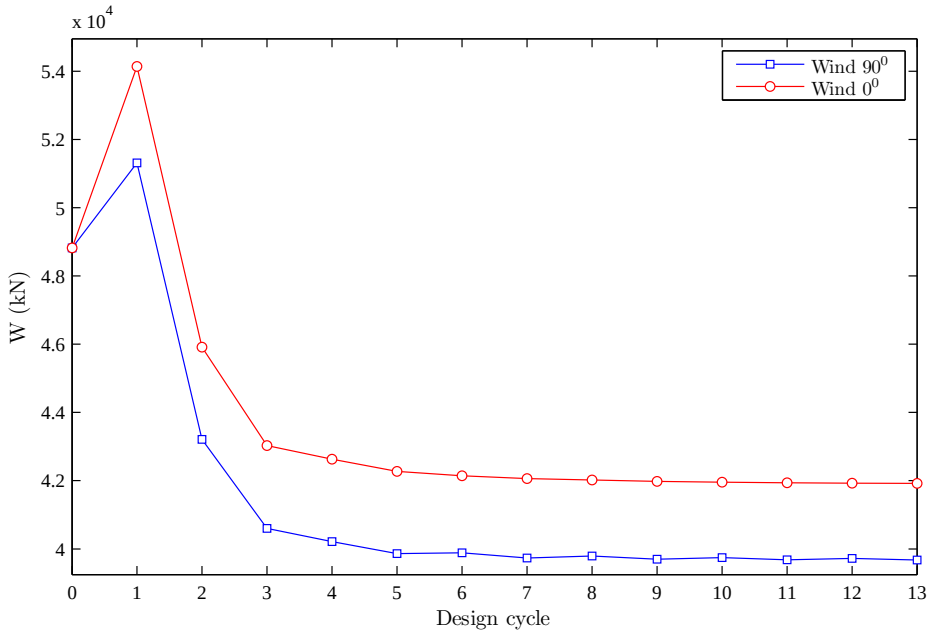

Figure 7.8: Objective function design history

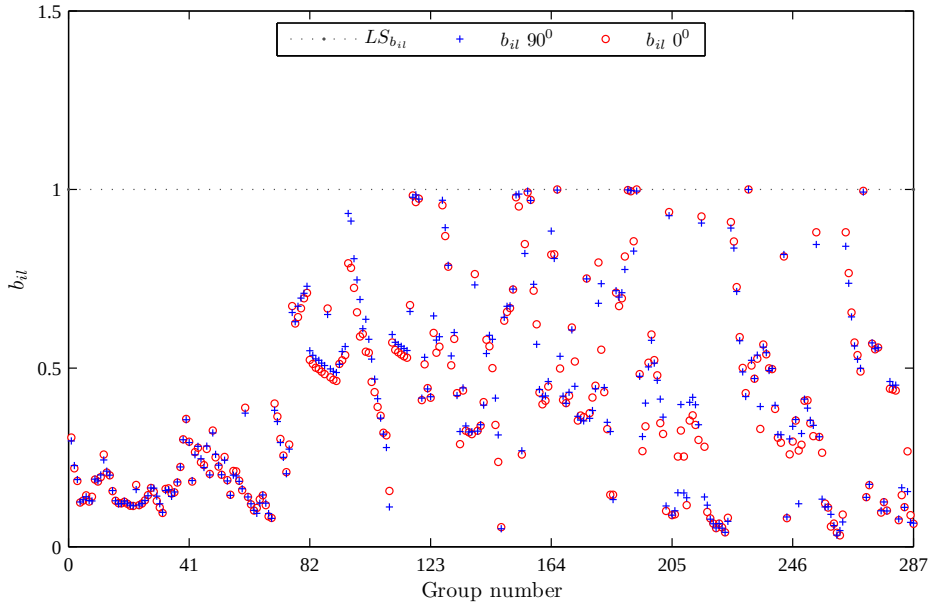

Figure 7.9: Optimized factored member capacity performance for $P_{f,b_{il}}^{accept} = 0.02$

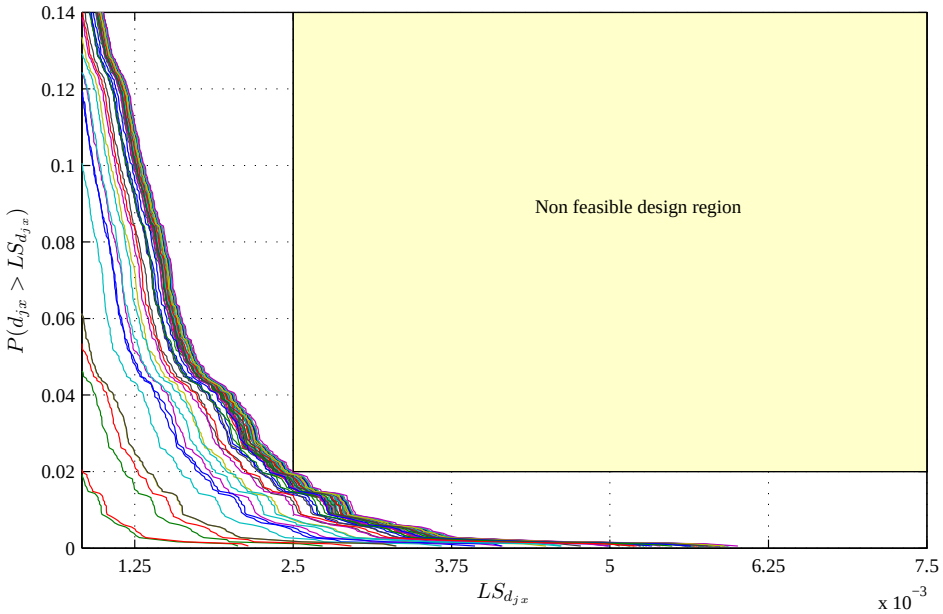

Figure 7.10: Failure distributions, $P_{f,d_{jx}}$, of the optimized inter-story drift ratios

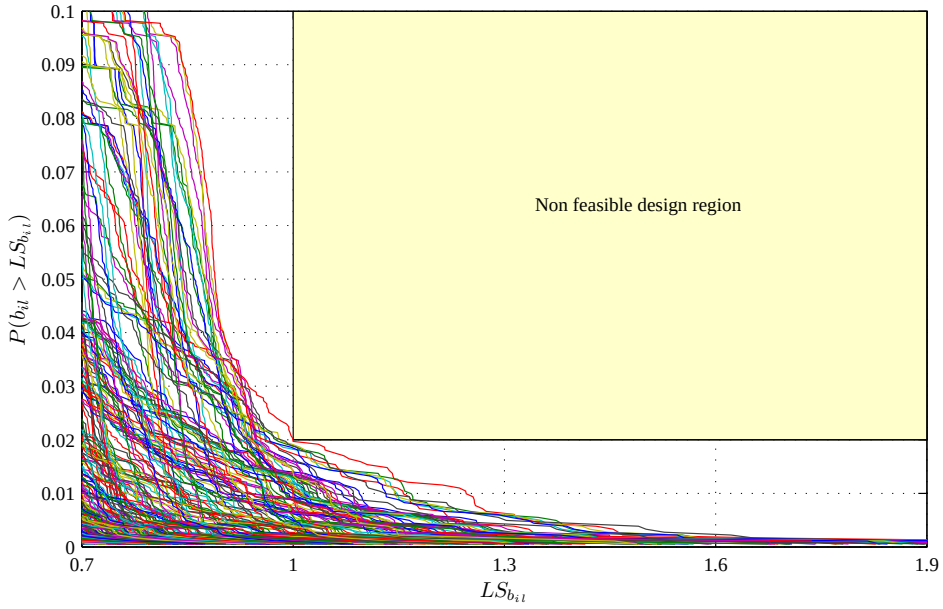

Figure 7.11: Failure distributions, $P_{f,b_{il}}$, of the optimized member capacity ratios

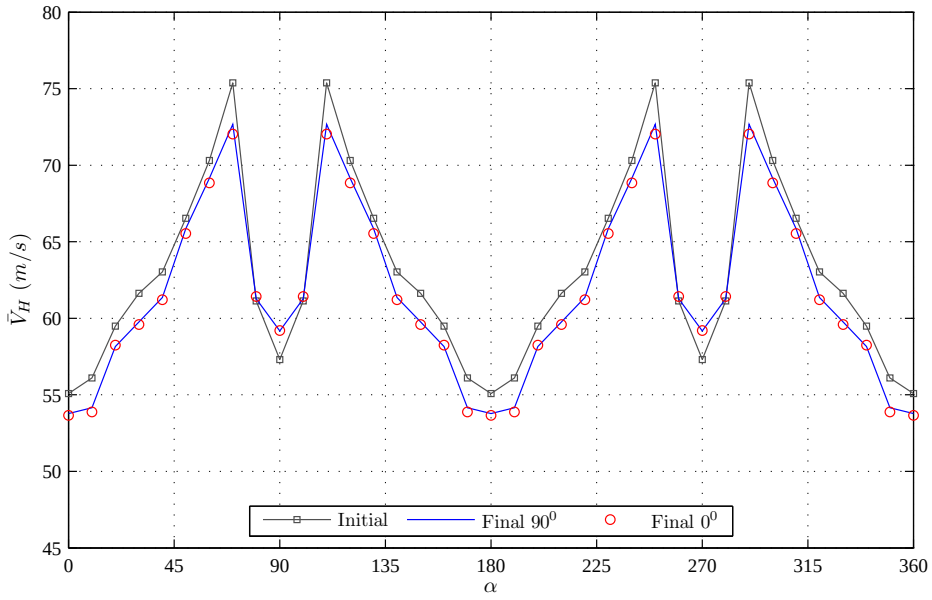

Figure 7.12: Level cut set, $\bar{V}_H^{d_{jx}}$, for the 60th floor drift ratio response with $P_{f,d_{jx}}^{accept} = 0.02$

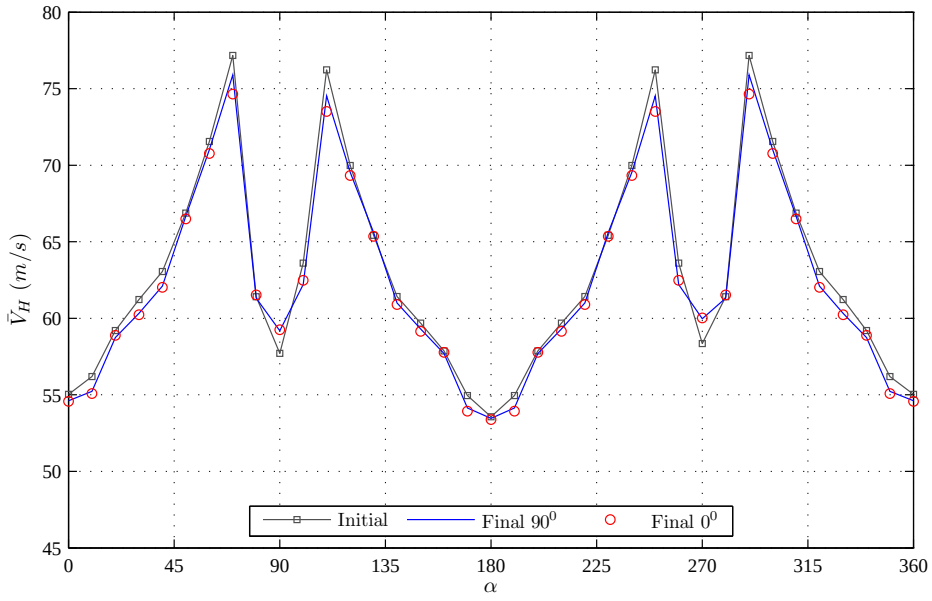

Figure 7.13: Level cut set, $\bar{V}_H^{b_{il}}$, for the factored capacity ratio response for member 177 with $P_{f,b_{il}}^{accept} = 0.02$

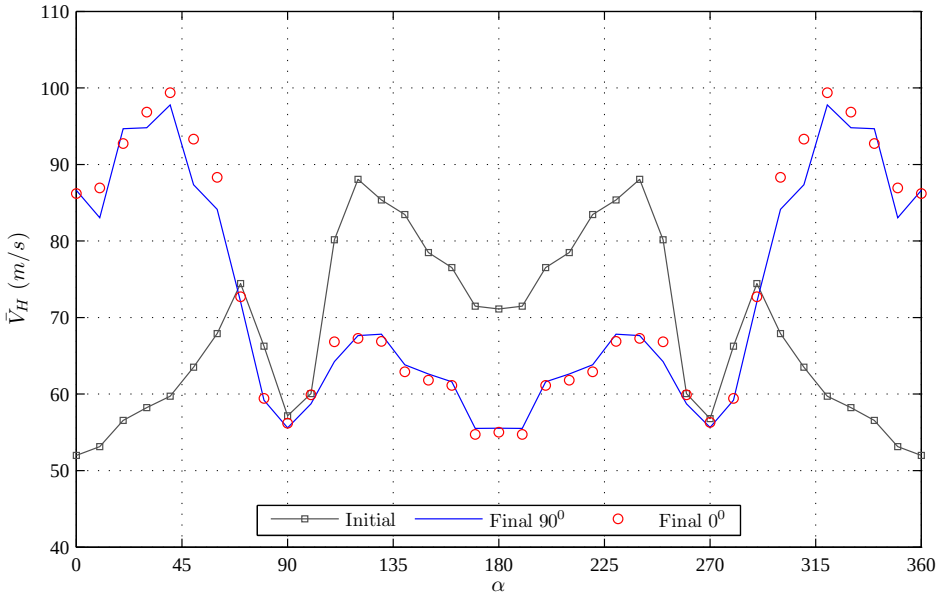

Figure 7.14: Level cut set, $\bar{V}_H^{b_{il}}$, for the factored capacity ratio response for member 295 with $P_{f,b_{il}}^{accept} = 0.02$

7.6 Concluding remarks

In this chapter an efficient RBDO procedure is proposed for the member size optimization of tall buildings subject to multiple loading conditions and time variant experimentally determined wind loads. The reliability of the system is guaranteed through a component wise strategy based on the definition of performance constraints on all important response parameters. The solution of the optimization problem is obtained by transforming the reliability optimization problem into a more conventional problem with inequality constraints defined by the limit state functions evaluated, however, in correspondence of the acceptable failure probabilities of the original performance constraints. This is achieved through the adoption of the reliability model proposed in chapter 6 yielding rigorous estimations of the level cut sets containing the wind speeds causing limit state function response levels for specified failure probabilities. By assuming these speeds independent of the design variable vector an optimization procedure is presented based on defining a sequence of explicit sub-problems in terms of the second order response statistics of the constrained limit state functions. At convergence of each sub-problem the reliability model is updated therefore ensuring consistent reliability level at the final optimum design. The applicability of the proposed procedure is then demonstrated on a full scale planar frame set in a 3D wind environment.

Bibliography

[7.1] AISC. *Manual of steel construction: load and resistance factor design, 3rd Edition*. Chicago, IL, 2001.

[7.2] J. S. Arora. *Introduction to optimum design - 2nd ed.* Elsevier Inc., San Diego, 2004.

[7.3] J. S. Arora and Q. Wang. Review of formulations for structural and mechanical system optimization. *Struct. Multidisc. Optim.*, 30:251–272, 2005.

[7.4] A. S. o. C. E. ASCE 7-05. *Minimum design loads for buildings and other structures*. Reston, VA, 2005.

[7.5] W. F. Baker. Sizing techniques for lateral systems in multi-story steel buildings. In *Proceedings, 4th World Congress on Tall Buildings: 2000 and Beyond*, pages 545–553, Hong Kong, 1990.

[7.6] M. Bruyneel, P. Duysinx, and C. Fleury. A family of MMA approximations for structural optimization. *Struct. Multidisc. Optim.*, 24:263–276, 2002.

[7.7] CEN-ENV. *Eurocode 3, Design of steel structures. Part 1.1: General rules for buildings*, 1993.

[7.8] CEN-ENV. *Eurocode 8, Design provisions for earthquake resistant structures*, 1994.

[7.9] C. M. Chan. An efficient resizing technique for the design of tall steel buildings subject to multiple drift constraints. *The Structural Design of Tall Buildings*, 2:17–32, 1993.

[7.10] C. M. Chan. Optimal stiffness design to limit static and dynamic wind responses of tall steel buildings. *Engineering Journal, AISC*, (Third Quarter):94–105, 1998.

[7.11] C. M. Chan, J. K. L. Chui, and M. F. Huang. Integrated aerodynamic load determination and stiffness design optimization of tall buildings. *The Structural Design Of Tall Buildings, John Wiley Sons, Ltd.*, 2007.

[7.12] C. M. Chan, D. E. Grierson, and A. N. Sherbourne. Automatic optimal design of tall steel building frameworks. *Journal of Structural Engineering, ASCE*, 121(5):838–847, 1995.

[7.13] X. Chen and A. Kareem. Coupled dynamic analysis and equivalent static wind loads on buildings with three-dimensional modes. *Journal of Structural Engineering*, 131(7):1071–1082, 2005.

[7.14] X. Chen and A. Kareem. Dynamic wind effects on buildings with 3D coupled modes: Application of high frequency force balance measurements. *Journal of Engineering Mechanics*, 131(11):1115–1125, 2005.

[7.15] A. G. Davenport. Note on the distribution of the largest value of a random function with application to gust loading. *Proceedings Institution of Civil Engineering*, 28:187–196, 1964.

[7.16] A. Der Kiureghian and E. Polak. Reliability-based optimal design: a decoupled approach. In A. S. Nowak, editor, *Reliability and optimization of structural systems*, pages 197–205, Chelsea (MI), 2001.

[7.17] X. Du and W. Chen. quential optimization and reliability assessment method for efficient probabilistic design. *ASME J. Mech. Des.*, 126(2):225–233, 2004.

[7.18] I. Enevoldsen and J. D. Sorensen. Reliability-based optimization in structural engineering. *Struct. Safe*, 15(3):169–196, 1994.

[7.19] M. Grigoriu. A model for directional hurricane wind speeds. *NIST Government Contractor Report*, 06-905, 2006.

[7.20] M. Grigoriu. Algorithms for generating large sets of synthetic directional wind speed data for hurricane, thunderstorm, and synoptic winds. *NIST Technical Note*, 1626, 2009.

[7.21] R. T. Haftka and Z. Gurdal. *Elements of structural optimization.* Kluwer, Dordrecht, 1992.

[7.22] A. Harish. *Reliability based design optimization: formulations and methodologies.* PhD thesis, University of Notre Dame, 2004.

[7.23] J. Holmes. Effective static load distributions in wind engineering. *Journal of Wind Engineering and Industrial Aerodynamics*, 90:91–109, 2002.

[7.24] H. A. Jensen. On the structural synthesis of uncertain systems subjected to environmenatal loads. *Struct. Multidisc. Optim.*, 20:37–48, 2000.

[7.25] H. A. Jensen, A. Marillanca, and O. Peñaloza. A computational procedure for response statistics-based optimization of stochastic non-linear FE-models. *Comput. Methods Appl. Mech. Engrg.*, 198:125–137, 2008.

[7.26] H. A. Jensen, M. A. Valdebenito, and G. I. Schuëller. An efficient reliability-based optimization scheme for uncertain linear systems subject to general gaussian excitation. *Comput. Methods Appl. Mech. Engrg.*, 198(1):7287, 2008.

[7.27] B. S. Kang, G. J. Park, and J. S. Arora. A review of optimization of structures subjected to transient loads. *Struct. Multidisc. Optim.*, 31:81–95, 2006.

[7.28] C. K. Kim, H. S. Kim, J. S. Hwang, and S. M. Hong. Stiffness-based optimal design of tall steel frameworks subject to lateral loading. *Structural Optimization, Spinger-Verlag*, 15(4-3):180–186, 1998.

[7.29] C. K. Kim, H. S. Kim, J. S. Hwang, and S. M. Hong. Development of drift design model for high-rise buildings subjected to lateral and vertical loads. *The Structural Design Of Tall And Special Buildings, John Wiley Sons, Ltd*, 2007.

[7.30] N. S. Knot, L. Berke, and V. B. Venkayya. Comparison of optimality criteria algorithms for minimum weight design of structures. *AIAA Journal*, 17(2):182–190, 1979.

[7.31] Q. S. Li, X. K. Zou, J. R. Wu, and Q. Wang. Integrated wind-induced response analysis and design optimization of tall steel buildings using micro-GA. *The Structural Design Of Tall And Special Buildings, John Wiley Sons, Ltd*, 2009.

[7.32] E. Nikolaidis and R. Burdisso. Reliability based optimization: a safety index approach. *Comput. Struct.*, 28(6):781–788, 1988.

[7.33] H. S. Park and H. Adeli. Data parallel neural dynamics model for integrated design of large steel structures. *Microcomputers in Civil Engineering, Blackwell Publishing, Inc.*, 12:311–326, 1997.

[7.34] P. E. Pinto, R. Giannini, and P. Franchin. *Seismic Reliability Analysis of Strucutures*. IUSS Press, Pavia, Italy, 2004.

[7.35] J. Royset, A. Der Kiureghian, and E. Polak. Reliability-based optimal structural design by the decoupling approach. *Reliab. Eng. Syst. Safe*, 73(3):213–221, 2001.

[7.36] L. A. Schmit and H. Miura. Approximation concepts for efficient structural synthesis. *NASA CR 2552*, 1976.

[7.37] G. Schuëller and H. A. Jensen. Computational methods in optimization considering uncertainties - an overview. *Comput. Methods Appl. Mech. Engrg.*, 198(1):2–13, 2008.

[7.38] Y. Zhou and A. Kareem. Gust loading factor: new model. *Journal of Structural Engineering*, 127(2):168–175, 2001.

[7.39] S. Zou, T. Mahadevan. A direct decoupling approach for efficient reliability-based design optimization. *Struct. Multidisc. Optim.*, 31:190–200, 2006.

Chapter 8

Conclusions

The need to better understand the behavior of tall buildings with complex geometric forms and coupled dynamic systems constituted one of the objectives of this thesis. The other was the development of automatic design procedures that guarantee both reliability and optimality in a risk consistent environment independently of the dynamic characteristics of the system and the random nature of the response.

The first stage of this work involved wind tunnel tests using simultaneously measured pressure taps carried out on two tall building models characterized by their geometric form. These were used to estimate the forcing functions of two equivalent dynamic systems. The difference between the systems was in their coupled and uncoupled nature. The coupled system was associated to the irregular geometric form. A complete characterization of the dynamic response of the two systems was then carried out. In particular the importance of considering higher modes when estimating the Root Mean Square (RMS) dynamic response of coupled systems with complex geometric forms was clearly shown. The assumption that the response of tall buildings is gaussian was then investigated. The results showed in an unequivocal fashion that this hypothesis is not true. Strong non-gaussian features were seen for both systems. The results were shown to depend tremendously on the incident wind direction. The system with irregular geometric form was seen to be particularly sensitive to this parameter. This result is particularly important in light of the common assumption of gaussianity when calculating the peak factors for the design of tall buildings. This stage concluded with the demonstration of the important role played by the background response for tall coupled tall buildings with irregular profile.

The second stage of this thesis concerned two main points. Firstly, the definition of appropriate models for the rigorous combination of the directional aerodynamics and wind climatological information was investigated. In particular a specific component-wise reliability model was developed. The model is based firstly transforming the time variant reliability problem into a time invariant model by defining component response surfaces, in terms of directional aerodynamics, with prescribed vulnerability levels. The time invariant model is then exclusively defined in terms

of the directional wind climate. The resolution of this last yields rigorous estimates of the component response levels with specified Mean Recurrence Intervals (MRIs). Secondly, a Reliability-Based Design Optimization (RBDO) procedure for the member size optimization of tall frameworks subject to probabilistic constraints on the member capacity and inter-story drift ratios was developed. The procedure is based on the concept of decoupling the optimization loop from the reliability assessment therefore guaranteeing efficiency. This is achieved by considering the level cut sets of the component response surfaces with prescribed vulnerability to be independent of changes in the design variable vector. This allows the definition of a classic non linear programming problem that is solved independently of the reliability analysis. Once the optimization problem has converged a new reliability analysis is performed defining an iterative overall optimization process. The capability of the procedure is demonstrated through the application to a structure with thousands of probabilistic constraints.

This thesis presented the work briefly outlined above. The work was divided into three parts. In the first part the dynamic response and optimization of tall buildings was thoroughly reviewed.

A brief overview of the wind hazard was given in chapter 1. The types of storms that constitute the hazard were outlined, together with their probabilistic nature. The principal measures used to characterize the turbulent nature of strong straight winds were defined. At the end of the chapter an often overlooked problem was described. More precisely the wind directionality problem was introduced. Two methods commonly adopted for the resolution of this problem were then presented highlighting the shortcomings of both the methods.

In chapter 2 the structural dynamics of tall buildings was thoroughly reviewed. The concept of a coupled and uncoupled dynamic system was defined. Modal analysis and the generalized quantities were presented as a resolution method for wind excited tall building systems. The definition of the fundamental vibration modes were given, as was the concept of a coupled mode shape. The distinction between background and resonant response was made. The frequency domain approach for the resolution of the dynamic response was presented in detail. In particular the difficulty of recombining the modes through appropriate modal correlation coefficients was highlighted together with the common assumptions made in estimating these coefficients. The shortcomings associated with the traditional application of this approach were noted. At the end of the chapter the High Frequency Force Balance (HFFB) for estimating the wind load on tall buildings was introduced. The reason for this being an effective method for estimating the fundamental generalized forces of an uncoupled system with linear mode shapes was shown. The difficulty of applying the method to more general coupled systems was explained as was the concept of mode correction schemes in obtaining this goal.

In chapter 3 a thorough review of structural optimization was presented. Various algorithms were reviewed with an eye to identifying the most opportune for solving large scale problems. Mathematical program algorithms, evolutionary strategies,

simple stochastic searches were all critiqued. The identification of the OC algorithms as an effective approach for large scale problems was made. At the end of the chapter the dynamic response optimization problem was introduced together with the most current methods used for its resolution.

In the second part of this thesis the experimental campaign was detailed together with the results of the investigation into the response of coupled dynamic systems with complex geometric profiles.

Chapter 4 reported the experimental tests carried out for the first stage of work briefly outlined at the beginning of these conclusions. The chapter was dedicated to presenting the extensive experimental program of wind tunnel tests carried out at the CRIACIV (Italian Inter-university Research Center in Aerodynamics of Constructions and Wind Engineering) located in Prato, Italy. Two 1/500 scale rigid tall buildings differing only by their geometric profiles were analyzed. Both buildings had the same height and square footprint. However, while one building had a simple prismatic form the other had the complex geometric profile of the Bank of China building. Simultaneously recorded pressure measurements using 126 carefully placed taps and a sampling frequency of 250 Hz were then used to estimate the forcing functions of two equivalent dynamic systems representing the two buildings.

Chapter 5 focuses on the experimental response analysis of coupled and uncoupled building systems. The chapter begins with an introduction to the problem of mode truncation and the reasons behind this being a common assumption are outlined. Then follows the description of the building systems considered throughout the chapter. In particular, care was taken to calibrate the dynamic system of the Bank of China building so as to achieve the same non-linear coupled mode shapes and frequencies as found in literature. The regular prismatic building was dynamically modeled to possess uncoupled quasi-linear mode shapes.

The two building systems were first used to investigate the effects of mode truncation on estimating the Root Mean Square (RMS). For the regular system the effects were consistent with what can be found in literature indicating the validity of the experimental data obtained during the first part of this study and the effectiveness of considering only the fundamental modes. In the case of the coupled irregular system the situation was shown to be very different. Very large errors were seen when the higher modes are neglected. This was especially true for the torsional response where errors of up to 60% were seen. This behavior was observed for all important response components including the displacements, accelerations and shears. The results were particularly sensitive to the incident wind direction. Indeed, both strong underestimates and overestimates can be seen for the same response by simply changing the direction of the incident wind. This implies the important role played by the modal response correlation coefficients when working in a frequency domain setting with coupled dynamic systems with complex geometry. The next investigation focused the traditional hypothesis that the response of tall buildings can be characterized as gaussian in nature. Skewness and kurtosis coefficients were estimated for both systems and for a variety of response param-

eters. The results were quite astonishing. Strong non-gaussian features were seen for all response parameters except the skewness of the acceleration due to its strong resonant contribution. Kutosis was seen to reach values of 4.5 in total contrast to what is commonly expected for this type of system. The sensitivity of the results to wind direction was noteworthy. For instance, in the case of acceleration of the regular system, non-gaussianity was seen at all levels for a wind direction of 45°. The sensitivity of the irregular system was seen to be far greater with various directions causing strong non gaussian features at all levels. It was seen that these results are not affected by higher modes which tend simply to increase the variability of the maximum and minimum skewness and kurtosis experienced over the height of the structure. Theses results are of tremendous importance as they indicate that the peak factors commonly used in the design of this type of structure could be inadequate, at least for certain wind directions. The final investigation was into the importance of the background component in accurately estimating the RMS response and higher order moments of complex coupled systems. It was seen how the errors could be dramatically reduced if a full background representation was adopted. This important result highlights the inadequacy of using the HFFB to estimate the response of this type of system even with sophisticated mode shape corrections as this will not change the incapability of the method in estimating the background contribution of higher order generalized forces.

The third part of this thesis was firstly dedicated to the development of reliability models for the rigorous combination of the directional aerodynamics and wind climatological information, and secondly to the development of efficient RBDO procedures for the optimization of tall buildings.

In chapter 6 a method was proposed for the rigorous combination of the directional aerodynamics of tall buildings with the directional climatological information of extreme wind climates in the estimation of responses with specified MRIs. In particular, the method is based on the construction of time invariant limit state functions where the inherent dependency on time is eliminated by specifying acceptable levels of component vulnerability. This allows for the rigorous estimation of the component failure probability, and therefore the associated MRI, by solving time invariant reliability integrals over what are shown to be highly non linear limit states. The proposed model is compared to those commonly used for the wind analysis of tall buildings. In particular the non directional approach, adopted by most codes and standards, is compared alongside the popular and intuitive sector-by-sector directional approach. The comparison is made on a case study consisting of a 74 floor planar frame analyzed in a three dimensional directional extreme wind climate considering forcing functions estimated from the directional wind tunnel tests of chapter 4. The results of the comparison seem to indicate the significant inadequacy of the sector-by-sector approach for estimating responses with specified MRIs for both global responses, such as inter-story drift, and for local level member capacity requirements. Concerning non directional methods severe under estimates of the responses with specified MRIs are seen for certain wind directions indicating

the importance of identifying the most important aerodynamic directions if this method is to give reasonable results. Finally appropriate values of the wind directionality factor are investigated showing the inadequacy of adopting a flat value such as that proposed in the ASCE 7-05. In conclusion this study would seem to indicate the importance of adopting reliability based models if accurate estimates of the responses with specified MRIs are required.

In chapter 7 a procedure for the efficient reliability-based design optimization of wind excited tall buildings has been proposed based on the concept of decoupling the traditionally nested reliability and optimization procedures. The method rigorously accounts for the directional site specific aerodynamic and climatological characteristics through the component-wise reliability model proposed in chapter 6. The results of the reliability analysis are then used to define an implicit deterministic optimization problem in terms of the second order response statistics. In particular the optimization problem is characterized by replacing the traditional integral form component reliability constraints with equivalent constraints on the peak response functions that are to be constrained. These last are evaluated in a discrete number of points belonging to the level cut sets of the component response surfaces with prescribed vulnerability/first excursion probabilities. The optimization loop is then decoupled from the reliability analysis by assuming the mean wind speeds and directions of the level cut sets, derived from the reliability analysis, independent of the design variable vector. This hypothesis guarantees a sequence of designs with conservative estimates of the failure probabilities. The decoupled optimization problem is then solved by defining a sequence of approximate explicit sub-problems in terms of the second order response statistics evaluated in the wind speeds of the level cut sets. At convergence of each sub-problem the reliability model is updated therefore ensuring consistent reliability level at the final optimum design. A specific algorithm of the proposed RBDO procedure is then developed for the case of tall steel frameworks. Finally the proposed algorithm is tested on a full scale planar frame subject to thousands of reliability constraints and analyzed in an extreme directional 3D wind environment. The efficiency of the proposed algorithm is clearly seen from the rapid and steady convergence history. In particular an impressive number of constraints are seen to be active or near active at the optimum.

To summarize, this thesis clearly demonstrated the inadequacy of traditional methods for the analysis of modern tall buildings characterized by complex geometric forms and coupled dynamic systems. The assumption that the response of these types of structures can be considered gaussian was clearly shown to be erroneous. Particular sensitivity of the gaussianity on wind direction was seen. The difference in the importance of the background response between irregular coupled and regular uncoupled dynamic systems was shown. A component-wise reliability model was proposed that rigorously combines the site specific aerodynamic and climatological information. It is seen from this model how the commonly adopted non-directional models concerning extreme wind climates can be inaccurate. Finally an efficient RBDO procedure is proposed for the automatic design of tall buildings. The effi-

ciency and applicability of the procedure is demonstrated through the application of the proposed procedure to a full scale planar frame set in a 3D wind environment.

Appendix A

Validation example

In this appendix a simple structure subject to dynamic loading with assigned spectrum is optimized using the procedure proposed in chapter 7.

A.1 The structure

The structure considered in this example consists of a column fixed at the base, with a box section (figure A.1). The cross section of the column is constant over its length and is entirely defined by the mid-line diameter as shown in figure A.1. The time-dependent load $f(t)$, considered stationary, is applied to the free end of the structure. The objective of this example is to minimize the weight of the column while ensuring that the peak displacement taken at the top of the structure is within a prescribed maximum.

The time history of the stationary random forcing function $f(t)$ is given by:

$$f(t) = a + bf_d(t) \tag{A.1}$$

where a and b are constants while $f_d(t)$ is a normalized gaussian random variable with correlation structure given by $\rho^{|\alpha|}$ where α is the time lag between two points. From a numerical point of view $f_d(t)$ can be generated by the following formula:

$$f^{(i+1)} = \rho f^{(i)} + \sqrt{1-\rho^2} Wh^{(i)} \tag{A.2}$$

where ρ is the correlation between two successive points of the time history while $Wh^{(i)}$ is the ith point of a generic white noise signal.

In this example $a = 40000$ N, $b = 20000$ N while the correlation is taken as $\rho = 0.9$. A sampling frequency of 80 Hz and a total signal duration of 750 s were considered. The forcing function and associated spectra are shown in figure A.2.

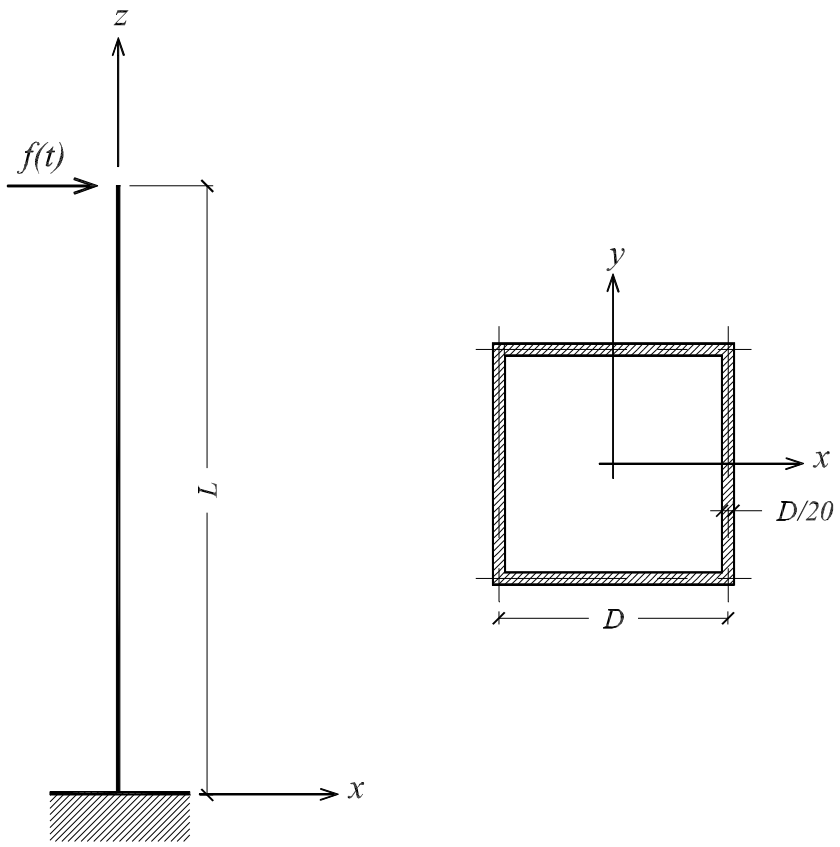

Figure A.1: Scheme.

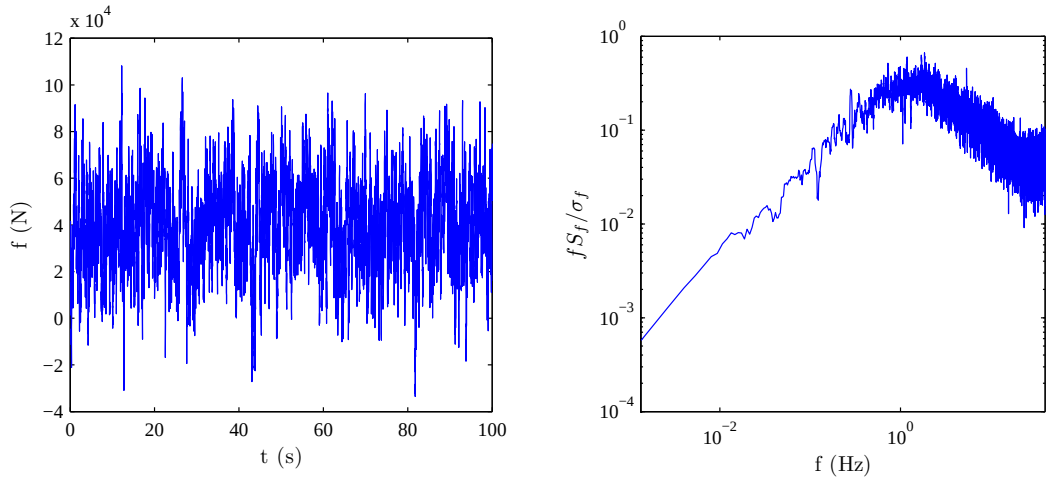

(a) (b)

Figure A.2: Forcing function: (a) 100 s of time history, (b) smoothed PSD.

A.2 Equations of motion

The dynamic response of the column can be modeled by a single degree of freedom system and is therefore governed by the following equation:

$$m\ddot{x} + c\dot{x} + kx = f(t) \tag{A.3}$$

where m is the lumped mass at the top of the column taken as half of the mass of the structure, c is the damping coefficient while k is the stiffness of the column concerning horizontal displacements (x-direction in figure A.1). For this example m, c and k are given by:

$$\begin{cases} m = \frac{\rho_s LA}{2} \\ \frac{1}{k} = \frac{L^3}{3EI_x} + \frac{L}{GA_x} \\ c = 2\sqrt{km}\xi \end{cases} \tag{A.4}$$

where L is the length of the column, A is the cross sectional area, ρ_s is the mass density of steel, I_y is the moment of inertia around the y-axis, A_x is the shear area in the x-direction while ξ is the damping ratio taken equal to 0.015.

To estimate the response of this system any numerical integration scheme may be used. In this example the Newmark scheme was adopted.

A.3 Optimization

In this section the procedure proposed in chapter 7 is used to solve the following optimization problem:

$$\text{minimize} \qquad W = \gamma LA \tag{A.5}$$

subject to:

$$\hat{x} = \mu_x + g\sigma_x \leq x^U \tag{A.6}$$

where μ_x is the mean value of the response process $x(t)$, σ_x is the standard deviation of $x(t)$, g is the peak factor, x^U is the upper limit posed on the displacement at the top of the column while γ is the specific weight of steel.

The first step in the optimization process is the definition of the explicit link functions (see section 7.3.1). Taking the mid-line diameter of the column, D, as the design variable the following functions can be defined:

$$\begin{cases} \frac{1}{A} = \chi_1(D) = \frac{5}{D^2} \\ \frac{1}{A_x} = \chi_2(D) = \frac{19}{2D^2} \\ \frac{1}{I_y} = \chi_3(D) = \frac{30}{D^4} \end{cases} \tag{A.7}$$

The next step is the definition of the functions Γ_2 and Γ_3 (see section 7.3.1), where Γ_1 is not necessary for this example due to the absence of axial force. Γ_2 and Γ_3 may

be defined by first applying a unit load at the top of the column in the x-direction therefore defining the following functions (see section 7.3.1):

$$\begin{cases} f_2^* = \frac{v^*}{G} = \frac{1}{G} \\ f_3^* = \frac{m_y^*}{E} = \frac{L-z}{E} \end{cases} \tag{A.8}$$

where v^* is the shear due to the unit loading while m^* is the bending moment around the y-axis. f_2^* and f_3^* can then be used to define F_2^* and $F_3^{*(1)}$ as:

$$\begin{cases} F_2^* = Lf_2 = \frac{L}{G} \\ F_3^{*(1)} = \frac{L}{6}(2f_3^{*(1)} + f_3^{*(2)}) = \frac{L^2}{3E} \end{cases} \tag{A.9}$$

in which the apexes (1) and (2) indicate that the internal forces have been evaluated in the initial and final cross sections of the member. Finally, Γ_2 and Γ_3 may be calculated as:

$$\begin{cases} \Gamma_2(t) = F_2^* V_x(t) = \frac{L}{G} V_x(t) \\ \Gamma_3(t) = F_3^{*(1)} M_y^{(1)}(t) = \frac{L^2}{3E} M_y^{(1)}(t) \end{cases} \tag{A.10}$$

where $V_x(t)$ is the time varying shear while $M_y^{(1)}(t)$ is the time varying bending moment calculated in the initial section of the column. The dynamic internal forces may be calculated from the solution of the dynamic equilibrium of equation (A.3) through the following influence coefficients:

$$\begin{cases} \vartheta_{V_x} = k \\ \vartheta_{M_y^{(1)}} = Lk \end{cases} \tag{A.11}$$

From the knowledge of ϑ_{V_x} and $\vartheta_{M_y^{(1)}}$ the dynamic internal forces are given by:

$$\begin{cases} V_x(t) = \vartheta_{V_x} x(t) = Lkx(t) \\ M_y^{(1)}(t) = \vartheta_{M_y^{(1)}} x(t) = kx(t) \end{cases} \tag{A.12}$$

From the knowledge of Γ_2, Γ_3 and $\chi_2(D)$, $\chi_3(D)$, equation (7.25) can be used to define the following approximate explict expression in terms of D around the current design point for the constrained function of equation (A.6):

$$\hat{x} = \chi_2 \mu_{\Gamma_2} + \chi_3 \mu_{\Gamma_3} + g\sqrt{\chi_2 \chi_2 C_{\Gamma_2\Gamma_2} + \chi_3 \chi_3 C_{\Gamma_3\Gamma_3} + 2\chi_2 \chi_3 C_{\Gamma_2\Gamma_3}} \tag{A.13}$$

where $C_{\Gamma_2\Gamma_2}$, $C_{\Gamma_3\Gamma_3}$ and $C_{\Gamma_2\Gamma_3}$ are the covariance coefficients between the Γ functions defined in equation (A.10).

A.3.1 Calibration of the OC algorithm

In order to find the optimal solution of the problem outlined in equations (A.5) and (A.6) the OC algorithm presented in chapter 3 may be used. In particular,

the expression (3.19) for the design variable, D, and the expression (3.22) for the associated Lagrange multiplier, λ, are necessary for defining the OC algorithm. In order to use these expressions the following functions and derivatives are necessary:

$$\begin{cases} \frac{dW}{dD} = \frac{2D\gamma L}{5} \\ \hat{x} = \frac{19}{2D^2}\mu_{\Gamma_2} + \frac{30}{D^4}\mu_{\Gamma_3} + g\sqrt{\frac{361}{4D^4}C_{\Gamma_2\Gamma_2} + \frac{900}{D^8}C_{\Gamma_3\Gamma_3} + \frac{570}{D^6}C_{\Gamma_2\Gamma_3}} \\ \frac{d\hat{x}}{dD} = -\frac{19}{2D^2}\mu_{\Gamma_2} - \frac{120}{D^5}\mu_{\Gamma_3} - g\left(\frac{\frac{361}{D^5}C_{\Gamma_2\Gamma_2}+\frac{7200}{D^9}C_{\Gamma_3\Gamma_3}+\frac{3420}{D^7}C_{\Gamma_2\Gamma_3}}{\sqrt{\frac{361}{4D^4}C_{\Gamma_2\Gamma_2}+\frac{900}{D^8}C_{\Gamma_3\Gamma_3}+\frac{570}{D^6}C_{\Gamma_2\Gamma_3}}}\right) \end{cases} \tag{A.14}$$

From the knowledge of these last, equations (3.19) and (3.22) are fully defined taking the following form:

$$D^{(\tau+1)} = D^{(\tau)}\left[1 + \frac{1}{\eta}\left(-\frac{\lambda\frac{d\hat{x}}{dD}}{\frac{dW}{dD}} - 1\right)\right]_\tau \tag{A.15}$$

$$\lambda^{(\tau)}\left(\frac{D\left(\frac{d\hat{x}}{dD}\right)^2}{\frac{dW}{dD}}\right)_\tau = -\left(D\frac{d\hat{x}}{dD}\right)_\tau - \eta(x^U - \hat{x}^{(\tau)}) \tag{A.16}$$

where $(\tau+1)$ and (τ) are the iteration numbers.

A.3.2 Numerical example

In this section a numerical example is developed for the structure shown in figure A.1. In particular L was taken as 6 m while the upper limit on the horizontal displacement x^U was taken as 0.4 m. A peak factor g of 3.5 was considered alongside the following initial design variable $D^{(0)} = 0.3$.

By analyzing the initial structure the following covariance matrix, $\mathbf{C}_\Gamma$, for $\Gamma_2(t)$ and $\Gamma_3(t)$ is calculated:

$$\mathbf{C}_\Gamma = \begin{bmatrix} 1.81\text{e-}11 & 8.11\text{e-}11 \\ 8.11\text{e-}11 & 36.33\text{e-}11 \end{bmatrix}$$

From equations (A.14) and $\mathbf{C}_\Gamma$ it is possible to calculate the function and derivative values:

$$\begin{cases} \frac{dW}{dD} = 56520\ \text{Nm} \\ \hat{x} = 0.301\ \text{m} \\ \frac{d\hat{x}}{dD} = -6.674\ \text{m}^2 \end{cases}$$

Substituting these values into equation (A.16) and solving for the Lagrange multiplier while considering $\eta = 3$ the following initial value is calculated:

$$\lambda^{(0)} = \frac{-\left(D\frac{d\hat{x}}{dD}\right)_0 - \eta(x^U - \hat{x}^{(0)})}{\left(\frac{D\left(\frac{d\hat{x}}{dD}\right)^2}{\frac{dW}{dD}}\right)_{(0)}} = 7212.2 \tag{A.17}$$

From this intial value of the Lagrange multiplier it is now possible to calculate the updated value for the design variable $D^{(1)}$ from equation (A.15):

$$D^{(1)} = D^{(0)} \left[1 + \frac{1}{\eta} \left(-\frac{\lambda \frac{d\hat{x}}{dD}}{\frac{dW}{dD}} - 1 \right) \right]_{(0)} = 0.2852 \,\mathrm{m} \tag{A.18}$$

By successively applying equations (A.17) and (A.18) convergence is reached for D and λ. The iteration history is reported in table A.1.

From table A.1 it is evident that after around 10 iterations the OC algorithm has converged.

If the structure was not subject to any resonant effects this minimum would represent the final optimum design. However due to the presence of significant dynamic amplification, after convergence of this problem (defined as the explicit sub-problem in chapter 7) the dynamic equilibrium must be recalculated through solving equations A.3 having updated the mass and stiffness of the system. From the newly estimated dynamic response the sub-problem is redefined and solved once again. Each update of the dynamic equilibrium is termed a design cycle.

For the example under consideration in this section figures A.3(a) to A.4(b) show the design cycle history for the weight W, design variable D, frequency $f = \sqrt{\frac{k}{m}}$ and peak response $\hat{x}$. It is immediately evident how after a limited number of redesigns, around four, the overall procedure converges. The results of the design cycles are also reported in table A.2.

Iteration (τ)	Design variable $D^{(\tau)}$	Peak response $\hat{x}$	L. multiplier λ	Weight W
0	0.3000	0.3010	7212.2	8478.0
1	0.2852	0.3685	6012.8	7660.2
2	0.2815	0.3880	5707.4	7464.2
3	0.2802	0.3953	5598.8	7394.9
4	0.2797	0.3981	5557.2	7368.4
5	0.2795	0.3993	5540.8	7358.0
6	0.2794	0.3997	5534.3	7353.8
7	0.2794	0.3999	5531.7	7352.2
8	0.2794	0.4000	5530.7	7351.5
9	0.2794	0.4000	5530.3	7351.2
10	0.2794	0.4000	5530.1	7351.1
11	0.2794	0.4000	5530.0	7351.1
12	0.2794	0.4000	5530.0	7351.1
13	0.2794	0.4000	5530.0	7351.1
14	0.2794	0.4000	5530.0	7351.1

Table A.1: Iteration history.

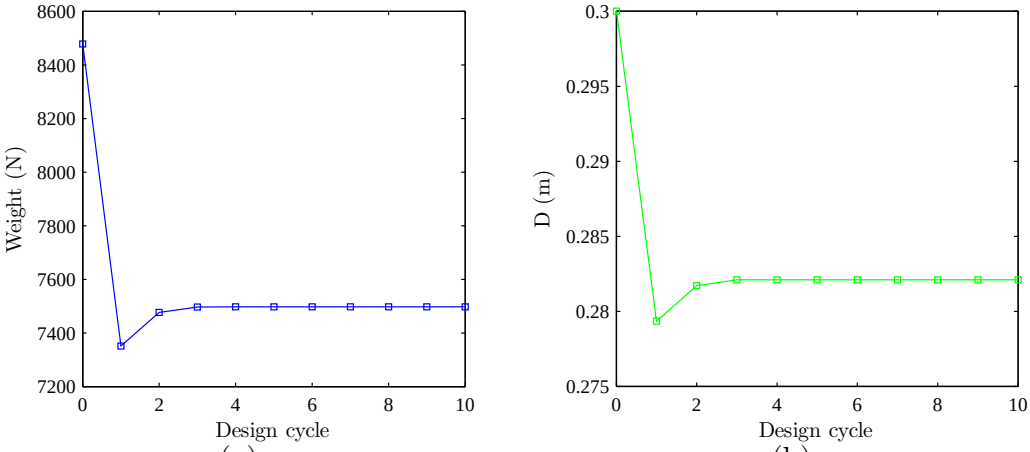

(a) (b)

Figure A.3: Design cycle history: (a) weight W, (b) design variable D.

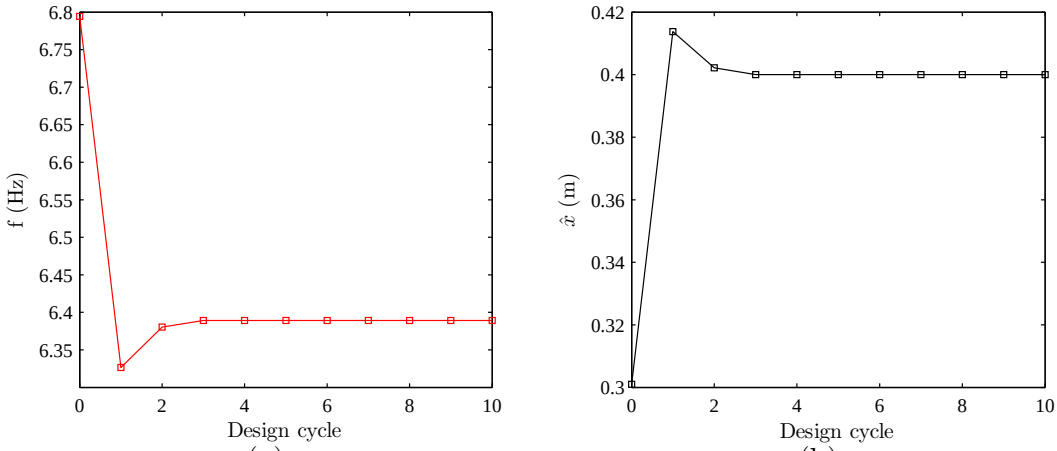

(a) (b)

Figure A.4: Design cycle history: (a) frequency f, (b) peak response $\hat{x}$.

Design cycle	D	$\hat{x}$	f	W
0	0.3000	0.3010	6.7942	8478.0
1	0.2793	0.4137	6.3265	7351.1
2	0.2817	0.4022	6.3804	7476.7
3	0.2821	0.4000	6.3890	7497.0
4	0.2821	0.4000	6.3892	7497.3
5	0.2821	0.4000	6.3892	7497.3
6	0.2821	0.4000	6.3892	7497.3
7	0.2821	0.4000	6.3892	7497.3
8	0.2821	0.4000	6.3892	7497.3
9	0.2821	0.4000	6.3892	7497.3
10	0.2821	0.4000	6.3892	7497.3

Table A.2: Design cycle history.